



Peer Reviewed

Title:

Capturing the Impact of Riverine Nutrient Delivery on Coastal Ocean Biogeochemistry

Author:

[Olhsson, Elizabeth Halley](#)

Acceptance Date:

2014

Series:

[UC Berkeley Electronic Theses and Dissertations](#)

Degree:

Ph.D., [Environmental Science, Policy, & Management](#)[UC Berkeley](#)

Advisor(s):

[Powell, Thomas M](#), [Getz, Wayne](#)

Committee:

[Baldocchi, Dennis](#), [Dietrich, William](#)

Permalink:

<http://escholarship.org/uc/item/34k135nq>

Abstract:

Copyright Information:

All rights reserved unless otherwise indicated. Contact the author or original publisher for any necessary permissions. eScholarship is not the copyright owner for deposited works. Learn more at http://www.escholarship.org/help_copyright.html#reuse



eScholarship
University of California

eScholarship provides open access, scholarly publishing services to the University of California and delivers a dynamic research platform to scholars worldwide.

Capturing the Impact of Riverine Nutrient Delivery on Coastal Ocean Biogeochemistry

By

Elizabeth Halley Olhsson

A dissertation submitted in partial satisfaction of the

requirements for the degree of

Doctor of Philosophy

in

Environmental Science, Policy and Management

in the

Graduate Division

of the

University of California, Berkeley

Committee in charge:

Professor Thomas M. Powell, co-Chair

Professor Wayne Getz, co-Chair

Professor Dennis Baldocchi

Professor William Dietrich

Fall 2014

Abstract

Capturing the Impact of Riverine Nutrient Delivery on Coastal Ocean Biogeochemistry

by

Elizabeth Halley Olhsson

Doctor of Philosophy in Environmental Science, Policy and Management

University of California, Berkeley

Professor Thomas M. Powell, co-Chair

Professor Wayne Getz, co-Chair

Rivers smaller than the Amazon tend to be excluded from earth system modeling efforts. Does it matter? Do sub-grid-scale rivers have significant impacts on offshore primary productivity? Using the Eel River in northern California, the river with the largest sediment yield per drainage area in the continental United States, as a test case, this question is explored using two approaches. First, a data-driven analysis of relevant time series taken on land, by buoy, and from space, demonstrates very little evidence of direct impact of Eel River discharge on contemporaneous coastal ocean primary productivity – but to the extent that that evidence exists, it seems to occur during years of greatest river discharge. To further analyze mechanistic drivers, a coupled mesoscale modeling framework unifying ocean, watershed and atmospheric representations is formulated and run in hindcast over the 2002-2010 period. Monthly average climatologies, interannual variabilities, and event-driven analysis of each year's largest river discharge are all examined for evidence of a river-ocean connection expressed through primary production. Storm event-generated turbulence appears to dominate the primary productivity during the winter months. The impact of the river seems to be largely independent of nutrient load, because its dissolved nitrate is less than that of the coastal ocean. There is no evidence that riverine delivery of gradually bioavailable detritus has a significant effect. Although a sufficiently super-nitrous river shows the ability to sustain a plume-nutrient-driven-bloom even at periods of extremely low flow, this is not currently a realistic scenario for the Eel River. The possibility remains that another micronutrient not studied in the modeling framework, such as iron, could be important to this system.

Dedication

For Gary, my dad.

Table of Contents

Abstract	1
Dedication	i
Table of Contents	ii
List of Figures	v
List of Tables	x
Introduction	xii
Acknowledgements	xv

Chapter 1: Eel River Data Analysis

1.1 Introduction	1
1.2 The Eel River: Overview	1
1.3 The Eel River: Literature Review	3
1.3.1 1910-1979	3
1.3.2 1980-1989	4
1.3.3 1990-1999	4
1.3.4 2000-present	6
1.3.5 Empirical Sediment Models and the Eel	7
1.4 Data Analysis: Overview	9
1.5 Estimation of NPP from ocean color data	11
1.6 MODIS data	12
1.7 NBDC buoy data	13
1.8 USGS gauging station data	14
1.9 Methodology: Granger's Test for Predictive Causality	14
1.10 Results: Granger Causality	15
1.11 Methodology: Canonical Correlation Analysis	18
1.12 Results: CCA	20
1.13 Discussion and Conclusion	22

Chapter 2: Methodology

2.1 Introduction and Literature Review: Previous Relevant Modeling Efforts	34
2.2 Modeling Framework Overview	36
2.3 Atmospheric Forcing	37
2.3.1 NARR	38
2.3.2 Bulk flux approximations in ROMS, 10 km horizontal resolution	38
2.3.3 ERA-Interim	38
2.3.4 Comparison: ERA-Interim vs. NARR, regional scale	39
2.3.5 Comparison: ERA-Interim vs. NARR vs. Daymet data, local scale	49
2.4 Hydrological Modeling: HydroTrend	54
2.4.1 HydroTrend Description	54
2.4.2 HydroTrend Discharge	55
2.4.3 HydroTrend Sediment	58
2.4.4 HydroTrend Parameterization	60
2.5 Ocean Modeling: Regional Ocean Modeling System	63

2.5.1 Equations of Motion	63
2.5.2 Curvilinear Coordinates	65
2.5.3 Vertical Coordinates	65
2.5.4 Domain and Grid Resolution	66
2.5.5 Bathymetry	68
2.5.6 Temporal Resolution and Numerics	69
2.5.7 Horizontal Diffusion and Viscosity	70
2.5.8 Vertical Mixing Parameterization	70
2.5.9 Boundary Conditions	71
2.5.9.1 Lateral Boundary Conditions	71
2.5.9.2 Bottom Boundary Conditions	72
2.5.10 Surface Model Forcing	73
2.5.11 River Forcing	74
2.5.12 Model Initialization and Spinup	75
2.6 Biogeochemical Modeling: Nutrient-Phytoplankton-Zooplankton-Detritus	76
2.6.1 NPZD description and limitations	76
2.6.2 NPZD ROMS dynamics	79
2.6.3 NPZD initial and boundary conditions	79
2.6.4 NPZD riverine input	79
2.7 Model Experimental Design	83
2.8 Model Results	84
2.8.1 Results: HydroTrend	84
2.8.2 Results: ROMS, 10 km resolution	87
2.8.2.1 Climatological validation	87
2.8.2.2 Short timescale validation	91
2.8.3 Results: ROMS, 1 km resolution	93
2.9 Conclusion	95
Chapter 3: Results	
3.1 Introduction	96
3.2 MODIS validation; coverage and cloud gap-filling	98
3.3 Climatological comparisons	102
3.4 Interannual variability comparisons	106
3.4.1 Correlative analysis of December 2002-2009	106
3.4.2 Empirical Orthogonal Function analysis of December Interannual Variability	110
3.4.3 Comparison of Decembers with varying river conditions	113
3.4.4 Summary of interannual variability comparisons	122
3.5 Event-driven comparisons	124
3.5.1 Large river, deep mixed layer	126
3.5.2 Small river, deep mixed layer	128
3.5.3 Large river, shallow mixed layer	130
3.5.4 Small river, shallow mixed layer	132
3.5.5 Summary of event-driven comparisons	134
3.6 No-nutrient river modeling	134
3.7 Extra-nutrient river modeling	138
3.8 Chl:C sensitivity testing	140

3.9 Southwestern model artifact and nonlinear model drift	140
3.10 Discussion	142
3.11 Future Directions	145
3.12 Conclusion	146
Bibliography	147

List of Figures

Figure 1.1: The Eel River watershed (Lisle 1990).	3
Figure 1.2: The NPP (blue left Y axis) and Wind (red, right Y axis) Indices, 2003-2012.	10
Figure 1.3: Yearly NPP and Wind Index plots, with upwelling and significant months of river flow shaded.	11
Figure 1.4: Simplified visualization of where satellite data are selected for analysis.	13
Figure 1.5: Granger causality test results, Wind and NPP Indices during the upwelling-dominated period.	17
Figure 1.6: Granger causality test results, Wind and NPP Indices during the storm-dominated period.	18
Figure 1.7: The matrix F to be decomposed into EOFs, mapped to have each row as one year's worth of time series, and each column a time series of observations for a given date within a year. Figure adapted from (Bjornsson and Venegas 1997).	19
Figure 1.8: The first and largest modes of covariation (EOF1) for NPP (A) and Wind (B) in the case where we analyze the system without removing the interannual mean from each point, and for NPP (C) and Wind (D) when we study the covariance of the anomalies. The x-axis is day of year. With the upwelling signal (seen in A and B) removed, other patterns (seen in C and D) emerge to represent most of the covariation.	21
Figure 1.9: The fifth modes of covariation (EOF5) for NPP (A) and Wind (B) in the case where we analyze the system by removing the interannual mean/seasonality from each point. The x-axis is day of year. C plots the expansion coefficients/time amplitudes for A, with the x-axis now showing the 1-7 years of the analysis (2003-2009). D shows water year river discharge for each of the same years.	22
Figure 1.10: A reference volume of mixed layer in the ocean. \bar{w}_1 is the horizontal velocity of Ekman transport offshore, \bar{w}_2 is the upwelling velocity, \bar{T} is the surface wind stress, L is a reference length of coastline, D is the distance offshore, and H is the depth of the mixed layer.	24
Figure 2.1: The coupled modeling framework.	37
Figure 2.2: 1985-2010 January climatology of precipitation, ERA-Interim subtracted from NARR, and a histogram of the values that went into the climatologies.	41
Figure 2.3: 1985-2010 July climatology of precipitation, ERA-Interim subtracted from NARR, and a histogram of the values that went into the climatologies.	42
Figure 2.4: 1985-2010 January climatology of temperature, ERA-Interim subtracted from NARR, and a histogram of the values that went into the climatologies.	43
Figure 2.5: 1985-2010 July climatology of temperature, ERA-Interim subtracted from NARR, and a histogram of the values that went into the climatologies.	44
Figure 2.6: 1985-2010 January climatology of U (east-west) winds, ERA-Interim subtracted from NARR, and a histogram of the values that went into the climatologies.	45
Figure 2.7: 1985-2010 July climatology of U (east-west) winds, ERA-Interim subtracted from NARR, and a histogram of the values that went into the climatologies.	46

Figure 2.8: 1985-2010 January climatology of V (north-south) winds, ERA-Interim subtracted from NARR, and a histogram of the values that went into the climatologies.	47
Figure 2.9: 1985-2010 July climatology of V (north-south) winds, ERA-Interim subtracted from NARR, and a histogram of the values that went into the climatologies.	48
Figures 2.10 (top) and 2.11 (bottom): mean monthly temperature and precipitation for the Daymet Dataset, the North American Regional Reanalysis, and ERA-Interim.	50
Figure 2.12: Comparison of the within-month standard deviation of Daymet temperature data to the monthly average difference between Daymet data and the North American Regional Reanalysis.	51
Figure 2.13: Comparison of the within-month standard deviation of Daymet precipitation data to the monthly average difference between Daymet data and the North American Regional Reanalysis.	52
Figure 2.14: Comparison of the within-month standard deviation of Daymet temperature data to the monthly average difference between the Daymet data and the ERA-Interim.	53
Figure 2.15: Comparison of the within-month standard deviation of Daymet precipitation data to the monthly average difference between the Daymet data and the ERA-Interim.	54
Figure 2.16: Partitioning and transport within the water cycle, in HydroTrend 3.0.	55
Figure 2.17: The spatial extent of the two ROMS domains.	67
Figure 2.18: A graphical representation of the terrain-following vertical structure of the grid, taken across a vertical transect from eastern to western boundary. The x-axis is longitude. Note that the long flat stretch to the west is land, and masked off from the simulation.	68
Figure 2.19 (from Banas 2009b): The structure of an NPZD-type ecosystem model.	78
Figure 2.20: Figure by Dr. Jonah Piovia-Scott. USGS nutrient concentrations at Scotia, CA taken between 1959-present, and monthly climatological averages.	80
Figure 2.21: Figure by Dr. Jonah Piovia-Scott. USGS nutrient flux at Scotia, CA calculated by multiplying nutrient concentration at time of measurement by measured river discharge at time of measurement, and monthly climatological averages. The flux is clearly dominated by the increased river discharge in the winter.	81
Figure 2.22: A graphical representation of the transformation of HydroTrend output into NPZD nutrients.	82
Figure 2.23: Annual average discharge vs. sediment load for HydroTrend results versus the USGS validation data. Note that this is a fairly tight cluster far from zero, but zoomed in on both axes in order to be able to see the differences.	85
Figure 2.24a: ERA-Interim driven HydroTrend vs. USGS gauging data for discharge, 1998-2010.	86
Figure 2.24b: HydroTrend results vs. USGS data, 1998-2010.	87
Figure 2.25: ROMS 10 km results (left) and SODA (right) for sea surface temperature, zonal (east-west) velocity and meridional (north-south) velocity climatologies for the month of January, 2000-2010.	89
Figure 2.26: ROMS 10 km results (left) and SODA (right) for sea surface temperature, zonal (east-west) velocity and meridional (north-south) velocity climatologies for the month of July, 2000-2010.	90

Figure 2.27: ROMS vs. satellite sea surface temperature for a 48-hour period around 6/22/2001. The mouth of the Eel River is starred.	91
Figure 2.28: Taylor Diagram for 10 km ROMS results from section 2.8.2.	92
Figure 2.29: 1 km ROMS in the coupled modeling framework, producing a river plume on 12/24/2004. Units are psu. The bottom plot is the same as the top with the colorbar zoomed in.	94
Figure 3.1: Daily averaged values of phytoplankton concentration in the first week of December 2004, taken at 40.5 N, -124.5 W, at the sea surface and at 10m depth.	100
Figure 3.2: Daily averaged values of phytoplankton concentration in the first week of July 2004, taken at 40.5 N, -124.5 W, at the sea surface and at 10m depth.	101
Figure 3.3: ROMS chlorophyll climatologies (A, D, G), MODIS chlorophyll climatologies (B, E, H), and the ROMS climatology integrated vertically across the water column, for water years 2002-2010, with the no-river model control subtracted (C, F, I). Monthly climatologies are sorted by row for November (top), December (middle) and January (bottom). Units are mg chl-a per cubic meter (square meter, in the case of the integration).	104
Figure 3.4: ROMS chlorophyll climatologies (A, D, G), MODIS chlorophyll climatologies (B, E, H), and the ROMS climatology integrated vertically across the water column, for water years 2002-2010, with the no-river model control subtracted (C, F, I). Monthly climatologies are sorted by row for February (top), March (middle) and April (bottom). Units are mg chl-a per cubic meter (square meter, in the case of the integration).	105
Figure 3.5: ROMS chlorophyll climatology (A), MODIS chlorophyll climatology (B), and the ROMS climatology integrated vertically across the water column, for water years 2002-2010, with the no-river model control subtracted (C). Climatologies are for the month of May, the latest month in which significant Eel river discharge is found to ever occur from 2000-2010. Units are mg chl-a per cubic meter (square meter, in the case of the integration).	106
Figure 3.6: Correlations between mixed layer depth and A: surface stress, B: mean river discharge, C: shortwave radiation, and E: phytoplankton concentration, as well as phytoplankton concentration vs. D: mean river discharge and F: shortwave radiation flux.	109
Figure 3.7: The first three empirical orthogonal functions of the 32-point time series comprised of four 8-day averages per December from 2002-2009, and their variation in time of amplitude.	111
Figure 3.8: 8-day averaged time series of Eel River discharge (A), annual Oceanic Nino Index (B) and Pacific Decadal Oscillation (C) for December 2002-2009. Red and blue bars are positive and negative anomalies respectively.	112
Figure 3.9: Daily mean Eel River discharge for December 2003, 2005 and 2008.	113
Figure 3.10: 8-day average chlorophyll-a concentrations as seen from space by MODIS for Decembers of interest: 2003, 2005 and 2008. The mouth of the Eel River is starred.	114

Figure 3.11: 8-day averaged model results for December 2003. A: Chlorophyll at 4m depth produced by the fully coupled modeling framework. B-E: Vertical transect of the model at 40.64 N, out to 10 km offshore, with the no-river control subtracted from the full model, for chlorophyll (B), salinity (C), temperature (D) and meridional velocity (E).	116
Figure 3.12: 8-day averaged model results for December 2005. A: Chlorophyll at 4m depth produced by the fully coupled modeling framework. B-E: Vertical transect of the model at 40.64 N, out to 10 km offshore, with the no-river control subtracted from the full model, for chlorophyll (B), salinity (C), temperature (D) and meridional velocity (E).	119
Figure 3.13: 8-day averaged model results for December 2008. A: Chlorophyll at 4m depth produced by the fully coupled modeling framework. B-E: Vertical transect of the model at 40.64 N, out to 10 km offshore, with the no-river control subtracted from the full model, for chlorophyll (B), salinity (C), temperature (D) and meridional velocity (E).	121
Figure 3.14: 8-day average starting at 12/31/2005, the highest Eel River discharge day in the 2002-2003 water year. A: ROMS phytoplankton. B: MODIS phytoplankton. C: ROMS results minus the no-river control model results for phytoplankton. D, E, F: ROMS phytoplankton, detritus, and nitrate respectively, at a 40.64 vertical transect (5 km north of the Eel River mouth) out to 124.45 W. G, H, I: As D, E, F, with the no-river control subtracted from the results. J, K: ROMS salinity and temperature along the same vertical transect. L, M: As J and K, with the no-river control subtracted from the results.	127
Figure 3.15: As Figure 3.14, for the 8-day average starting at 12/27/2006, the highest Eel River discharge day in the 2006-2007 water year.	129
Figure 3.16: As Figure 3.14, for the 8-day average starting at 02/18/2004, the highest Eel River discharge day in the 2003-2004 water year.	131
Figure 3.17: As Figure 3.14, for the 8-day average starting at 01/05/2008, the highest Eel River discharge day in the 2007-2008 water year.	133
Figure 3.18: 8-day averaged phytoplankton results from the no-nutrient river control subtracted from the with-nutrient river, beginning 02/02/2006, which is also the time of delivery of the second-largest river discharge event of the water year. Note that ambient phytoplankton concentration at the mouth of the Eel River is 1.5 mg chl-a/m ³ , such that this difference accounts for no more than 4% of the total.	135
Figure 3.19: 8-day averaged phytoplankton results from the no-nutrient river control subtracted from the with-nutrient river, beginning 02/09/2006. Note that ambient phytoplankton concentration at the mouth of the Eel River is 0.5 mg chl-a/m ³ , such that this difference accounts, as in Figure 3.18, for no more than 4% of the total.	136
Figure 3.20: 8-day averaged phytoplankton results from the no-nutrient river control subtracted from the with-nutrient river, beginning 02/17/2006. Note that ambient phytoplankton concentration at the mouth of the Eel River is 0.5 mg chl-a/m ³ , such that this difference accounts, as in Figures 3.18-.3.19, for no more than 4% of the total.	137
Figure 3.21: A large phytoplankton bloom generated by the coupled modeling framework during low-flow conditions in July, with the Eel River given 400x its normal load of dissolved inorganic nitrogen.	139

Figure 3.22: 11/25/05 example of the model artifact vortex created by momentum over the Mendocino Triple Junction, and further interactions with the unstable southern boundary.	141
--	-----

List of Tables

Table 1.1: Granger causality test results.	16
Table 1.2: The squared covariance fractions of the first 8 modes of covariation for the NPP and Wind Indices with and without the mean of each annual time point removed. Without removing the mean, there are seven significant modes of variation; removing the mean creates a system with only six.	20
Table 1.3: 2000-present Eel River papers by topic. Literature reviews and other particularly useful papers are highlighted. Internal watershed dynamic literature is excluded.	26
Table 2.1: Parameters used in HydroTrend calculations.	61
Table 2.2: Definitions of terms used in section 2.5.	64
Table 2.3: Lateral boundary conditions used for the ocean circulation model.	71
Table 2.4: Atmospheric forcing fields and their units, as applied directly to the sea surface with the ERA-Interim dataset.	74
Table 2.5: Powell et al. (2006) parameters used for Powell-NPZD.	78
Table 2.6: Summary of differences between 10 and 1 km model applications.	83
Table 2.7: Summary of model experiments.	84
Table 2.8: HydroTrend results summary for discharge and sediment. Visualized in Figure 2.23.	84
Table 3.1: Average over-ocean chlorophyll-a satellite coverage in the 39.5-41.5 N, 123-125 W region of interest near Cape Mendocino for the November-June 2002-2010 climatologies.	98
Table 3.2: Average over-ocean chlorophyll-a satellite coverage in the 39.5-41.5 N, 123-125 W region of interest near Cape Mendocino for the 8-day averages within December 2003, 2005 and 2008.	99
Table 3.3: Average over-ocean chlorophyll-a satellite coverage in the 39.5-41.5 N, 123-125 W region of interest near Cape Mendocino for the 8-day averages surrounding each of the largest Eel River discharge events in the 2002-2009 water years. (The event falls in the second of three 8-day averages in all years.)	99
Table 3.4: Pattern cross-correlation values (R) and normalized standard deviations for the November-June model climatologies (2002-2010) as compared to MODIS climatologies over the same period.	103
Table 3.5: December mixed layer depths and maximum phytoplankton concentrations at 40.64 N, -124.36 W, ocean depth 290m.	107
Table 3.6: Pattern cross-correlation (R) values and normalized standard deviation comparisons between December 2003 model results and MODIS data.	117
Table 3.7: Pattern cross-correlation (R) values and normalized standard deviation comparisons between December 2005 model results and MODIS data.	120
Table 3.8: Pattern cross-correlation (R) values and normalized standard deviation comparisons between December 2005 model results and MODIS data.	122
Table 3.9: Summary of conditions near the Eel River mouth during the largest discharge event of each water year. Maxima and minima have been highlighted.	124
Table 3.10: Categorization of oceanic conditions and relative strength of the largest Eel River discharge event of each water year.	124

Table 3.11: Pattern cross-correlation (R) values and normalized standard deviations for the 8-day averages around 2002 and 2005 events, comparing the model results with to MODIS data.	126
Table 3.12: Pattern cross-correlation (R) values and normalized standard deviations for the 8-day averages around 2006 and 2008 (water year; 2008's event falls in early 2009) events, comparing the model results with and without the river with MODIS data.	128
Table 3.13: Pattern cross-correlation (R) values and normalized standard deviations for the 8-day averages around the 2003 (water year; the event occurs in early 2004) event, comparing the model results with and without the river with MODIS data.	130
Table 3.14: Pattern cross-correlation (R) values and normalized standard deviations for the 8-day averages around the 2004, 2007 and 2009 (water year; all events occur in winter-spring of the following year) event, comparing the model results with and without the river with MODIS data.	132
Table 3.15: The absolute magnitudes of November minus No River November climatological results within 10 km of the mouth of the Eel River.	142

Introduction

When considering the importance of rivers worldwide to coastal primary productivity, the Amazon, Mississippi, Congo, Ganges and Yangtze all come to the forefront as examples of key players. They drain millions of square kilometers apiece, discharging thousands of cubic meters of freshwater per second into the ocean, delivering massive loads of nutrients and sediment. But in earth system models, these massive conduits are the only sorts of rivers that appear; anything less becomes a sub-grid-scale parameterization. For example, in the Community Earth System Model (Gent et al. 2011), land cells transport a mass of what is functionally distilled water across their grid. Eventually this perfectly fresh water is spread evenly throughout the adjacent ocean, in an effort to close the water budget. Little attempt is made to capture lesser river-driven effects on coastal productivity.

Does it matter? That is the key question that motivates this thesis. *Do sub-grid-scale rivers have significant impacts on offshore primary productivity?* If so, effort must be made to include them more rigorously, for predictive capability at scales helpful to city, state, and regional policymakers. But there are thousands of smaller rivers in immensely variable settings worldwide. The best place to start is with a smaller river that seems especially likely to have a significant impact on offshore environment through its delivery of more than simply freshwater (its only representation in most global climate models) to the ocean. If such a river fails to alter offshore dynamics significantly, we can potentially discard many similar rivers with smaller loads. An obvious candidate in North America is the Eel River, California.

The Eel River discharges into the North Pacific at 40° 38.5' N, just north of Cape Mendocino in Northern California, delivering large loads of sediments, as well as nutrients, organic matter and organisms. Its annual discharge ($\sim 270 \frac{m^3}{s}$, Lisle 1990) is about 1% that of the Mississippi, but its sediment yield (which has historically reached as high as 15 million tons/year) is the highest for its drainage area ($\sim 9500 \text{ km}^2$) in the entire continental US (Brown and Ritter 1971). Furthermore, the Eel River is an especially advantageous choice for a test case because its annual behavior is dramatic and potentially very sensitive to changes in climate. Driven by the Mediterranean climate of northern California, it is characterized by low flow during the long, hot dry season. Then, each winter and spring, storm events flush nutrients down the river to the ocean, in large pulses (Goñi et al. 2013, Leithold et al. 2005).

These storm flows are out of phase with the other major nutrient input to local coastal biology: late spring and summer upwelling of cold, nutrient-rich ocean water to the photosynthetically active surface, as the west coast of North America is the setting for one of the world's largest coastal upwelling regions (Smith 1992). The timing and magnitude of these storm events (and thus the timing (and potentially, the magnitude) of Eel River nutrient delivery) have a great deal of interannual variability and may be altered by climate change (Morehead et al. 2001, Andrews and Antweiler 2012, Warrick et al. 2013).

Furthermore, evidence suggests that the fluxes from the Eel River may contribute to phytoplankton blooms offshore. Ocean color can be used as a surrogate measurement for chlorophyll and therefore primary productivity (Saba et al. 2011). Satellite imagery off of Cape

Mendocino has demonstrated spatial, seasonal and interannual variability of ocean color, north and south of the Eel River's discharge (Legaard and Thomas 2006, NOAA 2012a).

In order to evaluate the potential impact of the Eel River on coastal ocean productivity, two approaches are taken. In Chapter One, a data-driven analysis unifies satellite ocean color data, buoy wind measurements, gauging station river discharge rates, and estimations of upwelling strength. These time series are immensely noisy and complex. Evidence of connection between the river and the ocean are sought, using statistical techniques (Granger 1969) and empirical orthogonal functions (Barnett and Preisendorfer 1987). Eel River research literature is also reviewed, in an effort to summarize the many decades of work that have gone into understanding the watershed system and offshore processes.

Chapter Two describes a modeling approach used to study the Eel River's impact on the ocean at three timescales (climatologically, interannually, and daily events) in Chapter Three. If indeed the Eel River and other systems like it have a significant impact on coastal productivity, a regional model that can capture the intricacies of that behavior is a necessary tool for prediction. Water systems are vital for wildlife, for agriculture, for urban management; improving the field's capability to predict outcomes from and feedbacks to rivers is thus equally vital. Extensive and expensive field data studies such as the products of the River Influences on Shelf Ecosystems project (Hickey et al. 2010) have been used to drive regional models that examine large rivers; it is important to discover the extent to which a simpler approach, using existing data from sources such as the USGS, can be used to create a realistic simulation.

This dissertation constructs a coupled modeling framework to explore the connections between variability in weather (potentially modulated, slowly, by climate trends), river nutrient delivery to the ocean, and coastal phytoplankton productivity. Furthermore, it links models from multiple fields; whereas efforts have been made to force ocean circulation models with real river data (Castellano and Kirby 2011, Hickey et al. 2010, Warner et al. 2005, Li et al. 2005, Pullen and Allen 2001, Pullen and Allen 2000), this is an effort to connect an ocean model to a watershed model, unified beneath the same atmospheric representation. This framework has direct application to global climate modeling efforts; as a mesoscale entry to the earth system modeling field, it could be nested within larger simulations that explore a wide variety of climate scenarios. Although this study is limited to hindcasts, creating a modeling framework that could be used to create forecasts offers a lens through which to consider a related question: *how might climate change alter the behavior of the river, the coastal ocean, and the nutrient sources for coastal primary productivity?*

Furthermore, models allow us to conduct mechanistic experiments (Sasaki et al. 2006, Gruber et al. 2006, Capet et al. 2004). Comparing the results of a model with a river similar to that of the global climate models – which is to say, without any nutrients – with that of a river bearing a realistic set of nutrients, or an unrealistically large set of nutrients, allows consideration of the questions that go hand-in-hand with simply ‘does the river matter’: *If so, how and why does the river matter? Is the impact on primary productivity driven by physical or biogeochemical concerns? How does it compare relative to other oceanic processes such as upwelling? How might it interact with them? How do these relationships vary from season to season, year to year?* It is these questions that Chapter Three focuses on, through an examination of model

monthly climatologies, interannual variability, and event-driven analyses of the largest river deliveries of each water year between 2002 and 2010.

Data analysis and modeling efforts attempt to isolate a potentially very small signal in an extremely noisy system. But small impacts can accumulate over longer timescales (Allison et al. 2007). If the Eel River appears to have a significant effect on offshore primary productivity, its inclusion – and that of rivers like it – may be necessary to capture this link in earth system of land, ocean, and atmosphere.

Acknowledgements

All my gratitude goes to everyone who supported me throughout this program, from faculty, to students, to staff. Thanks to my advisor, Zack, and the rest of my committee, Wayne, Dennis and Bill. Special thanks also to Inez Fung, Mary Power, Jeff Dorman, Jonah Pilvia-Scott and Albert Kettner for their assistance, encouragement, and mentorship, and to Dave, Myrrh, Rebecca, Celia, Daala, Alice, Jill, Lain, Trudy, Gull, Lonny, Anna, Melissa, Jon and Cyrene for their tireless support. Thanks above all to my family: Mycol, Ryan, Mom and Gary, without whom this would not have been possible.

Chapter 1

1.1 Introduction

1.2 The Eel River: Overview

1.3 The Eel River: Literature Review

1.3.1 1910-1979

1.3.2 1980-1989

1.3.3 1990-1999

1.3.4 2000-present

1.3.5 Empirical Sediment Models and the Eel River

1.4 Data Analysis: Overview

1.5 Estimation of NPP from ocean color data

1.6 MODIS data

1.7 NBDC buoy data

1.8 USGS gauging station data

1.9 Methodology: Granger's Test for Predictive Causality

1.10 Results: Granger Causality

1.11 Methodology: Canonical Correlation Analysis

1.12 Results: CCA

1.13 Discussion and Conclusion

1.1 Introduction

In order to characterize the possible importance of smaller rivers on coastal ocean primary productivity, the Eel River is chosen as a test case for its depth of previous research and extremity of behavior, with most of its discharge occurring over a few days a year as driven by winter storms. After reviewing historical research on the Eel River, data are selected for analysis in an attempt to find connections between river and ocean behavior. By combining satellite ocean color data as an estimate of Net Primary Productivity and time series of river discharge, wind direction near the mouth of the river, and a monthly Upwelling Index (to identify times when the system is experiencing upwelling), it is possible to estimate when the river might be important to offshore primary productivity. It is also possible to estimate which direction its plume might be going, with sediments and nutrients entrained within for possible biological uptake.

Although qualitative observation of the time series provides some interesting insight, in order to more robustly search for the river's signal amid the noise of everything else going on, Granger causality (Granger 1969) and Canonical Correlation Analysis (Barnett and Preisendorfer 1987) techniques are used to examine the time series quantitatively. Finally, results and implications are discussed in detail, in terms of what can be gleaned from these analyses in order to direct further research.

1.2 The Eel River: Overview

The Eel River is the third largest watershed entirely contained in the state of California. It is 315 km long, flowing across 9540 km² of basin, and has the South, Middle, and North Fork Eel Rivers, plus the Van Duzen River, as tributaries (see Figure 1.1). It begins on Bald Mountain in the Pacific Coast Range, 1903 meters above sea level. It is used for groundwater recharge, recreation, industry, agriculture and for municipal water supply (Brown and Ritter 1971). This water use does not seem to heavily influence the nutrient content of the river (Madej et al. 2012, Goñi et al. 2013).

The Eel River's discharge is storm-driven, with virtually no precipitation from July-September producing, in turn, low flow during that time. The winter storm flow season begins, at the earliest, in late November, with the majority of the discharge occurring between December and March; on average, 90 percent of all precipitation falls between October and April (Lisle 1990).

These flows can be astonishing in scope, up to 26,500 $\frac{m^3}{s}$ on 12/23/1964, which comprises the largest recorded peak discharge of any river in California (Lisle 1990).

This event-driven flow, combined with the Coast Ranges' erosive bedrock, rapid uplift, and human disturbances (logging practices, primarily), also produces a stunning riverine sediment load, historically averaging $\sim 2.6 \times 10^7$ metric tons of suspended sediment a year (Brown and Ritter 1971; Syvitski et al. 1999; Wheatcroft and Borgeld 2000), although in recent decades there is strong evidence that the sediment load is in decline (EPA 1999, 2002, 2003, Warrick et al. 2013, Warrick 2014). Because the river has a very small flood plain and virtually no estuary, the majority of the suspended sediment load is transported directly into the Pacific Ocean (Wheatcroft et al. 1997). Initial plume deposition of the sediment can range up to 100 km from the river mouth, but secondary resuspension of sediment by gravity waves during storms causes perhaps the majority of the transport, both along and across-shelf (Puig et al. 2004). Warrick 2014 suggests that previous studies have overestimated secondary transport of sediment across the shelf and into deeper waters.

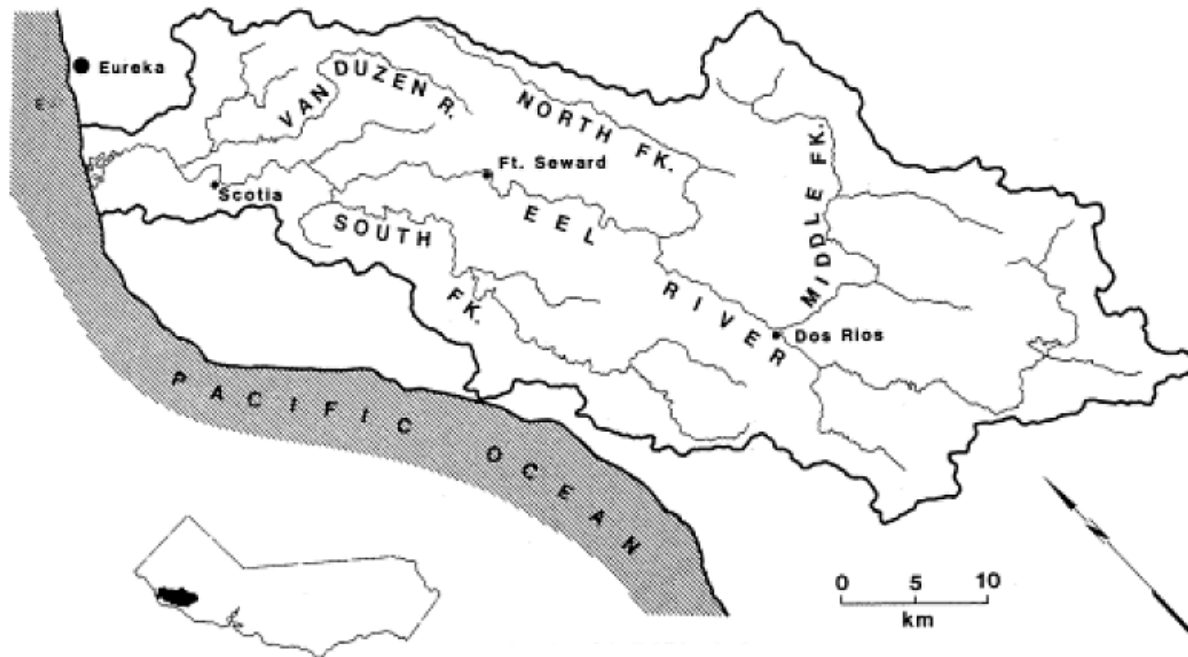


Figure 1.1: The Eel River watershed (Lisle 1990)

1.3 The Eel River: Literature Review

1.3.1 1910 - 1979

Though there were a few earlier management recommendation reports, as well as United States Geological Survey (USGS) discharge data collected as early as 1910, research on the Eel River began in earnest in the early 1950s, including USGS water quality sampling that began in 1951. Surveys of fish populations by the California Fish and Game department, and academic geomorphological studies (Maxon 1952), were the primary interests at the time. There were a few major Eel River floods over these decades, most notably in 1955 and the infamous Christmas flood of 1964, the worst flood in recorded history. In 1959, perhaps spurred on by the former event, the USGS began collecting suspended sediment concentration and total discharge, and continued to do so until late 1980. (USGS 2012)

A 1971 USGS Water Supply Paper by Brown and Ritter (Brown and Ritter 1971) is the first expansive published report about Eel River sediment transport, and Ritter another USGS report considering Eel River sediment (Ritter 1972). However, non-government-report literature pertaining to offshore Eel River sediments only begins to appear in the mid-1970s (Piper 1976), with the first academic study of the whole region, rather than a specific physical feature, coming out of UC Santa Cruz in 1980 (Griggs and Hein 1980). Griggs and Hein present an estimate of total sediment delivery utilizing USGS gauging data, sediment mineral composition data, as well as a spatial analysis of suspended sediment being transported via river plumes using the 1970s satellite LANDSAT. Other inferences of currents on the Eel River shelf via satellite data occurred throughout the 1970s, (Carlson and Harden 1975, Pirie and Steller 1977), as well as drift card studies (Carlson and Harden 1975) and studies of historical wind records (Nelson 1977).

1.3.2 1980 – 1989

Offshore sediment studies continued through the 1980s, including research on thermogenic hydrocarbons (Kvenvolden 1981), oxygen isotopic composition of fossils (Dodd 1984), and paleogene rocks (Underwood 1985). In 1985, on the basis of physiographical and sedimentological criteria, Borgeld et al. (1986) defined the Eel River shelf to extend across 55 km from Cape Mendocino to Trinidad Head. In 1986, a study entered the literature providing data on Eel River gravity wave heights and periods (Corson et al. 1986). Finally, at the end of the decade, a University of Washington study (Leithold 1989) demonstrated that fine-grained shelf deposits of sediment do preserve a distinguishable, if subtle, record of depositional processes and individual events.

Importantly, in 1982, NOAA launched a buoy about 20 km offshore of the Eel River mouth at 40.724° N, 124.578° W, called Station 46022 (LLNR 500). Time series of wind direction, speed, peak gust speed, significant wave height, dominant wave period, average wave period, mean wave direction, sea level pressure, air temperature, sea surface temperature, dewpoint temperature, station visibility, pressure tendency and tidal levels are available from this period onwards. The buoy received a sensor upgrade in 1996, adding continuous (rather than averaged) winds data and spectral wave density data. (NOAA 2012a)

1.3.3 1990-1999

Biology's interest in the Eel River exploded with the publication of local freshwater ecology experiments in 1989-1990 (Feminella 1989, Power 1990a), culminating in a landmark Science paper (Power 1990b), and several major Ecology papers in 1992 (Power 1992a, 1992b, 1992c; Power's extensive Eel River-related bibliography can be found at Power 2014). Power and her collaborators have produced many dozens of papers and several books on Eel River biology, from ecological experiments to genetic structure analysis and everything in between, between then and now, with an increasing focus on nitrogen limitation in the Eel River, and its relationship to storm event-driven river scouring effects (Marks et al. 2000), as well as the growth of *Cladophora* and other nitrogen-fixing algae found to grow along the river annually (Schade 2010). The possibility that storm-scouring leads to infrequent delivery of nitrogen-fixing *Cladophora* to the Eel River mouth as a source of nitrogen for coastal ocean productivity is a line of thought that came out of this research. River-watershed exchange (Sabo and Power 2002; Bastow et al. 2002) was also a major topic of study. Nor were they the only ones; made aware of this interesting system, biological study within the Eel River basin has intensified ever since. However, as this thesis does little with internal watershed dynamics from the biological standpoint, Eel River watershed biological systems research will not be further reviewed here.

Eel River sediment studies continued as well. There were a few cruises looking at specific locations of geomorphological interest, but the major results from the 1990s came from the continued work of Borgeld, notably joined by Wheatcroft, Sommerfield and Nittrouer in 1996-1997 (Wheatcroft 1996; Wheatcroft 1997), who were very interested in the rapid and widespread dispersal of flood sediment on the northern California margin.

Led by Nittrouer and joined by many others, the **STRATA FORMation on Margins** (STRATAFORM) Program, supported by the Office of Naval Research, was created in the late 1990s (Nittrouer 1999) to study and model the relationships between marine and terrestrial events, physical processes, and stratigraphy; it had two major research sites, and one was Cape Mendocino and the Eel River (while the other was in New Jersey). STRATAFORM produced an enormous number of publications and laid the foundations for a research program that continues to collect data to this day under various auspices.

In 1999, Volume 154 of *Marine Geology* published 27 STRATAFORM-related papers, most of these focusing on the Eel River, and data collected between 1995-1997, most notably during the major 1995 flood event. Important results included measurements of the size and settling velocity of sediment particles (Sternberg et al. 1999), sediment flux measurements taken with moored sediment traps (Walsh and Nittrouer 1999), results from monitoring tripods measuring hourly currents, bottom pressure, suspended-sediment concentration, and seabed roughness (Ogston and Sternberg 1999; Cacchione et al. 1999), camera and sonar studies of sediment bed features (Wright et al. 1999; Goff et al. 1999), replicate box cores were collected across many cruises to study biogeochemical signatures in particulate organic carbon and physical spatial variability (Drake 1999; Leithold and Hope 1999; Alexander and Simoneau 1999), acoustic swath bathymetric mapping and GIS analysis (Borgeld et al. 1999; Lee et al. 1999), a towed electromagnetic survey to study shelf porosities (Evans et al. 1999), ^7Be , ^{210}Pb and ^{137}Cs geochronological studies of Eel River muds (Sommerfield and Nittrouer 1999; Sommerfield et al. 1999), and analyses of offshore subsurface gas (Yun et al. 1999) and Dissolved Organic Phosphorus (Monaghan and Ruttenberg 1999). None of this data is used directly in this thesis, but laid the foundation for further analysis throughout the following decade that we consider below in section 1.3.4.

There were also modeling efforts in early STRATAFORM. An analytical model to represent two-dimensional, laminar, non-hydroplaning mudflow resulting from deep water submarine slides (Huang and Garcia 1999) was validated against laboratory flows rather than STRATAFORM data, while a sediment-transport model involving bed-armoring was designed to understand important parameters in that process (Reed et al. 1999). Another analytical model, this one utilizing 2-D solutions to the state of stress on an infinite slope, was utilized to understand slope-failure mechanics (Mello and Pratson 1999). A two-dimensional, across-shelf sediment-transport model was forced with Eel River shelf storm waves to understand storm deposition (Zhang et al. 1999).

Finally, among the STRATAFORM modeling publications in 1999 were a pair of papers were by James Syvitski's group, about estimating Eel River sediment discharge to the ocean (and to some degree the fate and transport of that sediment offshore by the river plume): (Syvitski and Morehead 1999; Morehead and Syvitski 1999); a literature review of this modeling effort and its heritage can be found in section 1.3.5.

1.3.4 2000-present

From 2000 onwards, there is simply too much research to go through; a table of relevant Eel River papers sorted by topic is listed at the end of the chapter, in Table 1.3. Each topic, however, can be briefly discussed in terms of major findings, lines of research, and interesting arguments.

- Biogeochemical cycling - anaerobic conditions: Early in the decade, there were a variety of papers looking at methane seeping from sediments, ultimately reviewed in (Levin et al. 2010). Most interesting were distinct microhabitats of microbial mats, which oxygen was unable to penetrate, thus creating anaerobic conditions at sediment depths that would normally have significant oxygen content. Starting in 2009, both iron and manganese oxidation-reduction biogeochemistry have been explored in depth; it appears that benthic manganese fluxes from the Eel River continental shelf are an order of magnitude higher than other regional shelf settings (McManus et al. 2012), and multiple groups have found evidence of co-variation of redox rate with organic carbon content. It has been proposed that reactive organic carbon from riverine discharge may remobilize otherwise unavailable iron (Severmann et al. 2010); for the latest review and results, see (Roy et al. 2013).
- Biogeochemical cycling – biological perturbation of shelf-held sediments: A few studies were performed looking for biological alteration of how flood deposits are physically structured; there is evidence that bioturbation intensity has been constant for thousands of years (Sommerfield et al. 2001).
- Biogeochemical cycling – characterization of Eel River-delivered organic matter: A particularly crucial topic, the major result of the past decade of research on this topic is that organic matter in sediments appears to break down much more slowly than had been expected (Blair et al. 2003, Drenzek et al. 2009). There is a wide variety of measurements available, including Carbon to Nitrogen ratios and isotopic characterization of various particle types. Most recently, particulate organic matter was thoroughly characterized during both low and high flow regimes (Goñi et al. 2013).
- Sediment fate and transport – physical characterization: Studies on this topic look particularly at physical concerns, such as flocculation, accumulation, and settling velocity. There is strong evidence that large portions of flood sediment are delivered to the Eel River Canyon (Mullenbach and Nittrouer 2006); evidence is contradictory, however, about whether or not periods of extreme sediment concentration induce massive floc sizes (and settling rates).
- Sediment fate and transport – gravity flows: By far the most research has gone into the discovery (summarized in Wright et al. 2001) and subsequent characterization of a secondary mechanism for sediment transport other than plume delivery from the inner shelf to the midshelf. It was a major surprise when storm resuspension of older sediments into gravity-driven fluid muds were found to occur far more often than had been thought possible (Puig et al. 2003). It is now believed that this secondary process dominates sediment fate on the continental shelf (Guerra et al. 2006). Numerous efforts have been made to conceptually and empirically model this effect, culminating in a three-dimensional hydrodynamic model of sediment transport mechanisms (Harris et al. 2005). An excellent literature review is provided in (Wright and Friedrichs 2007). Most recently, the idea that this secondary mechanism is unnecessary to explain sediment

transport due to an overestimation of total sediment delivered to the shelf has presented a major challenge to these findings (Warrick et al. 2013, Warrick 2014).

- Sediment fate and transport – sequence stratigraphy and climate change: There have been attempts to characterize and interpret stratigraphic preservation of flood events as a climate change signal. Whether it is climate change (Sommerfield et al. 2002) or land use (Leithold et al. 2005) driving the recent stark increase in marine sedimentation is a subject of debate. What is clear is that intense biological mixing intensity on the Eel River shelf dissipates most signals captured in heterogeneity between 3-15 years (Wheatcroft and Drake 2003), except for episodic sedimentation from Eel River flood events, which can preserve event beds and transient signals for at least a thousand years (Sommerfield and Wheatcroft 2007). A book, *From Sediment Transport to Sequence Stratigraphy*, provides an overarching look at the topic (Nittrouer et al. 2007).
- Modeling efforts – 3D ocean circulation: This ‘topic’ comprises only two papers, but their direct significance to our subsequent modeling effort makes them worthy of discussion. A purely physical three dimensional model at 1 km resolution, run as a 40-day simulated the major 1997 Eel River flood (Pullen and Allen 2000). They used the Princeton Ocean Model (POM) in its Naval Research Laboratory's Pacific West Coast Model (NRL PWC; Clancy et al. 1996) configuration for this purpose, and were able to reasonably reproduce the onshore velocity fields measured by STRATAFORM tripods. They found that coastline irregularities were important to generating local eddies, and that the mixing of the freshwater plume influences the velocity structure of the shelf flow. A later followup study (Pullen and Allen 2001) performed 3 km and 9 km resolution model runs, documented strong alongshore variability in wintertime flow, and reproduced it with good agreement. They also noticed a robust anticyclonic eddy that forms when strong poleward winds weaken and reverse direction during winter storms.

1.3.5 Empirical Sediment Models and the Eel River

Empirical sediment models are designed to provide data rich estimations of a watershed's river discharge and sediment transport. Given atmospheric forcing (typically based on temperature and precipitation), and parameterized based on specific attributes of the watershed being modeled, they can often generate useful predictive results. Their weakness is a lack of portability (as what is good for the Mississippi may not be good for the Hudson) and a tendency to obscure basic mechanics with their major simplifications. They are unsuitable for trying to tease out new knowledge and understanding of the mechanistic nature of watersheds – but very useful as a first-order approximation of watershed behavior.

In 1995, an empirical model called RIVER3 was developed to simulate the discharge and sediment load of rivers (Syvitski and Alcott 1995). The hydrology portion of this model was exceedingly simple, however, running at constant temperature with pre-defined "seasons" for precipitation distribution into snow, ice and rain. In 1998, the first version of the lumped empirical model HydroTrend was published (Syvitski et al. 1998a), adding a great deal of missing detail, not just about atmospheric input but also canopy interception, improved subsurface flow, and flood algorithms. HydroTrend shared the same sediment load models as RIVER3, without adjustment: suspended load and bedload calculated separately, using empirical sediment rating curves.

These curves have been used and improved by engineers for most of the 20th century (reviewed in Syvitski et al. 2000). In 1992, Syvitski analyzed data from 280 rivers and found sediment loads to be a log-linear function of basin area and maximum elevation (Milliman and Syvitski 1992). As part of an effort to generalize sediment rating curves to ungauged basins, and understand their sensitivity to various environmental variables, 57 rivers, including the Eel River, were studied (Syvitski et al. 2000); later the Eel River was included in an effort to characterize global variability of sediment flux from concentration and discharge (Meybeck et al. 2003; Syvitski et al. 2003). Separately but relevantly, a worldwide analysis of small mountainous river systems and their delivery of particulate organic carbon created a set of POC rating curves (Wheatcroft et al. 2010).

Sediment rating curves are often too simple, as only rivers that drain high sediment-yield, single-source areas demonstrate a simple first-order relationship of suspended load versus discharge (Syvitski et al. 1998a). RIVER3 (and HydroTrend) addressed the seasonal hysteresis of sediment concentration vs. river discharge by separately calculating suspended sediment production for each individual source of water (overland flow, groundwater flow, snowmelt). Bedload transport was then determined through an estimate involving sand grain and fluid density, gravity, the slope of the river bed, bedload efficiency and the limiting angle of repose of sediment grains lying on the river bed (Bagnold 1966).

HydroTrend was applied to the Eel River on both daily and interannual timescales, and did a reasonable job of reproducing Eel River discharge. Its sediment production lacked some of the variability of the actual data, since, for example, it cannot capture the first flood of the water year containing a higher sediment concentration than subsequent floods.

Simultaneously, Syvitski published PLUME1.1 (Syvitski et al. 1998b), a two-dimensional advection-diffusion equation modeling a turbid hypopycnal plume emanating from the river mouth. PLUME1.1 was a significant advance over GRAIN2 (Syvitski and Alcott 1993), which traced individual streamlines out from the river mouth, solving a simple reaction equation for each one. It could use HydroTrend output as forcing, but, of course, only captured initial advection and deposition of sediment, rather than the important secondary transport along the Eel River shelf. Once again this model was applied to the Eel River, but with limited success in accurately depicting accumulation rate on the shelf.

The following year, PLUME was forced by STRATAFORM data to reproduce the plume during the 1995 flood event from January 7-15 (Morehead and Syvitski 1999). It estimated the plume traveling over 60 km north of the Eel River mouth, with most sediment deposited within 30 km. Furthermore, they attempted a climatic paleo simulation at 18,000 years before the present, but this is less compelling, as PLUME's lack of ability to capture secondary processes makes it not useful for long time scales. They also simulated the Eel River using collected climatic statistics for the last fifty years (Syvitski and Morehead 1999), with general success regenerating USGS statistics for Eel River discharge and sediment loads.

The next model developed in the chain was SEDFLUX (Syvitski and Hutton 2001), which integrated a suite of process-based models to predict the lithologic character of basin

stratigraphy. They attempted to reproduce the Eel River Margin (Morehead et al. 2001), but again did very little with gravity flows. SEDFLUX had the capacity to capture hyperpycnal flows and debris flows, but it only attempted to add cross-shore transport due to ocean wave sediment resuspension in Sedflux2.0 (Hutton and Syvitski 2008). Application of Sedflux2.0 to the Eel River for long-term sediment accumulation has not been published; it used the Po River as its test case.

HydroTrend also received an update in 2008, becoming HydroTrend 3.0 (Kettner and Syvitski 2008). HydroTrend 3.0 enjoys new suspended sediment algorithms, an improved routine to simulate sediment delivery fluctuations from ice storage and release, a sediment trapping routine to account for lakes or reservoirs, multiple delta outlets, and a sequential rather than statistical use of climate observations, for direct comparison and validation. It uses much of the sediment rating curve analysis from Syvitski et al. (2003), and additionally includes basin lithology and human activity as parameters (Syvitski and Millman 2007).

The other notable modeling effort for empirical sediment processes in the Eel River is much more modern; an artificial neural network (ANN) model was developed and trained by linking six single-station models (Nourani and Kalantari 2010). It enjoyed reasonable results, and led to a second ANN model based not on linked single stations but geomorphology (Nourani et al. 2014), which produced better performance by employing spatially variable factors of the subbasins, rather than being a fully lumped model. Simultaneously but independently, the ability of least square support vector machine (LSSVM) modeling to capture Eel River behavior was explored (Kisi 2012), and it slightly outperformed the first ANN model. Both methods were superior to sediment rating curve modeling for upstream stations, but downstream, the sediment rating curves were still superior. However, when both stations were integrated to provide a total flux, LSSVM and ANN both outperformed the sediment rating curve model.

1.4 Data Analysis: Overview

With this surfeit of available data, an analysis is in order, to estimate the first-order effects of the sediment and nutrient-laden Eel River storm plumes on coastal Net Primary Productivity. There are four easily accessible, immediately relevant time series:

- 1) The Oregon State University Net Primary Productivity dataset (Behrenfeld 2005)
- 2) The NOAA NBDC buoy closest to the mouth of the Eel River, which provides wind direction (NOAA 2014)
- 3) The USGS gauging station best suited to continuous time series of discharge, which tells us when significant Eel River plumes are occurring (USGS 2012)
- 4) The NOAA Coastal Upwelling Index, which tells us when significant coastal upwelling (and delivery of nutrients) is occurring (NOAA 2013a)

The combination of these time series are plotted in figures 1.2 and 1.3. The multi-year figure has clearly visible seasonal patterns, with the upwelling winds appearing as a negative (northerly) index value in summer simultaneous with a positive (north of the cape) NPP distribution, and then more southerly winds in winter coinciding with complex NPP behavior. The grid of single-

year figures have the upwelling and significant Eel River discharge months indicated to highlight the different behaviors visible in each season.

A simple statistical test that detects for the potential for causality rather than only correlation, called the Granger Test, can give us a sense of if or when the wind direction time series is a predictor of the location and magnitude of nearby coastal primary productivity – phytoplankton blooms affected by the Eel River plume (or lack thereof). A much more complex and nuanced analysis can be performed using the Canonical Correlation Analysis, the top tier of the hierarchy of correlative analysis tools. CCA looks for *modes of variation* within a given dataset, and co-variation between datasets, such as the NPP and wind direction time series. The relative amplitudes of these modes can give us insight into when a co-variation was important, and when it was not.

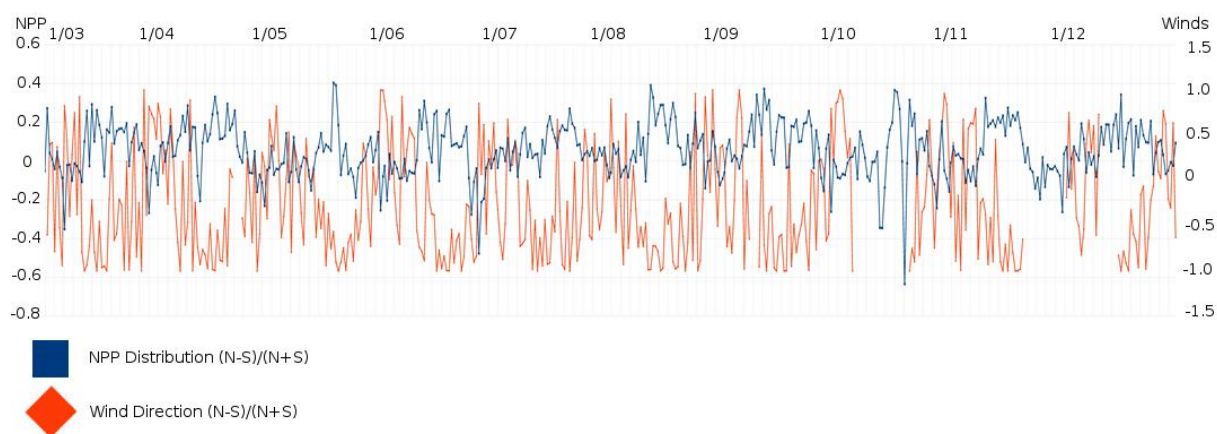


Figure 1.2: the NPP (blue, left Y axis) and Wind (red, right Y axis) Indices, 2003-2012. A positive value of the NPP index indicates more NPP to the north of Cape Mendocino than the south, while a negative value indicates the opposite. If it is zero, equal production is occurring in both regions. A positive value of the Winds index indicates that on average for that 8-day point, the wind spent more time blowing towards the north than the south; a negative value again indicates the opposite; and if zero, an equal amount of time was spent blowing in either direction. Note that during each summer, a strongly negative Winds index is observing upwelling conditions, a strong seasonal signal.

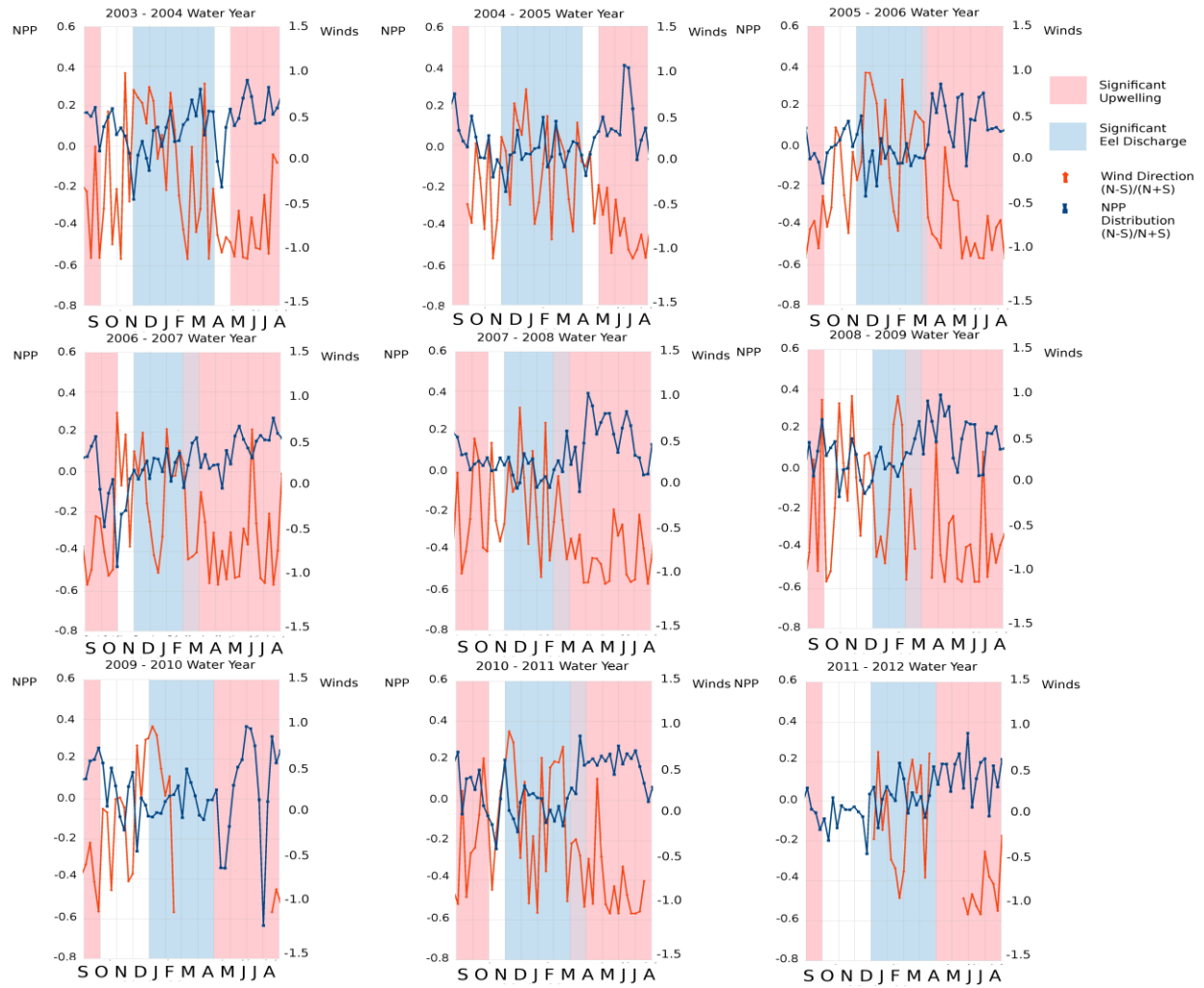


Figure 1.3: Yearly NPP and Wind Index plots, with upwelling and significant months of river flow shaded. See Figure 1.2 for interpretation of the NPP and Wind indices.

1.5 Estimation of Net Primary Productivity from Satellite Ocean Color Data

Ocean color can be used as a surrogate measurement for chlorophyll and therefore primary productivity (Saba et al. 2011). The Vertically Generalized Production Model (VGPM; Behrenfeld and Falkowski 1997a) is a commonly used “chlorophyll-based” algorithm for estimating Net Primary Production. It is similar in form to the early models of Ryther and Yentch (1957) and Talling (1957).

The VGPM assumes that NPP can be expressed as a function of chlorophyll concentration, but as NPP is a rate and chlorophyll is a standing stock, a chlorophyll-specific assimilation efficiency for carbon fixation must be estimated. This is a description of how photosynthetic efficiency under light-saturated conditions varies physiologically in the environment, called $P_{b_{opt}}$, based on daily integrated production measurements. $P_{b_{opt}}$ is the maximum daily net primary production found within a water column, in units of mg carbon fixed per mg chlorophyll per hour. In the standard VGPM, $P_{b_{opt}}$ is temperature dependent (Behrenfeld and Falkowski 1997b), and total water column NPP is a function of chlorophyll, $P_{b_{opt}}$, day length and a volume function that

combines euphotic depth (calculated using the Morel and Berthon 1989 Case I model) and a data-driven parameterization of light penetration into the water column (Platt and Sathyendranath 1993). Therefore, the data that goes into the ocean color analysis is chlorophyll, photosynthetically active radiation, sea surface temperature, and day length, all of which we get from MODIS.

1.6 MODIS data

MODIS (or Moderate Resolution Imaging Spectroradiometer) is an instrument aboard the Terra and Aqua satellites. Combining both satellites' reach, MODIS views the entire Earth's surface every 1-2 days, acquiring data in 36 spectral bands. This data analysis uses the new MODIS.R2013 reprocessing results for chlorophyll, cloud-corrected incident daily photosynthetically active radiation, sea surface temperature and day length, regridded to 1/12 of a degree in both latitude and longitude, and to 8-day averages in time (NASA 2013). NPP "north of the mouth of the Eel River" is considered to be from 40.5° to 41.08° N, roughly 50 km. Southern NPP is from 39.92° to 40.5° N. The analysis goes 0.83° W off the coast, following the shoreline to normalize the distance offshore.

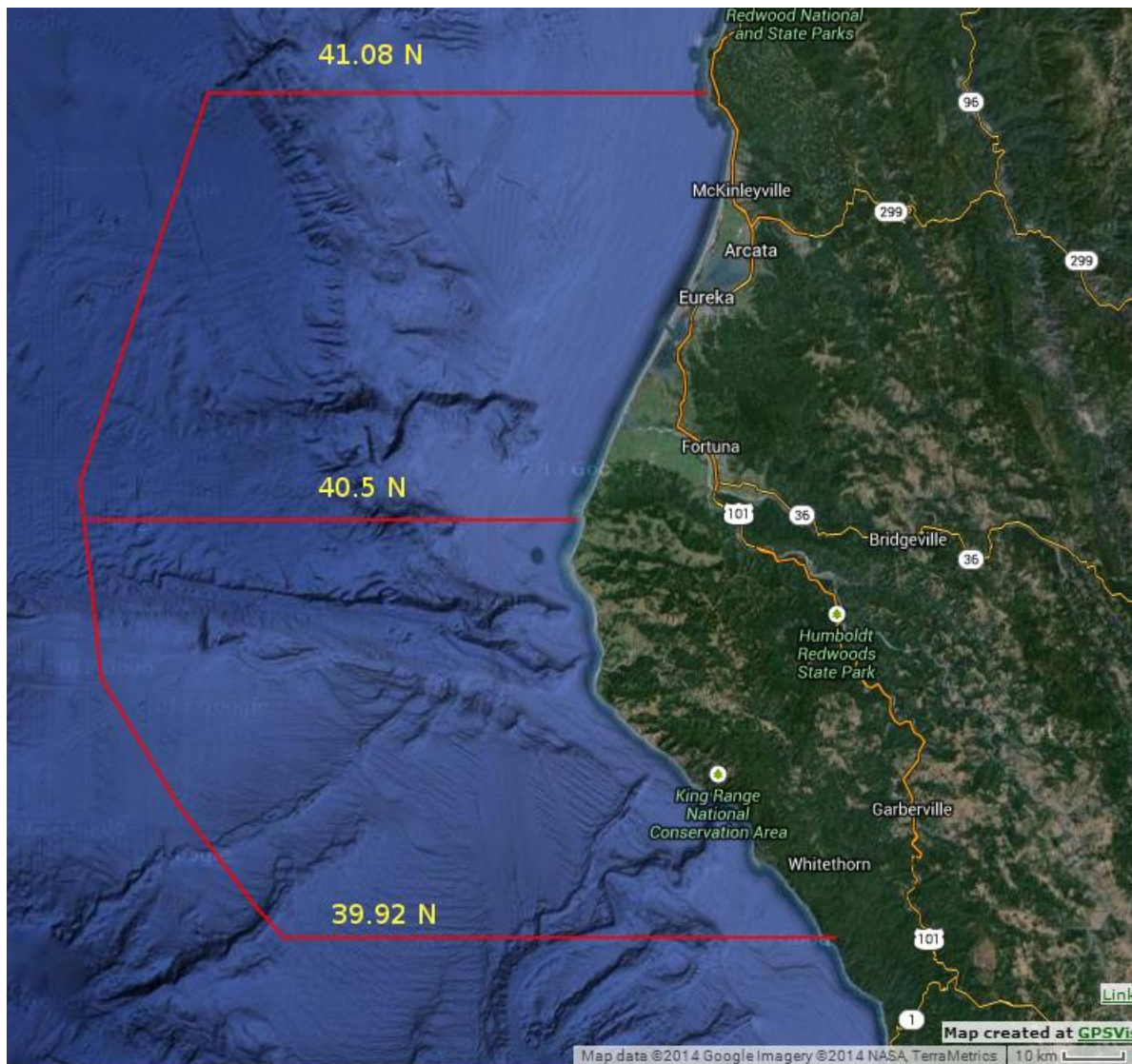


Figure 1.4: Simplified visualization of where satellite data are selected for analysis.

An index of geographic distribution is then constructed by simple normalization: the difference between northern and southern NPP, divided by their overall sum. When the NPP Index is 1, all growth is north of the cape; when it's 0, there is an equal amount of growth north and south of the cape; and when it's -1, all growth is occurring to the south.

1.7 NBDC Buoy Data

The National Data Buoy Center Station 46022 (LLNR 500) is a 3-meter discus buoy 17 nautical miles WSW of Eureka, California, at 40.724° N, 124.578° W. It maintains an ARES 4.4 instrumentation payload, measuring sea level height, air temperature at 4m above the sea surface, wind speed and direction at 5 meters above the sea surface, humidity at the sea surface, and sea surface temperature at 0.6 meters below the sea surface. Of these, we're mostly interested in wind direction, because it gives us an indicator of the direction that the Eel River freshwater

storm plume is being advected on the surface of the ocean. Once again we construct a directional index, this time of the frequency of southerly minus the frequency of northerly winds within a given period, divided by the sum of both frequencies. As the NPP data are in 8-day averages, that is the period chosen for the Wind Index as well.

The wind direction sensor ranges from 0-360 degrees, taking data at 1.71 Hz. It has averaging periods every 2 and 8 minutes, a resolution of 1.0 degree and accuracy of ± 10 degrees. A unit-vector average is used to calculate the average wind direction, in which unity serves as the length of the vector, and the wind direction observations serve as the orientation of the vector. The u and v components are then calculated for each observation. Then the average u and v components are computed, and the average wind direction is derived from $\arctan(\frac{u}{v})$ (NOAA 2014).

1.8 USGS gauging station data

USGS gauging station 11477000, Eel River at Scotia, CA (40.492° N, 124.099° W) has been collecting discharge and gauge height data since October 1910, and continues to this day. It collected suspended sediment concentration and total suspended sediment load from 1959-1980. From 1951-1998 water quality data was regularly collected, including temperature, total nitrogen, organic nitrogen, ammonia, nitrite and nitrate concentrations. This stream site drains over 80% of the Eel River Basin (it is, notably, missing the Van Duzen tributary). Nearest the mouth of the river, the Eel River at Fernbridge gauging station 11479560 only collects gauge height and a webcam image. Primarily our interest is in the discharge data, which is collected using a USGS Type AA Current Meter, which accurately measures streamflow velocities from 0.025-7.6 meters per second, which are then multiplied by a river subsection area to get that portion of the discharge. Whether or not Eel River flooding goes beyond the current-meter method's ability to estimate discharge is unknown, but the literature has taken these measurements as reasonable estimates for as long as literature has existed.

1.9 Methodology: Granger's Test for Predictive Causality

A time series X is said to Granger-cause Y if it can be shown through a series of tests on lagged values of X and Y that those X values provide statistically significant information about future values of Y (Granger 1969). Using the R package *lmtest* (Hothorn 2014), a Wald test is used to calculate a maximum likelihood estimate, compared against a chi-squared distribution. Failure to reject the null hypothesis is equivalent to rejecting the hypothesis that X does not Granger-cause Y (Toda and Yamamoto 1995). Granger causality is a useful tool, but one that must be used with care – clear conclusions are hard to find outside of a simple 2-dimensional system. Still, insights can be gained by examining where, when, and how strongly, Granger causality appears.

Applying Granger causality theory to two time series (the NPP and Wind indices) requires taking the first differences of each time series in order to render them stationary; otherwise the regression tests will be meaningless (Lutkepohl 2006). Furthermore, the time series were first detrended and deseasonalized with moving averages, in order to capture interannual variation rather than just the major seasonal signal. Finally, due to the extreme difference in dynamics

between summer and winter, Granger causality was tested for not the entire time series, but separately for the upwelling-dominated months of the time series, and for months of the time series in which extreme (greater than 1% annual discharge during a given day of year) Eel River discharge took place. A lag of 3 timepoints was used – that is to say, what is being tested is whether a model that uses both Wind and NPP to predict NPP, as well as just NPP by itself, using up to three values behind a given timepoint for that prediction.

1.10 Results: Granger Causality

Table 1.1 shows the probability that the null hypothesis, that is to say, that the Wind Index does not predict the NPP Index, and vice versa, is true. A small value indicates that the null hypothesis should be rejected, thus implying that the Wind Index is a potentially useful predictor of the NPP Index (or vice versa). Granger causality is tested in both directions, and is often useful for determining which variable is controlling which (commonly explained to be an attempt to solve the “chicken and the egg conundrum”). That is not a serious question in this case, however: since phytoplankton have no known feedback on atmospheric momentum dynamics, a result that NPP-predicts-the-Wind would be absurd to interpret at face value. However, given the fact that some wind events happen near the end of one 8-day average, thus potentially driving the next 8-day average NPP, or are split between two averages, that could explain the possibility of the lag apparently reversing, such that the NPP seems to be predicting the wind.

To the extent that a signal of the wind driving river plumes to induce phytoplankton blooms could be captured this way, it is reasonable that the signal would not appear equally strongly from year to year, because of a third factor: how much Eel River discharge is available to affect the system. To give us a sense of the relative presence of the river from year to year (mostly flowing, by definition, during the storm season), Table 1.1 includes the summed discharge from a given (September-August) water year.

Table 1.1: Granger Causality results.

Water Year (2003 is September 2003-August 2004)	Pr(>F): Wind predicting NPP, upwelling season	NPP predicting Wind, upwelling season	Wind predicting NPP, storm discharge season	NPP predicting Wind, storm discharge season	Total Water Year Discharge
2003	0.9988	0.7635	0.1103	0.7193	6.88E+009
2004	0.2215	0.2399	0.1362	0.6819	6.25E+009
2005	0.9782	0.3525	0.07097	0.08366	1.30E+010
2006	0.1095	0.04784	0.088	0.5001	3.77E+009
2007	0.5439	0.3473	0.3844	0.5667	4.51E+009
2008	0.3589	0.7414	0.6005	0.938	3.37E+009
2009	0.3396	0.9553	0.8082	0.8001	6.29E+009
2010	0.9127	0.0225	0.1439	0.1048	8.50E+009
2011	0.868	0.8137	0.2375	0.1824	4.28E+009

Table 1.1 is represented visually in Figures 1.5 (for the upwelling-dominated system) and 1.6 (for the potentially storm discharge dominated system). The first thing we see is that we cannot reject the null hypothesis, ever, at a 95% confidence level, with a single exception in the 2006 upwelling season. Given the complexity of the system, and the potentially very small effect of the signal of the Eel River on the coastal ocean, this is not surprising. However, patterns still emerge. During the upwelling season, other than in 2006 (and NPP-predicting-wind in 2010), there is never a significant possibility of wind direction predicting NPP geographic distribution in the positive direction, which is a reasonable result, since we know from the data that when upwelling winds (blowing towards the south) are strongest, NPP is larger in magnitude towards the north of the cape.

During the storm season, winds predict NPP far more significantly than the other way around in six out of nine years analyzed: 2003, 2004, 2005, 2006, 2007, and 2008. Winds predict NPP most successfully, at an 85% confidence level or better, during the years of most significant Eel River discharge: 2003, 2004, 2005, and 2010, which are all the years of relatively extreme Eel River discharge. 2009, which had more storm flow than 2004, is an outlier, lacking correlation. That NPP-predicting-Wind has drastic improvements in correlation in 2005 and 2010, the two main years of exceedingly high Eel River discharge, is also interesting, since we would expect, due to the weird lag effects discussed at the top of this section, for, when the time series prediction appears to reverse due to effects related to the river, the river to be important. Naturally, this could also all be coincidence. Further analysis of additional years added to the record over time will provide further insights, but in the end Granger causality's lack of strong results is just another way of saying that this system is complicated.

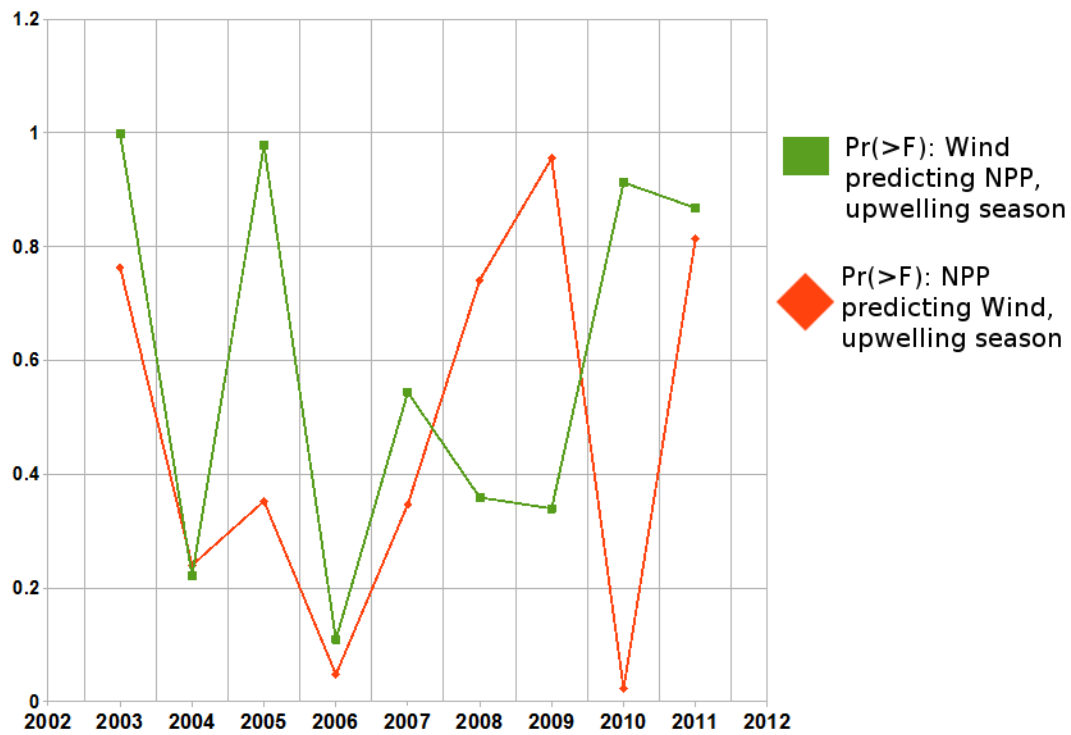


Figure 1.5: Granger causality test results, Wind and NPP Indices during the upwelling-dominated period.

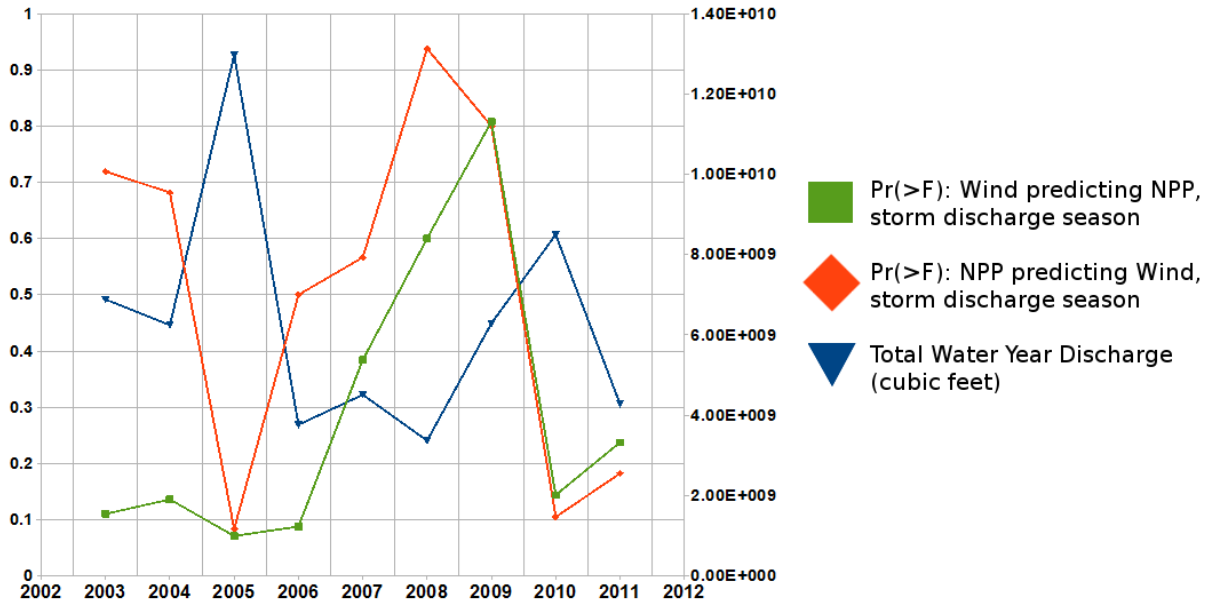


Figure 1.6: Granger causality test results, Wind and NPP Indices during the storm-dominated period.

1.11 Methodology: Canonical Correlation Analysis

Canonical Correlation Analysis (CCA) is at the top of the hierarchy of regression modeling approaches, described in detail in Barnett and Preisendorfer (1987) and then in a text, Preisendorfer (1988), and compared to other statistical methods used in climate research in Bretherton et al. (1992). CCA computes linear combinations of a set of predictors to maximize relationships, in a least square error sense, between a given set of time series. By breaking a field of data down into its empirical orthogonal functions (EOFs) using eigenvalues and eigenvectors, patterns in time and space emerge. Singular Value Decomposition (SVD) analysis of two fields makes it possible to examine covariability within them. The method is well-summarized in Bjornsson and Venegas (1997).

As we only have one spatial point for the wind (the NBDC buoy), we perform an analysis on the Wind Index and the three-dimensional NPP field (space by space by time) that has been reduced to two dimensions (space by time) when transformed into the NPP Index. Our row vectors are now composed of the 8-day average time series for a given year. Our column vectors are the same days-in-year point within varying years (see Figure 1.6). In this way we can study interannual variability, rather than spatial variability.

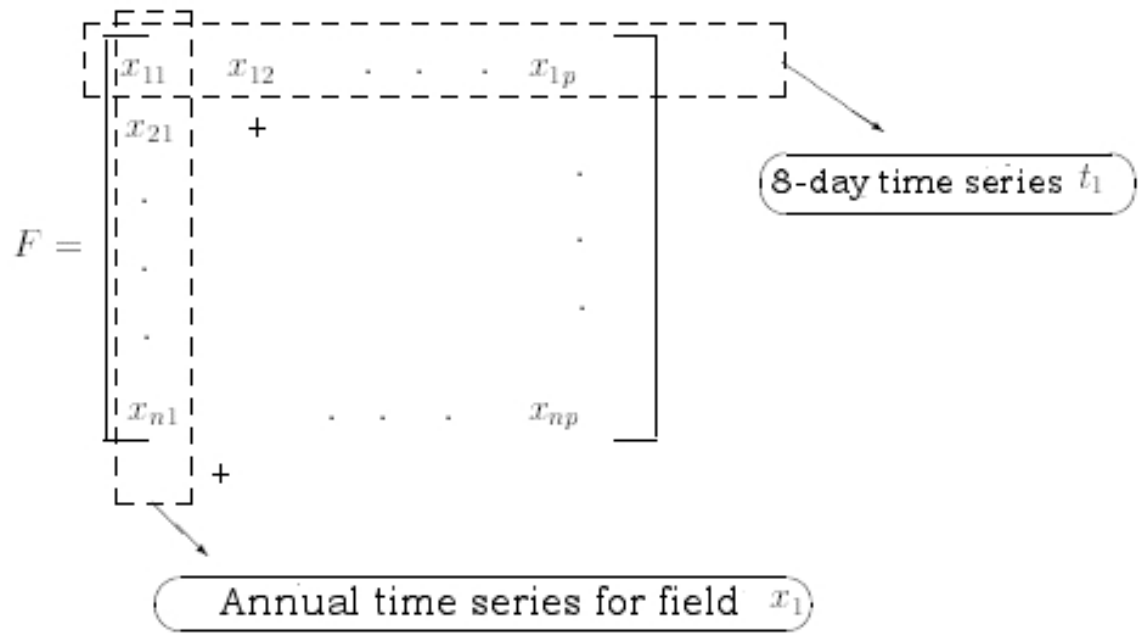


Figure 1.7: The matrix F to be decomposed into EOFs, mapped to have each row as one year's worth of time series, and each column a time series of observations for a given date within a year. Figure adapted from Bjornsson and Venegas (1997).

1.12 Results: CCA

By performing Canonical Correlation Analysis, we generate two sets of singular value decompositions: with and without the mean of each time point removed. It is a safe assumption that with the seasonality present, upwelling will dominate, but it is still interesting to see the patterns in which upwelling covaries with NPP.

Table 1.2: The squared covariance fractions of the first 8 modes of covariation for the NPP and Wind Indices with and without the mean of each annual time point removed. Without removing the mean, there are seven significant modes of variation (the largest of which is clearly upwelling); removing the mean creates a system with only six.

Mode of variation	Squared Covariance Fractions: Unmodified NPP and Wind Indices	Squared Covariance Fractions: NPP and Wind Index Anomalies
1st	0.474239	0.283305
2nd	0.150658	0.214903
3rd	0.114515	0.17581
4th	0.090237	0.140652
5th	0.075368	0.108192
6th	0.053594	0.077138
7th	0.041389	3.51E-17
8th	5.61E-17	3.05E-17

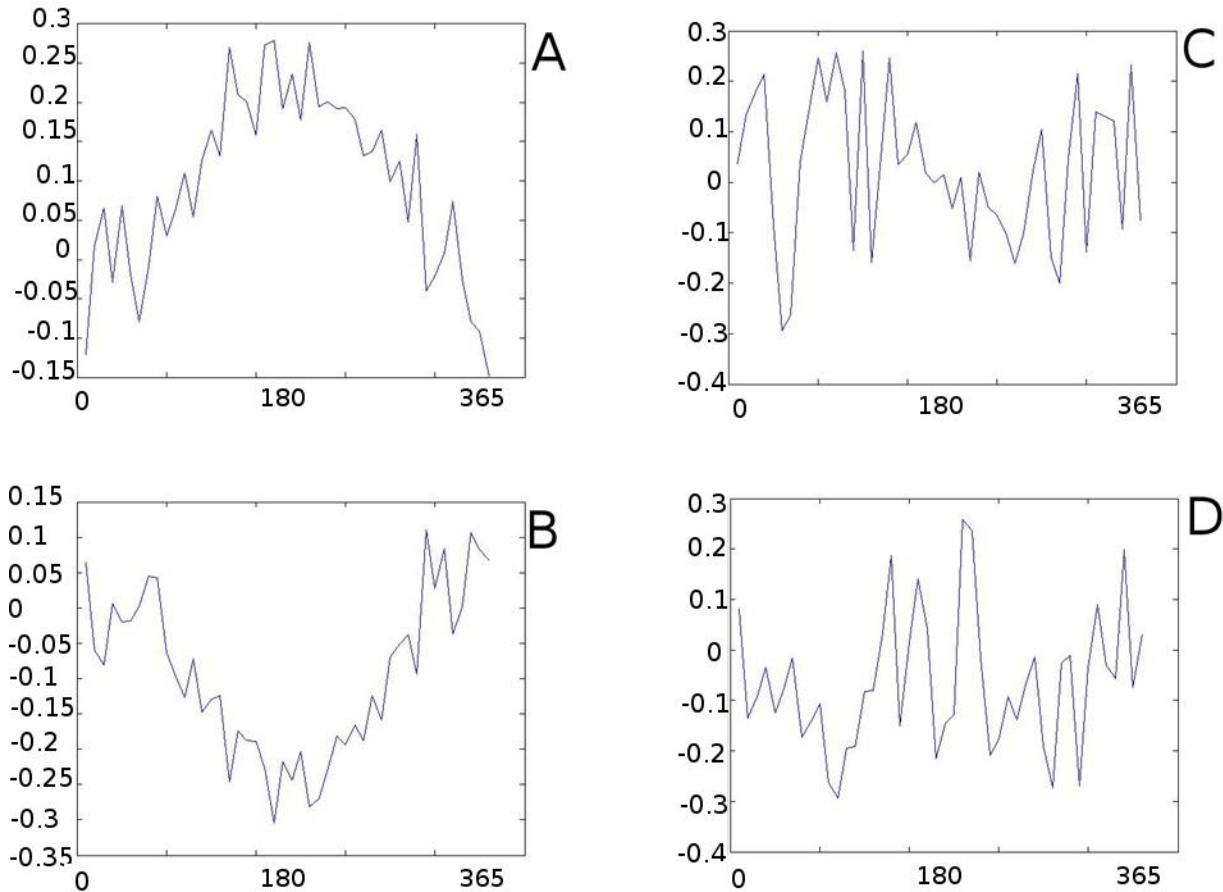


Figure 1.8: The first and largest modes of covariance (EOF1) for NPP (A) and Wind (B) in the case where we analyze the system without removing the interannual mean from each point, and for NPP (C) and Wind (D) when we study the covariance of the anomalies. The x-axis is day of year. With the upwelling signal (seen in A and B) removed, other patterns (seen in C and D) emerge to represent most of the covariance.

Without effectively removing the seasonality, the first mode of variation, upwelling (see Figure 1.8 A and B) accounts for 47% of the variation. It demonstrates a strong but opposite covariance: when upwelling winds are strongest (making the Wind Index most negative), NPP is concentrated north of the cape (with the NPP Index most positive). By analyzing the anomalies instead, thus removing the seasonal upwelling signal, the largest remaining signal (Figure 1.8 C and D) accounts for 28% of the variation, but what it represents is far less clear.

However, examining the expansion coefficients (also known as time amplitudes), which is to say how the strength of a given mode's effect on the system varies in time, provides an opportunity to identify mechanisms behind otherwise mysterious signals. And, with the mean removed, the fifth-largest Empirical Orthogonal Function shown in Figure 1.9 (accounting for 10.8% of the variability) has strikingly familiar-looking interannual variability in its time amplitudes.

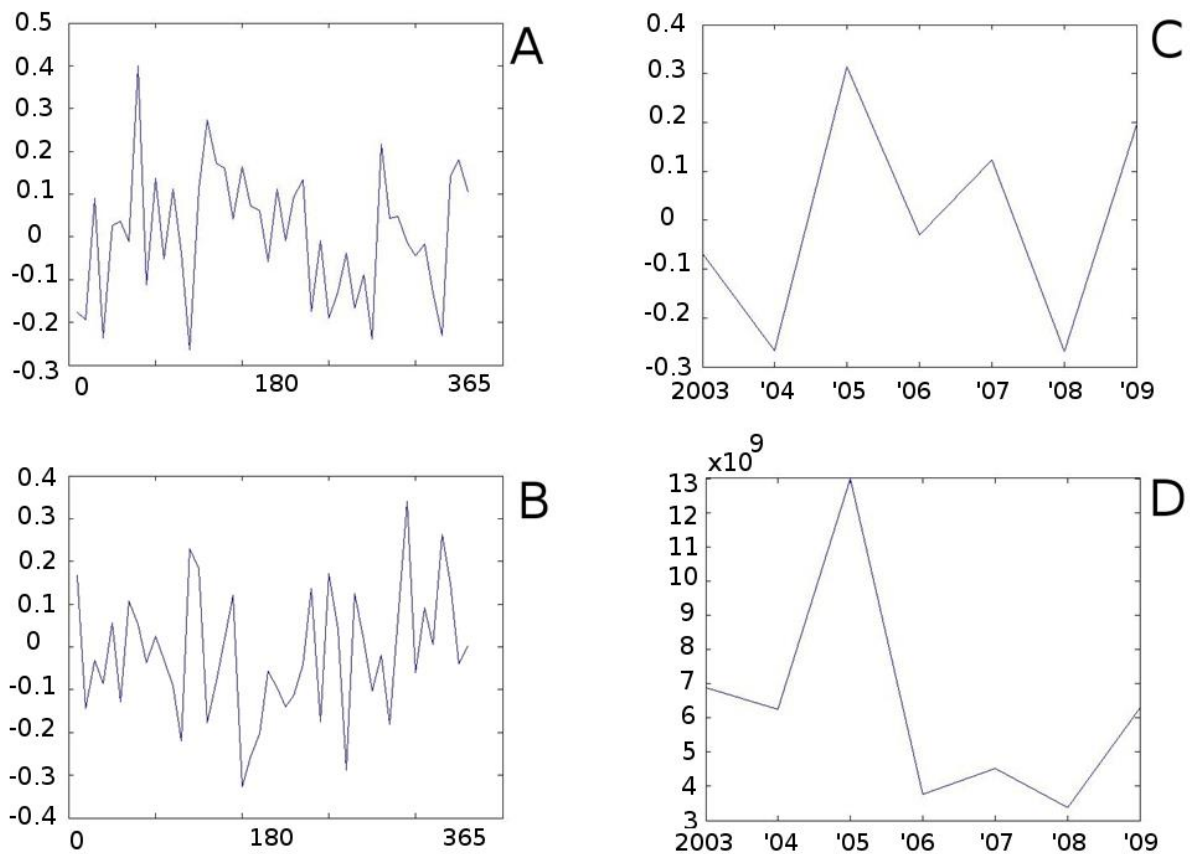


Figure 1.9: The fifth modes of covariation (EOF5) for NPP (A) and Wind (B) in the case where we analyze the system by removing the interannual mean/seasonality from each point. The x-axis is day of year. C plots the expansion coefficients/time amplitudes for A, with the x-axis now showing the 1-7 years of the analysis (2003-2009). D shows water year river discharge for each of the same years.

There is a clear similarity between the time amplitude of EOF5 and the interannual variability of Eel River discharge, with a maximum in water year 2005 and the sign of their derivatives identical throughout the period analyzed. Correlation, of course, does not guarantee causation, but it is possible that EOF5 is at least partially the signal of the river's impact on coastal variability.

1.13 Discussion and Conclusion

There is an abundance of research on the Eel River and the nearby Eel River Shelf, starting with USGS gauging as early as 1910 and expanding in the 1980s and 1990s into full-scale research programs of the shelf sedimentology (STRATAFORM) and the freshwater ecology of the river itself (at the UC Angelo Coast Range Reserve). Using Net Primary Productivity values estimated from MODIS ocean color data by Oregon State University, wind direction given by a NOAA buoy near the mouth of the river, and USGS gauging to flag the times in which the Eel River is significantly discharging its annual load, we can attempt to extract the possibly tiny

signal of short-term phytoplankton growth on Eel River storm-driven, nutrient-laden freshwater plumes.

Granger causality indicates that to the extent that winds can predict NPP, they do so most strongly during times of extreme Eel River R. discharge, and within that category, best during the years of the largest storms, especially the 2005-2006 water year. Canonical correlation analysis demonstrates that during upwelling season (as indicated by the NOAA upwelling index), NPP is more strongly concentrated north of the cape than south of the cape. There are many smaller modes of covariation between the two time series of winds and NPP, but the 5th shows interannual variability similar to that of Eel River discharge, again most strongly important to the overall system during the 2005-2006 water year.

Both Granger causality and CCA suggest that any direct connection between the NPP and wind direction (proxy of Eel River nutrient delivery) time series is small. How reasonable is this? In order to compare estimated magnitudes of Eel River discharge nutrient delivery to upwelling nutrient delivery, let us consider a simple box model.

The mass continuity equation (in x-y-z three dimensional space, with velocities u, v, and w in the respective directions) is

$$\frac{\partial u}{\partial x} + \frac{\partial v}{\partial y} + \frac{\partial w}{\partial z} = 0, \quad (1)$$

but it can also be expressed per Bernoulli's principle, such that for a continuous pipe of varying width, the scalar component of the velocity times the area through which an inviscid fluid flows is always constant:

$$w_1 A_1 = w_2 A_2. \quad (2)$$

This can be used to roughly estimate the rate at which upwelled, high-nutrient water enters the system to replace surface waters drawn offshore by Ekman transport, as driven by a surface wind stress, T.

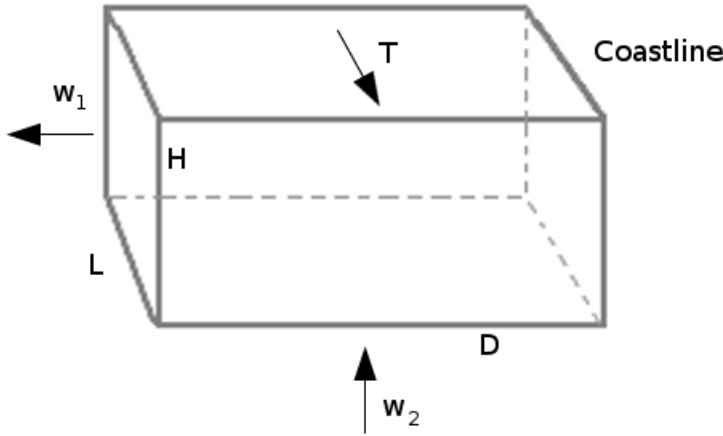


Figure 1.10: A reference volume of mixed layer in the ocean. w_1 is the horizontal velocity of Ekman transport offshore, w_2 is the upwelling velocity, \vec{T} is the surface wind stress, L is a reference length of coastline, D is the distance offshore, and H is the depth of the mixed layer.

Given a volume of the mixed layer in the ocean (as drawn in Figure 1.10), we can express that water being transported offshore must be equally replaced by upwelling as:

$$w_1 A_1 = w_2 A_2 \quad (3)$$

$$w_1 L H = w_2 L D \quad (4)$$

$$w_1 H = w_2 D \quad (5)$$

$w_1 H$ is simply the Ekman Volume Transport, which can be estimated from a given surface wind stress, water density ρ , and the Coriolis parameter f : $w_1 H = \frac{\vec{T}}{\rho f}$. Upwelling is not constant throughout its season, but time series of wind stress measurements have been taken over multiple years of upwelling seasons in the northern California Current, with a seasonal average of 0.1 N/m^2 (Bane et al. 2005), the density of water is $1000 \text{ kilograms per cubic meter}$, and at midlatitudes the Coriolis parameter is approximately 10^{-4} s^{-1} ; thus the Ekman Volume Transport, and $w_1 H$, is roughly equal to $1 \text{ m}^3/\text{s}$. We now have estimates for the left hand side of equation 5, and we want to solve for w_2 on the right. Let D be 10 kilometers , as both a typical Rossby radius (Pickett and Paduan 2003) and an estimate of how far offshore riverine nutrients might have an effect, since we are trying to directly compare river delivery to upwelling in that same region of interest. After the massive winter flood of January 1995, measurements in February and May found the across-shore flood deposit to be 8 km wide (Wheatcroft et al. 1996). With this estimate of D , a typical upwelling velocity is $w_2 = 0.1 \text{ mm/s}$; a smaller D would increase this value. The World Ocean Atlas gives a nitrate concentration of $40 \text{ micromoles per litre}$ in this region, at depths that will be upwelled to the surface (NOAA 2013c). This number may lack representativeness to the Eel River deposit zone, as the World Ocean Atlas has a 1° horizontal resolution. Now we can solve for the seasonal average upwelling transport rate of nitrate into the region of interest:

$$w_2 A_2 [\text{NO}_3^-] = w_2 D L [\text{NO}_3^-] = 10^7 \frac{\text{Litres}}{\text{second}} * 40 \frac{\text{umol}}{\text{Litre}} = 4e^8 \frac{\text{umol}}{\text{second}} \quad (6)$$

According to USGS gauging at Scotia (USGS 2012), between 2002-2010, daily Eel River discharge is above 5000 cubic feet per second, or 1.4×10^5 litres per second, 33.4% of the time; an average of four months each year. This threshold is useful, as below 5000 cubic feet per second discharge declines rapidly towards summer low-flow values. When flow is at or above this threshold in the 2002-2010 period, the average discharge is about 20,000 cubic feet per second/ 5.6×10^6 litres per second. Eel River nitrate concentrations in these winter months are often 8 micromoles per litre (USGS 2012; Figure 2.20), although it's worth noting that measured variability in the flood months can range over an order of magnitude in either direction, and a more representative average is 3 micromoles per litre; the higher value of 8 is selected in order to account for the probability of leeching effects during peak flow. Thus during winter, the Eel River might be delivering 4.4×10^7 micromoles of nitrate per second, an order of magnitude less than the rate of delivery during upwelling. When one considers that upwelling occurs over many months of the year (see Figure 1.3; from 2002-2010 upwelling season varies between 5-8 months in duration) and high flow is only for about 4 months, the difference in total annual nutrient delivery only widens. Of course, these two signals, upwelling nutrient delivery and riverine nutrient delivery, are out of phase, with summer upwelling and winter river flow. However, this analysis also overlooks the presence of riverine particulate nitrogen, and its potential uptake both upon delivery to the coastal ocean or after it has sunk (which could contribute to the nutrient supply during upwelling season), which could create linkages between the two seasons' coastal ocean productivity in a delayed mechanism.

Still, the difference in magnitude cannot be overlooked. It is thus not surprising that it is difficult to find first-order evidence of correlation between Eel River flow and primary productivity. If the Eel River nutrients are having an immediate impact on the coastal ocean, the signal is tiny. Still, based on the Granger causality and Canonical Correlation analyses, tiny indications exist – although they're well below the threshold of significance on an interannual timescale, it seems possible that a small signal that peaks during moments in 2005 (the year with the highest flow in the 2002-2010 period) might be related to the Eel River.

While the Eel River discharge/buoy wind measurement/NPP analysis does not get at longer-term lags (such as the possibility of iron deposition by the river taking a year or two to sink, become anoxic, and reduce, per the shelf capacitor hypothesis of (Chase 2007)), it demonstrates the possibility of further studying these short-term connections with temporally and spatially high-resolution modeling. A coupled modeling system that links hydrology and ocean circulation beneath a unified atmosphere, in a single framework would be a potentially useful tool to explore the importance of mountainous river discharge on the coastal ocean at timescales from hours to years. For the case of the Eel River, a focus on water year 2005-2006, with the most extreme storms of the decade (and the strongest indication of correlation, in both Granger and Canonical Correlation Analysis), is likely to have the strongest signal and produce the most interesting results.

Table 1.3: 2000-present Eel River papers by topic. Literature reviews and other particularly useful papers are highlighted. Internal watershed dynamic literature is excluded.

Topic	Authors	Year	Relevant details	Significant results
Biogeochemical cycling: anaerobic conditions	Levin et al.	2000	Metazoan microfauna from methane-seep sediments on the continental slope	
Biogeochemical cycling: anaerobic conditions	Hinrichs et al.	2000	Molecular and isotopic analysis of anaerobic methane-oxidizing communities in marine sediments	
Biogeochemical cycling: anaerobic conditions	Rathburn et al.	2000	As Hinrichs et al.	
Biogeochemical cycling: anaerobic conditions	Levin and Michener	2002	Stable isotope study at the Eel R. margin: Primarily sulfide-oxidizing bacteria, distinct microhabitats of microbial mats	Methane bubbles emanating from sediments beneath the mats
Biogeochemical cycling: anaerobic conditions	Levin et al.	2003	Further study of microbial mats	No oxygen could penetrate the mats; Oxygen can penetrate sediments down to 3-4 mm
Biogeochemical cycling: anaerobic conditions	Orphan et al.	2004	Overview of geological, geochemical and microbiological heterogeneity of the seafloor around methane vents	
Biogeochemical cycling: anaerobic conditions	Levin et al.	2010	Updated review on methane vent microbiology	
Biogeochemical cycling: anaerobic conditions	Beal et al.	2009	Mn and Fe-dependent marine methane oxidation study on Eel R. margin	Demonstrates that Fe and Mn delivered in Eel R. sediments can be used as electron acceptors in marine anaerobic oxidation of methane
Biogeochemical cycling: anaerobic conditions	Homoky et al.	2009	Eel R. sedimentary Fe redox cycling studied through measurement of isotopic iron in pore fluids; Depth profiles of nitrate, organic carbon, mn and iron species down to 20 cm depth	Results consistent with aerobic respiration at the surface, with dissimilatory iron reduction starting at about 5 cm; evidence for continuous reoxidation of iron to amorphous oxyhydroxides, with organic carbon necessary for full dissolution

Biogeochemical cycling: anaerobic conditions	Severmann et al.	2010	Isotopically distinct benthic iron flux measured	They propose it's remobilized from the particulate by the delivery of Eel R. reactive organic carbon to the sea floor by riverine discharge
Biogeochemical cycling: anaerobic conditions	McManus et al.	2012	Benthic Mn fluxes from the Eel R. continental shelf an order of magnitude higher than other regional shelf settings	Flux co-varies with the organic carbon oxidation rate
Biogeochemical cycling: anaerobic conditions	Roy et al.	2013	Expansion on McManus et al. 2012, studying Fe and Mn fluxes from the Eel R.	Found reactive iron and manganese concentrations in the Eel R. sediment positively correlating with organic carbon content
Biogeochemical cycling: biological perturbation of shelf-held sediments	Cutter and Diaz	2000	Sediment profile and surface image examination for biological alteration of the physically structured flood deposits	Mid-shelf deposits markedly altered by polychaete burrows
Biogeochemical cycling: biological perturbation of shelf-held sediments	Sommerfield et al.	2001	Comparison of distributions of C, S, Fe in both modern Eel Sediments and ancient mudrocks	Bioturbation intensity has been constant for a very long time
Biogeochemical cycling: biological perturbation of shelf-held sediments	Richardson et al.	2002	Evidence of large burrowing that is preferable for the proliferation of sediment biochemical reactions	Porosity turns out to be a good way to resolve small-scale biogenic variability
Biogeochemical cycling: characterization of Eel R.-delivered organic matter	Leithold and Blair	2001	Carbon isotopic, C:N and C:surface area ratios of particles in Eel Flood deposits expected to reflect rapid unloading of terrestrial carbon from discharged particles, but don't	Possibly particle delivery to and burial on continental shelf are so rapid that kerogen is not completely oxidized, and gets recycled again
Biogeochemical cycling: characterization of Eel R.-delivered organic matter	Blair et al.	2003	As Leithold and Blair 2001, supported with more data	

Biogeochemical cycling: characterization of Eel R.-delivered organic matter	Leithold et al.	2005	Isotopically characterization and analysis of wood fragments from Eel plume	Propose model for particulate organic carbon transport and burial
Biogeochemical cycling: characterization of Eel R.-delivered organic matter	Blair et al.	2004	Apply proposed model to both Eel and Amazon R.	
Biogeochemical cycling: characterization of Eel R.-delivered organic matter	Locat et al.	2002	Characterization of 15 cm depth core samples of sediment on the shelf	Organic matter on the order of 1-2% by mass; Whether OM had been broken down post-burial is unclear
Biogeochemical cycling: characterization of Eel R.-delivered organic matter	Drenzek et al.	2009	A re-evaluation of the importance of petrogenic organic carbon burial in marine sediments. Particularly good characterization of organic matter and their ages in Eel R. sediment	Previous assumption: vascular plant detritus spends little time sequestered in river deltas. However: plants can be sequestered for thousands of years in soils before being deposited as sediments!
Biogeochemical cycling: characterization of Eel R.-delivered organic matter	Goñi et al.	2013	Another thorough characterization of Eel R. particulate organic matter delivered to the ocean; Includes samples from low and high flow regimes	
Sediment fate and transport: physical characterization	Friedrichs et al.	2000	Bottom-boundary-layer velocity profile study	Fine sediment accumulates even in energetic environments like the eel if it dominates the source material and is abundant
Sediment fate and transport: physical characterization	Crocket and Nittrouer	2004	Characterized sandy fraction of sediment	50% accumulates on inner continental shelf
Sediment fate and transport: physical characterization	Mullenbach et al.	2004	Characterization of sediment	12% of sediment accounted for in upper Eel River Canyon
Sediment fate and transport: physical characterization	Mullenbach and Nittrouer	2006	Isotopic (be, th, pb) characterization of eel river canyon sediment	2% is accumulating rather than merely passing through
Sediment fate and transport: physical characterization	Hill et al.	2000	Settling velocities of suspended sediment in Eel River flood plume	During periods of extreme sediment, heavy flocs form and sink faster; there is both widespread dispersal of flood sediment off the shelf, and a consistent locus of deposition of flood layers on the shelf

Sediment fate and transport: physical characterization	Curren et al.	2002	Tested Hill et al. hypothesis, found no sediment between floc size/concentration	Found relationship between bulk mean settling velocity of plume sediments, and wind speed/direction
Sediment fate and transport: gravity flows	Geyer et al.	2000	Eel river storm plume data (1996-1998)	There must be a mechanism other than plume transport delivering sediment from inner shelf to midshelf
Sediment fate and transport: gravity flows	Traykovski et al.	2000	Acoustic backscatter data, water velocity profiles during depositional events	Proposed mechanism: density-driven fluid mud flows
Sediment fate and transport: gravity flows	Ogston et al.	2000	Bottom boundary layer tripods found near-bed layer of suspended sediment consistent with fluid mud	Two-stage conceptual model, plume sediment initially trapped on inner shelf, then transported seaward due to gravitational forcing
Sediment fate and transport: gravity flows	Puig et al.	2003	Same group... Tested model with 1999-2000 data	Found that storms can resuspend older sediments into fluid muds, delayed transport mechanism much more independent from the sediment delivery in any single plume, happens much more often than thought possible
Sediment fate and transport: gravity flows	Ogston et al.	2004	Longer, superior analysis of currents and suspended-sediment transport	Nearbed oscillatory flows and mesoscale eddies help determine transport along and across the shelf
Sediment fate and transport: gravity flows	Guerra et al.	2006	Update of Ogston et al. 2004 analysis with more details	Argue that secondary processes both dominate and make the inner shelf a line source of sediment nourishing the mid-shelf deposit (as opposed to a point source at the Eel River mouth)
Sediment fate and transport: gravity flows	Mullenbach and Nittrouer	2000	Isotopic analysis of 1997-1998 sediment cores	Storm resuspension and transport of older sediments is indicated
Sediment fate and transport: gravity flows	Wright et al.	2001	Capstone review of the papers from 2000: collects evidence for gravity-driven sediment resuspension and transport into a more coherent whole	

Sediment fate and transport: gravity flows	Scully et al.	2002	Analytical modeling of down-slope sediment transport and deposition by gravity-driven, wave-supported flows	Success in reproducing strataform time series of velocity and deposition is strong evidence for wave-supported gravity flows controlling Eel R. margin flood deposit
Sediment fate and transport: gravity flows	Wright et al.	2002	Analytical modeling to study pulsational timing of gravity-driven transport	
Sediment fate and transport: gravity flows	Friedrichs and Wright	2004	Further development of analytical model to test across multiple continental margins	
Sediment fate and transport: gravity flows	Scully et al.	2003	Two-dimensional numerical model of wave-supported sediment gravity flows	When river delivers sufficient sediment to critically stratify wave boundary layer, wave intensity and Eel River shelf bathymetry dominate deposition pattern
Sediment fate and transport: gravity flows	Harris et al.	2005	Three-dimensional hydrodynamic model of sediment transport mechanisms	Results indicate sensitivity to the specific settling properties of fine-grained sediment
Sediment fate and transport: gravity flows	Wright and Friedrichs	2007	Major literature review of gravity-driven sediment transport	
Sediment fate and transport: gravity flows	Kniskern et al.	2011	New analysis of discharge, wave, wind conditions to create gravity flows; compares Eel R. to other western US rivers	Excellent summary of available Eel River sediment data
Sediment fate and transport: gravity flows	Warrick et al.	2013	Systematic multi-year changes in Eel River sediment concentration are described	Sediment rating curve calculations are found to be highly sensitive to the nonstationarity of the sediment time series. Concern is raised that this causes an overestimation in previous source-to-sink sediment budgets on all time scales.
Sediment fate and transport: gravity flows	Warrick	2014	Eel River sediment discharge rate estimation is found to be overestimated by a factor of two	A new estimate that uses a time-dependent sediment rating curve accounts for most of the difference between this study and previous efforts.

Sediment fate and transport: sequence stratigraphy and climate change	Sommerfield et al.	2002	Examination of stratigraphic preservation of flood events and net sedimentation rate	Stark increase in marine sedimentation in recent decades is a response to documented climactic phenomena
Sediment fate and transport: sequence stratigraphy and climate change	Leithold et al.	2005	Direct counterargument to Sommerfield et al.: land use > climate change	
Sediment fate and transport: sequence stratigraphy and climate change	Wheatcroft and Drake	2003	Intense biological mixing intensity on Eel R. shelf dissipates signals between 3-15 years	Except for episodic sedimentation from Eel R flood events, which preserve event beds and transient signals
Sediment fate and transport: sequence stratigraphy and climate change	Bentley and Nittrouer	2003	As Wheatcroft and Drake 2003, expanded.	
Sediment fate and transport: sequence stratigraphy and climate change	Sommerfield and Wheatcroft	2007	Stratigraphic preservation of flood events study	Evidence of up to 1000-year-old Eel R. flood events
Sediment fate and transport: sequence stratigraphy and climate change	Wheatcroft and Sommerfield	2005	Study of other Pacific Northwest sediment sources and sinks	Eel R.'s dispersal system uniquely exhibits much greater off-shelf transport than other rivers in the region
Sediment fate and transport: sequence stratigraphy and climate change	Nittrouer et al.	2007	Book: From Sediment Transport to Sequence Stratigraphy	Good summary of previous research on sequence stratigraphy
Sediment fate and transport: sequence stratigraphy and climate change	Andrews and Antweiler	2012	A review of the influences of climate, geology and topography on the sediment fluxes of coastal California rivers.	Climate change is found to be potentially important.

Modeling efforts: 3D ocean circulation	Pullen and Allen	2000	Purely Physical 3D model at 1 km resolution using POM; 40 day simulation.	Coastline irregularities important to generating local eddies, mixing of freshwater plume influences velocity structure of shelf flow
Modeling efforts: 3D ocean circulation	Pullen and Allen	2001	3 km and 9 km resolution runs; Strong alongshore variability in wintertime flow, good reproduction	Robust anticyclonic eddy forms when strong poleward winds weaken and reverse direction during winter storms

Chapter 2: Methodology

2.1 Introduction and Literature Review: Previous Relevant Modeling Efforts

2.2 Modeling Framework Overview

2.3 Atmospheric Forcing

2.3.1 NARR

2.3.2 Bulk flux approximations in ROMS, 10 km horizontal resolution

2.3.3 ERA-Interim

2.3.4 Comparison: ERA-Interim vs. NARR, regional scale

2.3.5 Comparison: ERA-Interim vs. NARR vs. Daymet data, local scale

2.4 Hydrological Modeling: HydroTrend

2.4.1 HydroTrend Description

2.4.2 HydroTrend Discharge

2.4.3 HydroTrend Sediment

2.4.4 HydroTrend Parameterization

2.5 Ocean Modeling: Regional Ocean Modeling System

2.5.1 Equations of Motion

2.5.2 Curvilinear Coordinates

2.5.3 Vertical Coordinates

2.5.4 Domain and Grid Resolution

2.5.5 Bathymetry

2.5.6 Temporal Resolution and Numerics

2.5.7 Horizontal Diffusion and Viscosity

2.5.8 Vertical Mixing Parameterization

2.5.9 Boundary Conditions

2.5.9.1 Lateral Boundary Conditions

2.5.9.2 Bottom Boundary Conditions

2.5.10 Surface Model Forcing

2.5.11 River Forcing

2.5.12 Model Initialization and Spinup

2.6 Biogeochemical Modeling: Nutrient-Phytoplankton-Zooplankton-Detritus

2.6.1 NPZD description and limitations

2.6.2 NPZD ROMS dynamics

2.6.3 NPZD initial and boundary conditions

2.6.4 NPZD riverine input

2.7 Model Experimental Design

2.8 Model Results

2.8.1 Results: HydroTrend

2.8.2 Results: ROMS, 10 km resolution

2.8.2.1 Climatological validation

2.8.2.2 Short timescale validation

2.8.3 Results: ROMS, 1 km resolution

2.9 Conclusion

2.1 Introduction and Literature Review: Previous Relevant Modeling Efforts

Rivers are mostly absent from global climate modeling efforts. Although river and groundwater runoff into the ocean is a driver of ocean models by land models, rivers themselves are usually at the scale of subgrid variability, often parameterized as simply as a quantity of water and a direction of flow. For example, in the Community Earth System Model (Gent et al. 2011), the River Transport Model (Branstetter 2001, Branstetter and Famiglietti 1999) uses a linear transport scheme at 0.5° resolution to route water from each grid cell to its downstream neighboring grid cell, split into liquid and ice streams. They provide a freshwater flux to the ocean, and their main function is to provide closure to the water cycle. The potential importance of river effects on the land surface and coastal ocean is not significantly studied with this current, simple scheme. Similarly, GFDL's CM2 (Delworth et al. 2006) is simple in its treatment of rivers: river flow into the ocean is based upon a predetermined river drainage map that collects and routes runoff into the top 40m of the ocean, as a freshwater flux that instantly prescribes the temperature as the same as the sea surface (which causes a heat sink). Does this gap need to be addressed by improving the internal river modeling of global climate models? One way to approach this question is to construct a regional-scale earth system modeling framework that studies a specific basin/coastal ocean system. And at the regional scale, there is a long history of modeling efforts to draw upon.

There have been a variety of previous modeling efforts especially relevant to this study. Perhaps first among equals is the River Influences on Shelf Ecosystems program (Hickey et al. 2010) which combined extensive sampling of the Columbia River plume with a major modeling effort. They found that most plume nitrate originated from upwelled shelf water, and that there was no significance difference in phytoplankton species carried within the plume and found in the adjacent coastal ocean. The program used the Regional Ocean Modeling System (ROMS) to perform a 3-month hindcast of 2004 summertime circulation on the Washington and Oregon shelf, and within the Columbia River estuary (MacCready et al. 2009), with 20 vertical levels and a 51.75s baroclinic time step, constrained by the speed of surface ebb currents at the Columbia River mouth. They used USGS data for river flow and temperature, but did not model the river directly. The same hindcast was performed with an unstructured grid called SELFE (Zhang and Baptista 2008), which performed an analysis of the sensitivity of the plume to the choice of the vertical grid. The ROMS results were used offline to drive a particle tracking experiment (Banas et al. 2009a), which found that the Columbia plume seems to increase cross-shelf dispersion by about 25% when it is present. The ecosystem used in RISE was an NPZD four box model (Banas et al. 2009b), which was successfully implemented offline from ROMS and used to analyze the effect of the presence of the plume on local coastal biology. Although primarily studying the influence of El Niño, Columbia River flow was also included in a basin-scale model of the north Pacific that ran from 1996-2002 (Hermann et al. 2009). It was found to dominate anomalies of sea surface height in its region.

Nor is the Columbia Estuary the only application of ROMS to a river-ocean interface. Numerical simulations of the Hudson River estuary have been performed (Warner et al. 2005) that were able to capture large observed variations in stratification between neap and spring tides, though without solid reproduction of the vertical salinity structure. The Chesapeake Bay estuary has also been the study of a series of ROMS studies including (Li et al. 2005), which

analyzed the effect of differing turbulence closure schemes on the model results and found little difference. However, the salinity stratification in this case was found to be very sensitive to the background diffusivity, which is in turn strongly determined by the surface and bottom boundary layer representations. ROMS was also applied to the Delaware Bay estuary (Castellano and Kirby 2011) and demonstrated reasonable skill in predicting its hydrodynamic processes, but was driven by an immense amount of local data. Other worldwide river plumes simulated numerically from gauging data include the Mekong Delta (Hordior et al. 2006), Plata River (Pimenta et al. 2005), and Brisbane River (Yu et al. 2011). Spaulding et al. (2010) collects many of these efforts in one place for review.

The Eel River plume itself was modeled in a 1 km resolution, 40-day simulation of the December 30, 1996 – January 3, 1997 flood event (Pullen and Allen 2000). The Naval Research Laboratory's Pacific West Coast Model, an implementation of the Princeton Ocean Model, was used for this effort. A 100-day simulation at 4 km resolution (Pullen and Allen 2001) found strong variability and complex flow even in the absence of river run-off, and reported a robust anticyclonic eddy centered off the Eel River mouth that occurred in response to the transient wind forcing imposed by passing storms. This was a purely physical modeling effort, but an excellent demonstration of the usefulness of physically distributed numerical model applications to the region.

In 2006, ROMS was used at 15 km resolution with a nested 5 km grid, to drive an eddy-resolving plankton ecosystem California current model (Gruber et al. 2006). The model underestimated phytoplankton in the northern part of the domain. Gruber et al. theorized that this was due to the lack of short-term variations in the atmospheric forcing, though it is also true that coastal runoff was neglected. Importantly, they attempted to model a variable chlorophyll:carbon ratio. In the same region, the importance of coastal wind forcing to the ability of a model like ROMS to capture upwelling was analyzed (Capet et al. 2004), and they found that present wind analyses such as COAMPS do not adequately determine the most important wind properties, the strength of the nearshore curl and the speed drop-off near the coast. Further study and comparison of the strengths and weaknesses of wind fields such as QuickSCAT and the NCEP/NCAR reanalysis, as used to drive eddy-resolving simulations of the Pacific, found that satellite wind fields with small scale structures outperform reanalyses in high-resolution ocean simulations (Sasaki et al. 2006).

While there have been numerous modeling efforts to resolve river plumes (Spaulding et al. 2010), and equally numerous modeling efforts to resolve planktonic dynamics in the coastal ocean (Franks 2002), there have been very few that unify these two interests by using a modeled watershed rather than existing river gauging data. In order to test how well models can study the biological effects of riverine input to the coastal ocean, and as a first step to the possible inclusion of such an earth system modeling framework within the larger climate models, a test case is useful: the Eel River, with its dramatic behavior summarized in Chapter 1, is an obvious choice.

2.2 Modeling Framework Overview

In the coupled modeling framework (Fig. 2.1), the watershed is represented with the lumped empirical hydrology model HydroTrend (Kettner and Syvitski 2008; Section 2.4), which can generate high-frequency water and sediment time series. HydroTrend was selected due to its modest prior success at modeling the Eel River as a test case (Syvitski et al. 1998a), and its ability to be driven by the same atmospheric input as the ocean model, thus creating a unified earth system modeling framework. The ocean is represented with the Regional Ocean Modeling System (ROMS; Shchepetkin and McWilliams 2005; Section 2.5), a powerful, modular, physically distributed ocean circulation model that can efficiently solve the primitive equations on the rotating Earth for momentum, heat, and other tracers, on fine-scale resolution grids. ROMS is used at two horizontal resolutions: 10 km and 1 km. Transforming HydroTrend's output into a form suitable to force the ocean and biology (Section 2.6) models requires a coupling interface based on the generation of a three-dimensional, nutrient-laden freshwater plume (Sections 2.5.11 and 2.6.4). The atmosphere (Section 2.3) is represented in the 10 km horizontal resolution experiments with the NCEP North American Regional Reanalysis (NARR; Mesinger et al. 2006), a model and data assimilation tool. For the 1 km resolution model, due to the poor performance of NARR at fine scales using a bulk flux approximation, the ERA-Interim reanalysis data assimilation system (Dee et al. 2011) was used for atmospheric forcing instead.

The Eel River was modeled in HydroTrend from 1979-2010. The coastal ocean was modeled in ROMS from 2000-2010 with 10 km horizontal resolution, without inclusion of the river or biology. A nested 1 km resolution model was run from 2002-2010, and carried within it the Nutrient-Phytoplankton-Zooplankton-Detritus biological model (Powell et al. 2006; Section 2.6), as well as the physical and biological presence of the Eel River. Model experimental design is discussed in Section 2.7, while model results are discussed in Section 2.8.

The 10 km ROMS runs were computed on 64 parallel processors of the Hadley Computing Cluster at Lawrence Berkeley National Laboratory. The 1 km ROMS runs were computed on 256 parallel processors of the Yellowstone High-Performance Computing Cluster at the National Center for Atmospheric Research (CISL 2014).

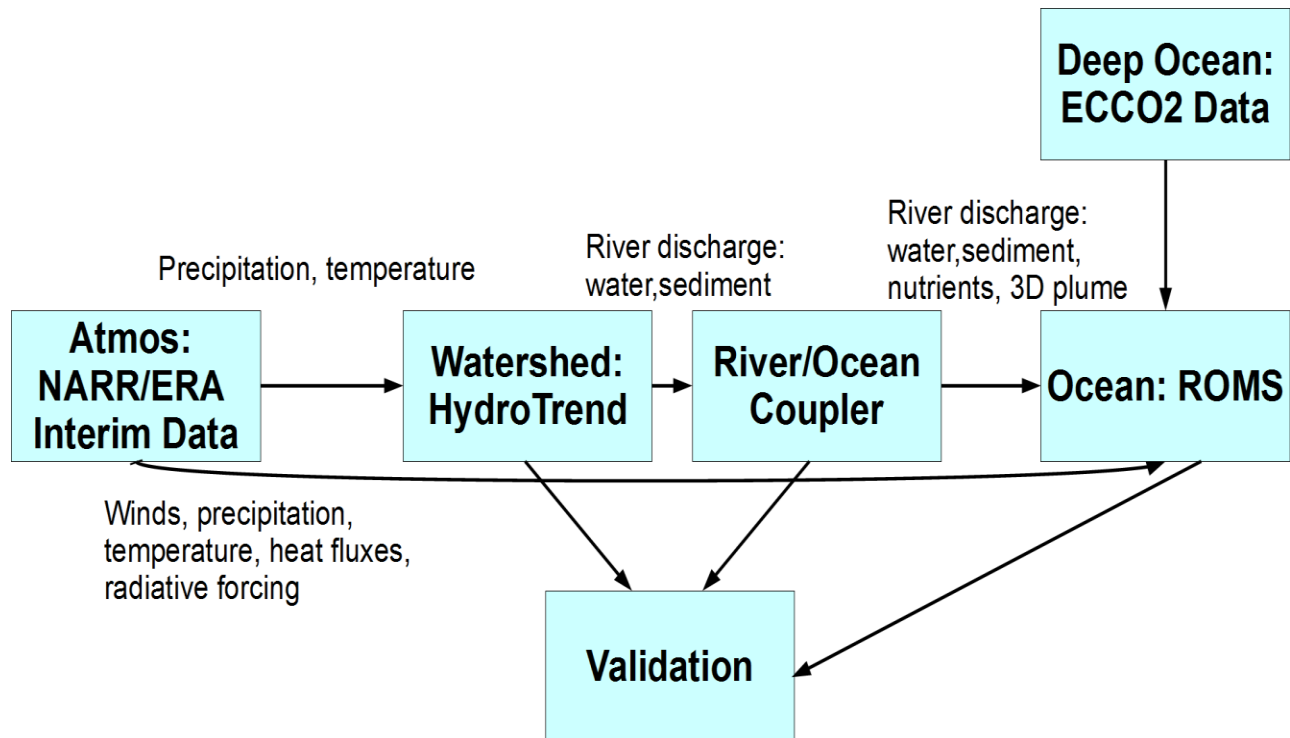


Figure 2.1: The coupled modeling framework.

2.3 Atmospheric Forcing

The choice of atmospheric forcing is critical to the land surface and ocean models – and the choice to use the same dataset for both models is ultimately what closes the circle of the modeling framework. Initially, the North American Regional Reanalysis was selected for its high resolution both temporally and spatially. However, in order to apply NARR to ROMS, bulk flux approximations were necessary, and the inadequacy of these approximations under conditions of low winds, particularly at 1 km horizontal resolution in ROMS, led to the search for an alternative atmosphere.

Use of the ERA-Interim dataset is a compromise. Its horizontal resolution is nearly an order of magnitude inferior to NARR, but its fields allow direct application of surface stress, as well as heat and water fluxes, onto and across the sea surface boundary. The use of ERA-Interim on 1 km ROMS significantly reduced sea surface temperature, which had previously been running several degrees too hot. However, the 10 km ROMS results were not rerun with ERA-Interim atmosphere due to the constraint of computational expense, so the influence of NARR and the bulk flux approximations remain in the initialization and boundary conditions of the 1 km results.

The difference between NARR and ERA-Interim atmospheres in HydroTrend is explored in section 2.3.5.

2.3.1 NARR

The North American Regional Reanalysis (Mesinger et al. 2006) is a long-term, consistent, high resolution climate dataset for the North American domain in both atmospheric and land surface hydrology. It spans 1979-present on a 32 km horizontal resolution and 38 vertical levels of pressure in the atmosphere. Sea surface temperatures were derived from the 1° Reynolds dataset (Reynolds et al. 2002). Notably, NARR 10 m winds have a slight negative bias in both winter and summer, while NARR's residual of the atmospheric water balance shows a significantly positive bias (due to excess precipitation) along much of the Northwest coast of CONUS, starting at roughly Cape Mendocino (Mesinger et al. 2006).

2.3.2 Bulk flux approximations in ROMS, 10 km horizontal resolution

The bulk flux approximations used in ROMS model an ocean-atmosphere boundary layer using air-sea exchange parameterizations from Liu et al. (1979). NARR provides surface U-wind (positive Eastward) and V-wind (positive Northward) components (m/s), air temperature (C), pressure (mb), relative humidity (%), cloud fraction (0 to 1), rainfall rate (kg/m²/s) and shortwave radiation flux (W/m²). As described in Liu et al. (1979), Monin-Obukhov similarity theory is then used to estimate the turbulent fluxes for wind, heat and moisture. However, the basic similarity profile assumption that the roughness length is much smaller than the Monin-Obukhov length is violated at wind speeds below about 0.5 m/s, a condition that occurs regularly in this system. For this reason, use of the bulk flux boundary layer was abandoned at the 1 km horizontal scale. At 1 km, the change in atmospheric boundary forcing accounted for approximately 2° Celsius of extraneous sea surface temperature, particularly in summer.

2.3.3 ERA-Interim

ERA-Interim (Dee et al. 2011) is the latest global atmospheric reanalysis produced by the European Centre for Medium-Range Weather Forecasts (ECMWF). It covers 1979-present on a 0.75-1.125° resolution horizontal grid, and uses a powerful 4-dimensional variational assimilation, as well as variational bias correction of satellite radiance data, and more extensive use of radiances with an improved fast radiative transfer model (Dee et al. 2011). Both 3-hour and 6-hourly surface parameters are available, within the 12-hourly analysis cycle of the sequential data assimilation scheme. In each cycle, available observations are combined with prior information from a forecast model to estimate the evolving state of the atmosphere and its underlying surface (Dee et al. 2011). Outputs include direct boundary conditions for ROMS: surface stress in the u and v directions, and fluxes of heat and moisture (for more information, see section 2.5.10). Excessive solar radiation in ERA-Interim causes a net heat flux into the ocean, but this bias is mostly concentrated in convective tropical areas; if anything the ocean is up to a degree too cold in our region of interest, while land surface temperatures average out within a degree in either direction depending on the time of year (Stopa and Cheung 2014). Wind speeds are slightly underestimated, but ERA-Interim's consistency through time (as opposed to carrying a large spin-up or spin-down bias) makes it especially useful for multi-year forcing and intercomparison (Stopa and Cheung 2014).

2.3.4 Comparison: ERA-Interim vs. NARR, regional scale

In order to understand differences introduced to the modeling framework by use of either of these atmospheric forcings, Figures 2.2 to 2.9 show comparisons of monthly climatologies (1985-2010) between ERA-Interim and NARR datasets for precipitation (12-hourly), temperature (6-hourly) and winds (6-hourly), for the months of January (when Eel storm events are important) and July (when upwelling is important), as both a spatial map and a histogram of the values that went into the map. In January (Figure 2.2), we see that NARR is wetter than ERA-Interim on the order of 3 mm/day, throughout much of the Eel River watershed. This highlights the misleading outcome of only looking at precipitation near Eureka and the mouth, since such a comparison shows ERA-Interim having heavier precipitation, on average. Over the ocean, NARR is 1-2 mm/day dryer than ERA-Interim. Nonparametrically, we see that NARR is generally more extreme than ERA-Interim, reaching greater maximum precipitation and a large region of minimal precipitation as well (which is over the ocean). In July (Figure 2.3), all precipitation is an order of magnitude less than in January, and the differences between datasets are similarly smaller, though in the same direction as January. For 2 m height air temperature in January (Figure 2.4), the datasets are essentially identical over the ocean but vary in isolated patches over land, with NARR 2-3° warmer than ERA-Interim throughout most of the Eel Watershed. The histograms are quite similar. In July (Figure 2.5), temperature over the ocean is again nearly identical, with a slight warming bias in NARR onshore. Over land, ERA-Interim is 2-3° warmer north of Eureka, and then steadily cooler as one progresses south past San Francisco. NARR reaches greater maxima of heat, but ERA temperatures are more widely distributed across the temperature range.

Given basin-averaged temperature and precipitation for HydroTrend, the net effect we would expect is more river discharge from NARR (since there is consistently more precipitation) offset to some degree by greater evaporation (since overland temperatures are higher), and less snowfall (since NARR is typically warmer) leading to a more continuous, less snowmelt-driven discharge rate in winter. In ROMS, the cooler, dryer ocean surface forcing of NARR would be expected to inhibit heat flux out of the ocean, while encouraging a net increase in water flux (generally defined as Evaporation – Precipitation), though the relative magnitude of NARR-driven versus ERA-driven evaporation would be moderately smaller due to the cooler air.

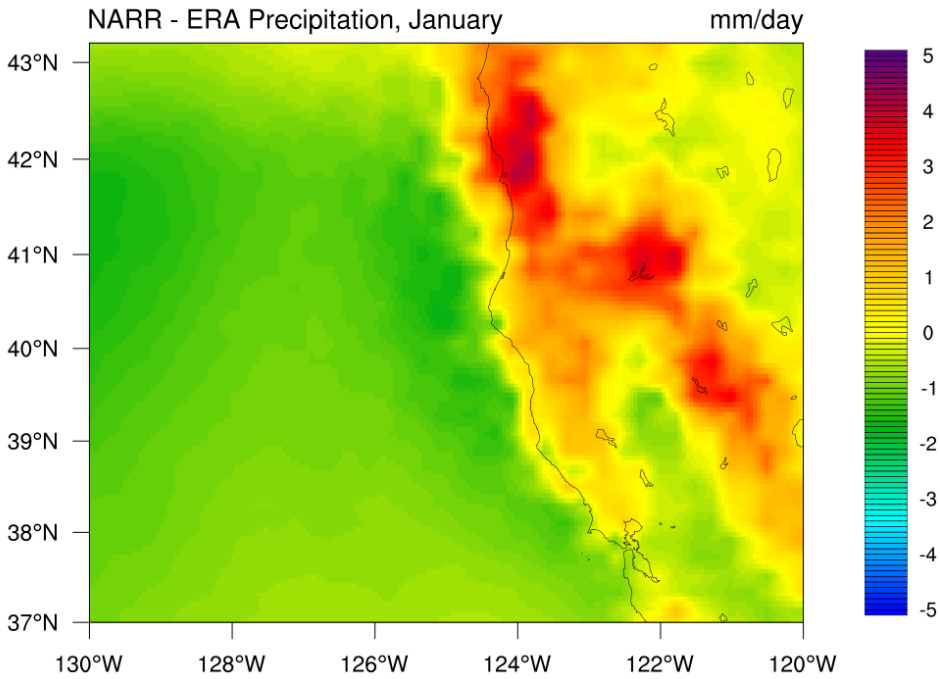
The histograms are especially useful for interpreting differences in NARR and ERA winds, as they can be negative, and the result of their direct subtraction can obfuscate issues related to their sign. Winds in the U (positive East, negative West) direction are similar over the ocean in January (Figure 2.6), with a trend towards stronger NARR winds over the ocean as one progresses south of Cape Mendocino. The NARR U-wind distribution is centered more positively than ERA, on the order of 0.5 m/s overall, 1-2 m/s overland and near the mouth of the Eel, which could have the effect of pushing Eel storm plumes onshore more strongly than ERA-Interim. V-winds (positive North, negative South), which drive coastal upwelling and are crucial during storm periods, are perhaps the most important of these four variables to compare. In January (Figure 2.8), the NARR winds are consistently stronger (and more positive/northward), with an exception: right at the mouth of the Eel River, heading north where the Eel storm plumes are often thought to be advected (Wheatcroft et al. 1997), ERA-Interim is about 0.5-1 m/s

stronger than NARR. Over land, NARR has consistently stronger southerly winds, often 3 m/s compared to ERA's more typical 1 m/s.

In July (Figure 2.7), NARR U-winds are consistently 1 m/s stronger than ERA-winds offshore, but onshore, in the upwelling zone, that bias weakens, nearing zero with any small positive bias going to ERA-Interim, instead. Over land, the two datasets remain similar in the Eel watershed, with small geographical patches of both NARR and ERA bias further south. In V-winds (Figure 2.9), the contrast is noticeable: NARR has consistently weaker upwelling winds north of Cape Mendocino, starting at 1 m/s weaker and going up to 2.5 m/s in the extrema, while this bias reduces along the coast, nearing zero south of Cape Mendocino. On shore, the northerlies are up to 4 m/s stronger in NARR, with a positive bias up to 4 m/s in ERA-Interim further inland.

The most significant wind differences in the atmospheric forcings are overland, which is irrelevant to HydroTrend and masked off in the ROMS ocean model. However, ERA-Interim's stronger upwelling winds are likely to have a significant impact on the biological component of the model during the summer season when the river is likely to be unimportant. In winter, ERA-Interim's slightly stronger southerlies near the mouth of the Eel River might have an impact on the fate and transport of river plumes, while acted upon by a NARR atmosphere those plumes might have been driven closer to shore by stronger U-winds.

For the purposes of the modeling framework, the most significant differences between the atmospheric datasets appear to come from precipitation (NARR being wetter than ERA-Interim during the storm season) and V-winds (ERA-Interim having stronger upwelling winds than NARR, and ERA-Interim having slightly stronger southerlies near the mouth of the Eel River during the winter). The temperature biases are markedly large, but they occur mercifully outside of our domain of interest.



ERA (solid) and NARR (hatched) Precipitation (mm/day), January

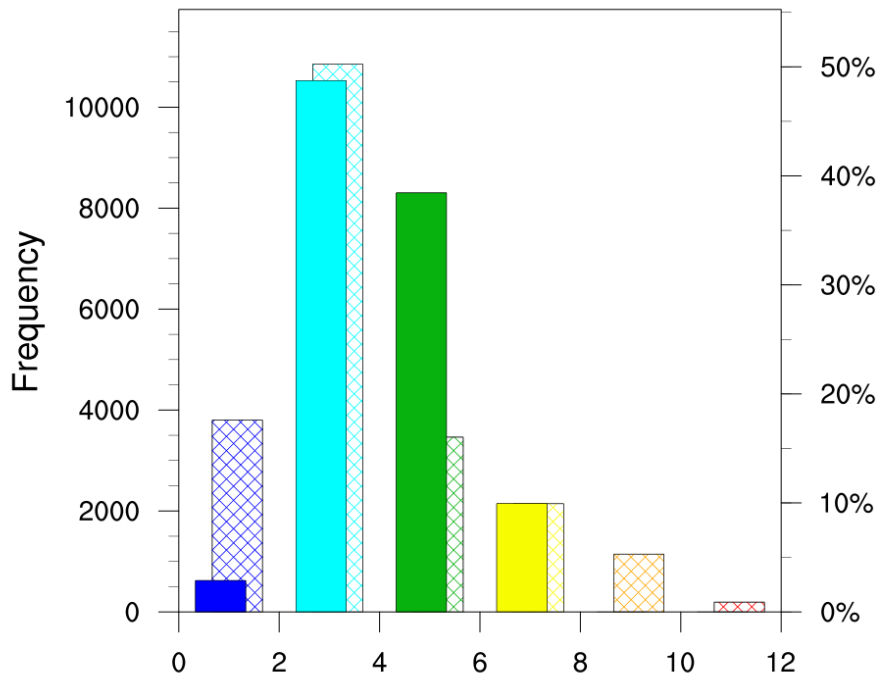
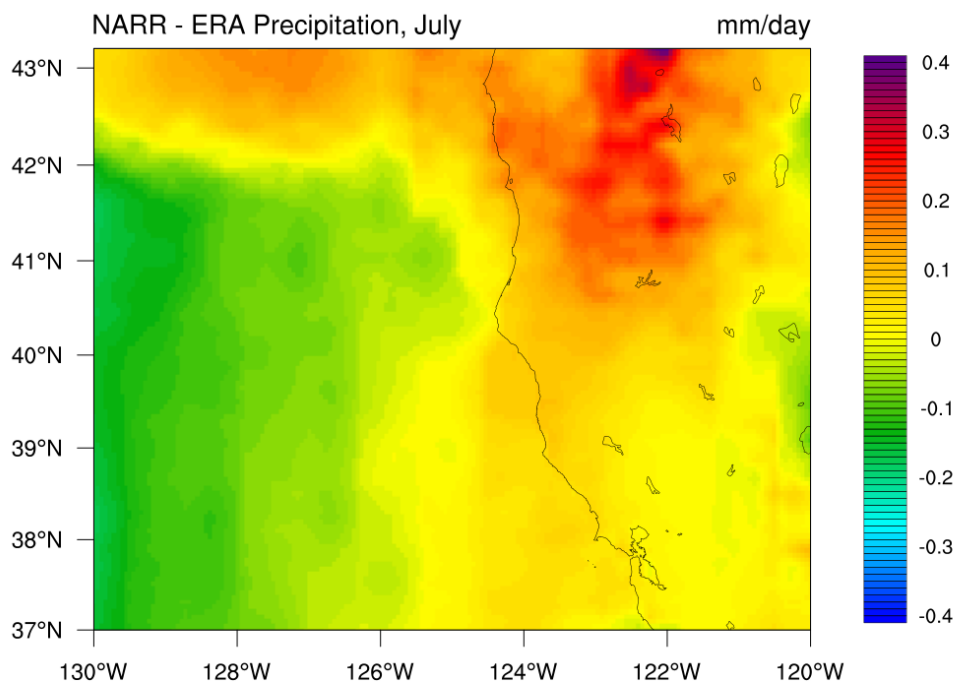


Figure 2.2: 1985-2010 January climatology of precipitation, ERA-Interim subtracted from NARR (top) and histogram comparing precipitation spatial distributions (bottom).



ERA (solid) and NARR (hatched) Precipitation (mm/day), July

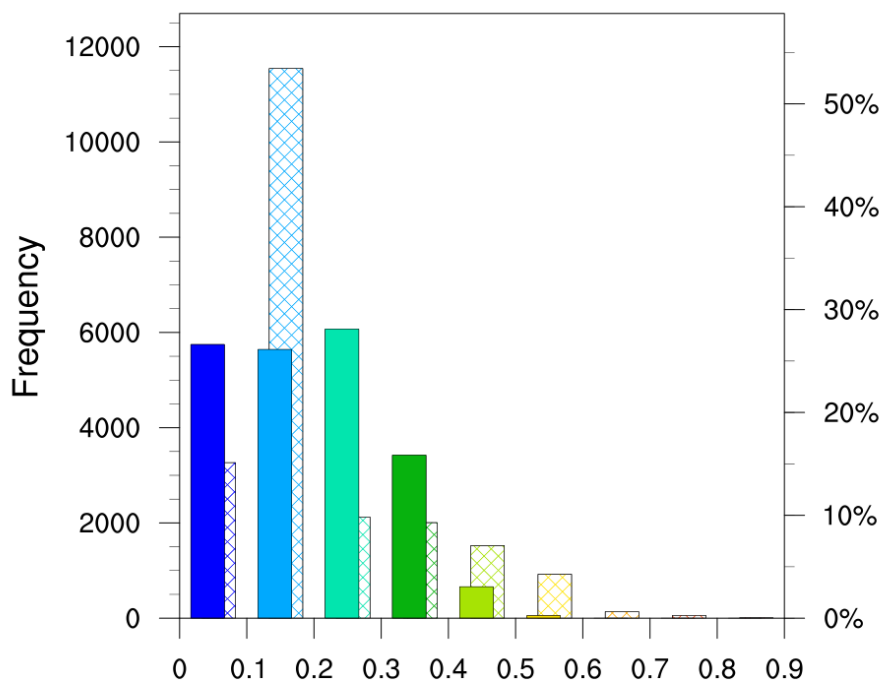
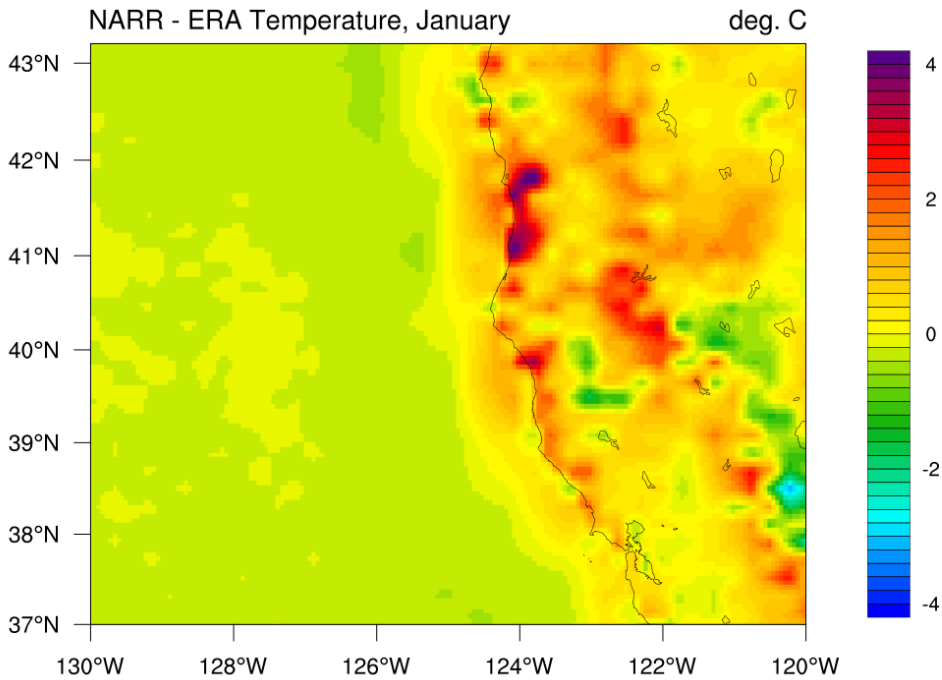


Figure 2.3: 1985-2010 July climatology of precipitation, ERA-Interim subtracted from NARR (top) and histogram comparing precipitation spatial distributions (bottom).



ERA (solid) and NARR (hatched) Temperature (deg. C), January

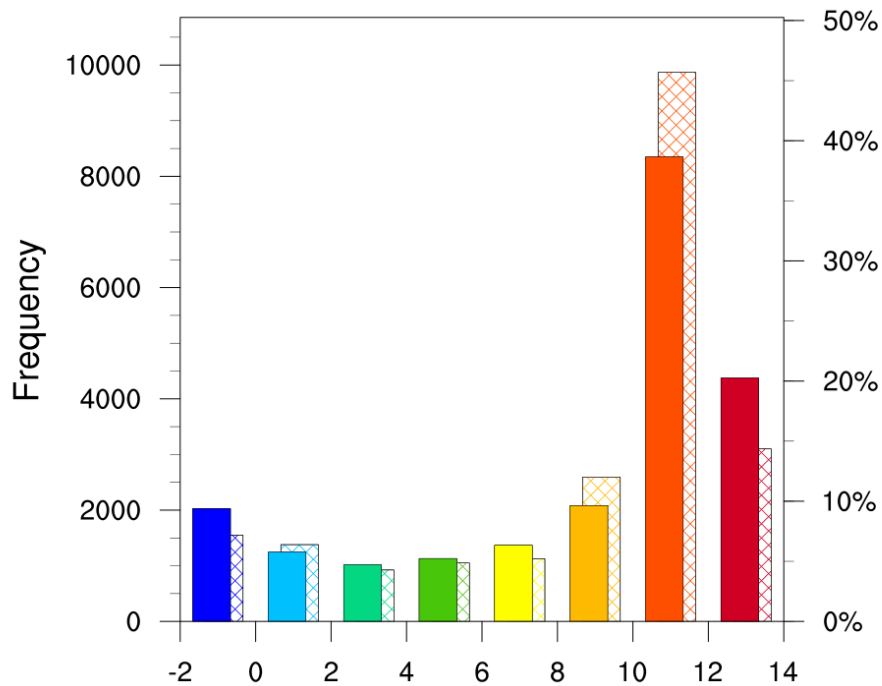
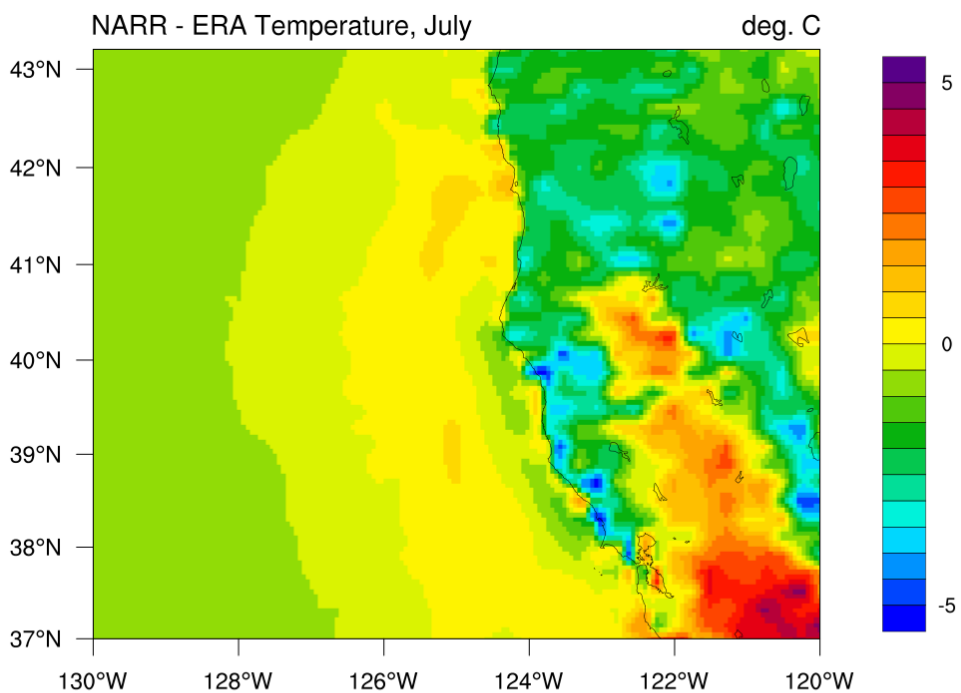


Figure 2.4: 1985-2010 January climatology of temperature, ERA-Interim subtracted from NARR (top) and histogram comparing temperature spatial distributions (bottom).



ERA (solid) and NARR (hatched) Temperature (deg. C), July

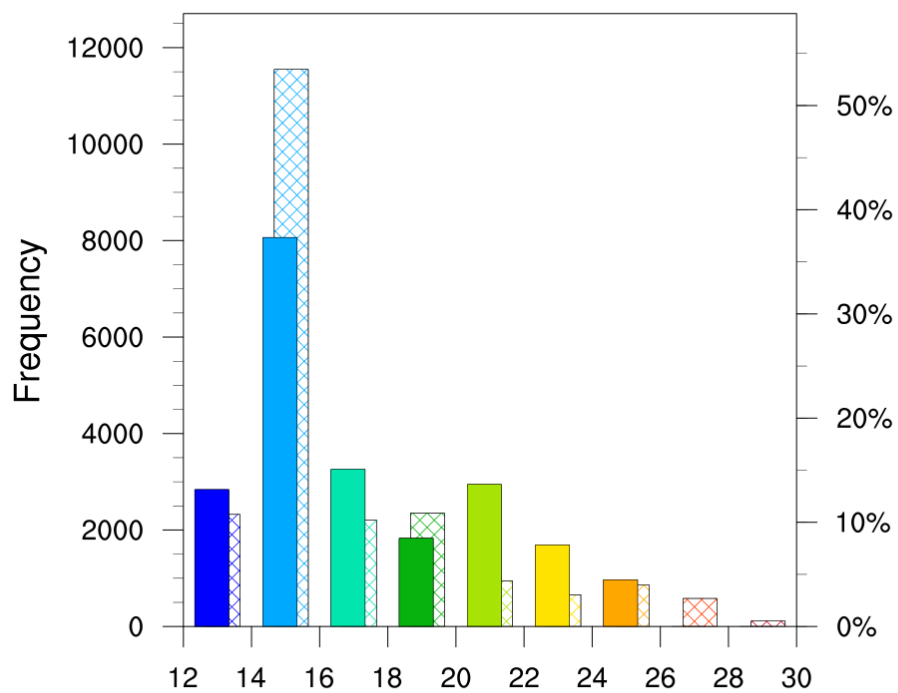
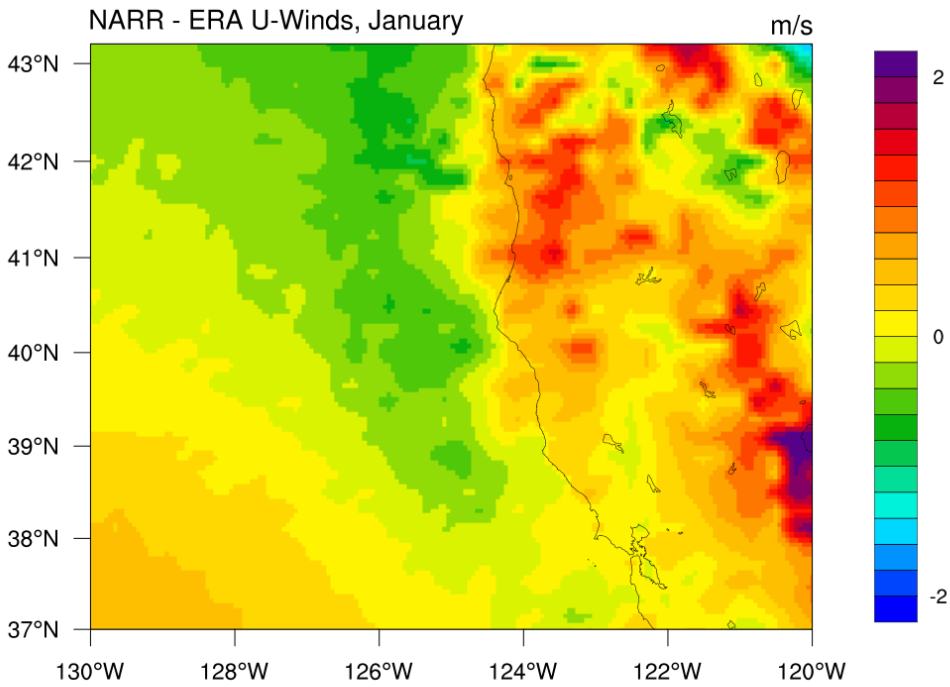


Figure 2.5: 1985-2010 July climatology of temperature, ERA-Interim subtracted from NARR (top) and histogram comparing temperature spatial distributions (bottom).



ERA (solid) and NARR (hatched) U-winds (m/s), January

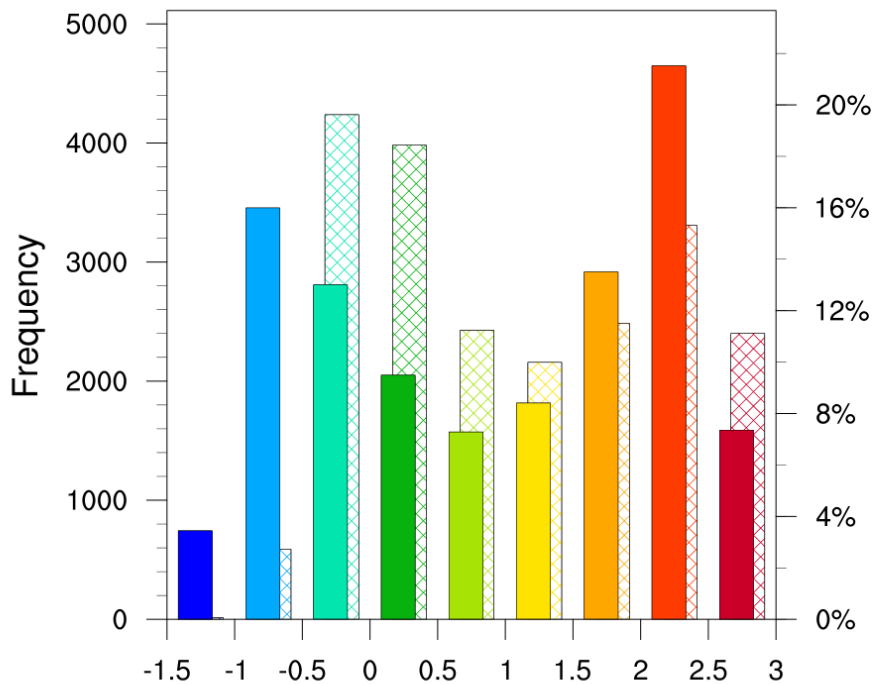


Figure 2.6: 1985-2010 January climatology of U (positive Eastward) winds, ERA-Interim subtracted from NARR (top) and histogram comparing spatial wind distributions (bottom).

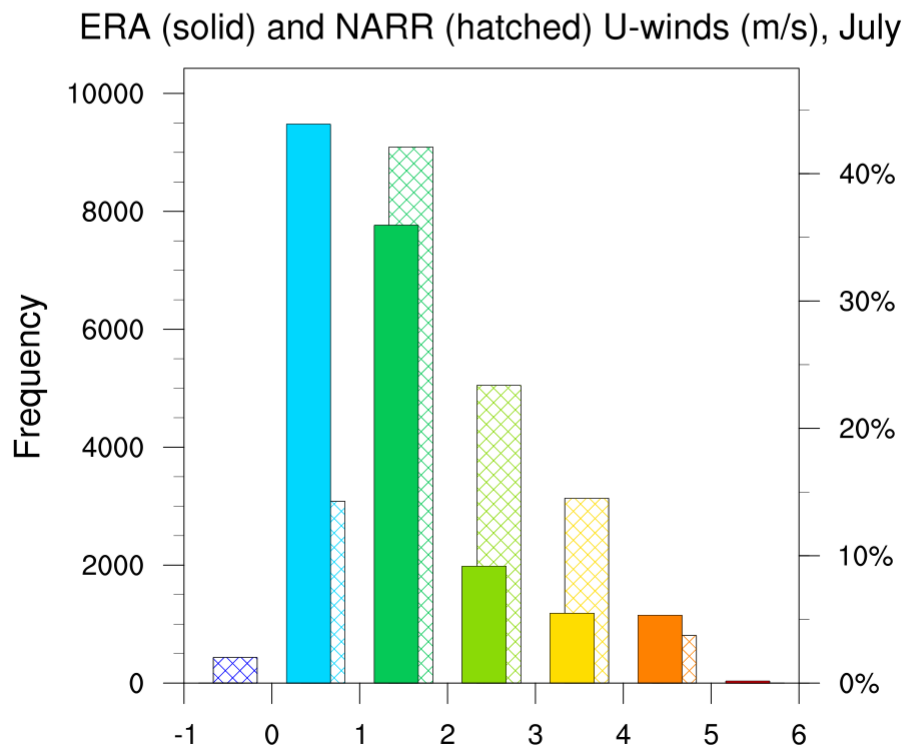
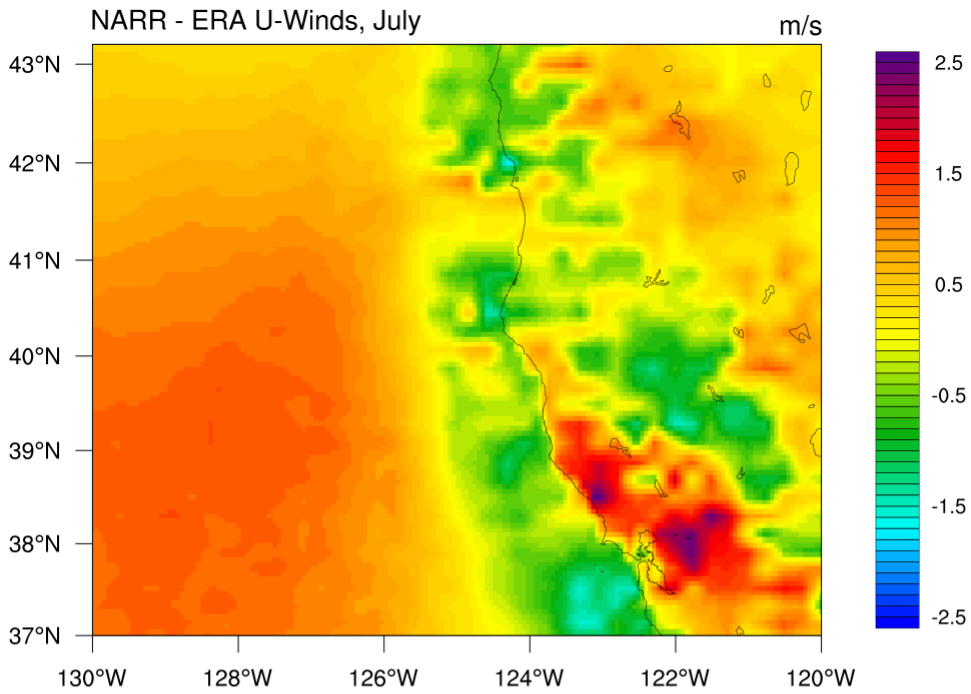
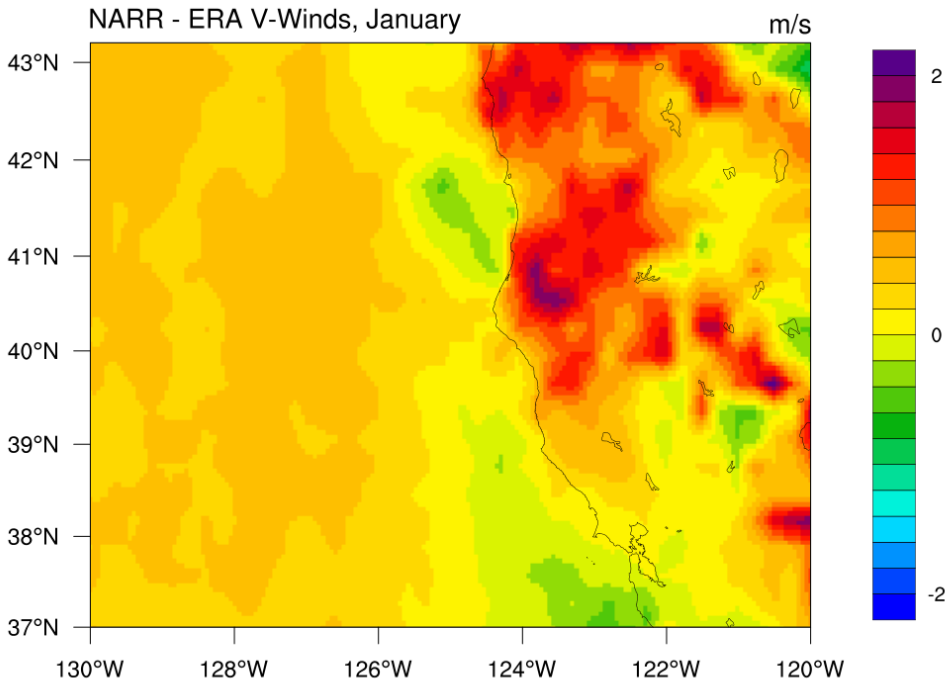


Figure 2.7: 1985-2010 July climatology of U (positive Eastward) winds, ERA-Interim subtracted from NARR (top) and histogram comparing spatial wind distributions (bottom).



ERA (solid) and NARR (hatched) V-winds (m/s), January

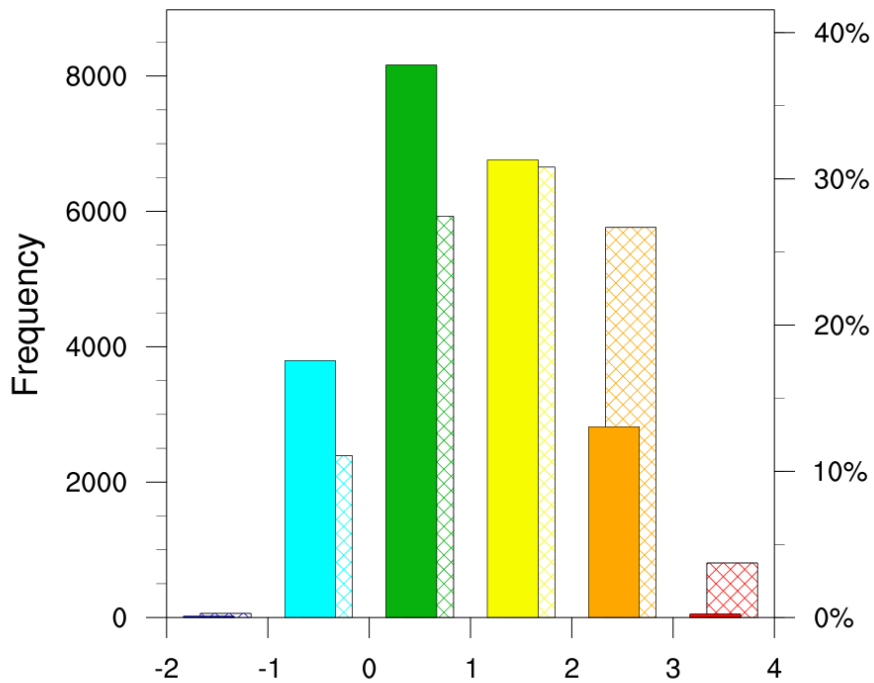


Figure 2.8: 1985-2010 January climatology of V (positive Northward) winds, ERA-Interim subtracted from NARR (top) and histogram comparing spatial wind distributions (bottom).

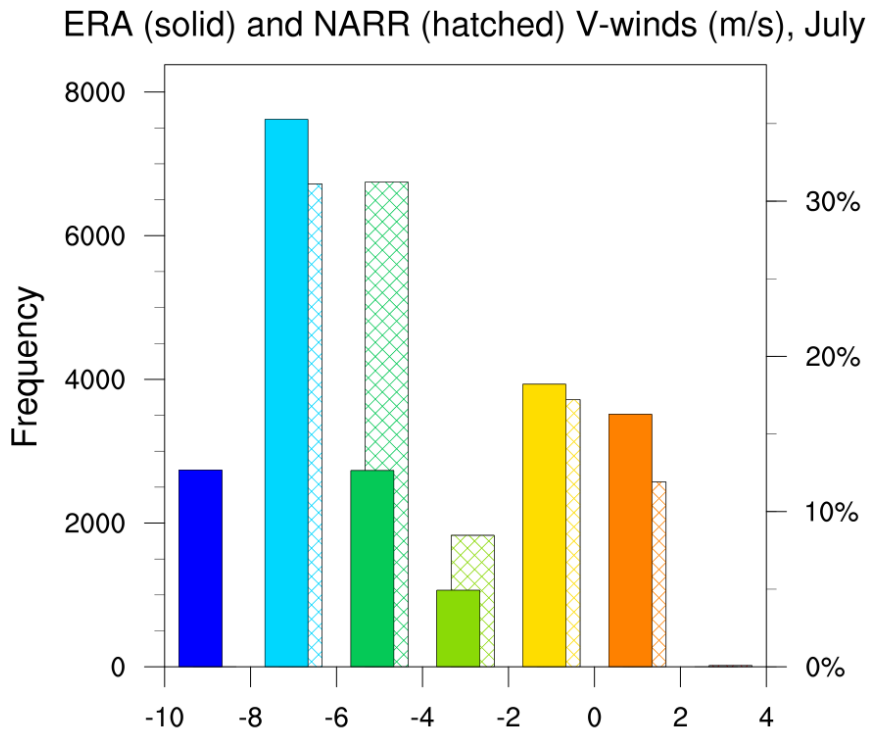
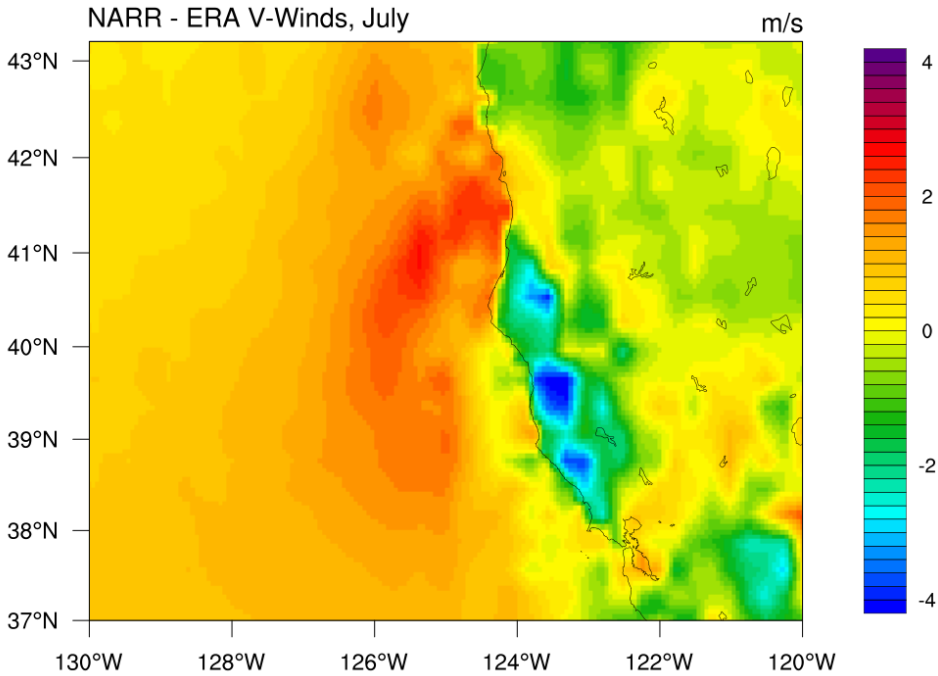


Figure 2.9: 1985-2010 July climatology of V (positive Northward) winds, ERA-Interim subtracted from NARR (top) and histogram comparing spatial wind distributions (bottom).

2.3.5 Comparison: ERA-Interim vs. NARR vs. Daymet data, local scale

HydroTrend (see section 2.4) requires input of sea level temperature and basin averaged precipitation. These can be delivered stochastically, by defining a set of climate parameters, or directly with time series. With two sets of atmospheric forcing data available, basic comparisons of these data to a ground truth is prudent.

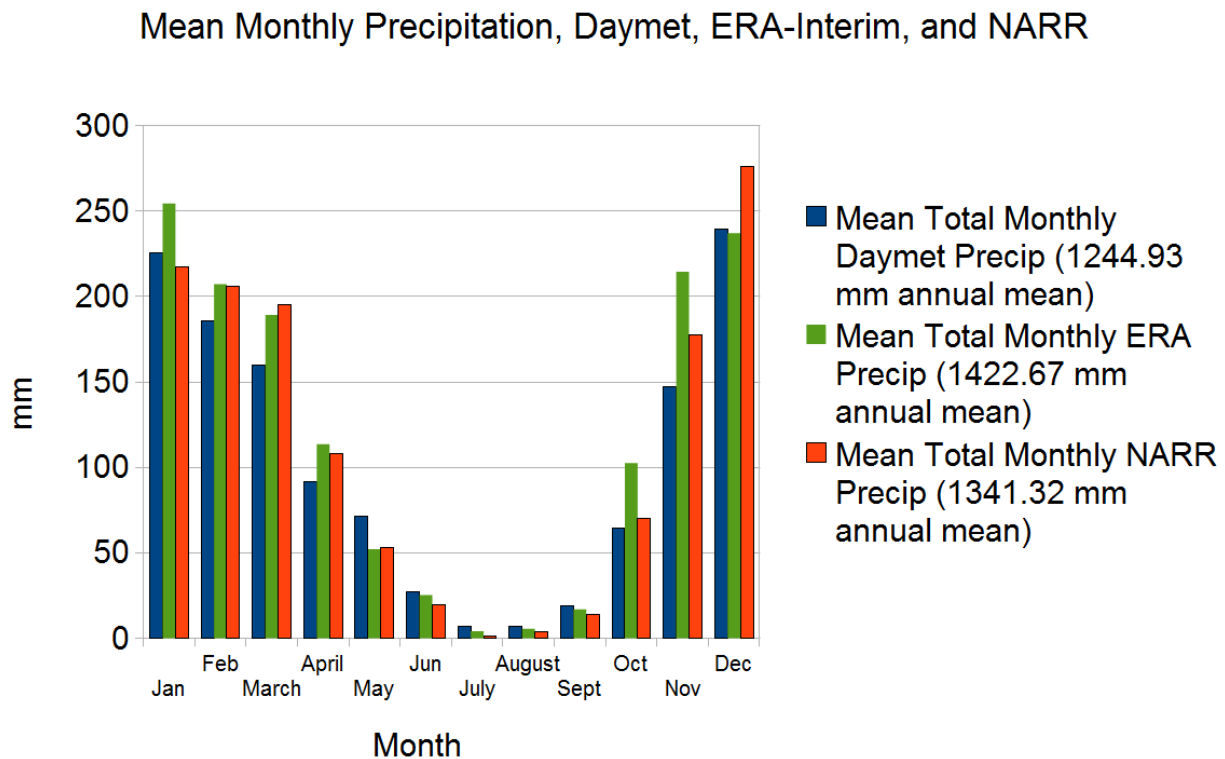
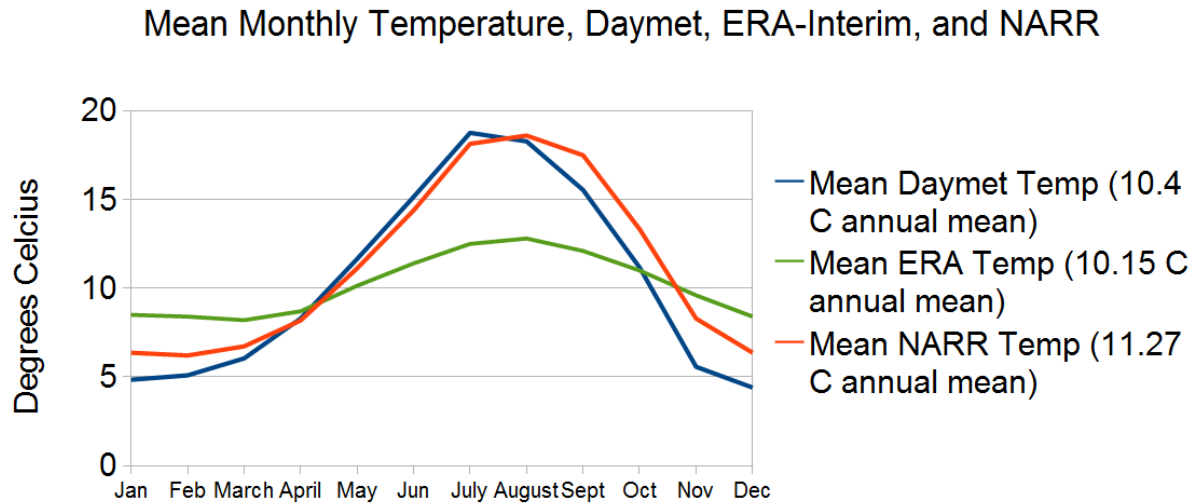
The Daymet (Thornton et. al. 2014) data set (1 km horizontal resolution) provides gridded estimates of weather parameters for North America, including continuous surfaces of minimum and maximum temperature and precipitation occurrence and amount. Monthly climatologies were constructed from 1985-2010 daily data spatially averaged from 40-42 N, -122 to -124 W, an area that includes much of the Eel River Basin.

The North American Regional Reanalysis (32 km horizontal resolution) has three-hourly estimated temperature and precipitation. The four overland points nearest the Eel River mouth were averaged together to generate a time series for HydroTrend from 1979-2010. Climate statistics were also calculated, for comparison to the on-the-ground data from the station.

The ERA-Interim Reanalysis (1.5° horizontal resolution) has six-hourly estimated temperature and precipitation. The two overland points nearest the Eel River mouth were averaged together to generate a time series for HydroTrend from 1998-2010 (and this difference in time coverage may account for some of the differences we see), with climate statistics also generated.

In Figure 2.10 we see that the Daymet and NARR monthly average temperatures agree well, with an earlier and shorter summer peak, and cooler winters, in Daymet. ERA fails to capture the extremity of the seasonality, with smaller differences in average temperature throughout the year. NARR's average temperature (11.27° C) is nearly a full degree warmer than Daymet's average (10.4° C) while ERA is modestly cooler (10.15° C). Figure 2.11 demonstrates that both the NARR (1342.32 mm) and ERA (1422.67 mm) annual average precipitation overestimate the Daymet data (1244.93 mm) by up to 115%. The reanalyses tend to underestimate precipitation in summer, and overestimate it in winter, but the differences are fairly small overall.

When compared to the within-month standard deviation of the Daymet data, the significance of the difference between the datasets becomes clear: the difference in precipitation is insignificant, while the difference in temperature is significant. Despite overestimating the Daymet precipitation on average, NARR and ERA precipitation falls well within one standard deviation of the Daymet data's variability (Figures 2.13 and 2.15), presumably because of the extreme behavior of winter storm events. The difference in temperature, however, is far greater than one standard deviation, any given month of the year, for ERA, and diverges significantly for NARR in the latter half of the year (Figures 2.12 and 2.14).



Figures 2.10 (top) and 2.11 (bottom): mean monthly temperature and precipitation for the Daymet Dataset, the North American Regional Reanalysis, and ERA-Interim.

Significance of difference between Daymet and NARR data, Temperature

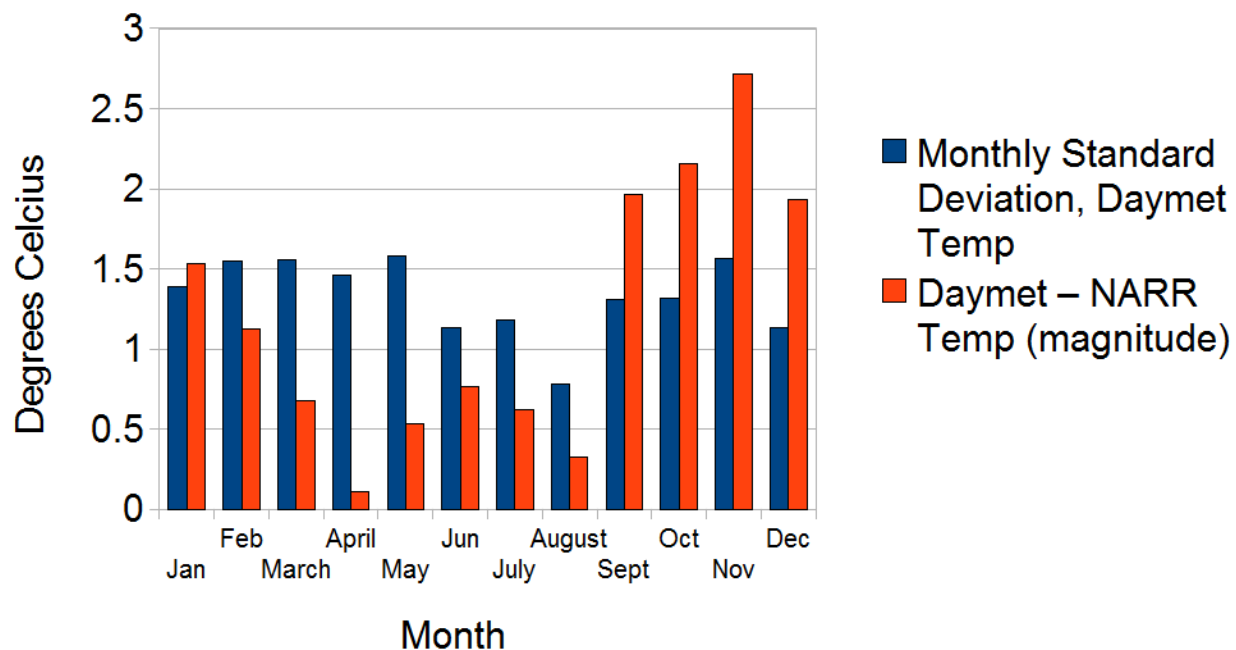


Figure 2.12: Comparison of the within-month standard deviation of Daymet temperature data to the monthly average difference between Daymet data and the North American Regional Reanalysis.

Significance of difference between Daymet and NARR data, precipitation

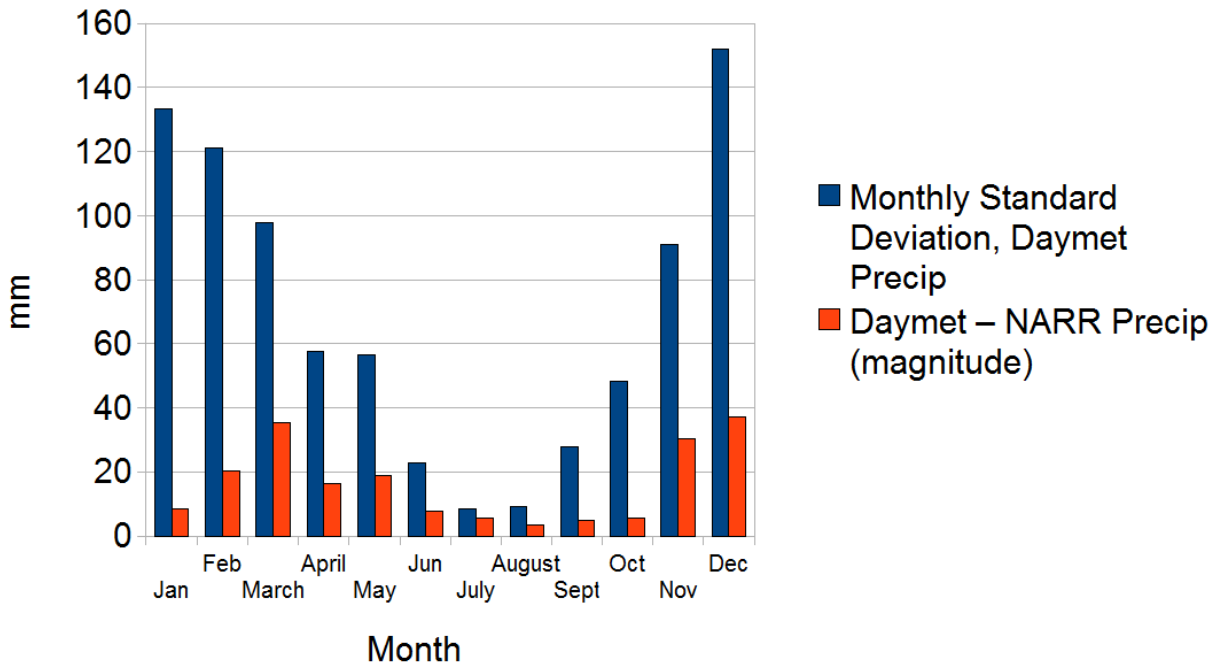


Figure 2.13: Comparison of the within-month standard deviation of Daymet precipitation data to the monthly average difference between Daymet data and the North American Regional Reanalysis.

Significance of difference between Daymet and ERA data, Temperature

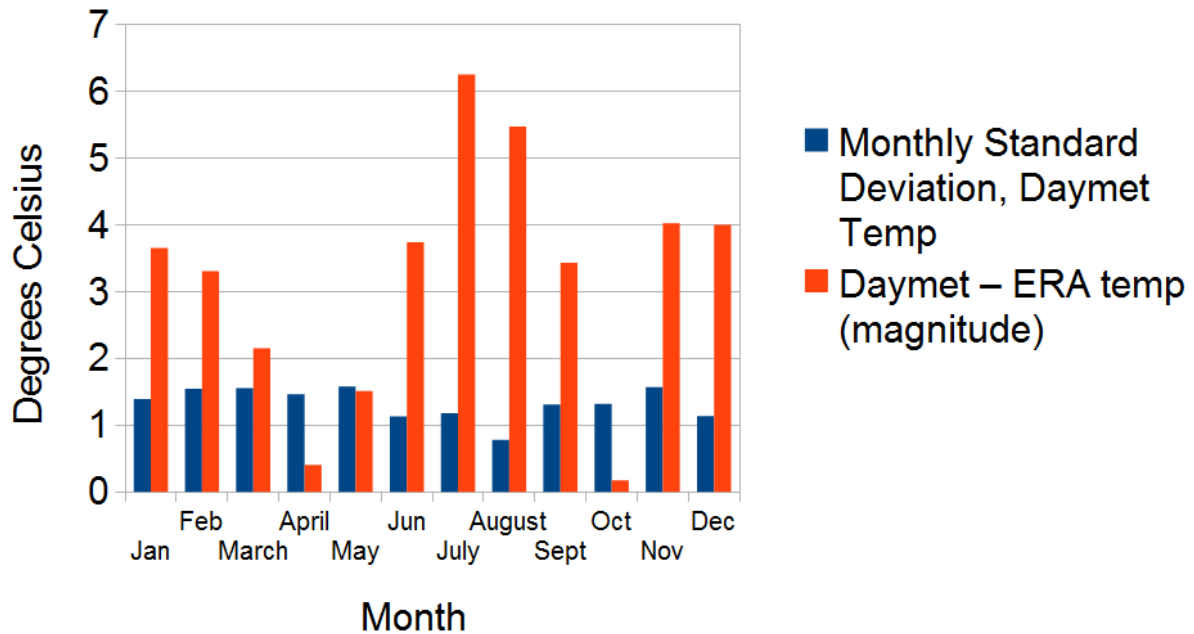


Figure 2.14: Comparison of the within-month standard deviation of Daymet temperature data to the monthly average difference between Daymet data and the ERA-Interim.

Significance of difference between Daymet and ERA data, precipitation

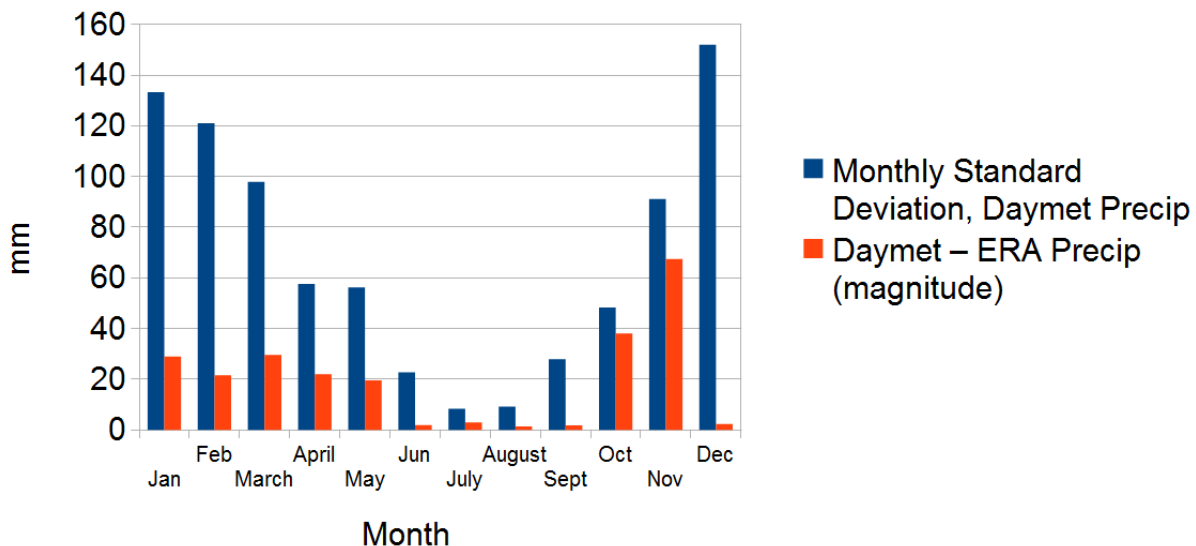


Figure 2.15: Comparison of the within-month standard deviation of Daymet precipitation data to the monthly average difference between Daymet data and the ERA-Interim.

To summarize: Comparing the fields of temperature, precipitation and winds overall, NARR appears to be wetter than ERA-Interim, with stronger winds, particularly upwelling winds. However, ERA-Interim appears to have slightly stronger southerly winds near the mouth of the Eel River during the winter. As compared to field data taken at the Eureka Weather Station, however, while both NARR and ERA-Interim have substantially more precipitation, it is not significant when compared to the extreme variability of the system's storm events – while their relative warmth in temperature does appear to fall outside of one standard deviation of the field data. Because of the necessity of using ERA-Interim at 1 km in ROMS, HydroTrend must be forced with it as well, in order for both parts of the framework to be acted upon by the same atmosphere.

2.4 Hydrological Modeling: HydroTrend

2.4.1 HydroTrend Description

HydroTrend (Kettner and Syvitski 2008) is an empirical, lumped watershed model. Given basin temperature, precipitation, hypsometry, relief, and qualities of the land surface parameterized for evapotranspiration and groundwater and glacial storage and flow, it outputs daily time series of water discharge and sediment load. Having been parameterized in HydroTrend1 (Syvitski et al. 1998) for use as an example, there was ample information available about how to parameterize the Eel River basin for HydroTrend3 (Kettner and Syvitski 2008). The physical delivery of Eel River discharge into the ocean circulation model ROMS is discussed in section 2.5.11, while the biogeochemical delivery of Eel River-borne nutrients is described in section 2.6.4.

To summarize the key outputs here, HydroTrend generates total water discharge, Q , and total sediment load $Q_{sed} = Q_s + Q_b$, where Q_s is suspended sediment and Q_b is bedload sediment. The calculation of Q and Q_{sed} is discussed below.

2.4.2 HydroTrend Discharge

HydroTrend conceptually uses a simple water balance model of (P)recipitation per unit (A)rea, reduced by (Ev)aporation and modified by water Storage and Release (Sr).

$$Q = A \sum_{i=1}^n (P_i - Ev_i \pm Sr_i) \quad (7)$$

In HydroTrend's calculations, the model simultaneously partitions water into five runoff processes: rain (Q_r), snowmelt (Q_n), glacial melt (Q_{ice}), groundwater discharge (Q_g) and evaporation (Q_{ev}). For each month i in equation 7, the total annual discharge Q can be estimated from:

$$Q = Q_r + Q_n + Q_{ice} - Q_{Ev} \pm Q_g \quad (8)$$

However, what ultimately defines daily discharge is the sum of surface runoff (q_s) and subsurface storm flow (q_{ss}), as visualized in Figure 2.16. It is these that we describe below.

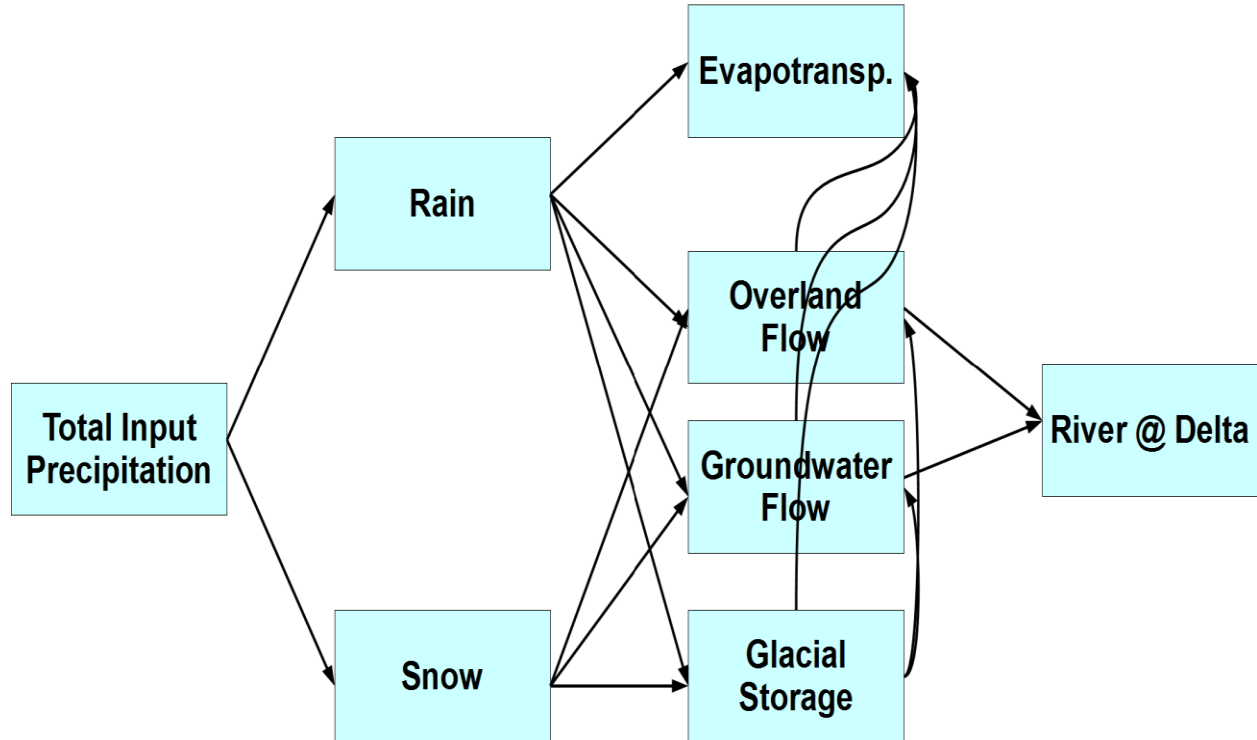


Figure 2.16: Partitioning and transport within the water cycle, in HydroTrend 3.0.

Surface runoff q_s : P_d is simply daily precipitation. The discharge due to rain, Q_r , is reduced by evaporation due to canopy interception (e_c), and then by groundwater evapotranspiration (e_{gw}).

If the rainfall rate is greater than the canopy interception, then the amount of precipitation that reaches the ground, P_g , is:

$$P_g = \begin{cases} \alpha_g + \beta_g P_d & \text{when } \alpha_g + \beta_g P_d > 0 \\ 0 & \text{otherwise} \end{cases} \quad (9)$$

Where α_g and β_g are ground-precipitation coefficients (mm/d and unitless respectively) (Sivapalan et al. 1996), with typical values of -0.1 mm/d and 0.8-0.9 respectively. Thus canopy evaporation is simply the difference between total daily rainfall and what reaches the ground; all canopy interception is assumed to evapotranspire.

$$e_c = P_d - P_g \quad (10)$$

From there, P_g must be partitioned into surface runoff and groundwater infiltration. The surface runoff q_s is equal to the sum of saturation excess runoff (q_{se}) and infiltration excess (q_{ie}), all in cubic meters per second:

$$q_s = q_{se} + q_{ie} \quad (11)$$

The saturation excess runoff (equation 12) is a function of how full the groundwater storage pool is, and the rain rate, modified by α_c and β_c , the unitless saturation excess coefficient and exponent (Sivapalan et al. 1996), with typical values of 0.98 and 1.0 respectively. Maximum and minimum levels of groundwater storage pools (in cubic meters) are given parameters, GW_{max} and GW_{min} , while current amount of groundwater storage, GW_{store} , varies with each timestep:

$$q_{se} = \begin{cases} 0 & \text{when } GW_{store} < GW_{min} \\ \alpha_c \left(\frac{GW_{store} - GW_{min}}{GW_{max} - GW_{min}} \right)^{\beta_c} P_g & \text{otherwise.} \end{cases} \quad (12)$$

The other component of surface runoff as defined in equation 11, infiltration excess q_{ie} , is simply what remains of the precipitation rate that reaches the ground after the infiltration rate f_s (mm/d) and the saturation excess q_{se} have been removed. Infiltration excess is constrained to be greater than or equal to zero.

$$q_{ie} = \begin{cases} 0 & \text{when } P_g - q_{se} - f_s \leq 0 \\ P_g - q_{se} - f_s & \text{otherwise.} \end{cases} \quad (13)$$

The method used to calculate f_s , the groundwater infiltration rate, is dependent on precipitation (equation 14).

$$f_s = \begin{cases} P_g \text{ Area } C_1 & \text{when } P_g \leq P_{cr} \\ K_0 \text{ Area } C_1 & \text{when } P_g \geq P_{max} \\ C_1 P_g \left(\frac{K_0 - P_{cr}}{P_{max} - P_{cr}} \right) \text{ Area} & \text{when } P_{cr} < P_g < P_{max} \end{cases} \quad (14)$$

where C_1 is a conversion constant and

$$Area = 1 - \left(\frac{GW_{store} - GW_{min}}{GW_{max} - GW_{min}} \right) \quad (15)$$

If the rain rate is less than a minimal infiltration rate ($P_{cr} = 10$ mm/d for the Eel River (Syvitski et al. 1998)), then all of the rain will infiltrate, while when the rain rate is high enough (P_{max} , 400 mm/d for the Eel River (Syvitski et al. 1998)) to force the maximum hydraulic conductivity ($K_0 = 374.0$ mm/d [Freeze 1974; Freeze and Cherry 1979]), then the infiltration rate reaches its maximum, constant value. Between the two extremes, a linear fit estimates the infiltration rate accordingly. P_{max} is set to 400.0 mm/d based on previous calculations (Syvitski et al. 1998). There is no strong justification in Syvitski et al. 1998 for these numbers; the largest recorded 24-hour precipitation event measured at Eureka, CA was 172mm on December 27, 2002 (National Weather Service 2014), and while Eureka is not representative of the entire basin, this huge difference in magnitude suggests that modeled watershed conditions will never reach this maximum value, creating a probable underestimation of the groundwater infiltration rate.

Subsurface storm flow q_{ss} : Having calculated q_s by adding the results of (12) and (13), the surface runoff term is now known. What remains is to estimate the contribution of groundwater to river discharge, q_{ss} . In terms of the total amount of groundwater present during a given timestep, GW_{store} , the groundwater pool for rainfall uses the previous calculations for infiltration rate to fill itself, while a user-specified fraction of the daily total ice melt and snowmelt is allocated to groundwater flow, made to lag a user-specified number of days behind the day that caused the melt (see Table 2.1 for these parameters).

The discussion of ice and snowmelt in HydroTrend will be kept brief as these terms are fairly small in the Eel River system. Snowfall is partitioned from total precipitation by estimating the Freezing Level Altitude from the adiabatic lapse rate, and from there the fraction of the area above the FLA (as defined by the hypsometric, height-per-area, curve for the Eel River watershed) experiences snow instead of rain. Snow can be stored, or melt. This hypsometric curve was calculated from the USGS National Elevation Dataset (USGS 2011).

Evapotranspiration from the groundwater pool is defined as

$$e_{gw} = \alpha_{gw} \left(\frac{GW_{store}}{GW_{max}} \right)^{\beta_{gw}} \quad (16)$$

where α_{gw} (10 mm/d) and β_{gw} (1, unitless) are the groundwater evaporation coefficient and exponent respectively (Syvitski et al. 1998), dependent on the depth of the groundwater pool and the type and abundance of vegetative cover. Finally, the subsurface storm flow q_{ss} (m³/s, from groundwater to the river) is defined as

$$q_{ss} = \alpha_{ss} \left(\frac{GW_{store} - GW_{min}}{GW_{max} - GW_{min}} \right)^{\beta_{ss}} \quad (17)$$

where α_{ss} (700 m³/s) and β_{ss} (1.3, unitless) are subsurface storm-flow coefficient and exponent set through curve fitting the discharge event after a rain event that is thought to be solely due to groundwater discharge (Syvitski et al. 1998).

Thus what ultimately comprises Q , total river discharge, is the sum of (11) and (17).

2.4.3 HydroTrend Sediment

HydroTrend separately estimates suspended sediment load and bedload, the sum of which is used to estimate Eel River remineralizable detritus delivery to the coastal ocean (in section 2.6.4).

$$Q_{sed} = Q_s + Q_b \quad (18)$$

Empirical relations that relate sediment load (Q_s) to basin area, discharge, relief, temperature, average basin lithology and human activity (BQART) were created for HydroTrend by analyzing observational data of 340 rivers globally (Syvitski and Milliman 2007).

$$\begin{aligned} Q_s &= \omega B \bar{Q}^{0.31} A^{0.5} R T \text{ (for } T \geq 2 \text{ }^\circ\text{C)} \\ Q_s &= \omega B \bar{Q}^{0.31} A^{0.5} R \text{ (for } T < 2 \text{ }^\circ\text{C)} \end{aligned} \quad (19)$$

A , R , and \bar{Q} are drainage basin area, maximum relief (calculated from the hypsometric curve) and long-term average discharge respectively, the latter derived from a long-term average of the Q calculated in section 2.4.2. ω is a constant of proportionality defined as $\omega = 0.02 \text{ kg/s/km}^2$. T is basin averaged temperature (based on ERA-Interim, the atmospheric forcing, in this case), $B = L(1-T_e)E_h$, where T_e is the trapping efficiency of a reservoir or lake, L is the lithology and E_h is the anthropogenic factor. L ranges from 0.5 for basins comprised of hard, acid plutonic or high-grade metamorphic rocks, up to 3 for basins having an abundance of exceptionally weak material, such as crushed rock, loess deposits, or shifting sand dunes. The anthropogenic factor E_h has methods of estimation described in Syvitski and Milliman (2007), typically ranging from 0.5 to 8. It can be higher given exceptional human impact on sediment, as with the Eel River's logging practices (Grant and Wolff 1991).

There are many reasons to be cautious in the use of sediment rating curves. One consideration is the reliability of the accuracy of the data from which sediment rating curves are fit; while errors in sediment load estimation can result from sample collection techniques and laboratory procedures, the greatest errors appear to result from the inadequacy of a sampling program in defining the detailed temporal record of suspended sediment concentration (Walling 1977a). Walling (1977a) found it broadly worthwhile to use different curves for different seasons, and for periods of rapidly increasing discharge (rising stage) and periods of declining river discharge (falling stage); he notes that the concentration-streamflow relationship for individual storm runoff events demonstrate a marked hysteretic effect, with concentrations for a given discharge being considerably higher on the shorter-duration rising limb of a hydrograph. Even taking stage and season into consideration, he found that annual loads could be overestimated by as much as 30%, and errors in estimation of monthly loads could vary between +900% and -80%. These results refer specifically to instantaneous rating curves used in combination with hourly flow data; different findings could result from the use of daily or annual rating curves. Thomas

(1988) also studies the effects of sampling methodology on the quality of rating curves. By sub-sampling a large dataset in four different ways, in order to simulate different choices of when to measure sediment in a river, he found systematically different patterns of sediment rating curve position, and thus estimates of total suspended sediment yield.

Walling (1977b) tested his concerns pertaining to data collection frequency by using daily (rather than hourly) mean flow data; he found underestimation errors of up to 50% for six east Devon streams and three larger Devon rivers, with a tendency of the magnitude of the error to decrease with increasing basin size. He considered three causes of scatter in the relationship between sediment concentration or load, and water discharge: scatter related to inaccuracies of field and laboratory measurements, scatter related to the dynamics of erosion and sediment yield, and scatter resulting from marked non-stationarity of basin response to discharge. He considered the second group the most important, but also proposed that on short timescales, the rating relationships of individual storms might indicate the effect of successive storm depletion, with sediment concentrations decreasing from one storm to the next. This non-stationarity effect turned out to be very important for the case of the Eel River and other coastal northern California rivers on much longer timescales (Warrick et al. 2013, Warrick 2014, see below).

A later study of sediment rating curves attempted a more theoretical approach to statistical estimation of the bias in the use of linear least squares regression to estimate logarithms of unmeasured concentration (Ferguson 1986). Linear least squares regression was shown to often create a 50% underestimation of river loads no matter how intense the sampling; a bias correction term was proposed that saw popular use (for example used in Thomas (1988), and reviewed in Asselman [2000]). Thomas 1988 observes that the effect of this bias correction is still dependent on sampling method and storm size, while Asselman (2000) abandons linear least squares regression entirely (after reproducing the finding that rating curves created by these measures underestimate long-term sediment transport rates by 10-50%), and found that he could obtain better estimates using nonlinear least squares regression. He also expressed concern about the potential lack of stationarity of rating coefficients, and the lack of means of judging that stationarity at all. Horowitz (2003) again found that the sediment rating-curve method tends to underpredict high suspended sediment concentrations, but furthermore overpredicts low suspended sediment concentrations. Like Walling (1977a) and (1977b), he found that higher temporal resolution of the estimates reduced the magnitude of the error, as did basing sampling times on the ongoing hydrology (eg, rising and falling stage in Walling [1977a]) rather than arbitrarily based on the calendar. He also found that using separate rating curves for each year based on available data could improve the output.

For the specific case of the Eel River, Wheatcroft and Borgeld (2000) created sediment rating curves that included the Ferguson (1986) bias correction and an unweighted least squares method. By creating curves with and without 1) consideration of hysteresis, 2) consideration of pre-1970 data, and 3) allowance of suspended sediment concentration unsupported by the data, they saw that these choices changed the estimate considerably. Hysteresis was found to have only a minor impact on the load estimates, but that they could remove seasonality as a potential bias by using only data from the winter rainy season. However, this was still a technique that used stationary coefficients, and non-stationarity was discovered to be critical to the system. Warrick et al. (2013) showed that systematic multi-year changes in Eel River sediment

concentration led to a halving of 1965's maximum suspended-sediment concentration approximately every decade -- and that these changes made rating curve calculations highly sensitive to time dependencies of sediment concentrations. In Warrick (2014) he followed up on this concern with further analysis, and found that Eel River sediment discharge rates were overestimated by a factor of two in Wheatcroft and Borgeld (2000), as well as other stationary rating curve calculations, including the HydroTrend calculations of Syvitski et al. (1998a). It is thus virtually guaranteed that the HydroTrend-based calculations in this work suffer from a similar large positive bias. Future work will need to incorporate nonstationary estimates, as described in Warrick (2014).

Daily bedload is simulated depending on the delta plain slope S and the daily mean water discharge $Q_{[i]}$ after the modified (Bagnold 1966) equation:

$$Qb_{[i]} = \left(\frac{\rho_s}{\rho_s - \rho} \right) \frac{\rho g Q_{[i]}^\beta S e_b}{g \tan \varphi} \text{ when } u \geq u_{cr} \quad (20)$$

where ρ_s is sand density, ρ is fluid density, e_b is the bedload efficiency, β is a dimensionless bedload rating term, φ is the limiting angle of repose of sediment grains lying on the river bed, u is stream velocity, and u_{cr} is the critical velocity needed to initiate bedload transport.

Thus the total sediment load is calculated by adding the results of (19) and (20).

2.4.4 HydroTrend Eel Parameterization

Based on HydroTrend's basin-wide Eel River parameters from earlier model implementations by the creators (Syvitski et al. 1998), plus climatology statistics from the ERA-Interim atmospheric forcing, the chosen parameters are listed in Table 2.1.

Table 2.1: Parameters used in HydroTrend calculations.

Symbol	Meaning	Value (and units)
	Start Year	1979
	Number of years run	64 (the first half is thrown away as spin-up, the 1979-2010 climate repeats twice)
GW_{max}	Maximum groundwater storage	$1.2e8 \text{ m}^3$
GW_{min}	Minimum groundwater storage	$1.0e5 \text{ m}^3$
GW_{store}	Initial groundwater storage	$5.0e5 \text{ m}^3$
P_{cr}	Critical rainfall rate for minimal infiltration	10 mm/d
P_{max}	Rainfall rate to force maximum hydraulic conductivity	400.0 mm/d
K_0	Saturated hydraulic conductivity	374.0 mm/day
	Moist adiabatic lapse rate to calculate freezing line	8.9°C/km
α_{gw}	Groundwater evaporation coefficient	10 mm/d
β_{gw}	Groundwater exponent coefficient	1 (unitless)
α_{ss}	Groundwater subsurface storm flow coefficient	$700 \text{ m}^3/\text{s}$
β_{ss}	Groundwater subsurface storm flow exponent coefficient	1.3 (unitless)
ω :	BQART constant of proportionality	0.02 kg/s/km/C
T	Basin-averaged Temperature:	11.9 deg. C, standard deviation 0.54, derived from ERA-Interim
A	Total basin Area	8063 km^2
L	Lithology factor	2.0 (unitless)
E_h	Anthropogenic factor	5.6 (unitless)
T_e	Reservoir trapping efficiency	0 (unitless)
	Average river velocity	2.3 m/s
S	Delta plane slope (rise-over-run)	0.0007 m/m (unitless)
β	Bedload rating term	1.0 (unitless)
e_b	Bedload efficiency	0.1 (unitless)
u_{cr}	Critical flow rate for bedload transport	$800 \text{ m}^3/\text{s}$

Using these parameters in the equations above in sections 2.4.2 and 2.4.3, HydroTrend generates time series of discharge Q , and sediment $Q_s + Q_b$. The subsequent circulation of that discharge is

modeled directly in the Regional Ocean Modeling System, described in section 2.5.11. Both discharge and sediment are used to estimate Eel River nutrient loads in section 2.6.4.

In many respects HydroTrend is a pseudo-physics model; it has numerous fudge factors and some broad assumptions (such as an arbitrarily imposed lag on groundwater discharge from infiltration to export). Its inclusion in the modeling framework was an attempt to have riverine output driven by the same atmosphere as the ocean model (since atmospheric forcing products are themselves a product of some interpolation and estimation, with according uncertainties). However, if this project was not an effort to use and connect models across land, atmosphere and ocean, simply using USGS daily gauging data, and empirical estimates of sediment load such as that which appears in Warrick et al. (2014), would certainly create a more realistic simulation.

2.5 Ocean Modeling: Regional Ocean Modeling System

2.5.1 Equations of Motion

As briefly described in section 2.2, the Regional Ocean Modeling System (Shchepetkin and McWilliams 2005; Haidvogel et al. 2008; Arango 2014) solves the primitive equations on a rotating Earth with finite difference approximations, advecting, diffusing and conserving momentum, heat, salinity and (for our purposes) biological tracers of nitrate, phytoplankton, zooplankton, and remineralizable detritus.

The primitive equations in Cartesian coordinates are reproduced here as expressed in Hedstrom (2012). The momentum balance equations in the x- and y-directions are expressed as:

$$\begin{aligned}\frac{\partial u}{\partial t} + \vec{v} \cdot \nabla u - fv &= -\frac{\partial \phi}{\partial x} - \frac{\partial}{\partial z} \left(\overline{u'w'} - v \frac{\partial u}{\partial z} \right) + F_u + D_u \\ \frac{\partial v}{\partial t} + \vec{v} \cdot \nabla v + fu &= -\frac{\partial \phi}{\partial y} - \frac{\partial}{\partial z} \left(\overline{v'w'} - v \frac{\partial v}{\partial z} \right) + F_v + D_v\end{aligned}\quad (21)$$

The time evolution of a scalar concentration field $C(x,y,z,t)$ (e.g. salinity, temperature, or nutrients), is governed by the advective-diffusive equation:

$$\frac{\partial C}{\partial t} + \vec{v} \cdot \nabla C = -\frac{\partial}{\partial z} \left(\overline{C'w'} - v_\theta \frac{\partial C}{\partial z} \right) + F_C + D_C \quad (22)$$

The equation of state is given by $\rho = \rho(T,S,P)$, density as a function of temperature, salinity, and total pressure. In the Boussinesq approximation, density variations are neglected in the momentum equations except in their contribution to the buoyancy force in the vertical momentum equation. Under the hydrostatic approximation, it is further assumed that the vertical pressure gradient balances the buoyancy force:

$$\frac{\partial \phi}{\partial z} = -\frac{\rho g}{\rho_0} \quad (23)$$

The final equation expresses the continuity equation for an incompressible fluid:

$$\frac{\partial u}{\partial x} + \frac{\partial v}{\partial y} + \frac{\partial w}{\partial z} = 0 \quad (24)$$

For the moment, the effects of forcing and horizontal dissipation will be represented by the schematic terms F and D , respectively. These equations are closed by parameterizing the Reynolds stresses and turbulent tracer fluxes as:

$$\overline{u'w'} = -K_M \frac{\partial u}{\partial z}; \quad \overline{v'w'} = -K_M \frac{\partial v}{\partial z}; \quad \overline{C'w'} = -K_C \frac{\partial C}{\partial z} \quad (25)$$

An overbar represents a time average and a prime represents a fluctuation about the mean. The variables used above (and at other points in this section) are shown in Table 2.2:

Table 2.2: Definitions of terms used in section 2.5.

D_u, D_v, D_C	diffusive terms, with horizontal and vertical mixing schemes in ROMS
F_u, F_v, F_C	external forcing terms
$f(y)$	Coriolis parameter
g	acceleration of gravity
$h(x, y)$	bottom depth
ν, ν_θ	molecular viscosity and diffusivity
K_m, K_C	vertical eddy viscosity and diffusivity
P	total pressure $P \approx -\rho_o g z$
$\phi(x, y, z, t)$	dynamic pressure $\phi = (\frac{P}{\rho_o})$
$\rho_o + \rho(x, y, z, t)$	total <i>in situ</i> density
$S(x, y, z, t)$	salinity
t	time
$T(x, y, z, t)$	potential temperature
u, v, w	the (x,y,z) components of vector velocity \vec{v}
x, y	horizontal coordinates
z	vertical coordinate
$\zeta(x, y, t)$	the surface elevation
$\xi(x, y)$ and $\eta(x, y)$	curvilinear coordinate systems
$m(\xi, \eta)$ and $n(\xi, \eta)$	scale factors relating the differential distances of the curvilinear coordinate system to actual physical arc lengths
$S(x, y, \sigma)$	nonlinear vertical transformation functional
σ	fractional vertical stretching coordinate
$C(\sigma)$	monotonic, nondimensional vertical stretching function
h_c	critical depth for vertical stretching functions
θ_s and θ_B	surface and bottom control parameters for vertical stretching functions
$\overline{H_z}$	grid-box volume
\overline{mn}	
$\overline{H_z \Omega}$	finite-volume flux across the moving grid-box interface
\overline{mn}	
γ	1/8, in ROMS
i, j, k	grid cell indices in the ξ, η and σ directions
N	number of vertical levels (40)
Q_C	surface concentration flux
τ_s^x and τ_s^y	surface wind stress
τ_b^x and τ_b^y	bottom stress
C_p	specific heat of dry air

2.5.2 Curvilinear Coordinates

ROMS adopts a curvilinear grid in order to best resolve irregular boundaries and locally increased grid resolution. Such a grid is created by introducing an appropriate orthogonal coordinate transformation in the horizontal. Our new coordinates, $\xi(x,y)$ and $\eta(x,y)$, allow our equations of motion to be re-written as per Arakawa and Lamb (1977), while leaving all of our boundary conditions unchanged.

2.5.3 Vertical Coordinates

ROMS has a generalized terrain-following vertical coordinate system. There are two vertical transformation equations available (Arango 2014) such that $z = z(x,y,\sigma,t)$:

$$z = z(x, y, \sigma, t) = S(x, y, \sigma) + \zeta(x, y, t) \left[1 + \frac{S(x, y, \sigma)}{h(x, y)} \right] \quad (26)$$

$$S(x, y, \sigma) = h_c \sigma + [h(x, y) - h_c] C(\sigma)$$

(Transformation 1)

or:

$$z(x, y, \sigma, t) = \zeta(x, y, t) + [\zeta(x, y, t) + h(x, y)] S(x, y, \sigma) \quad (27)$$

$$S(x, y, \sigma) = \frac{h_c \sigma + h(x, y) C(\sigma)}{h_c + h(x, y)}$$

(Transformation 2)

where $S(x, y, \sigma)$ is a nonlinear vertical transformation functional, $\zeta(x, y, t)$ is the time-varying free-surface, $h(x, y)$ is the unperturbed water column thickness and $z = -h(x, y)$ corresponds to the ocean bottom, σ is a fractional vertical stretching coordinate ranging from $-1 \leq \sigma \leq 0$, $C(\sigma)$ is a nondimensional, monotonic, vertical stretching function ranging from $-1 \leq C(\sigma) \leq 0$, and h_c is a positive thickness controlling the stretching.

Although Transformation 2 is widely considered the superior choice, because it recovers the true sigma-coordinate system as $h_c \rightarrow \infty$, provides equally-spaced sigma coordinates in shallow regions, and reduces pressure gradient errors (Schepetkin and McWilliams 2005), it was found in this project to be the source of unconditional instability. Blow-ups both at the northwest and southeast boundary corners, as well as over the complex bathymetry of the Mendocino Triple Junction, were not present when using transformation 1 instead. However, transformation 2 was used successfully at 10 km resolution. This is one of many differences between the 10 and 1 km models, summarized in section 2.7.

There are also four vertical stretching functions available (Arango 2014), $C(\sigma)$. This is a dimensionless, nonlinear, monotonic, continuous differentiable (or at least differentiable

piecewise with smooth transition) function, that must be discretized at fractional stretched vertical coordinate σ ,

$$\sigma(k) = \begin{cases} \frac{k-N}{N}, & \text{at vertical } W \text{ points, } k = 0, \dots, N \\ \frac{k-N-0.5}{N}, & \text{at vertical } \rho \text{ points, } k = 1, \dots, N \end{cases} \quad (28)$$

Finally, $C(\sigma)$ must be constrained by $-1 \leq C(\sigma) \leq 0$, that is,

$$C(\sigma) = \begin{cases} 0, & \text{for } \sigma = 0, \text{ at the free - surface;} \\ -1, & \text{for } \sigma = -1, \text{ at the ocean bottom.} \end{cases} \quad (29)$$

The original stretching function, $Vstretching = 1$, from (Song and Haidvogel 1994) behaved best for our 1 km model (though we used $Vstretching = 4$ for the 10 km resolution application):

$$Vstretching = 1 \rightarrow C(\sigma) = \frac{(1-\theta_B)\sinh(\theta_s\sigma)}{\sinh(\theta_s)} + \theta_B \left[\frac{\tanh[\theta_s(\sigma+\frac{1}{2})]}{2\tanh(\frac{1}{2}\theta_s)} - \frac{1}{2} \right] \quad (30)$$

where θ_s and θ_B are the surface and bottom control parameters. Their ranges are $0 < \theta_s \leq 20$ and $0 < \theta_B \leq 1$, respectively. For our application, $\theta_s = 5$, and $\theta_B = 0.3$.

2.5.4 Domain and Grid Spatial Resolution

Due to the nature of curvilinear coordinates, the model's grid cells have some variation in size. To achieve an average horizontal grid size of 1 km, and to keep the open boundaries sufficiently far from the region of interest in order to minimize the effect of inevitable boundary difficulties, ROMS was configured to range from 39.0036 to 42.1966 N, -123.507 to 128.993 W, with 374 x 453 interior horizontal points. The 10 km grid ranged from 37-47 N, -132-123 W, with 275 x 556 interior horizontal points. ROMS only performs ocean circulation calculations; thus, land was masked off using the NOAA Medium Resolution Shoreline (NOAA 2012b), which has an average scale of 1:70,000. All grid cells beneath the land mask are not part of the calculations; the ocean-coastline boundary is a simple closed wall, disallowing water transport further inland. No atmosphere-land interactions or river modeling, is performed beneath the land mask; generation of riverine boundary conditions is performed by HydroTrend (section 2.4) and implemented as described in section 2.5.11. The grid was created with the SeaGrid grid generation MATLAB package (Signell 2013).

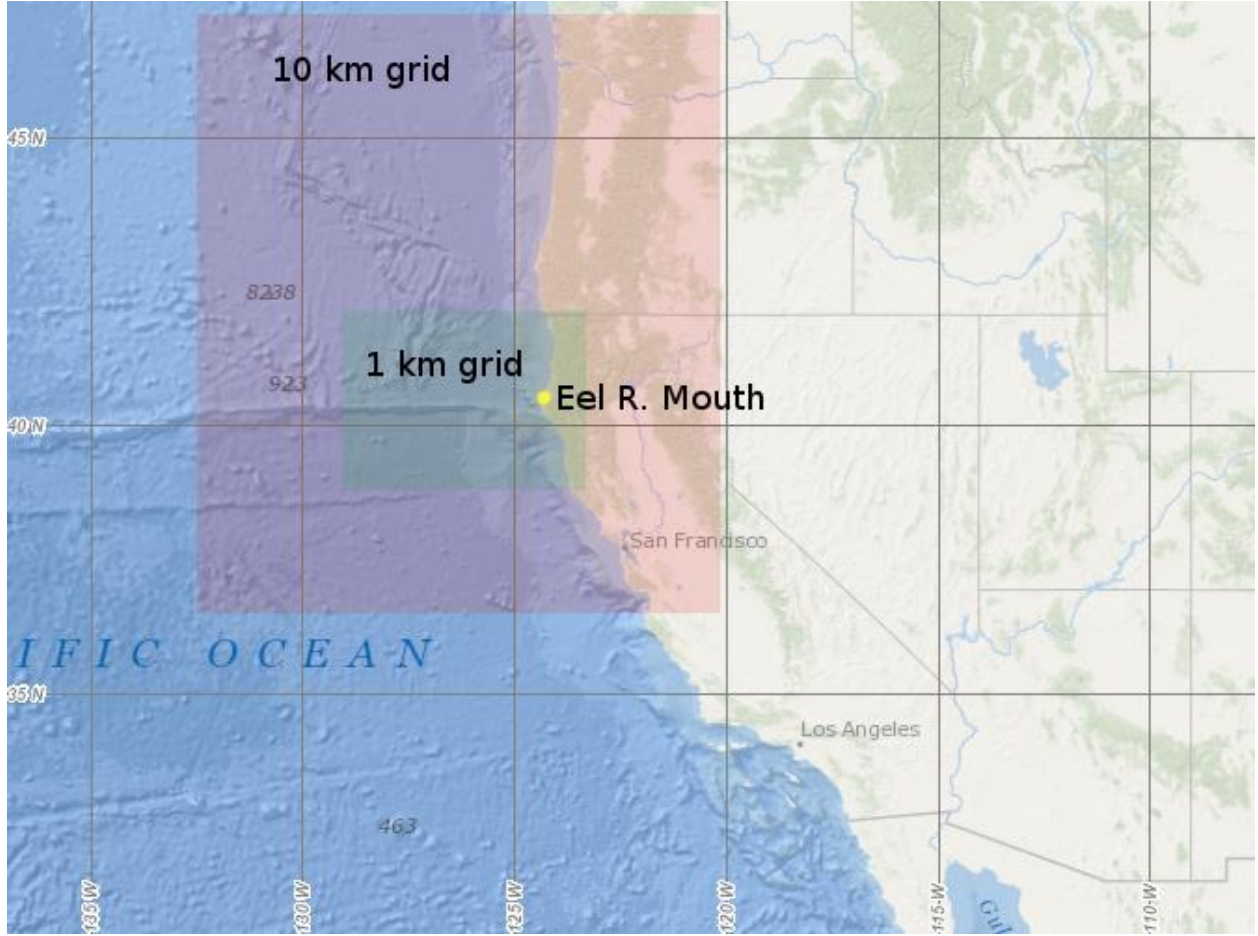


Figure 2.17: The spatial extent of the two ROMS domains.

The vertical structure of the grid consists of terrain following levels, discussed in section 2.5.3. However, beyond curvilinear coordinates and stretching functions, s-levels are also defined such that:

$$S(x, y, \sigma) = \begin{cases} 0, & \text{if } \sigma = 0, C(\sigma) = 0, \text{ at the free - surface;} \\ -1, & \text{if } \sigma = -1, C(\sigma) = -1, \text{ at the ocean bottom;} \end{cases} \quad (31)$$

The use of s-levels allows all measurements at the s-level closest to the surface to happen at roughly the same depth, regardless of the bathymetry of the area. The “true” sigma-coordinate system is recovered as h_c approaches infinity. This application of ROMS uses 40 vertical levels. Our choice of stretching parameters puts the majority of the vertical resolution at the surface, where the plume will be resolved, while having enough resolution at the bottom to not create undue numerical instability, and to resolve Ekman transport and upwelling dynamics as realistically as possible.

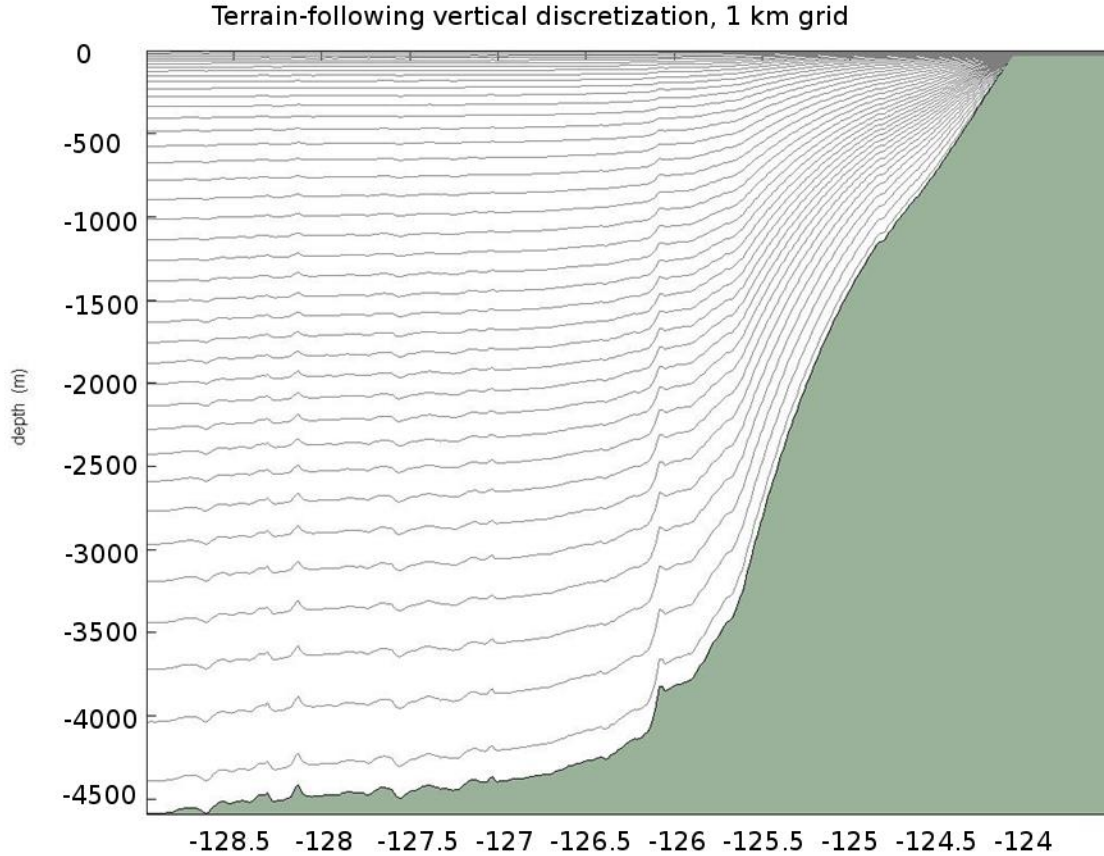


Figure 2.18: A graphical representation of the terrain-following vertical structure of the grid, taken across a vertical transect from eastern to western boundary at a latitude of 40 N. The x-axis is longitude. Note that the long flat stretch to the west is land, and masked off from the simulation.

2.5.5 Bathymetry

The bathymetry in our grid was initially extracted from the STRM30_PLUS V8.0 dataset, a global 30 arcsecond grid (Becker et al. 2009). To reduce poor behavior over sharp slopes, it was considerably smoothed using second and fourth-order Shapiro filters (Shapiro 1970) until all adjacent grid cells had an r-factor $\frac{(h_1-h_2)}{(h_1+h_2)}$ less than 0.35. The Shapiro filter is a high order horizontal filter that efficiently removes small grid scale noise without affecting the physical structures of a field. Despite this smoothing, care was taken to preserve the important local features, including the offshore Eel Canyon where most Eel sediment has historically been found to deposit (Mullenbach et al. 2004) and the Mendocino Scarp, a 1500m interface between two tectonic plates, the Pacific Plate and the Juan de Fuca Plate. Along with the North American Plate, these plates create the Mendocino Triple Junction: a geologic triple junction where the San Andreas Fault meets the Mendocino Fault and the Cascadia subduction zone. While the geologic-timescale dynamics are not of interest to us, this is a bathymetrically complex region of the ocean floor, and creates considerable difficulties in ROMS with false pressure gradients and

unstable deep water masses. It is the obvious culprit for an important model artifact (see Chapter 3.8), but this is preferable to smoothing it completely away and losing all the physical dynamics its presence imposes on local ocean circulation.

2.5.6 Temporal Resolution and Numerics

ROMS uses a split timestep, resolving barotropic and baroclinic equations separately (Haidvogel et al. 2008). Although many ROMS applications on the mesoscale can run on timesteps of five or ten minutes or more, the 1 km model runs on a 30 second baroclinic timestep, and a 1 second barotropic timestep. This was necessary not because of the horizontal resolution but because of the implementation of the river; the salinity gradients created by freshwater entering the ocean are numerically unstable, quick to become negative, or explode to unreasonably high values.

Using $m(\xi, \eta)$ and $n(\xi, \eta)$ as the scale factors which relate the differential distances ($\Delta\eta, \Delta\xi$) to the actual (physical) arc lengths, the advection of a tracer C has an equation (Arango 2014) of the form

$$\frac{\partial}{\partial t} \frac{H_z C}{mn} = - \frac{\partial}{\partial \xi} F^\xi - \frac{\partial}{\partial \eta} F^\eta - \frac{\partial}{\partial \sigma} F^\sigma \quad (32)$$

where we have introduced the advective fluxes:

$$F^\xi = \frac{H_z u C}{n}; \quad F^\eta = \frac{H_z v C}{m}; \quad F^\sigma = \frac{H_z \Omega C}{mn} \quad (33)$$

Horizontal momentum was discretized with a third-order upstream bias advection scheme with velocity dependent hyper-viscosity. The two-dimensional scheme in ROMS is called UTOPIA (Uniformly Third-Order Polynomial Interpolation Algorithm: Rasch 1994, Shchepetkin and McWilliams 1998). UTOPIA can be used on variables with both positive and negative values, making it suitable for momentum calculations as well as scalars such as temperature and salinity. For the u -velocity, we have:

$$\begin{aligned} F^\xi &= \left(u - \gamma \frac{\partial^2 u}{\partial \xi^2} \right) \left[\frac{H_z u}{n} - \gamma \frac{\partial^2}{\partial \xi^2} \left(\frac{H_z u}{n} \right) \right] \\ F^\eta &= \left(u - \gamma \frac{\partial^2 u}{\partial \eta^2} \right) \left[\frac{H_z v}{m} - \gamma \frac{\partial^2}{\partial \xi^2} \left(\frac{H_z v}{m} \right) \right] \\ F^\sigma &= \frac{H_z w}{mn} \left[-\frac{1}{16} u_{i,j,k-1} + \frac{9}{16} u_{i,j,k} + \frac{9}{16} u_{i,j,k+1} - \frac{1}{16} u_{i,j,k+2} \right] \end{aligned} \quad (34)$$

while for the v -velocity we have:

$$\begin{aligned} F^\xi &= \left(v - \gamma \frac{\partial^2 v}{\partial \xi^2} \right) \left[\frac{H_z u}{n} - \gamma \frac{\partial^2}{\partial \xi^2} \left(\frac{H_z u}{n} \right) \right] \\ F^\eta &= \left(v - \gamma \frac{\partial^2 v}{\partial \eta^2} \right) \left[\frac{H_z v}{m} - \gamma \frac{\partial^2}{\partial \xi^2} \left(\frac{H_z v}{m} \right) \right] \\ F^\sigma &= \frac{H_z w}{mn} \left[-\frac{1}{16} v_{i,j,k-1} + \frac{9}{16} v_{i,j,k} + \frac{9}{16} v_{i,j,k+1} - \frac{1}{16} v_{i,j,k+2} \right] \end{aligned} \quad (35)$$

In all these terms, the second derivatives are evaluated at an upstream location.

Vertical momentum was discretized with a fourth-order, centered differences scheme:

$$F^s = \frac{H_z w}{mn} \left[-\frac{1}{16} C_{i,j,k-1} + \frac{9}{16} C_{i,j,k} + \frac{9}{16} C_{i,j,k+1} - \frac{1}{16} C_{i,j,k+2} \right] \quad (36)$$

There is some implicit viscosity associated with this discretization, as the numerical error is diffusive in nature, though not as serious as it would be with a first or second-order upwinding scheme (Haidvogel et al. 2008). This error, however, helps to counteract the tendency of the model to destroy its own onshore water column stratification, which is functionally spurious numerical *upwelling*. (For more on model viscosity, see section 2.5.7.)

Although the model could resolve temperature, salinity, and the biological tracers (phytoplankton, zooplankton, NO₃ and detritus) using UTOPIA, this configuration uses what is called recursive MPDATA (Multidimensional Positive Definite Advection Transport Algorithm, Smolarkiewicz 1984, 1986, 1990) three-dimensional advection instead. MPDATA provides a hard clamp on the positivity of tracer values; it is monotonic and maintains the extrema. Without it, salinity and zooplankton, in particular, have a tendency to go unphysically negative. It is marginally more computationally expensive, but ultimately worth the price. An example of MPDATA's discretization scheme is found in (Tsujino 2010).

2.5.7 Horizontal Diffusion and Viscosity

The model uses linear bottom friction of momentum, but second-order diffusion for the tracers (8 m²/s, a standard value seen in common use [Arango 2014]), and second-order viscosity for momentum. In ROMS, the viscosity is derived from the horizontal divergence of the deviatoric stress tensor (Wajsowicz 1993); in our specific application we use viscosity to reduce spurious numerical upwelling by simply making the water resist motion a little more, and so its value is increased to 20 m²/s. This is still well within values found in the literature, which in large-scale applications can range as high as 1000 m²/s (Jochum et al. 2008). The mixing of momentum and tracers is applied along geopotential (constant depth) levels.

2.5.8 Vertical Mixing Parameterization

K-profile vertical parameterization (Large et al. 1994) of the viscous and diffusive coefficients is perhaps the most widely used ocean mixing schemes in ROMS and certainly the default (Arango 2014). Although it was usable for our 10 km model (see section 2.7), it was an arduous process to pick apart the scope of its inability to resolve pressure gradients for the 1 km application. Eventually it was replaced with the Mellor-Yamada 2.5 closure scheme (Mellor and Yamada 1982), modified as described in Galperin et al. 1988 and Allen et al. 1995.

2.5.9 Boundary Conditions

2.5.9.1 Lateral Boundary Conditions

By dint of being along the west coast of the United States, the domain (see Figure 2.17) has three open lateral boundary conditions, to the west, north, and south. (The east is simply a closed wall boundary for the coastline.) Doing a good job with open boundaries has been a major challenge of ocean circulation modeling for decades, a challenge that persists now (Marchesiello et al. 2001). One mitigating solution is to place the boundaries much further from the region of interest in the model than they might otherwise be, moving the modeling artifacts safely away at the expense of computational cost. That was done here, as there is no need to simulate all the way up to Washington State to resolve questions about the Eel River's impact on coastal ocean primary productivity. The southern boundary is considerably closer to Cape Mendocino, but avoids having to deal with San Francisco Bay, which seemed to have larger impacts than a more distant boundary. The major model artifact (Chapter 3.8) is due to the southeastern corner of the model poorly advecting momentum that has come off the Mendocino Triple Junction, interacting with southern boundary instability.

Lateral boundary conditions must be specified for the free-surface, 2D and 3D horizontal velocity, mixing turbulent kinetic energy, temperature, salinity, and biological tracers. For a summary of the boundary conditions used, see Table 2.3:

Table 2.3: Lateral boundary conditions used for the ocean circulation model.

Free-surface	Chapman Boundary Conditions
2D UV Momentum	Flather Boundary Conditions
3D UV Momentum	Radiation+Nudging with sponge layer
Temperature	Radiation+Nudging with sponge layer
Salinity	Radiation+Nudging with sponge layer
Phytoplankton, Zooplankton	Radiation+Nudging
NO ₃ , Detritus	Radiation+Nudging

Flather Boundary Conditions: In Flather 1976, it was proposed to radiate out deviations of barotropic velocity from exterior values at the speed of external gravity waves:

$$\bar{u} = \bar{u}^{ext} - \sqrt{\frac{g}{D}} (\zeta - \zeta^{ext}) \quad (37)$$

Chapman Boundary Conditions: The equivalent of Flather for surface elevation was invented by Chapman (1985); it assumes all outgoing signals leave at the shallow-water wave approximation speed of \sqrt{gE} , where E is depth. Then, the rate of change of the free elevation in time is simple the gradient of the free elevation in space times the speed, solved implicitly rather than explicitly in ROMS:

$$\frac{\partial \zeta}{\partial t} = \pm \sqrt{gE} \frac{\partial \zeta}{\partial \xi} \quad (38)$$

Radiation-Nudging Boundary Conditions: In order to properly resolve simultaneous inflow and outflow along the same boundary, sometimes even at different depths at the same horizontal location, a radiation boundary condition was formulated (Orlanski 1976) that uses a local normal phase velocity to radiate things out; in Raymond and Kuo 1984 the issue of transport approaching the boundary at an angle was improved.

$$\frac{\partial \phi}{\partial t} = - \left(\phi_{\xi} \frac{\partial \phi}{\partial \xi} + \phi_{\eta} \frac{\partial \phi}{\partial \eta} \right) \quad (39)$$

where

$$\begin{aligned} \phi_{\xi} &= \frac{F \frac{\partial \phi}{\partial \xi}}{\left(\frac{\partial \phi}{\partial \xi} \right)^2 + \left(\frac{\partial \phi}{\partial \eta} \right)^2} \\ \phi_{\eta} &= \frac{F \frac{\partial \phi}{\partial \eta}}{\left(\frac{\partial \phi}{\partial \xi} \right)^2 + \left(\frac{\partial \phi}{\partial \eta} \right)^2} \\ F &= - \frac{\partial \phi}{\partial t} \end{aligned} \quad (40)$$

To handle inflow, nudging to a known exterior value is performed per Marchesiello et al. (2001); physical exterior values were provided by NASA's ECCO2 dataset (Menemenlis et al. 2008) for the 10 km model, and by 10 km results for the 1 km model. Biological exterior values came from the World Ocean Database (NOAA 2013b) and World Ocean Atlas (NOAA 2013c; see section 2.6.3 for both WOD and WOA descriptions), for phytoplankton and nitrogen respectively; zooplankton were assumed to be 10% of phytoplankton, while detritus was set to a constant value of 0.001 mmol/m³. In both cases, monthly climatologies were calculated and used for the boundary conditions. Inflow nudging is applied once per day, while outflow nudging is applied once per four months (since the majority of outflow is handled by the radiation condition).

Furthermore, nudging is applied over a sponge layer, which is to say, the ten outermost points of the grid are all nudged with a strength of (100-10*distance from the boundary), such that the boundary point experiences the full, 100% strength of nudging, while the point ten inwards experiences 10% of that effect. This improves the numerical stability of the boundary by preventing large gradients from forming over only a couple of grid cells.

2.5.9.2 Bottom boundary conditions

The horizontal velocity has linear bottom friction applied as a bottom stress. Because tracers cannot move below the ocean floor, their concentration flux is set to zero. Hedstrom (2012) summarizes their prescription as follows:

Top boundary ($z = \zeta(x, y, t)$):

$$\begin{aligned}
K_m \frac{\partial u}{\partial z} &= \tau_s^x(x, y, t) \\
K_m \frac{\partial v}{\partial z} &= \tau_s^y(x, y, t) \\
K_c \frac{\partial C}{\partial z} &= \frac{Q_c}{\rho_o C_p} \\
w &= \frac{\partial \zeta}{\partial t}
\end{aligned} \tag{41}$$

Bottom boundary ($z = -h(x, y)$):

$$\begin{aligned}
K_m \frac{\partial u}{\partial z} &= \tau_b^x(x, y, t) \\
K_m \frac{\partial v}{\partial z} &= \tau_b^y(x, y, t) \\
K_c \frac{\partial C}{\partial z} &= 0 \\
-w + \vec{v} \cdot \nabla h &= 0
\end{aligned} \tag{42}$$

where Q_c is the surface concentration flux, τ_s^x and τ_s^y comprise the surface wind stress, and τ_b^x and τ_b^y the bottom stress.

2.5.10 Surface Model Forcing

The surface boundary conditions are controlled by the atmosphere; winds impose surface stress of momentum, while heat radiates in and out. We have reviewed the spatial and temporal resolution of the atmospheric forcing datasets used in section 2.3. To apply them in ROMS, they are first interpolated onto the horizontal grid; at each timestep, ROMS takes a weighted average of the two nearest forcing time points, and applies the result. While in the 10 km model, bulk flux approximations (Tsujino 2010 has an excellent summary, not reproduced here) were used to estimate surface stress from wind speed, the breakdown of the Monin-Obukov equations when assumptions of atmospheric stability are no longer true, caused them to behave poorly (see Section 2.3.2). For the 1 km model, surface stress provided directly from the ERA Interim analysis was used instead, reducing model error. Additionally, ERA surface freshwater flux (evaporation minus precipitation), net surface radiation, and net surface heat flux were applied. Monthly climatologies of sea surface temperature and sea surface salinity from the same analysis were used to correct the net heat flux and freshwater flux, nudging them on a daily timescale much like the lateral boundary conditions described in Section 2.5.9.1, with the commonly used surface net heat flux sensitivity to sea surface temperature $dQ_{net}/dSST$ of $-40 \text{ W/m}^2/\text{Celsius}$.

Atmospheric deposition of nitrogen was not considered in this model as previous studies have found it to be of relatively little importance in this region (Krishnamurthy et al. 2009, Okin et al. 2011), and surface forcing of phytoplankton, zooplankton and detritus were all zero as well.

Table 2.4: Atmospheric forcing fields and their units, as applied directly to the sea surface with the ERA-Interim dataset.

Forcing Field	Units
surface U-momentum stress	Pa (N/m ²)
surface V-momentum stress	Pa (N/m ²)
net shortwave radiation flux	Watts/m ²
net longwave radiation flux	Watts/m ²
net sensible heat flux	Watts/m ²
sea surface salinity	PSU
sea surface temperature	Celsius
surface net heat flux sensitivity to SST	Watts/m ² /Celsius
net surface heat flux	Watts/m ²
net surface freshwater flux	cm/day

2.5.11 River Forcing

The river was applied as a lateral boundary condition. In order to resolve advection properly, the river channel cut into the land mask was a bare minimum of three grid cells wide – at 1 km resolution this makes for an excessively wide Eel River, but it was an unavoidable compromise, as the model could not support variable widths or depths, nor increased horizontal resolution due to the computational expense. In effect, this modeling framework perpetually assumes an Eel River in extreme flood conditions, because that is the time that the river is most likely to have immediate short-term impacts on coastal primary productivity as it delivers its large nutrient load. Naturally this introduces a loss of realism. The mouth of the Eel River includes a 30m wide channel that widens to 400m by the time it crosses the sand flats and reaches the ocean (Schlosser and Eicher 2012). During major storm events the Eel River often floods (and thus widens) considerably, as captured by satellite and aircraft imagery (Leithold 1974, NASA 2012), but 3 km is still typically an order of magnitude too wide.

However, images like these also capture the large physical scales of offshore transport; sediment and nutrients are caught up by ocean circulation and advected by 10 km, 25 km, or more, and a 1 km horizontal resolution can simulate many of the eddies and currents in play. The ability of a 1 km horizontal resolution, 3 km wide Eel River channel numerical simulation to capture physical properties of the plume has been tested for the January 1997 floods (Pullen and Allen 2000, Pullen and Allen 2001), and modeling at this scale was generally successful at reproducing measurements of plume extent, depth and velocity.

Since the Eel River is not always flooding, however, this channel width creates vastly lower input velocities (in order to distribute the water-per-time across such an input volume), and even at high levels of discharge these lower velocities could not carry bedload. This is the major reason why the model does not attempt to simulate sediment transport directly; instead (as described in section 2.6.4) it simulates dissolved and particulate nitrogen.

Additionally, applying the river across these three cells right at the mouth creates enormous salinity gradients that become numerically unstable very quickly; therefore the river ‘begins’ three grid cells back, at the end of a short channel. Out of concern for possible lags in plume delivery, this distance was determined across multiple short experiments to be the best compromise between a softer initial salinity gradient and time lag for the river to travel down the channel – its lag is negligible, though the gradient is large enough to necessitate extremely short timesteps to maintain numerical stability.

As noted in section 2.4, HydroTrend results provide a daily time series of freshwater discharge and sediment mass. The water is distributed into the forty vertical levels of the 10 m deep channel, and split across the three cells such that the initial velocity in the central cell is 50% greater than that of the sides, which should be experiencing drag. The water temperature profile is constant throughout the column to represent the extreme turbulence of storm conditions (and while this is certainly wrong much of the year, those are precisely those times of year that the river is very small). Temperature is dictated by a monthly climatology calculated from USGS data (USGS 2012) gauged at Scotia, CA, 23 miles north of the mouth. Satellite and aircraft imagery (Leithold 1974, NASA 2012) as well as during-storm cruises of STRATAFORM (Wheatcroft et al. 1997) make it clear that the Eel plume is often advected on the surface of the ocean rather than experiencing hyperpycnal flow (eg, so dense with sediment that it flows along the bottom of the shelf, rather than the surface); however, the colder water in January and February from the Scotia climatology was sinking as compared to the ROMS ocean purely due to temperature effects on density. This seemed unrealistic, so allowing for the possibility that the river is warming between Scotia and the mouth, the values for January and February were increased to a minimum of 9°C for this effect to not dominate the flow in the model.

For the description of the biological aspects of the river in ROMS, see section 2.6.4.

2.5.12 Model Initialization and Spinup

The model must be initialized with values of momentum, temperature, salinity, and pressure at every point on the grid. Although the 10 km ROMS results could easily provide initial values for the 1 km version, initializing with ECCO2 (Menemenlis 2008) created more consistent numerical stability. This sensitivity to initialization is due to the model’s tendency to have large motions of water masses as the stratification works itself out; the pressure gradient errors are at their maximum within the first few time steps, and indeed it takes many time steps to spin up sufficiently such that results can be collected.

Conversely, running a model like ROMS for too long causes cumulatively accumulating errors of spurious diapycnal diffusion to eventually cause unstable water masses and a total breakdown of onshore stratification. This is a known issue in the modeling community, and an active area of research in advection schemes that combat the issue (Marchesiello et al. 2009, Lamrie et al. 2012), but no ROMS-Rutgers schemes were found to be useful. The 10 km results, which were generated by a continuous run from 1998-2010, begin to suffer from this starting around 2008, though they are still suitable for boundary conditions as the boundaries are by definition almost entirely far from shore. The 1 km model’s results become notably infected with this error after

about eighteen months, so a continuous decadal run at this higher resolution was out of the question.

Thus eighteen months of continuous modeling was available to be distributed between spin-up and results collection. A collection period of a full year was desired in order to have within-year internal consistency on the various nonlinear footprints of numerical error (which vary from year-to-year because of the variable atmospheric forcing), which left a maximum of six months for spinup. Common practice in ROMS is to spin up for more like three months (Arango 2014); however, this conventional wisdom did not prove out in the 1 km application. Even at six months there were still vestiges of an initial model artifact, momentum being falsely reflected around the southwestern corner; this artifact is discussed in further depth in section 3.9. In hindsight, it would be worthwhile to spin up for 8 months and collect for 10; it is not even particularly necessary to calculate results for September and October, since the river is at its minimum during that period. Unfortunately the computational expense and sheer amount of model runtime made such a re-run prohibitive for this thesis.

Each year of continuously collected data runs from November through the following October (since Eel storm events between 1998-2010 occur no earlier than November). Thus the model initializes on May 1, works out the worst of its instabilities over the summer, and is ready to manage the storm events come autumn, when the Eel River begins delivering its nutrient loads.

2.6 Biogeochemical Modeling: Nutrient-Phytoplankton-Zooplankton-Detritus

2.6.1 NPZD description and limitations

The coupled modeling framework uses the NPZD ([total] Nitrogen-Phytoplankton-Zooplankton-Detritus) model coupled into the Regional Ocean Modeling System from Powell et al. (2006). In the same paper, a literature review of modeling efforts leading up to that point is described. Since 2006, Powell-NPZD has been used in many applications, including expansions such as iron limitation (Fiechter et al. 2009), superior parameter estimation using surrogate-based optimization (Priess et al. 2013) and Bayesian hierarchical modeling (Fiechter et al. 2013; Milliff et al. 2013). A thorough analytical analysis of NPZD's internal dynamics identifies three equilibria, one where there are available nutrients but no organisms taking them up; and two where nutrients, phytoplankton and detritus exist in a balanced state (Heinle and Slawig 2013). Absent from Powell-NPZD is a distinction between forms of nitrogen, multiple size (or other distinct) classes of phytoplankton or zooplankton, and any effects from higher trophic levels.

As described in Powell et al. (2006) and visualized in Figure 2.19, Powell-NPZD is a four-element, nitrogen-based trophic model, in which nitrogen is partitioned between the dissolved (N) and particulate (D) phases, as well as between phototrophic phytoplankton (P) and herbivorous zooplankton (Z). In the model, local time derivatives and an advective term are balanced by vertical mixing, and a given element's growth and mortality.

$$\frac{\partial N}{\partial t} + \mathbf{u} \cdot \nabla N = \delta D + \gamma_n GZ - UP + \frac{\partial}{\partial z} \left(k_v \frac{\partial N}{\partial z} \right) \quad (43)$$

$$\frac{\partial P}{\partial t} + \mathbf{u} \cdot \nabla P = UP - GZ - \sigma_d P + \frac{\partial}{\partial z} \left(k_v \frac{\partial P}{\partial z} \right) \quad (44)$$

$$\frac{\partial Z}{\partial t} + \mathbf{u} \cdot \nabla Z = (1 - \gamma_n)GZ - \zeta_d Z + \frac{\partial}{\partial z} \left(k_v \frac{\partial Z}{\partial z} \right) \quad (45)$$

$$\frac{\partial D}{\partial t} + \mathbf{u} \cdot \nabla D = \sigma_d P + \zeta_d Z - \delta D + w_d \frac{\partial D}{\partial z} + \frac{\partial}{\partial z} \left(k_v \frac{\partial D}{\partial z} \right) \quad (46)$$

$$G = R_m(1 - e^{-\Lambda P}) \quad (47)$$

$$I = I_0 \exp(k_z z + k_p \int_0^z P(z') dz') \quad (48)$$

$$U = \frac{V_m N}{k_N + N} \frac{\alpha I}{\sqrt{V_m^2 + \alpha^2 I^2}} \quad (49)$$

U represents the photosynthetic growth and uptake of nitrogen by phytoplankton; G represents grazing on phytoplankton by zooplankton, mortality is represented with σ_d for phytoplankton and ζ_d for zooplankton, and sinking and remineralization of detritus (w_d and δ respectively). Light at depth z assumes exponential attenuation by seawater (k_z) and phytoplankton (k_p). A Michaelis-Menten curve is used to describe the change in phytoplankton uptake rate as a function of nitrogen concentration, while zooplankton grazing uses the Ivlev function, including the possibility of “sloppy feeding” causing some nitrogen to go directly to detritus instead of the zooplankton element. Mortality and remineralization are linear functions of concentration, allowing dead plankton to become detritus, and detritus to be remineralized to dissolved nitrogen.

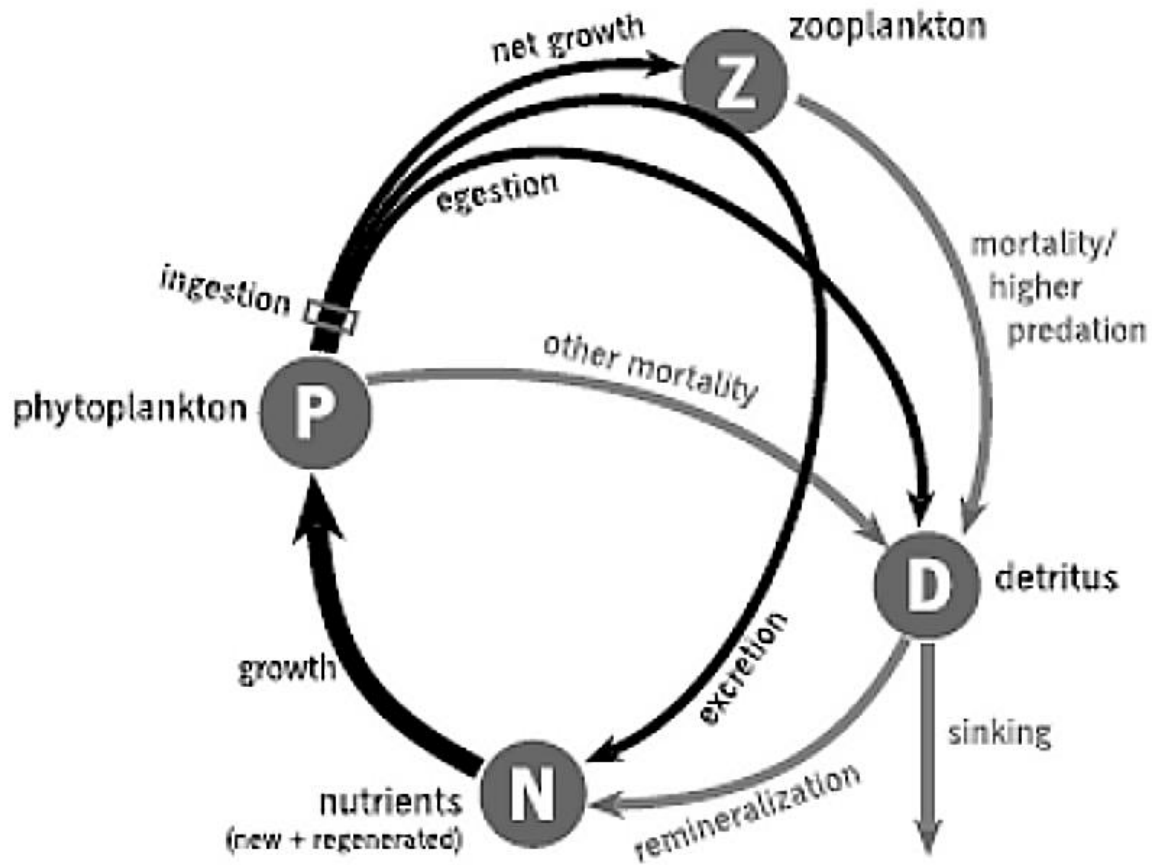


Figure 2.19 (from Banas 2009b): The structure of an NPZD-type ecosystem model.

The parameters provided by Powell et al. (2006) are well-tested in both the California current and off of Oregon, making them suitable for use in northern California.

Table 2.5: Powell et al. (2006) parameters used for Powell-NPZD.

Parameter name	Symbol	Value	Dimension
Light extinction coefficient	k_z	0.067	m^{-1}
Self-shading coefficient	k_p	0.0095	$\text{m}^2 \text{mmol-N}^{-1}$
Initial slope of P-I curve	α	0.025	$\text{m}^2 \text{W}^{-1}$
Surface irradiance	I_0	158.075	W m^{-2}
Nitrate uptake rate	V_m	1.5	d^{-1}
Uptake half saturation	k_N	1.0	mmol-N m^{-3}
Phytoplankton senescence	σ_d	0.1	d^{-1}
Zooplankton grazing rate	R_m	0.52	d^{-1}
Ivlev constant	Λ	0.06	$\text{m}^3 \text{mmol-N}^{-1}$
Excretion efficiency	γ_n	0.3	
Zooplankton mortality	ζ_d	0.145	d^{-1}
Remineralization	δ	1.03	d^{-1}
Detrital sinking rate	w_d	8.0	m d^{-1}

2.6.2 NPZD ROMS dynamics

Nitrogen, Phytoplankton, Zooplankton and Detritus are advected and diffused with the temperature and salinity fields. Unlike in Powell et al. (2006), positive definite behavior is proscribed with use of the MPDATA advection scheme (see section 2.5.6). This was necessitated by both the nitrogen and zooplankton terms going negative despite the application of a conservative filter. In choosing MPDATA, the conservative filter could be removed. Lateral harmonic horizontal diffusion constants were set to 4 m²/s. Radiation-Nudging lateral boundary conditions were applied to Powell-NPZD terms, as described in section 2.5.9.1.

2.6.3 NPZD initial and boundary conditions

The World Ocean Database (NOAA 2013b) has an array of cruise-sampled phytoplankton concentration data, which can be interpolated geographically and temporally to create a set of monthly averages to be applied each year. This data was used for both initial and boundary conditions of phytoplankton, with zooplankton and detritus initialized to 10% of the phytoplankton value. It is, however, in units of micrograms of chlorophyll-a (chl-a) per litre of water. As Powell-NPZD is a nitrogen-based model, a unit conversion is necessary:

$$\frac{\mu\text{g chl-a}}{\text{L}} \frac{\mu\text{g C}}{\mu\text{g chl-a}} \frac{\mu\text{mol C}}{\mu\text{g C}} \frac{\mu\text{mol N}}{\mu\text{mol C}} = \frac{\mu\text{mol N}}{\text{L}} \quad (50)$$

The Redfield Ratio of atomic mass in phytoplankton (C:N:P = 106:16:1; Redfield 1934) is applicable, but the key uncertainty here is in the chl-a/Carbon ratio, which varies widely based on environmental conditions and phytoplankton speciation. It is not constant, changing under the effects of light, nutrients, and temperature. 50 C:Chl is a reasonable compromise taken from a study of this ratio in the California current (Li et al. 2010); for more discussion of the model uncertainty introduced by this unknown parameter, see section 3.8.

The World Ocean Atlas (NOAA 2013c) is a set of objectively analyzed (1° grid) climatological fields, including in situ nitrate, which was used to create both initial and boundary conditions for nitrogen. As for the physical fields, all initial and boundary condition interpolation was performed in MATLAB.

2.6.4 NPZD riverine input

Riverine dissolved inorganic nitrogen (ammonia, ammonium, and nitrate, though in the Powell-NPZD model there is only one “nitrate” variable for all of these) was calculated from USGS data (USGS 2012) and found to be, on average, constant throughout the year (Figures 2.20 and 2.21). The USGS total nitrogen data in Figures 2.20 and 2.21 was collected between 1954-1998 at Scotia, surely using a variety of sampling and analysis methods over the 40 year period. Based on Fishman et al. 1994, which lists all USGS organic and inorganic analysis methods and the years in which they were used by the agency, it is most likely that total nitrogen as nitrate plus nitrite was most often measured using colorimetry analysis, typically with a cadmium reduction-diazotization, as described in Fishman and Friedman 1989 and Fishman 1993. A measurement

of total nitrogen by digestion-distillation titrimetry was also widely used from 1978-1988 (Fishman and Friedman 1989) which is when many of these measurements were taken.

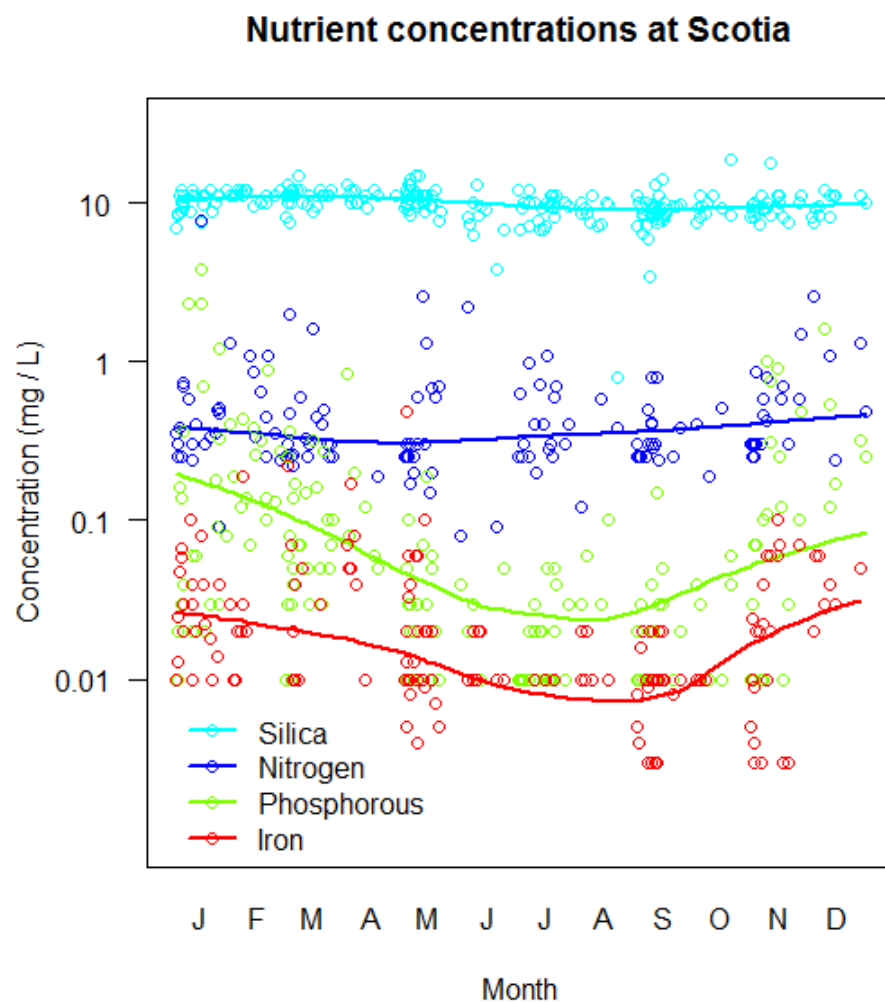


Figure 2.20: Figure by Dr. Jonah Piovia-Scott. USGS nutrient concentrations at Scotia, CA taken between 1959-present, and monthly climatological averages.

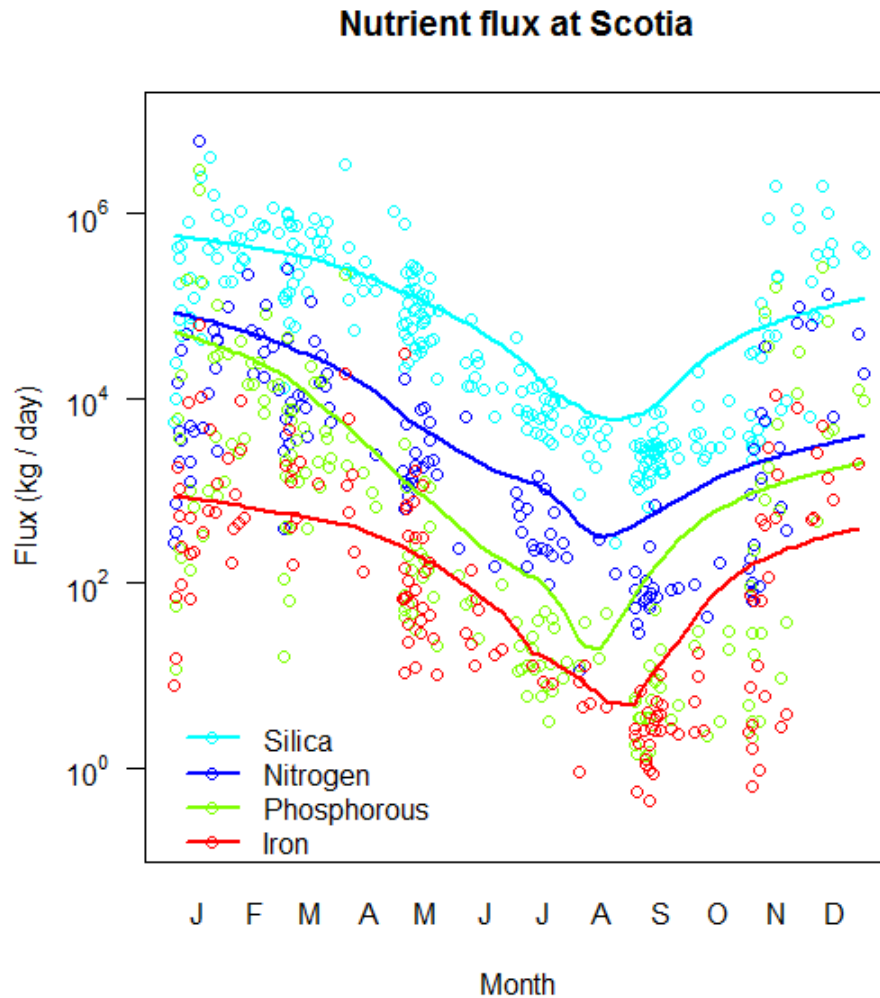


Figure 2.21: Figure by Dr. Jonah Piovia-Scott. USGS nutrient flux at Scotia, CA calculated by multiplying nutrient concentration at time of measurement by measured river discharge at time of measurement, and monthly climatological averages. The flux is clearly dominated by the increased river discharge in the winter.

Figures 2.20 and 2.21 indicate that during storm events there is a larger flux of nitrogen due to more water discharged, but the nitrogen concentration within that water seems to remain the same. It is possible that very short-term effects of leaching could be detected with a high-frequency data sampling, and the model climatology updated accordingly, but that is beyond the scope of this thesis.

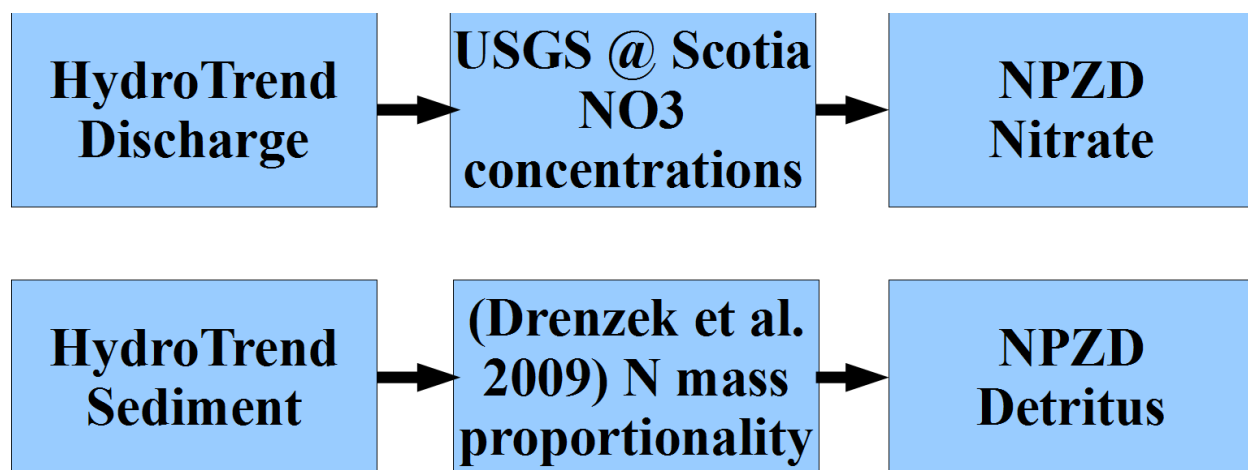
The possibility of the river delivering living microorganisms who would then prosper in the ocean (phytoplankton and zooplankton) was not tested in the model, but river detritus was considered seriously as a possible source of local, short-timescale pulses of phytoplankton productivity, as they uptake what is available to them in the freshly delivered organic matter of Cape Mendocino; additionally, due to the remineralization rate allowed for in the biological model, river “detritus” could include slowly bioavailable nutrients in the sediments themselves.

Therefore, HydroTrend's estimate of sediment mass transport of the river was used, in turn, to estimate time series of detritus transport.

Sediment cores collected from Eel deposition on the coastal margin (Drenzek 2009) indicate a total organic carbon/total nitrogen ratio of ~20, and that terrestrial organic carbon comprises 25-75% of the sediment carbon. The sediment is mostly lithogenic by mass, but can have high fractions of biogenic and combustible flux (Walsh and Nittouer 1999). Particulate organic matter measured and characterized at the mouth of the Eel River found C:N ratios varying from 10 (at low flows and low POM concentrations) to 15 (at high flows and high POM concentrations) (Goñi et al. 2013). Taken in combination with Drenzek (2009), this implies that 25-50% of the particulate organic nitrogen delivered by the Eel River is relatively rapidly bioavailable (though some of the uptake presumably occurs on the shelf rather than by plankton in the water column). Goñi et al. (2013) also directly estimates annual yields of N in 2008 and 2009 as 0.03-0.04% of the total suspended solids. Thus the model estimating "bioavailable particulate nitrogen held in Eel detritus" as 5% of HydroTrend's total sediment is a very high upper bound, while giving us a daily time series that is event-driven by weather conditions. In the event that the results are nutrient-driven, running experiments that reduced that percentage could do a better job of estimating it. (This turned out to not be the case, as described in section 3.6 – thus, given this overestimate, it seems very unlikely that Eel nitrogen from detritus has a significant short-term effect on coastal ocean productivity.)

In summary, the total freshwater discharge entering ROMS from HydroTrend is loaded with a monthly average dissolved nitrogen concentration based on the USGS data shown in Figure 2.20. 5% HydroTrend sediment mass is added directly as a detritus (particulate nitrogen) input to the NPZD model. This model does not model other possible micronutrients of interest, such as iron; discussion of potential methods of iron modeling for future work is found in Chapter 3.11.

Figure 2.22: A graphical representation of the transformation of HydroTrend output into NPZD nutrients.



2.7 Model Experimental Design

Differences between the 10 and 1 km model applications have been mentioned throughout Chapter 2, and are compiled here for direct comparison. The most significant differences are the application of an atmospheric formulation, and the vertical mixing parameterization, which had to be changed at 1 km when the K-Profile parameterization failed to sustain ocean stratification for any significant period.

Table 2.6: Summary of differences between 10 and 1 km model applications.

Model Differences	10 km ROMS model	1 km ROMS model
Atmosphere	NARR, bulk flux parameterization	ERA-Interim, direct flux application
Domain	37-47 N, -132-123 W	39 to 42.1966 N, -128.993-123.507 W
Interior Points	275 x 556	374 x 453
Transformation Function	2	1
Stretching Function	4	1
Baroclinic Timestep	180 seconds	30 seconds
Inclusion of Biology	No	Yes
Inclusion of River	No	Yes
Initialization dataset	ECCO2	10 km results, WOD, WOA
Vertical Mixing Parameterization	K-profile	Mellor-Yamada 2.5
Period of hindcast	1998-2010, continuous run	2002-2010, 18-month overlapping runs
Spin-up model time	2 years	6 months

The fully-coupled model with a river that estimates Eel River nutrient load was run from 2002-2010. As a control, the same model without any river was run for the same time period. This examines the question of *does the river matter* – by comparing model results with and without the river we can begin to understand the river’s impact on the coastal environment. Additionally, to discriminate between whether the *nutrient load* of the river or the *physical presence* of the river was the dominant actor, a zero-nutrient river was run during the year with the largest storm event (2005-2006). A lack of significant difference between the with-nutrients river results, and the no-nutrients river results, would indicate that it is the physical effects (eg, the freshwater plumes) impacting coastal biology, rather than the nutrients delivered by said plumes.

In order to verify that the modeling framework could successfully resolve a nutrient-driven plume *at all*, just in case the model itself might be simply failing to connect river nutrients to ocean biology in some fundamental, mechanistic way, an extra-nutrient river was run for the same year. Providing 400 times the natural nitrate load of the Eel River to the coastal ocean should guarantee a biological response; failure to do so would indicate a critical problem with the modeling framework. Finally, to test the model’s sensitivity to the carbon:chlorophyll ratio (a possibly major uncertainty discussed in section 2.6), the model was run with double initial phytoplankton (the equivalent of a doubled choice of C:Chl ratio).

Table 2.7: Summary of model experiments.

Model Experiment	Years Run
1 km model with river	2002-2010
1 km model without river	2002-2010
1 km model with zero-nutrient river	2005-2006
1 km model with extra-nutrient river	2005-2006
1 km model with double initial phytoplankton	2005-2006

2.8 Model Results

In order to gauge the basic capabilities of the modeling framework to reproduce the physical system, we consider examples of the time series of HydroTrend discharge and sediment, 10 km Regional Ocean Modeling System climatologies in summer and winter as well as at short time scales, and a 1 km ROMS freshwater plume delivered during a storm event.

2.8.1 Results: HydroTrend

We begin by comparing three versions of the HydroTrend model to USGS historical results (USGS 2012; Syvitski and Morehead 1999; Figure 2.23): what differs is the atmospheric forcing. Older USGS results are used in order to look at data that includes both discharge and sediment loads, since the USGS did not continue sediment load measurements into the 2000s. The first model is forced by a stochastically generated climate based on data from the Eureka Weather Station of the National Weather Service (National Weather Service 2014). The Eureka National Weather Service Station (40.81 N, -124.16 W) lacks continuous data necessary to do a nonstochastic run, but has 1979-2010 monthly averages that were used to construct the climatic climatologies to generate HydroTrend's stochastic climate (the method is described in Kettner and Syvitski 2008).

Additionally, the model is forced by each of two nonstochastic time series, ERA-Interim (Dee et al. 2011) and the NARR (Mesinger et al. 2006).

Table 2.8: HydroTrend results summary for discharge and sediment. Visualized in Figure 2.23.

Model Description	Q (m³/s)	Qs (kg/s)
Eureka Weather Station-based stochastic climatology	200	441
NARR nonstochastic time series, 1979-2010	282	446
ERA nonstochastic time series, 1998-2012	280	463
USGS Historical Data (~1995; Syvitski and Morehead 1999)	200	445

The closest results to the USGS Historical Data (which are themselves likely overestimated by roughly a factor of 2, per Warrick et al. [2014]) come from the stochastically generated climate using statistics from the Eureka Weather Station. Unsurprisingly, given their additional rain (see section 2.3.5), extra discharge is created using the NARR and ERA time series. This is accompanied by more sediment: though the model produces about 140% of the USGS discharge, it only produces up to 104% of the USGS sediment. As expected, sediment follows discharge proportionally in both timing and magnitude.

To maintain the same atmospheric forcing throughout the modeling framework, it is the ERA results that must be fed into the 1 km ROMS model. Comparing them directly with USGS gauging station discharge (Figure 2.24a and 2.24b), HydroTrend successfully captures event timing, and moderately reproduces event magnitude. The flow generated by the most extreme storm events is underestimated by about a factor of two, while summer flows and smaller storm events are overestimated by roughly the same amount, thus spreading the discharge throughout the year. The underestimation bias of discharge during the major storm events has the potential to cancel the systematic overestimation overestimation of sediment described in Warrick et al. 2014, such that the sediment time series may be roughly correct during those particularly high-discharge events.

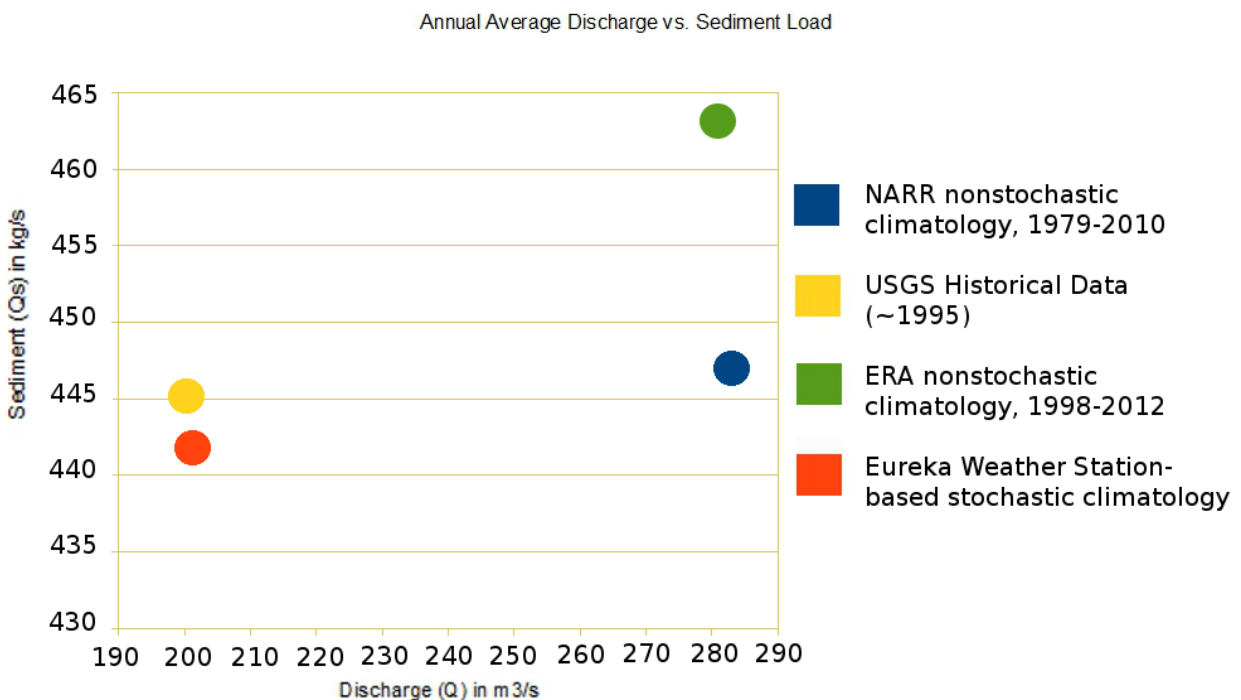


Figure 2.23: Annual average discharge vs. sediment load for HydroTrend results versus the USGS validation data. Note that this is a fairly tight cluster far from zero, but zoomed in on both axes in order to be able to see the differences.

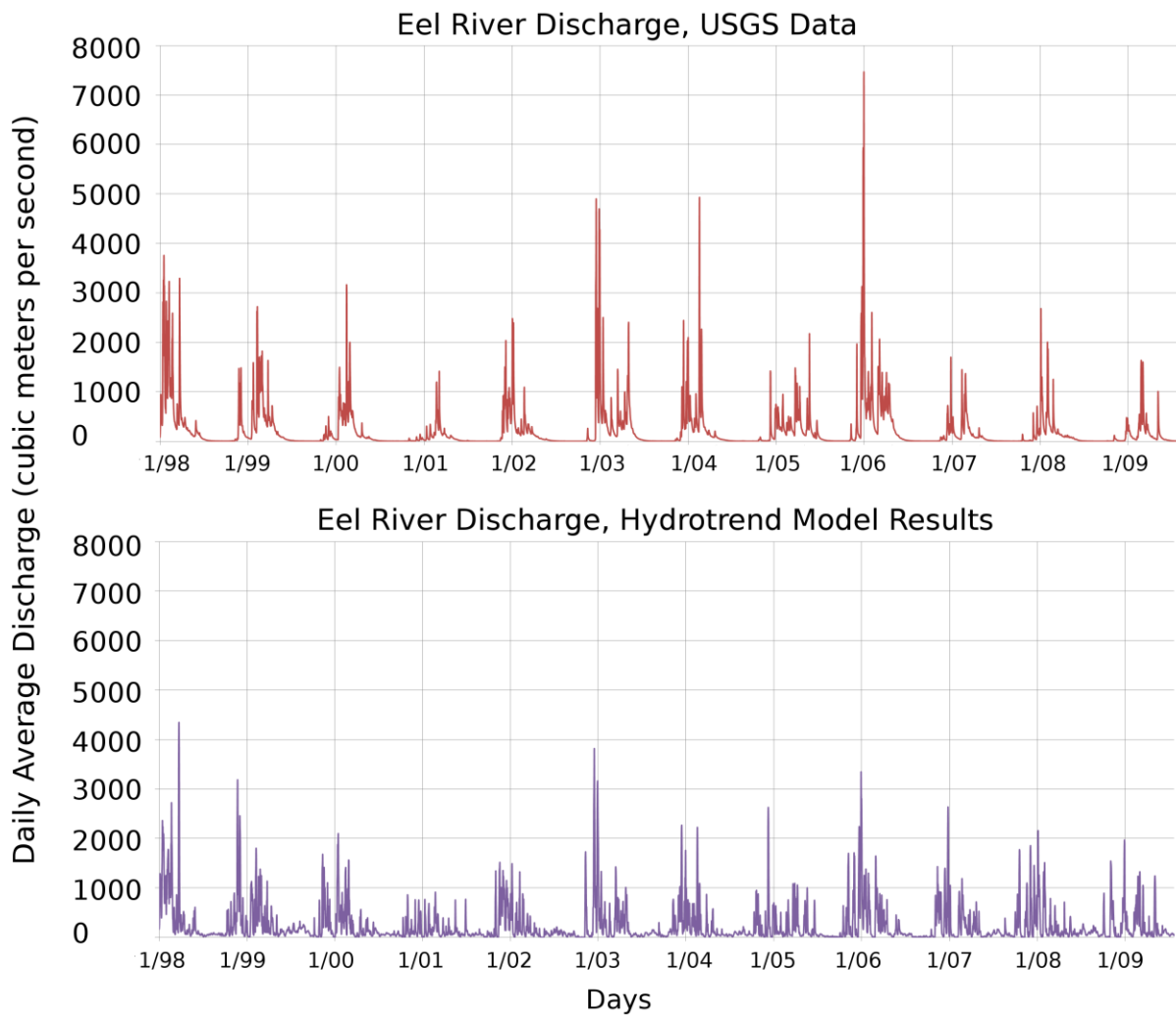


Figure 2.24a: ERA-Interim driven HydroTrend vs. USGS gauging data for discharge, 1998-2010.

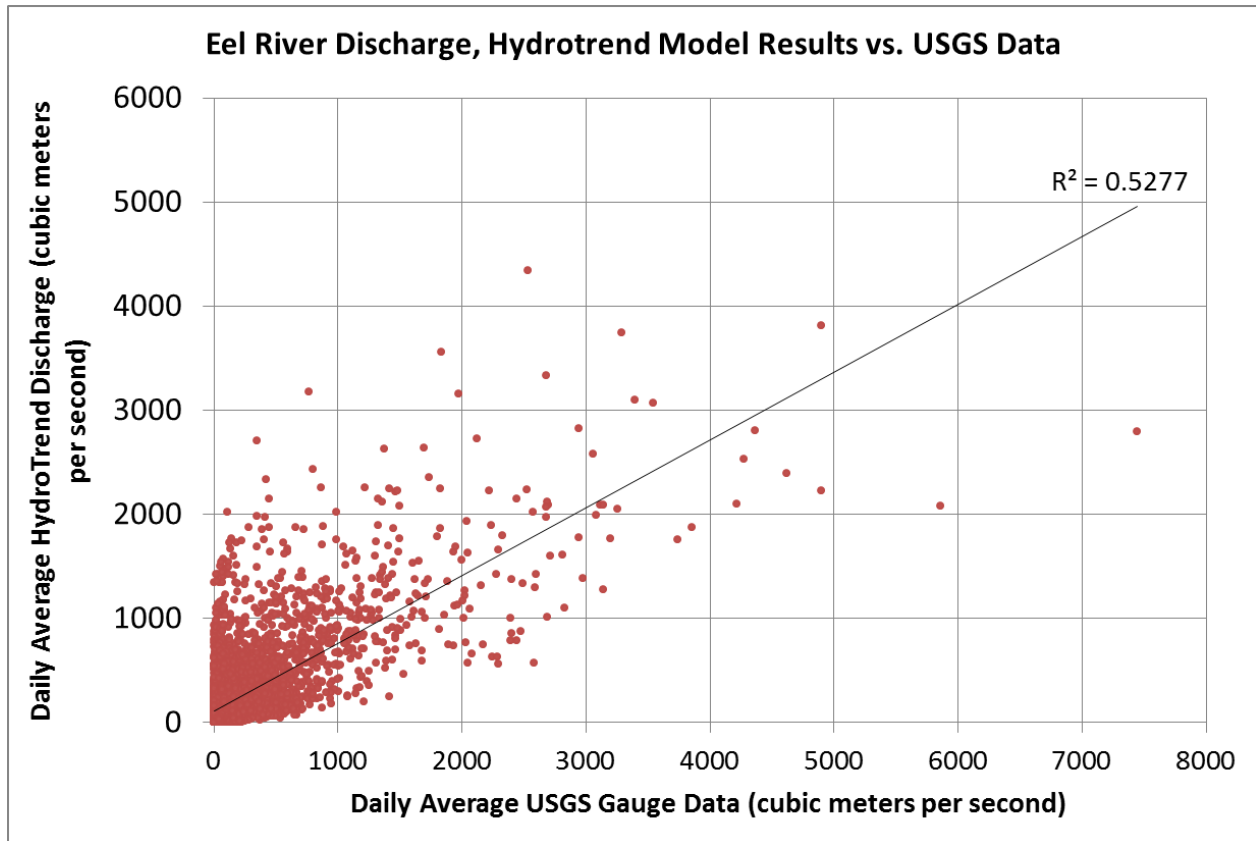


Figure 2.24b: HydroTrend results vs. USGS data, 1998-2010.

2.8.2 Results: ROMS, 10 km resolution

The 10 km resolution ROMS results are not the focus of this study, seeing as they lack any representation of the Eel River or any biology. However, they provide an excellent representation of the Northeastern Pacific in heat and momentum, and a brief overview of their results is presented.

2.8.2.1 Climatological validation

Figures 2.25 and 2.26 contain the major climatological results for the 10 km resolution ROMS model. They are compared to results from the Simple Ocean Data Assimilation (Carton and Giese 2008), a $0.25^\circ \times 0.4^\circ \times 40$ level model forecast that assimilates hydrographic profiles, ship intake measurements, moored hydrographic observations, and remotely sensed sea surface temperature. It is well-regarded as a useful set of estimates of ocean circulation, and useful for comparison. In January (Figure 2.25), sea surface temperature is roughly correct within a degree, with the caveat that ROMS displays a cooler bias, especially onshore, which disrupts an otherwise smooth north-to-south temperature gradient. The directional structures of the velocity fields are well reproduced, with ROMS about a factor of 1.5-2 faster at the various extrema. The width of the onshore north-flowing current is considerably narrower in ROMS, with the transition to south-flowing ocean occurring closer to 125°W , whereas in SODA this occurs near 126°W .

In July (Figure 2.26), upwelling is well reproduced, as evidenced by the similarity in onshore sea surface temperature. ROMS upwelling is considerably more detailed in its shore-following structure, a reasonable result given its higher horizontal resolution. Offshore, it is about one degree warmer than SODA. Once again, zonal and meridional velocity structures are well-reproduced spatially with ROMS momentum greater than SODA's by a factor of two onshore (and, meridionally, weaker offshore). All in all these results are quite robust; the major summer and winter features in heat and momentum are clearly being reproduced, making them well suited for boundary condition forcing in the 1 km model.

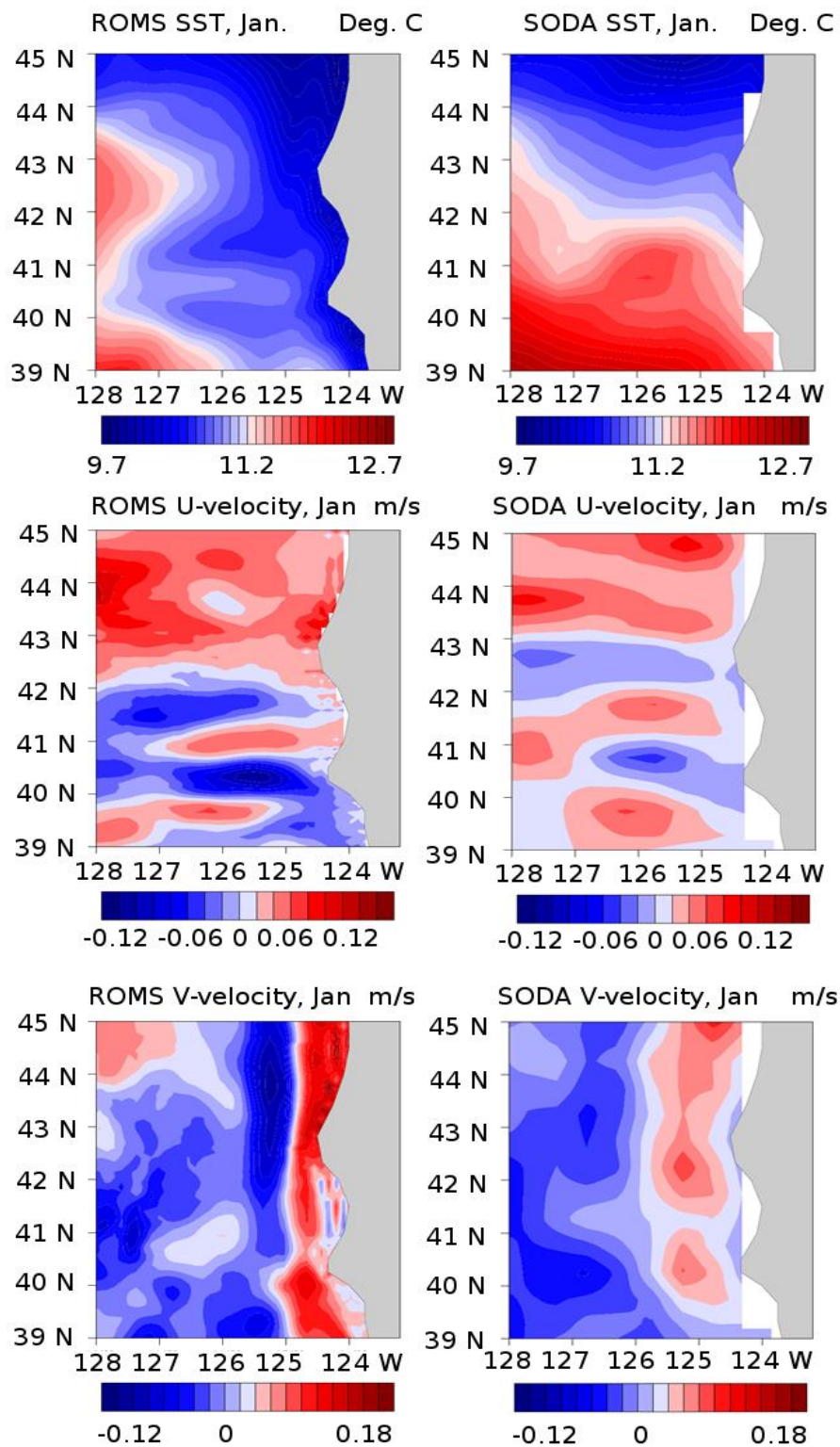


Figure 2.25: ROMS 10 km results (left) and SODA (right) for sea surface temperature, zonal (east-west) velocity and meridional (north-south) velocity climatologies for the month of **January**, 2000-2010.

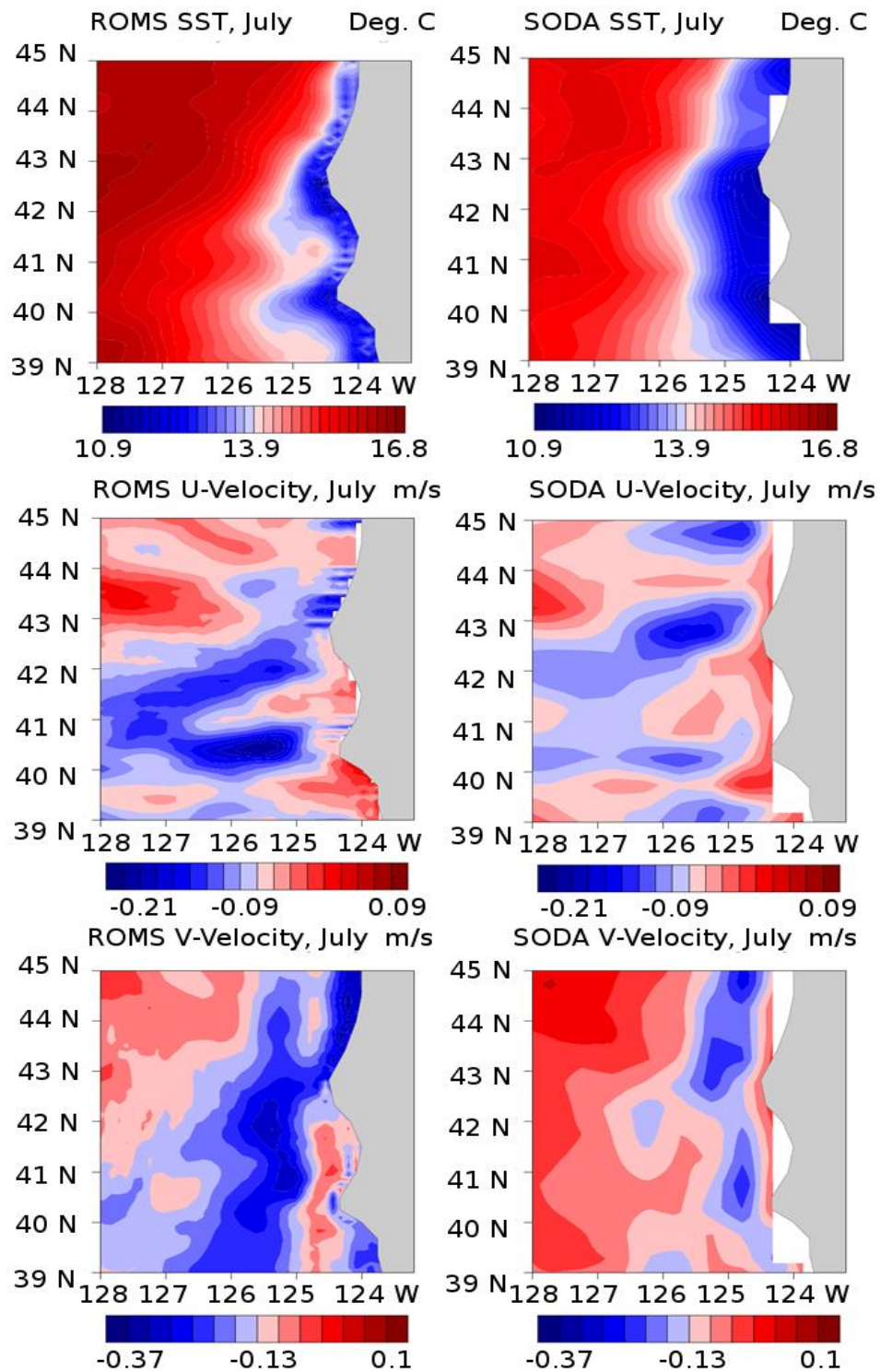


Figure 2.26: ROMS 10 km results (left) and SODA (right) for sea surface temperature, zonal (east-west) velocity and meridional (north-south) velocity climatologies for the month of **July**, 2000-2010.

2.8.2.2 Short Time Scale validation

We turn next to an example of shorter timescale validation. Upwelling, though not the focus of the biological study, often occurs in discrete events throughout the season, as larger gusts drive Ekman transport. One such event occurred in a roughly 48-hour span around 6/22/2001, on a clear day with very few clouds. Figure 2.27 compares ROMS results with satellite data from NOAA's AVHRR/HIRS sensor (NOAA 2012a). Both the temporal and spatial extent of this cooler region are well-reproduced, with ROMS' upwelling event generally 1-2 degrees colder (and therefore more extreme, in terms of the actual transport of cold deeper waters to the surface; the model is overpredicting upwelling). This is one example among many of the 10 km ROMS model's ability to simulate discrete physical events in the ocean.

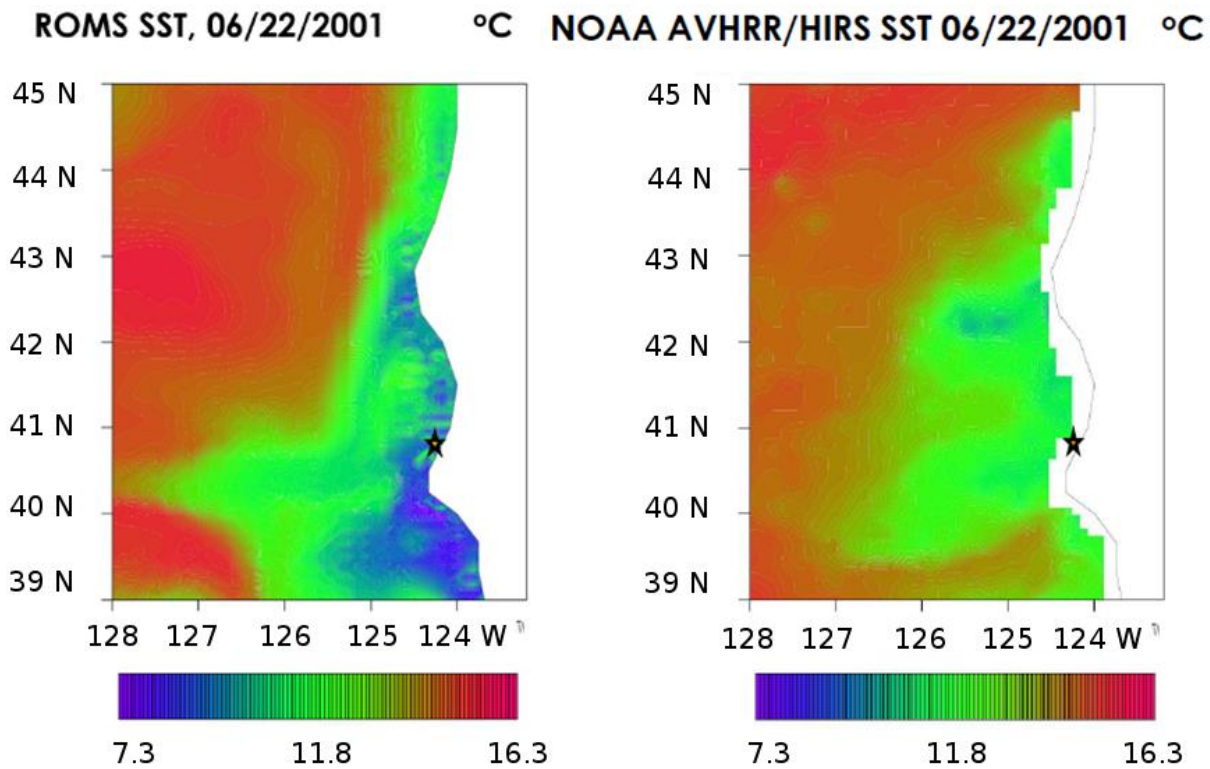


Figure 2.27: ROMS vs. satellite sea surface temperature for a 48-hour period around 6/22/2001. The mouth of the Eel River is starred.

Furthermore, we can consider these results, as well as the climatological results, statistically. Taylor Diagrams (Taylor 2001) are a readily available tool for this purpose. A modeled field (ROMS results) is cross-correlated with a reference field (SODA results in Figures 2.25-26, or for the short timescale validation in Figure 2.27, the AVHRR/HIRS sea surface temperature sensor), and this value is graphed along the circular axis to the right-hand side of the diagram. Standard deviations from the mean are graphed along a linear axis. By normalizing the standard deviations of the modeled fields to the standard deviation of the reference field, it becomes possible to put modeled variables with wildly different numerical values (such as sea surface temperature, in Celsius, and U-velocity, in meters per second) on the same diagram.

Thus, the “ground truth” (or, in this case, satellite values or SODA values) is at the ‘REF’ point, or a normalized standard deviation of 1.0, and falls at the very end of the circular axis, with a 1.0 correlation to itself. As modeled values diverge along the circular axis, their goodness-of-fit to this reference field worsens; when modeled values fall above the normalized standard deviation of 1.00, their variability is proportionally greater than that of the reference field; below 1.00, proportionally less.

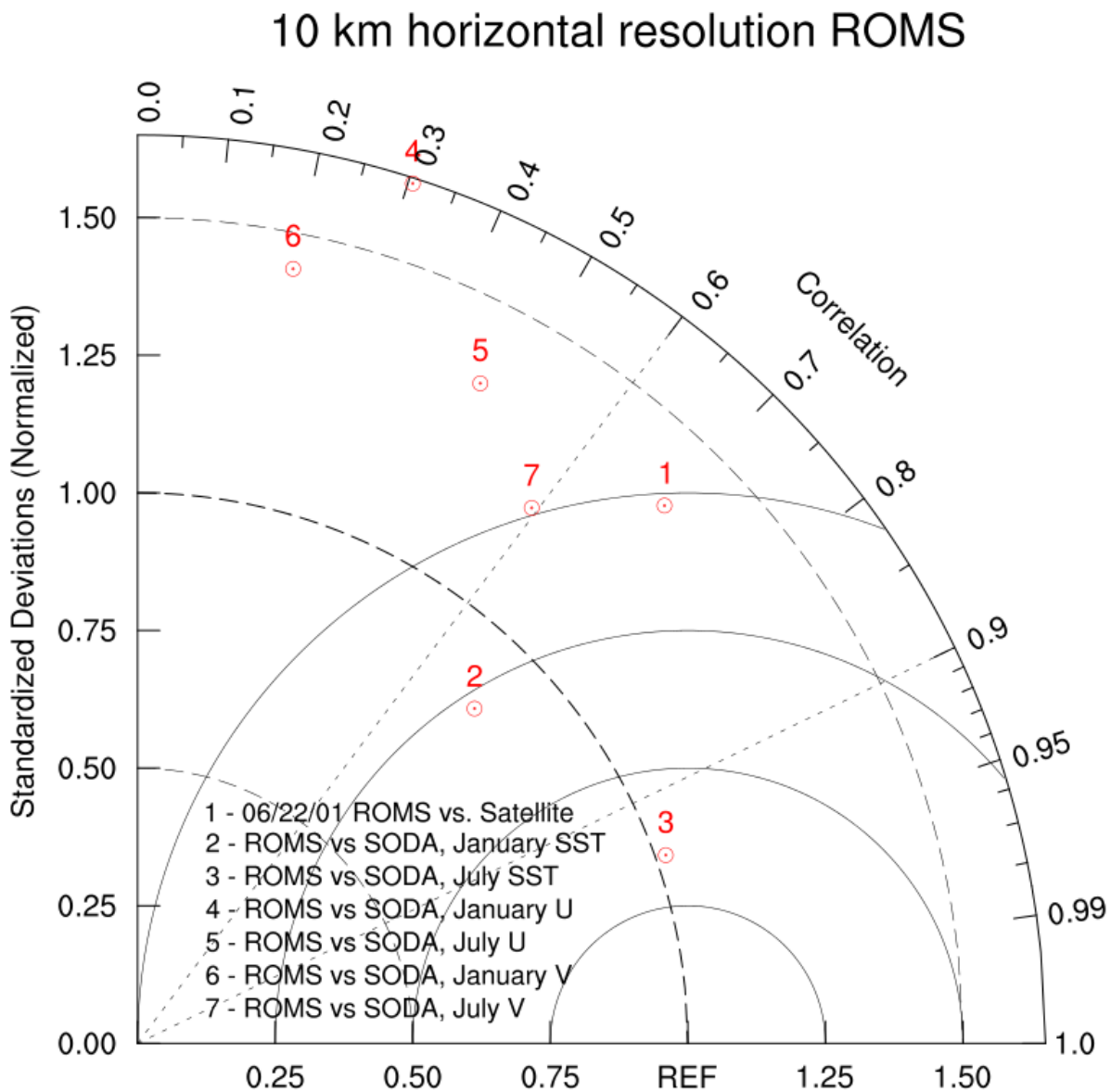


Figure 2.28: Taylor Diagram for 10 km ROMS results from section 2.8.2.

To interpret Figure 2.28, we begin with the observation that whether at a short or long timescale, sea surface temperature enjoys the best correlation with the reference fields (of satellite data and SODA), never less than 0.7. July SST is particularly good, with a cross-correlation above 0.95

and a standard deviation essentially identical to that of SODA; January SST has slightly less variability than SODA, and a correlation near 0.75, while ROMS compares to the satellite results on 06/22/01 with a correlation of 0.7, but quite a bit more variability across the field. This is easy to see up in Figure 2.27, where ROMS is, across the domain, both cooler and warmer than the satellite data in various places.

Velocity is less similar; July V-velocity has a cross-correlation value of 0.6 with SODA, and that's the closest they ever come, as cross-correlation values proceed to decline as low as 0.2 for January V-velocity. They uniformly experience greater standard deviations than the SODA results. That does not, however, mean that the 10 km results are poor; merely that in velocity they diverge considerably from SODA results. This is unsurprising. As remarked in section 2.8.1, the increased resolution of the ROMS results compared to lower-resolution SODA (which is itself a model) has created subtly (and less-subtly) different spatial patterns; while the largest features of SODA are reproduced, in ROMS they are often in slightly different places, with, usually, greater intensities. This increase in momentum is most likely the effect of jets and squirts off the California-Oregon coast, a well-known feature (Strub and James 2000, Keister and Strub 2008) of the northern California Current that relies on smaller-scale turbulent structures than SODA simulates.

2.8.3 Model Results: ROMS, 1 km resolution

At 1 km horizontal resolution, the coupled modeling framework includes the Eel River directly. Figure 2.29 shows a typical example of a storm-driven Eel River freshwater plume, several days into its delivery and drift. Driven by primarily southerly winter winds, most of the plume follows the shore northward, its impact felt over 10 km away. However, the plume is also acted on by features of greater ocean circulation; in this case, an eddy that captures some of the freshwater, dragging it off to the west. This behavior compares well to the STRATAFORM project that first observed via cruise, then reproduced via model, plume dynamics as altered by ocean eddies (Pullen and Allen 2001). The coupled modeling framework thus demonstrates the ability to simulate freshwater plumes on the daily timescales of the storm event-driven system.

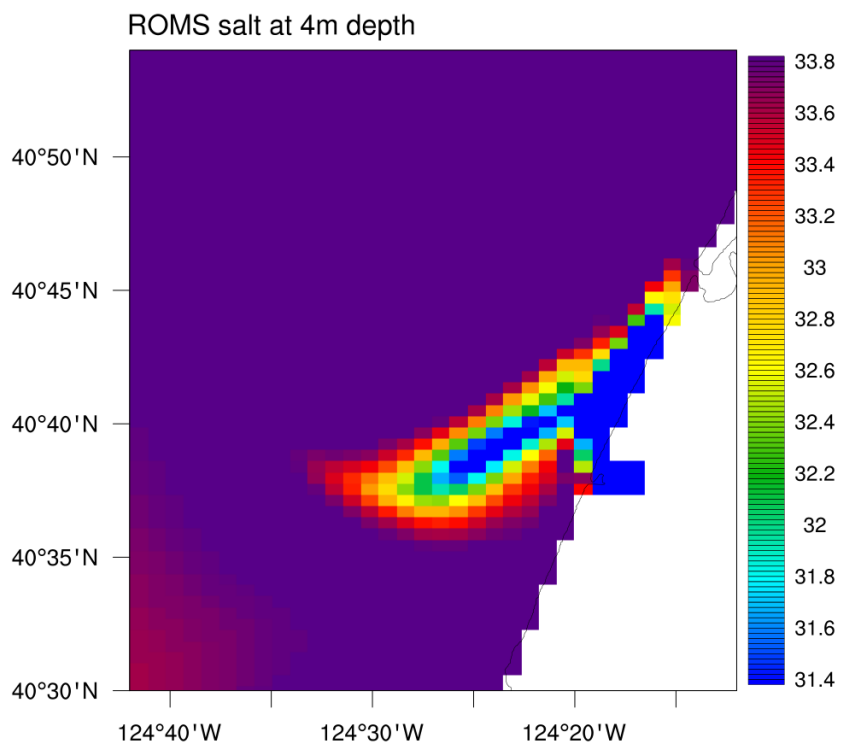
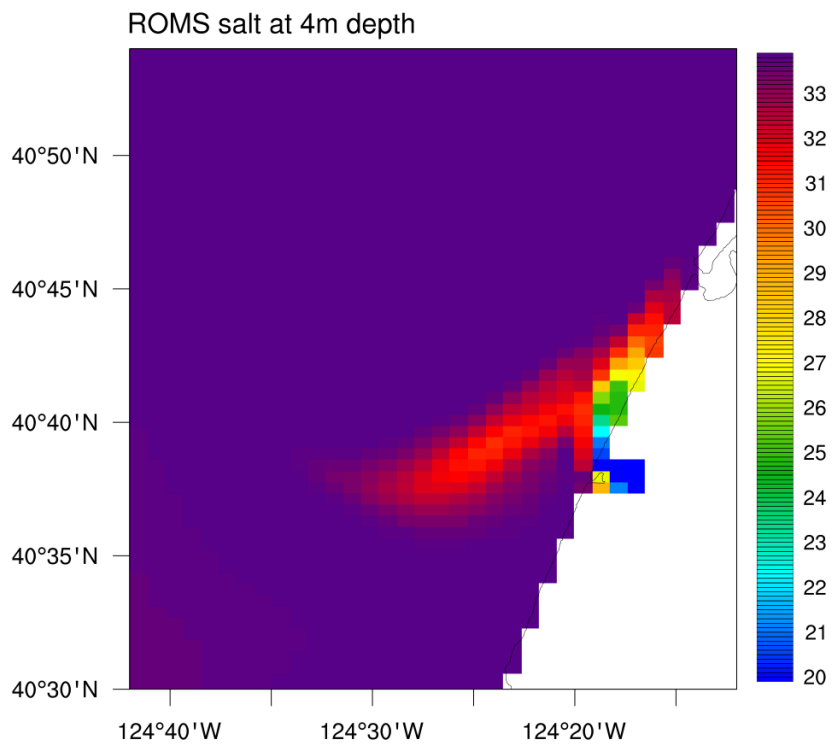


Figure 2.29: 1 km ROMS salinity in the coupled modeling framework, producing a river plume on 12/24/2004. Units are psu. The bottom plot is the same as the top with the colorbar zoomed in.

2.9 Conclusion

In order to examine the effect of Eel River physical and nutrient effects on coastal ocean biology, a coupled modeling framework was constructed unifying atmospheric forcing, a hydrological model (HydroTrend), an ocean circulation model (Regional Ocean Modeling System) and a biological model (NPZD-Powell). Experiments were performed across the 2000-2010 decade, adding and subtracting the presence of a river with various levels of nutrients. The results of these tests are discussed in Chapter 3.

A few revelations came out of the construction of the modeling framework: the ERA-Interim Reanalysis seems unable to correctly capture seasonal temperatures in the Eel River Basin in Northern California, being both too warm in the winter and too cool in the summer as compared to Daymet data. Within the Regional Ocean Modeling System, extremely small (~30 second) timesteps were necessary in order to preserve the CFL criterion at a 1 km horizontal resolution with the presence of the river. This could be a potentially important constraint on directly modeling small but extreme rivers in larger regional models. Additionally, the serious and unsolved problem of three-dimensional ocean circulation modeling being unable to retain onshore stratification at high horizontal resolutions remained an issue here, and would be a problem going forward within larger models, as computational expense for model spin-up increases with model domain.

HydroTrend reproduces time series of Eel River discharge and sediment that compare well to USGS data in both timing and magnitude. While not a perfect reproduction, it is adequate as a source for the 1 km Regional Ocean Modeling System's river, which successfully simulates freshwater plumes as acted on by local weather and larger circulation features. On a larger scale, the 10 km ROMS results (used as boundary conditions for the 1 km ROMS simulation) successfully reproduce the major physical features (i.e. temperature and momentum) of the northern California Current in both summer and winter. These results are compelling in quality and may well be useful for providing boundary conditions with a higher horizontal and vertical resolution than ECCO2 or SODA for other members of the modeling community. Broadly, each the large components of the coupled modeling framework, atmosphere, river, and ocean, function well as a physical simulation of ocean circulation.

If the biological results of these experiments (examined in Chapter 3) indicate river-driven trends, this framework could be nested within global climate models such as the Community Earth System Model in order to improve river-to-ocean processes, or simply forced forward by their results offline. As a mesoscale modeling framework that directly simulates the river (instead of using river data from gauges and cruises), it represents a potentially important advance in the field of Earth System modeling. The overarching question of the thesis, however, is whether smaller rivers are of sufficient importance to coastal biology as to make this advance *necessary*. To examine this question, we now turn to the biological results.

Chapter 3: Results

3.1 Introduction

3.2 MODIS validation; coverage and cloud gap-filling

3.3 Climatological comparisons

3.4 Interannual variability comparisons

3.4.1 Correlative analysis of December 2002-2009

3.4.2 Empirical Orthogonal Function analysis of December Interannual Variability

3.4.3 Comparison of Decembers with varying river conditions

3.4.4 Summary of interannual variability comparisons

3.5 Event-driven comparisons

3.5.1 Large river, deep mixed layer

3.5.2 Small river, deep mixed layer

3.5.3 Large river, shallow mixed layer

3.5.4 Small river, shallow mixed layer

3.5.5 Summary of event-driven comparisons

3.6 No-nutrient river modeling

3.7 Extra-nutrient river modeling

3.8 Chl:C sensitivity testing

3.9 Southwestern model artifact and nonlinear model drift

3.10 Discussion

3.11 Future Directions

3.12 Conclusion

3.1 Introduction

In order to search for the potentially small signal (as indicated by Chapter 1) that represents the Eel River's effect on coastal ocean productivity, a coupled modeling framework (Figure 2.1) was created that links hydrological models with ocean circulation models, unified beneath the same atmospheric forcing. The framework was run across 2002-2010, with a focus on 2005-2006, the water year with the most dramatic storm-driven Eel River water and nutrient deliveries to the ocean. The biogeochemical results of these model experiments are presented here.

In order to separate the questions of “does the Eel River have any effect on coastal ocean productivity” and “is this effect physical or biogeochemical in origin,” two kinds of experiments were run: comparisons of the fully coupled model to a control that wholly lacks the Eel River, and comparisons of the fully coupled model to a control that includes an Eel River that lacks any nutrients. In this way, if the absence of the Eel River leads to significantly different results, but the absence of Eel River nutrients does not, that implies a physically-driven impact. If the absence of Eel River nutrients creates a notable effect on the results, that implies that Eel River nutrient delivery is a significant driver on coastal ocean productivity.

In order to consider the results of the 1 km horizontal resolution ROMS, with inclusion of the Eel River and the Nutrient-Phytoplankton-Zooplankton-Detritus biogeochemical model (Powell et al. 2006), three timescales are considered in the search for effects of the Eel River on coastal ocean productivity. First, monthly climatologies constructed from the entire 2002-2010 results

are constructed and compared between the fully coupled model and the no-river control. As most river delivery events happen on weekly or daily timescales rather than monthly, it is not wholly surprising that the possible signal of riverine nutrient-driven ocean productivity is not well-resolved here. However, possibilities of accumulative effects (such as the sinking of river nutrients below the euphotic zone, upwelled later in the year) make the climatological examination potentially interesting.

Second, interannual variability is considered, specifically during the often high-discharge month of December. After initial correlative studies of phytoplankton concentration, mixed layer depth, surface stress, mean river discharge and shortwave radiation flux fail to indicate strong relationships, Empirical Orthogonal Functions (Bjornsson and Venegas 1997) are constructed to describe the set of eight consecutive December results, and their behavior compared to possible drivers including the Pacific Decadal Oscillation (Mantua 2014), the Oceanic Niño Index (NOAA 2014b), and Eel River discharge (USGS 2012). Finally, three Decembers of notably different Eel River behavior (“high flow” in 2005, “average flow” in 2003, “minimal flow” in 2008) are examined directly. While the model reproduces phytoplankton dynamics fairly well in timing and magnitude (though not spatial extent), evidence of riverine impact is small.

Finally, in an effort to more clearly resolve riverine effects, analysis turns to event-driven impacts, which is to say the largest Eel River discharge event of each water year. These vary greatly in timing and magnitude, and the state of the coastal ocean varies greatly as well, dominated by seasonal behavior. River plume behavior is inconsistent, seemingly overpowered by the state of the ocean at time of delivery, as highly turbulent oceans mix the river plume rapidly, while relatively stable oceans can support a freshwater plume across its surface for greater distances. In this case as well as the former two, to the extent that the Eel River appears to have an impact, it is a repressive, rather than positive, effect on phytoplankton growth, as the Eel River’s relative lack of nitrate compared to the coastal ocean appears to suppress growth.

Each of these timescale analyses is considering the overall effect (or lack thereof) of the modeled Eel River as compared to the no-river control. River nutrient effects are examined directly by looking at both the no-nutrient river control and an extra-nutrient river experiment. The latter is performed in order to demonstrate that the modeling framework has the ability to resolve river nutrient-driven phytoplankton growth at all, given the lack of effect under realistic conditions.

Throughout each of these analyses we acknowledge concern about model uncertainty; this is discussed in depth in its own section. Possible drivers of uncertainty include the unknown and variable Chlorophyll:Carbon ratio, boundary condition-created numerical noise, and model drift from the nonlinear differences between runs with and without the presence of the river. The framework also only considers nitrogen; the possibility remains that another micronutrient such as iron is the riverine nutrient delivery that has an impact on coastal ocean primary productivity. After discussion of the model results, possible future directions for this line of research are presented.

3.2 MODIS validation; coverage and cloud gap-filling

Using satellite imagery for validation, particularly in so cloudy a part of the world as coastal Northern California, comes with inevitable interference. It is vital that the cloudiness of these images be considered thoroughly, in order to recognize which graphics are truly robust for validation purposes, and which run the risk of creating false negatives. Throughout this work we use regridded MODIS Aqua satellite data (NASA 2013) that has been reprocessed by Oregon State University cloud gap-filling algorithms (OSU 2014). These algorithms replace missing pixels by searching an expanding zone around that pixel, looking for data. All points found in the zone are averaged together for the replacement value. There comes a point, however, where it is better to search forward and backwards in time (± 8 day averages, each of which is itself a composite of multiple images across those 8 days) than to search further and further away spatially; this algorithm defines that point as beyond an 80 km distance, and interpolates data accordingly. (The full white paper describing this algorithm is available online, OSU 2014). But how many gaps are being filled? And how big are the gaps?

MODIS monthly averages have excellent coverage in our region of interest; the November-June climatologies used in section 3.3 never have an average coverage less than 97% (eg, 3% missing pixels because of clouds), with an absolute minimum of 91% in January 2010. No gap-filling is necessary at all; however, that's because this NASA product simply averages every non-missing value for each pixel present, and manages to get at least one value for essentially every pixel at least once a month. This has an obvious problem: a bloom present in a pixel on one day, when all other values of that pixel throughout the month are covered by clouds, may not in fact persist throughout the month – nor might the *absence* of a bloom persist.

Table 3.1: Average over-ocean chlorophyll-a satellite coverage in the 39.5-41.5 N, 123-125 W region of interest near Cape Mendocino for the November-June 2002-2010 climatologies.

2002-2010	November	December	January	February	March	April	May	June
Average Coverage	99.3%	98.9%	98.1%	97.6%	98.2%	98.6%	97.4%	97.9%

The Decembers of interest in section 3.4 (2003, 2005 and 2008) are each composed of 4-5 MODIS 8-day average snapshots. Once again the coverage is often very good, though occasionally poor. It is often the case that adjacent 8-day averages will be sufficiently different ('very good' coverage next to 'clouds everywhere' coverage) that much of the gap-filling is occurring temporally instead of spatially. December 2005 has little coverage because of the extraordinary storms in that period. It is thus possible that the good agreement between model and 'data' late in the month is a false positive; however, what they are agreeing on is that there is very little phytoplankton growth, which is consistent with very little sunlight.

Table 3.2: Average over-ocean chlorophyll-a satellite coverage in the 39.5-41.5 N, 123-125 W region of interest near Cape Mendocino for the 8-day averages within December 2003, 2005 and 2008.

Weeks of 2003	Average Coverage	Weeks of 2005	Average Coverage	Weeks of 2008	Average Coverage
12/01/03	84.4%	12/01/05	83.8%	12/01/2008	98.3%
12/10/03	46.6%	12/10/05	98.2%	12/10/2008	99.5%
12/17/03	60.8%	12/17/05	55.5%	12/17/2008	99.5%
12/24/03	98.6%	12/24/05	3.2%	12/24/2008	24.8%
12/29/03	16.1%	12/29/05	71.4%	12/29/2008	91.8%

Finally, the largest river discharge events in each year described in section 3.5 have a widely variable range of coverage. It is not unusual to have poor coverage within one 8-day average of the event, and despite fears that the clouds that generated this discharge event would mask the satellite coverage, is never poor throughout the entire period. Helpfully, the year with the worst coverage, 2005-2006 (again coinciding with the problematic coverage in the December analysis) has its best coverage of the three, above 70%, on the actual averaged 8-day period of the 2005 event itself. Its gap-filling is thus spatial rather than temporal, and what it fills with is ‘very little phytoplankton present’ as the consistent behavior of the region.

Table 3.3: Average over-ocean chlorophyll-a satellite coverage in the 39.5-41.5 N, 123-125 W region of interest near Cape Mendocino for the 8-day averages surrounding each of the largest Eel River discharge events in the 2002-2009 water years. (The event falls in the second of three 8-day averages in all years.)

2002/03 Event	Average Coverage	2003/04 Event	Average Coverage	2004/05 Event	Average Coverage
12/09/02	78.6%	02/10/04	91.7%	05/10/05	91.1%
12/16/02	6.5%	02/18/04	60.4%	05/19/05	96.9%
12/23/02	75.2%	02/25/04	60.5%	05/26/05	95.2%
2005/06 Event	Average Coverage	2006/07 Event	Average Coverage	2007/08 Event	Average Coverage
12/24/05	3.2%	12/23/06	5.2%	12/30/07	26.0%
12/29/05	71.4%	12/31/06	83.9%	01/05/08	25.3%
01/07/06	11.0%	01/07/07	87.1%	01/13/08	58.5%
2008/09 Event	Average Coverage	2009/10 Event	Average Coverage		
02/25/09	18.9%	01/18/10	53.8%		
03/03/09	69.5%	01/26/10	70.0%		
03/11/09	97.1%	02/04/10	72.9%		

In order to digest the representativeness of these averages to represent phytoplankton blooms, we must also consider the timescales of the blooms themselves. Bloom duration is widely variable, with relevant environmental variables including light availability, nutrients, temperature, and

stratification of the water column, as well as initial phytoplankton stock size (Mann and Lazier 2007). Fully characterizing typical growth and decline rates of open-ocean phytoplankton around Cape Mendocino would require ‘ground truth’ data that does not exist, ideally taken by moored chlorophyll concentration sensors. This is, however, an opportunity for models to attempt to characterize the unknown. Although the model results presented in Chapter 3 are always 8-day averages, in order to match up with the satellite data, model results were calculated every 30 seconds, and collected daily. By studying the daily time series of phytoplankton growth and decline within a given grid cell, we can consider rates of change within our system, and what might be lost by the satellite snapshots and averages. A full analysis of time variability of phytoplankton in the region, as modulated by phytoplankton depth within the water column, is beyond the scope of this work (though an interesting future direction). Instead, the two figures below demonstrate typical examples of daily-timescale fluctuations.

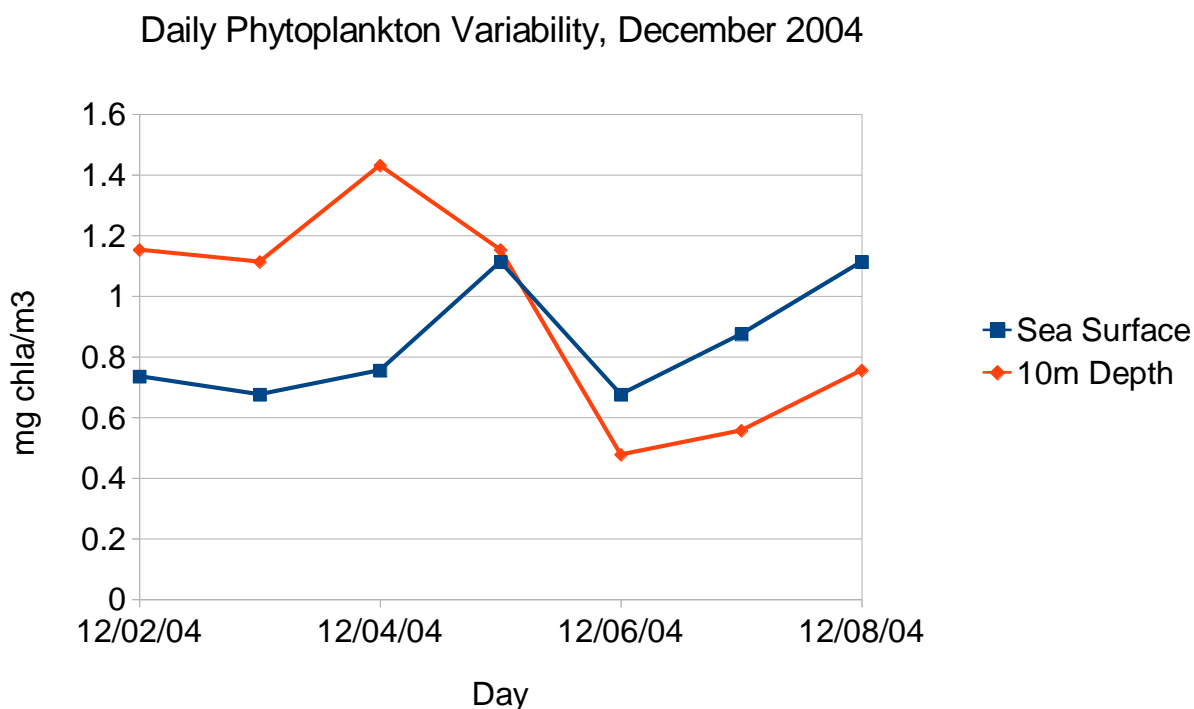


Figure 3.1: Daily averaged values of phytoplankton concentration in the first week of December 2004, taken at 40.5 N, -124.5 W, at the sea surface and at 10m depth.

In the winter, model phytoplankton concentrations are small. The fluctuations are also small, but are often rapid; this is a typical example of a distinct increase and decline in growth, followed by a slower increase. If a satellite took snapshots of this cell 12/2 and 12/8, it would essentially miss much of the internal variability; a snapshot on 12/4, taken alone, could falsely characterize the 10m depth concentration as higher than it is the rest of the time.

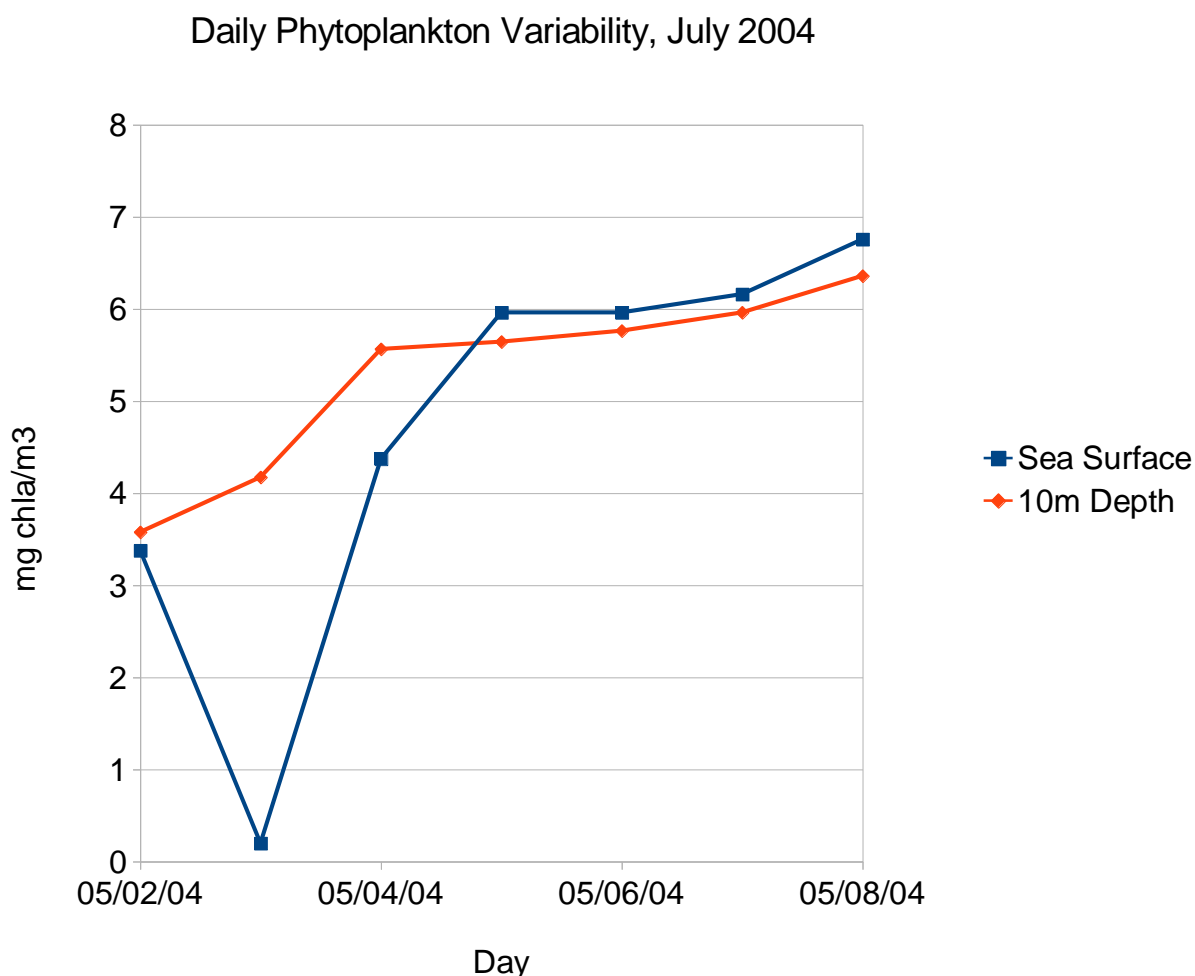


Figure 3.2: Daily averaged values of phytoplankton concentration in the first week of July 2004, taken at 40.5 N, -124.5 W, at the sea surface and at 10m depth.

In the summer, modeled blooms are more gradual in their growth and decline, and larger in magnitude. However, occasional daily-timescale fluctuations are not unknown; the minimum on 5/3/04 at the sea surface is not atypical. Coverage is often better in summer, particularly if the satellite passes overhead in the afternoon after the fog has burnt off; but conversely averages are sometimes more representative, given the smaller rates of change involved with these dense phytoplankton blooms.

There is a very real possibility that much of the difference between MODIS data and model results lies in the differences in their averaging (as MODIS averages once or twice within an 8-day period, likely sometimes entirely missing phytoplankton variability, while the model averages 8 daily-averaged timepoints). Furthermore, MODIS cannot always provide good coverage, and while cloudiness begets light-limitation and thus low concentrations of phytoplankton, sometimes the gaps that need to be filled are sufficiently large that MODIS 'data' is more of a best guess as to what's in the ocean. Fortunately, within our region of interest, satellite coverage is usually above 60%, and often above 80%. Finally, MODIS is this project's

validation of choice because it is essentially the only option; there is no alternative! It is commonly and widely used, but perhaps dangerously so. The field has a real need for more moored, stationary measurements of phytoplankton growth and decline over time in order to understand the ability of occasionally captured, time-averaged satellite pictures to describe these environmental systems.

3.3 Climatological comparison

Figures 3.3 to 3.5 (shown at the end of this section) summarize monthly climatological results, comparing the fully coupled modeling framework (left) to MODIS results (middle; NASA 2013) to a subtraction of the model results from the no-river control results, vertically integrated across the water column (right).

The magnitude of late Fall/early Winter onshore blooms is generally well-reproduced by ROMS during the winter months, at about 2 mg chlorophyll per cubic meter. Unlike in the MODIS data, however, blooms are strongly concentrated to the south rather than the north of the cape. In February, there is a sharp increase in model production by about 50% that is unmatched by the data, but in March, as upwelling begins, magnitudes are again similar. ROMS upwelling-driven productivity appears to occupy a much wider spatial band than MODIS, and fails to concentrate north of the cape. In April and May, ROMS productivity also fails to keep up with MODIS-reported production, underestimating by about 50%. These large differences force us to treat all further discussion of the model with due caution, particularly as pertains to upwelling. As the major river discharge occurs outside of upwelling months, however, there is still potentially insight to be gleaned.

If one expected the presence of the river in the model to stimulate production during the winter months of most extreme Eel River discharge (November-January), the ROMS results show almost totally opposite behavior. In November, the model with the river shows a minor average increase in productivity north of the cape, but south of the cape, as well as onshore in December and January, productivity appears to be slightly suppressed in the model with the river as compared to the control without. Starting in February, the presence of the river appears to slightly stimulate onshore production north of the cape. In April, however, with upwelling season often in full swing, there is both an increase in river-driven productivity far south of the cape, as well as a decrease around the cape's head. Finally, in May, the presence of the river in the model seems to allow for more onshore productivity, both north and south of the cape, but especially to the north, in the area of typical plume deposits.

The magnitude of all of these monthly averaged differences, however, is small, however, compared to the total chlorophyll: it is necessary to vertically integrate the water column in order to resolve them, and they account for only 7%-13% of the total chlorophyll present. Many of the differences are difficult to unpack from the scale of model uncertainty; as discussed in section 3.9, behavior south of the cape, in particular, is heavily impacted by boundary condition-driven numerical noise. The next two sections will show that in general, the slight suppression of phytoplankton production onshore during river-dominated months is consistent with nitrate limitation within plume-affected parts of the water column. The most potentially significant difference, the stimulated production in May (Figure 3.5), might be the signature of the “shelf-

capture nutrient capacitor” hypothesis (Chase et al. 2007), the concept that river nutrients sink out of the euphotic zone uneaten, then enhance productivity when subsequently upwelled later in the year. However, there was no indication that detritus (the slowly remineralizable nutrient in the model, and the one that might behave in this manner) accumulated over the winter on the shelf in such a manner as to explain this behavior. The source of the additional productivity in May is thus unclear.

To speak to these climatologies in a statistical framework (summarized in Table 3.4 below), a Taylor diagram (Taylor 2001) as used in section 2.8.2 might be appropriate, except that the pattern cross-correlations are dominated by the model artifact. It is easy to see in these figures that MODIS predicts stronger northward blooms, while the ROMS artifact lies to the south; thus, the cross-correlations are uniformly negative. The normalized standard deviations of the model as compared to MODIS are somewhat more interesting. Recall that for normalized standard deviations, a value of 1 indicates that the model result variability is equal to the satellite data variability. In November, December, January, February, May, and June, the model with the river exhibits variability more similar to MODIS than the model without; this does not hold for March and April. In the winter months, the model is overly variable as compared to MODIS; this reverses in spring, with the advent of upwelling, which is as noted previously not well-reproduced in the model’s biological response.

Table 3.4: Pattern cross-correlation values (R) and normalized standard deviations for the November-June model climatologies (2002-2010) as compared to MODIS climatologies over the same period.

Model	R	Ratio = var(model)/var(sat)
November Climatology w/River	-0.13	1.6513885753
November Climatology w/o River	-0.04	1.9936780312
December Climatology w/River	-0.25	1.1220779221
December Climatology w/o River	-0.225	1.3428571429
January Climatology w/River	-0.413	1.1531531532
January Climatology w/o River	-0.409	1.4774774775
February Climatology w/River	-0.322	1.7080924855
February Climatology w/o River	-0.463	1.9161849711
March Climatology w/River	-0.207	0.6755373593
March Climatology w/o River	-0.399	0.747185261
April Climatology w/River	-0.292	0.4810539523
April Climatology w/o River	-0.3008	0.5803011292
May Climatology w/River	-0.316	0.2946175637
May Climatology w/o River	-0.46	0.2507082153
June Climatology w/River	-0.46	0.2077294686
June Climatology w/o River	-0.59	0.1542540371

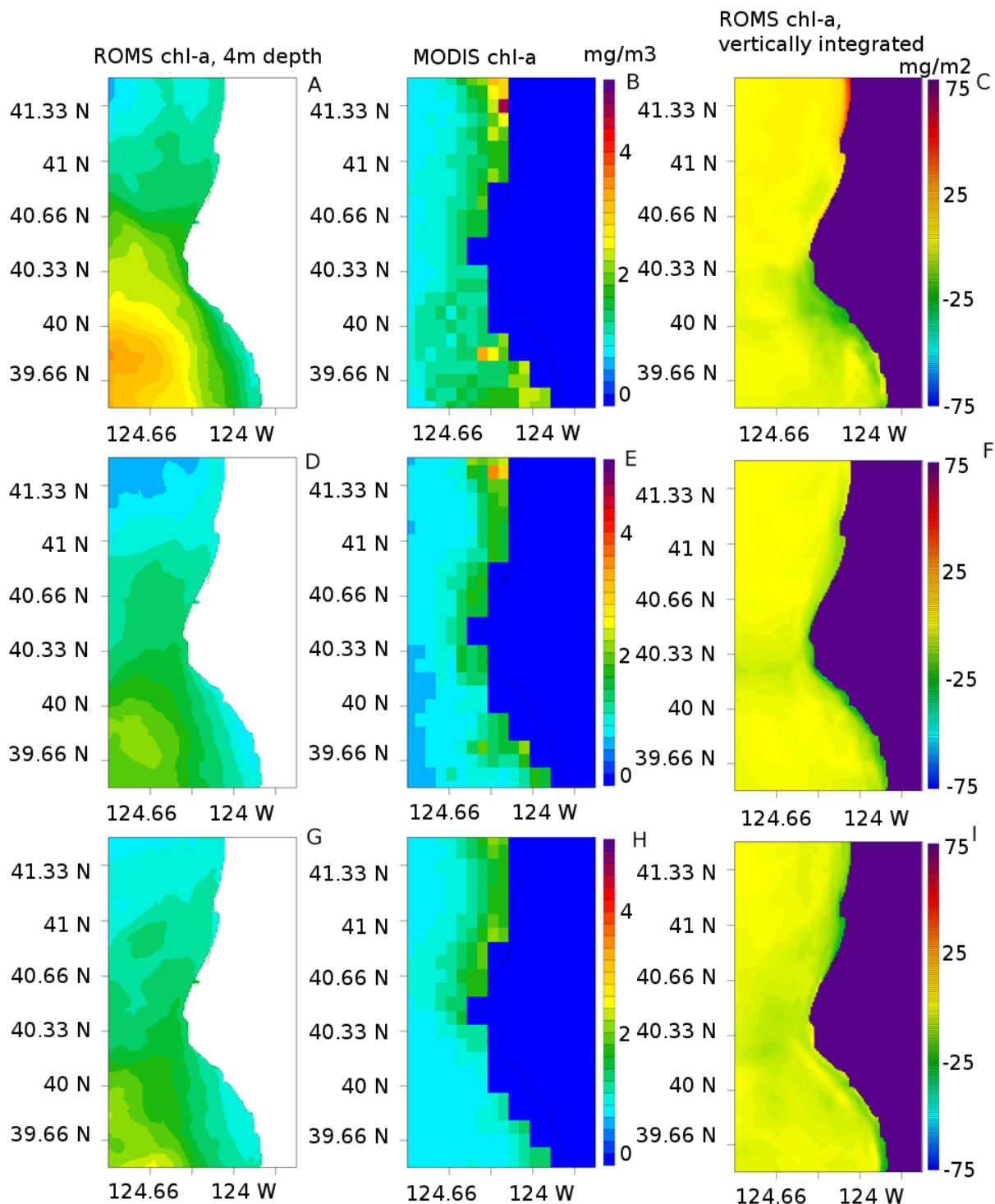


Figure 3.3: ROMS chlorophyll climatologies (A, D, G), MODIS (NASA 2013) chlorophyll climatologies (B, E, H), and the ROMS climatology integrated vertically across the water column, for water years 2002-2010, with the no-river model control subtracted off (C, F, I). Monthly climatologies are sorted by row for **November** (top), **December** (middle) and **January** (bottom). Units are mg chl-a per cubic meter (square meter, in the case of the integration).

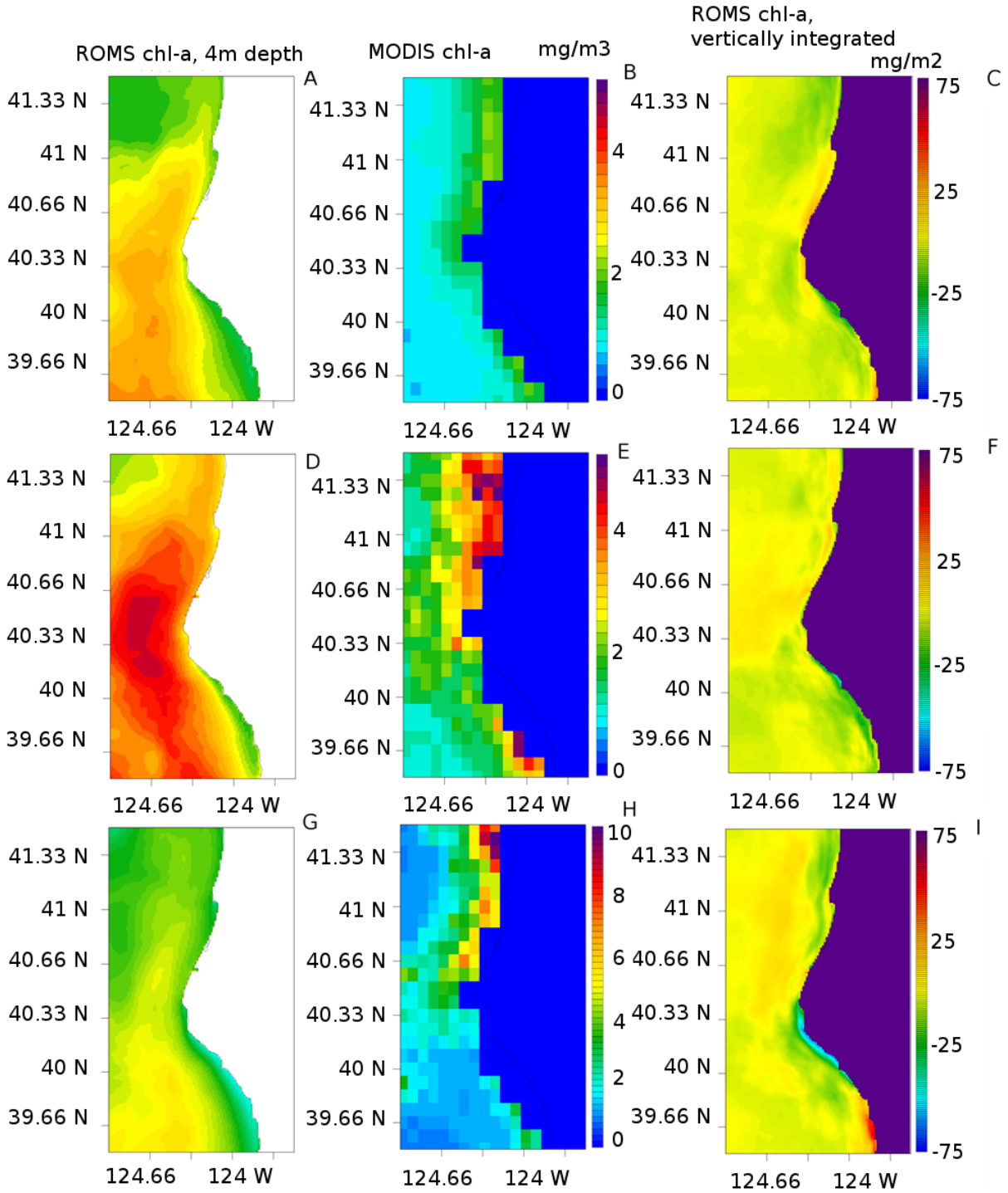


Figure 3.4: ROMS chlorophyll climatologies (A, D, G), MODIS chlorophyll climatologies (B, E, H), and the ROMS climatology integrated vertically across the water column, for water years 2002-2010, with the no-river model control subtracted off (C, F, I). Monthly climatologies are sorted by row for **February** (top), **March** (middle) and **April** (bottom). Units are mg chl-a per cubic meter (square meter, in the case of the integration).

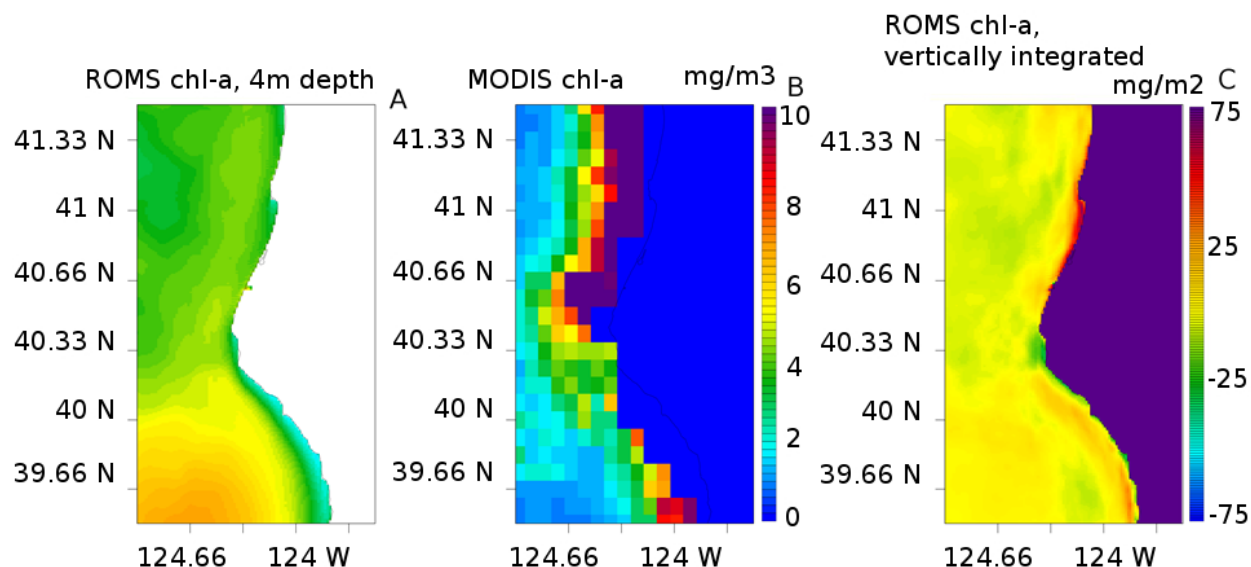


Figure 3.5: ROMS chlorophyll climatology (A), MODIS chlorophyll climatology (B), and the ROMS climatology integrated vertically across the water column, for water years 2002-2010, with the no-river model control subtracted off (C). Climatologies are for the month of **May**, the latest month in which significant Eel river discharge is found to ever occur from 2000-2010. Units are mg chl-a per cubic meter (square meter, in the case of the integration).

3.4 Interannual Variability Comparisons

In order to consider interannual variability of coastal ocean productivity as potentially driven by riverine impacts, the set of December results from 2002-2009 is analyzed correlatively, as well as direct comparisons of specific years of interest that span a range of river conditions.

3.4.1 Correlative analysis of December 2002-2009

The balance between nutrients and light drives the biology of phytoplankton in the mixed layer. As winter sets in, turbulence deepens the mixed layer, increasing its nutrient concentration but also the amount of time that phytoplankton spend below the euphotic zone. When the mixed layer shallows, there is an opportunity for growth dependent on these nutrients, until they become depleted (Mann and Lazier 2006).

The model's behavior in December reproduces this basic premise. A station at 40.65 N, -124.36 W (which is five kilometers north of the modeled river channel, with an ocean depth of 290m) is examined across all Decembers. As Table 3.5 shows, in 2002, 2005, 2006 and 2008, a relatively shallow mixed layer is already present at the beginning of the month along with a phytoplankton maximum, and phytoplankton concentration declines as the mixed layer deepens with the onset of winter storms. In 2003, 2004, and 2009, phytoplankton concentration increases in mid-December as the mixed layer shallows. And in 2007, phytoplankton concentration is markedly lower throughout the month compared to all other years, and declines throughout the month independently of mixed layer depth.

Table 3.5: December mixed layer depths and maximum phytoplankton concentrations at 40.64 N, -124.36 W, ocean depth 290m.

Year-Day of year	Mixed Layer Depth (m)	Maximum Phytoplankton Concentration (mmol-N/m ³)
2002-337	21	3.3
2002-345	40	2.75
2002-353	40	2.6
2002-361	40	1.7
2003-337	40	2.65
2003-345	10	4.1
2003-353	10	5
2003-361	21	4.74
2004-337	21	2.25
2004-345	14.5	5.1
2004-353	10	1.7
2004-361	21	3.75
2005-337	14.5	6.9
2005-345	14.5	6.9
2005-353	112	1.56
2005-361	80	1
2006-337	14.5	6.3
2006-345	21	5.25
2006-353	28	3.6
2006-361	14.5	3.4
2007-337	60	1.05
2007-345	28	0.66
2007-353	28	0.66
2007-361	40	0.32
2008-337	10	5.3
2008-345	10	3.25
2008-353	14.5	2.8
2008-361	21	2.8
2009-337	14.5	1.5
2009-345	10	4.25
2009-353	10	5.1
2009-361	10	4.3
Average	26.359375	3.329375

Figure 3.6 (below) plots a variety of potentially relevant parameters to phytoplankton concentration against each other. Surface stress (from strong winds) deepens the mixed layer through generation of turbulence; shortwave radiation flux provides (or limits) the light on which the phytoplankton can grow; if mean river discharge were strongly correlated with any quantity, that would of course be compelling, and mixed layer depth and phytoplankton concentration are

also plotted directly. In no cases is the R^2 value significant. However, as these data points are created by (and potentially controlled by) different conditions from year to year, we can still glean some insight by examining what patterns exist within the plots.

Figure 3.6.E shows the December relationships between mixed layer depth and phytoplankton concentration. While phytoplankton concentrations vary widely in the shallow mixed layer, the higher concentrations (3 mmol-N/m^3) are only reached in shallow conditions. Note that for the purposes of this study, mixed layer depth was defined as the lowest point of near-constant phytoplankton production, before it sharply falls off in response to physical stratification.

The most rudimentary expectation of the application of freshwater coastal runoff to the ocean is that runoff will make the surface layer more buoyant, preventing mixing, and thus, in light-limited conditions, produce a bloom by increasing the amount of light that phytoplankton in the mixed layer receive on average (Mann and Lazier 2006). However, Figure 3.6.B demonstrates the opposite behavior: in the seven cases of mean river discharge above 20,000 cubic feet per second, five coincide with conditions at or above the 78th percentile of mixed layer depth (thus comprising 5/8ths of the 78th percentile, as there are 8 cases total); these same five cases have phytoplankton concentrations well below average for the month (Figure 3.6.D).

Deeper (40+ meters) mixed layers universally coincide with below-average shortwave radiation (more clouds; see Figure 3.6.C), and near-universally with higher surface stress (more wind; see Figure 3.6.A) which, when considered in combination with the timing of discharge, is equivalent to saying that *the same storm events that produce Eel plumes are also deepening the mixed layer through turbulence*. Thus it appears the effect of the deeper mixed layer dominates the biogeochemistry of the water column, as compared to the effect of the river plume. Another reason plumes may fail to significantly buoy the mixed layer is thermal: in December, the modeled Eel River delivers a plume of 9.6 degrees Celsius (see Chapter 2.5.11), but average sea surface temperature is nearly 9.8 Celsius, and can range as high as 11.8. This further offsets the effect of the lower salinity by increasing plume water density. Furthermore, the location of the station at which this data are collected and compared is 5 km north of the Eel River mouth, meaning that the plume it sees has transported (and entrained ocean water) over a considerable distance. This was deliberate, in order to separate these events out from the effect of low-level continuous delivery of seawater to the ocean, but it does mean examination of specifically far-field plume effects. Finally, timescale is a consideration: due to the comparison to the MODIS 8-day averages, the most extreme, short-term behavior is lost, if a given plume is only in play for one or two days in a snapshot of eight; much of its momentary effect is averaged away in the results we see. For further discussion of buoyancy and river plume anatomy, see section 3.10.

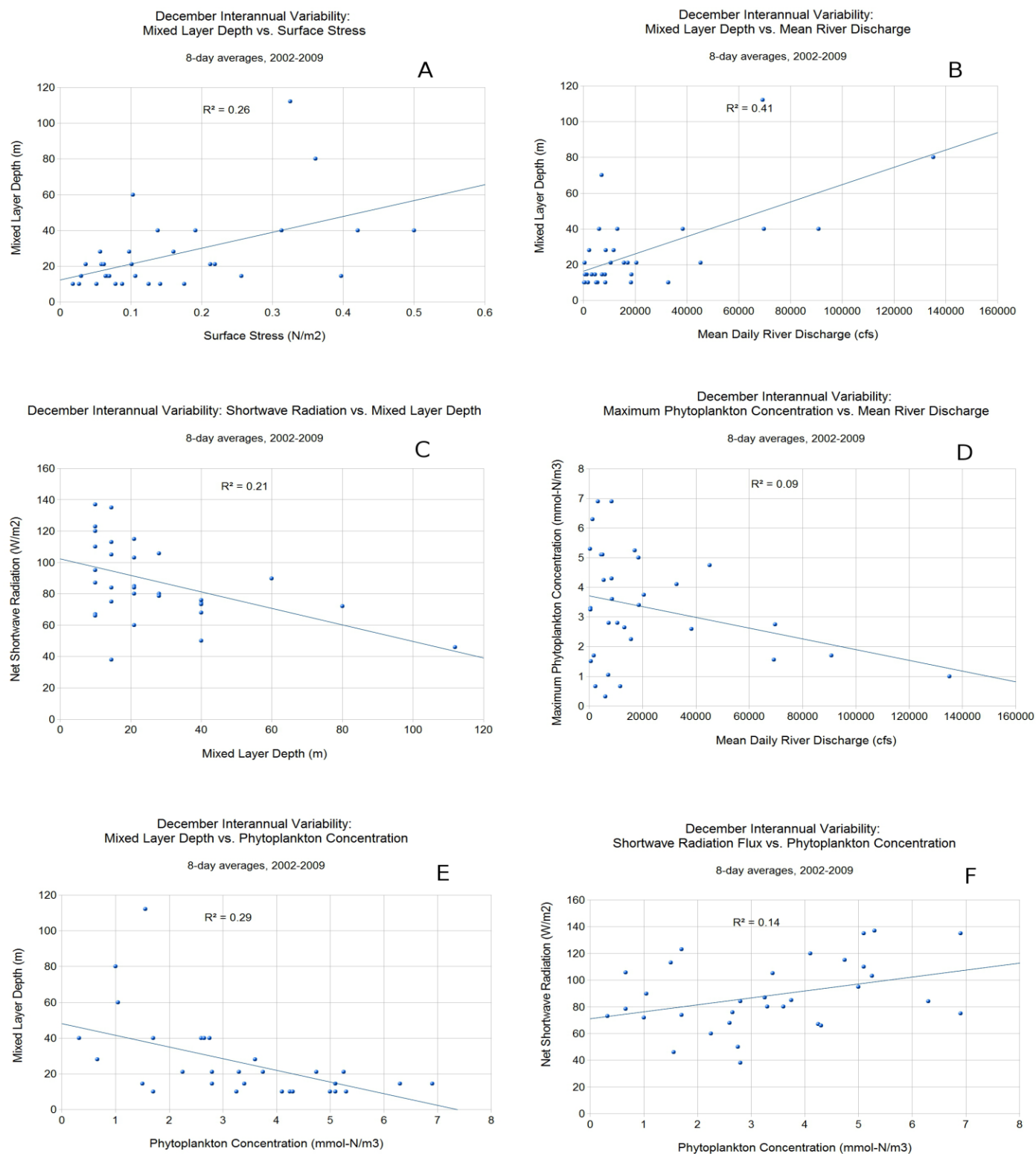


Figure 3.6: Correlations between mixed layer depth and A: surface stress, B: mean river discharge, C: shortwave radiation, and E: phytoplankton concentration, as well as phytoplankton concentration vs. D: mean river discharge and F: shortwave radiation flux.

3.4.2 Empirical Orthogonal Function analysis of December Interannual Variability

Taking the eight Decembers as a single time series and applying empirical orthogonal function analysis (summarized in Figure 3.7, left), we find a strong resemblance between EOF 1 and the climatological mean (previously shown in Figure 3.3), including anomalous blooms to the south of the cape. EOF 2 further captures this behavior, maximized right over the problematic Mendocino scarp (discussed in section 3.9). It is reasonable that the largest EOFs bear little to no resemblance to the riverine signal sought after. Chapter 1 demonstrated in detail that whatever impact the Eel River has on coastal ocean productivity, it is small, largely overpowered by other processes.

And after removing those two larger modes, EOF 3, accounting for nine percent of the variability, is a clearly northern signal, centered near the mouth of the river. 9% is a similar magnitude to the climatological impact of the river on water column productivity in section 3.3. Upon examination of the time amplitudes of each of these functions (Figure 3.7, right), the third bears some resemblance to the time series of river discharge (Figure 3.8.A), with its consistently positive anomalies in the first half of the decade, and consistently negative anomalies in the second half. The El Niño Southern Oscillation is a large signal capable of governing interannual variability, charted by NOAA 2014b and reproduced here in Figure 3.8.B; while it bears some resemblance to EOF1, they lack sufficient coherency to readily attribute the variability there. Similarly, the Pacific Decadal Oscillation, charted by (Mantua 2014) and reproduced in Figure 3.8.C has some coherency with EOF3 in the first half of the decade, but ceases to be a good predictor over the entire decade.

Across these last two sections, it is very difficult to find strong correlations between river discharge and coastal ocean productivity. Model artifacts dominate much of the behavior, particularly offshore and south of the cape; still, it is possible that the river drives a smaller mode of variability. Near-shore (such as the station studied in 3.4.1) behavior appears to be driven by many different forces, with riverine impacts largely subsumed by the effect of the mixed layer depth, as deepened by the storm events that created river discharge in the first place. Given the great interannual variability in conditions, and the relative lack of insight gained statistically, the next step to improve understanding is to look at particular Decembers in years of interest.

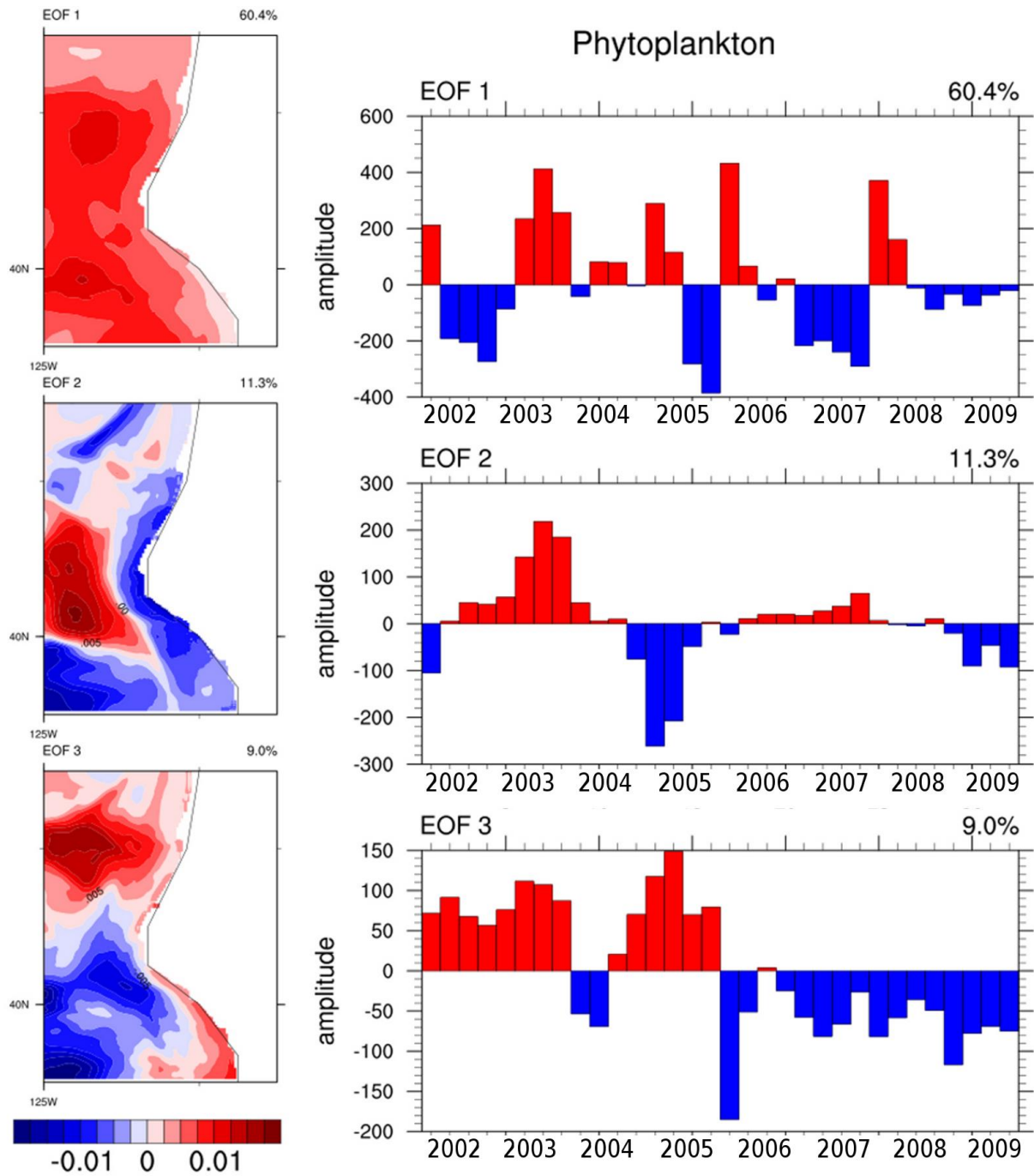


Figure 3.7: The first three empirical orthogonal functions of the 32-point time series comprised of four 8-day averages per December from 2002-2009, and their variation in time of amplitude.

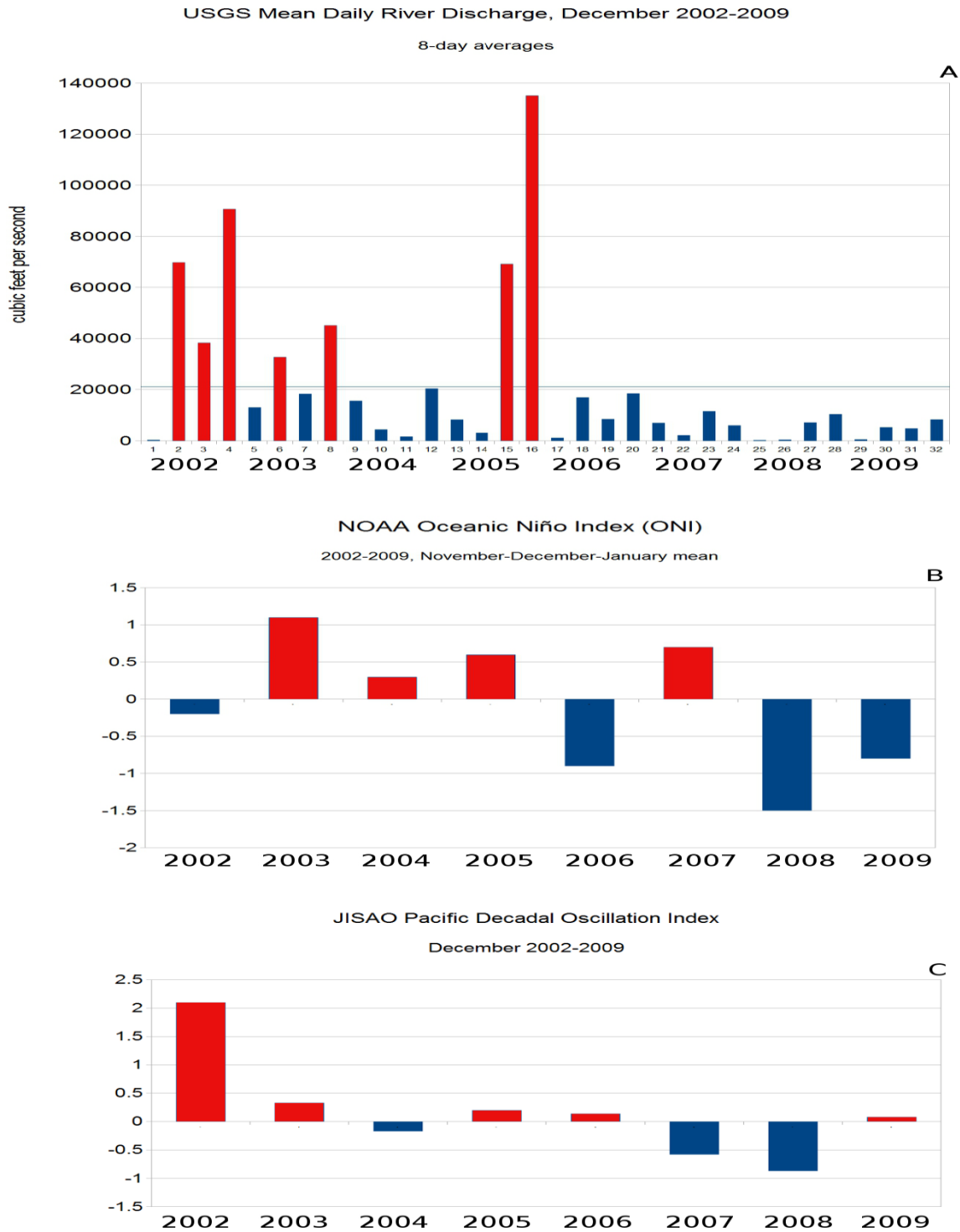


Figure 3.8: 8-day averaged time series of Eel River discharge (A), annual Oceanic Niño Index (B) and Pacific Decadal Oscillation (C) for December 2002-2009. Red and blue bars are positive and negative anomalies respectively; for discharge, above and below the mean value line (~20,000 cfs).

3.4.3 Comparison of Decembers with varying river conditions

To look more closely at possible effects of the river in December, 2003 (moderate discharge), 2005 (extreme discharge) and 2008 (minimal discharge) provide a wide variety of conditions. As Figure 3.9 demonstrates, 2003 had discrete discharge events spread throughout the month, on December 7, 11, 14, 21, 25, and 30. 2008 had minimal discharge until December 22, and then three very modest discharge events before the end of the month. 2005 begins with a discharge event on December 2, and then has minimal discharge until December 19, during which discharge is continuously elevated and reaches the maximum of the entire decade on December 31. 2003 and 2005 also have out-of-phase discharge events during the first two thirds of the month, further increasing their potential for comparison.

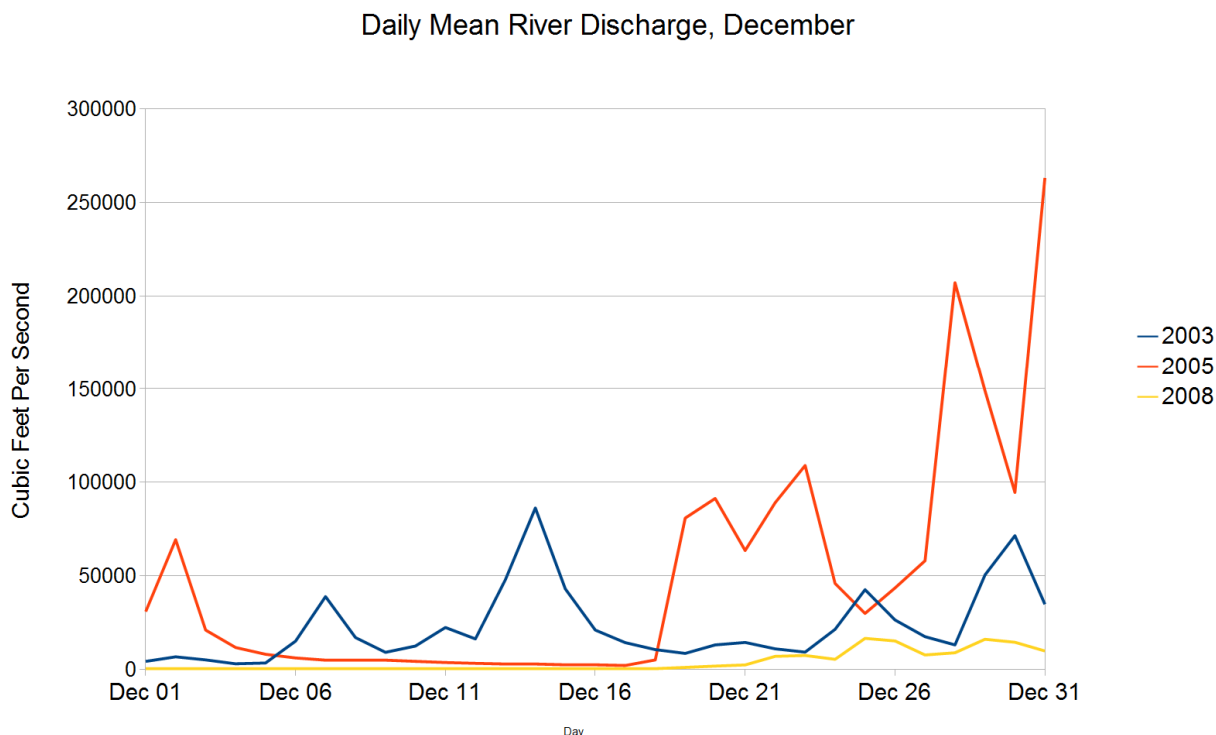


Figure 3.9: Daily mean Eel River discharge for December 2003, 2005 and 2008.

These Decembers also have markedly different phytoplankton timing and magnitudes. Figure 3.10 shows the estimates of chlorophyll-a concentration as seen by MODIS. In 2003, a distinct bloom arises, then fades, in the middle two weeks of the month. In 2005, the chlorophyll is at its maximum at the beginning of the month, then declines. And in 2008, an initial chlorophyll bloom fades to minimal activity by the third week, only for a new bloom to appear at the end of the month.

The timing of the 2003 bloom coincides well with the maximum river discharge (and a general period of river activity), but river discharge at the end of the month does not cause the bloom to sustain. In 2005, a river event occurs at the beginning of the month, coinciding with the phytoplankton maximum, but the decline thereafter accelerates as the extreme discharge arrives.

And in 2008, the initial bloom is clearly river-independent, but the final bloom does coincide with the small discharge events at the end of the month. But is this a real connection, or only coincidence? To examine possible effects of the river during this period, we turn to the model results.

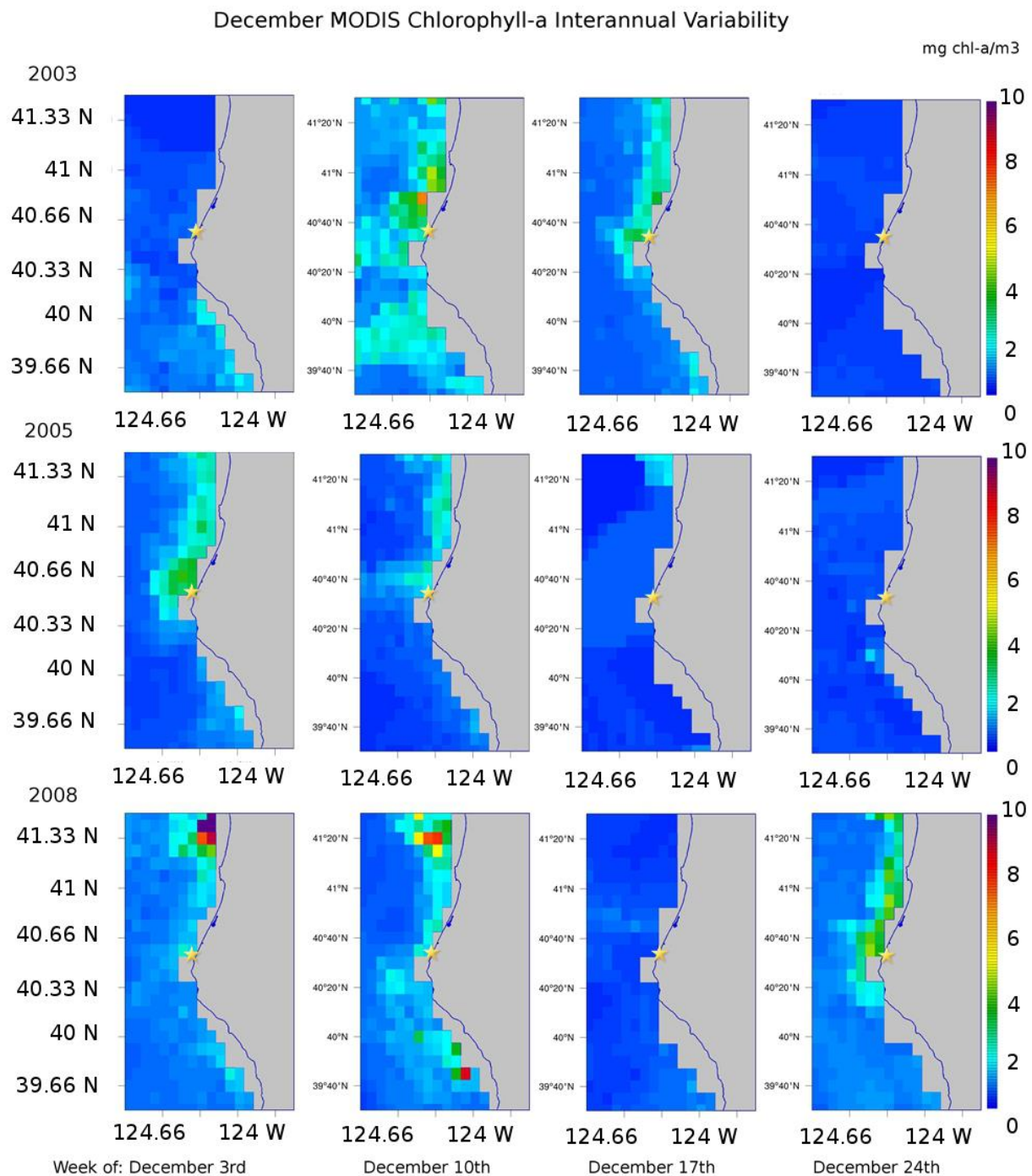


Figure 3.10: 8-day average chlorophyll-a concentrations as seen from space by MODIS (NASA 2013) for Decembers of interest: 2003, 2005 and 2008. The mouth of the Eel River is starred.

Figures 3.11, 3.12 and 3.13 show the model's reproduction of each of these respective years, with chlorophyll mapped horizontally for direct comparison with MODIS (Figure 3.10). In order to closely examine possible physical effects of the river, a vertical transect in phytoplankton, salinity, temperature and meridional velocity is taken at 40.64 N, five kilometers north of the river channel, with the no-river model control subtracted from the fully coupled modeling framework. Overall, the model roughly reproduces the timing and magnitude of bloom dynamics in 11/12 of these timepoints – the bloom appears at the right time, with roughly the right magnitude -- with the single major difference being the 2008 bloom that initiates in the week of December 24th, which is not produced by the model at all. Notably, the model tends to produce a bloom south of Cape Mendocino which is not present in the data (produced by the southern boundary artifact described in Chapter 3.9), and the blooms north of the cape often persist further offshore than the data would indicate.

2003

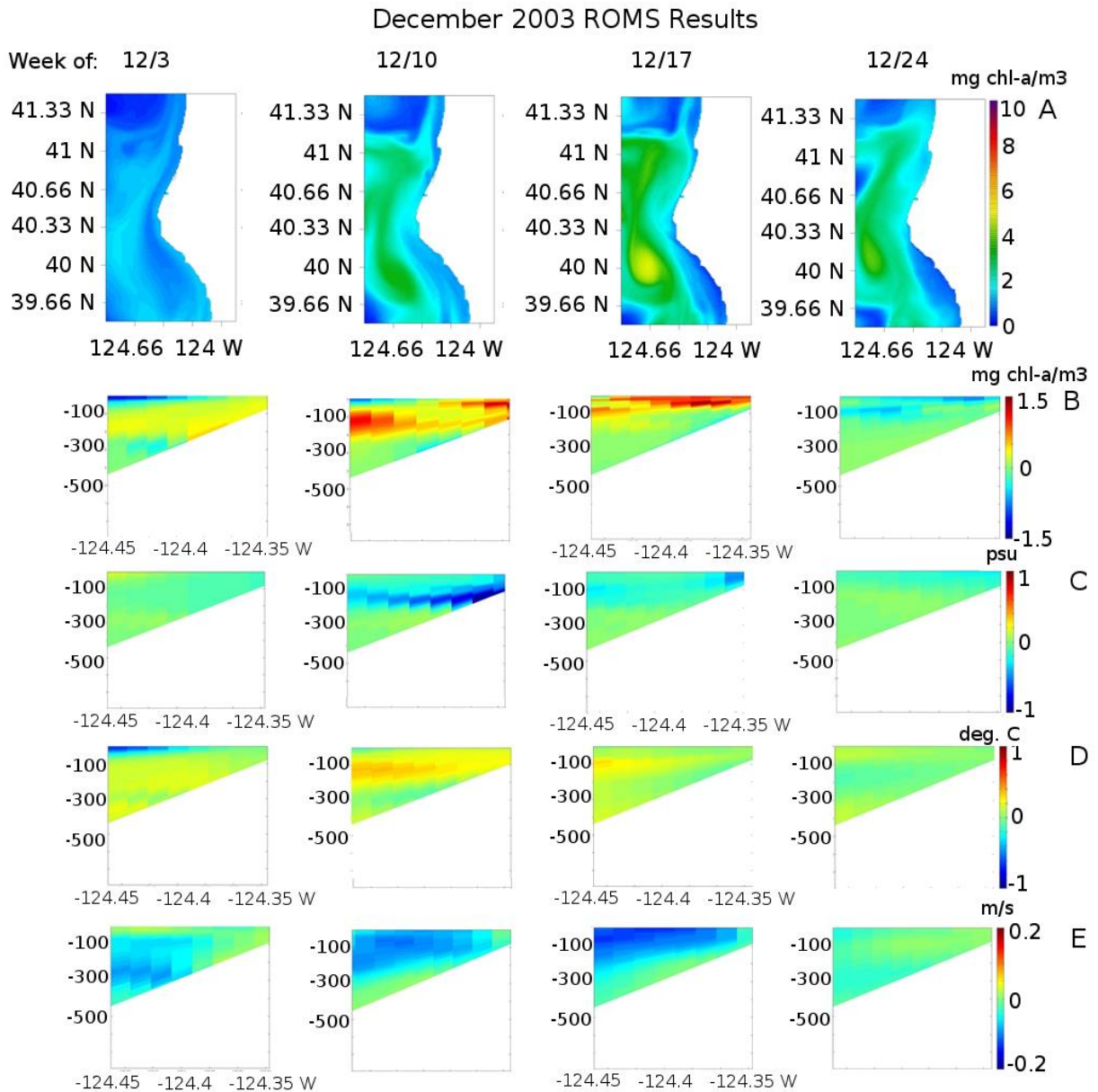


Figure 3.11: 8-day averaged model results for December 2003. A: Chlorophyll at 4m depth produced by the fully coupled modeling framework. B-E: Vertical transect of the model at 40.64 N, out to 10 km offshore, with the no-river control subtracted from the full model, for chlorophyll (B), salinity (C), temperature (D) and meridional velocity (E).

In 2003, the model correctly simulates little phytoplankton production in the first week of December, and then a roughly accurate bloom in the second. In the MODIS results, that bloom is in decline and isolated north of the cape in the third week, but in the model it is reaching its maximum, and is distributed both to the north and south of the cape, consistent with the climatological tendency for the model to concentrate blooms south of the cape that are not present in reality. Interestingly, though the bloom begins to decline, it retains a clear presence in the fourth week, whereas in reality it has been reduced to nearly zero. Still, in the time

derivative sense, the model is capturing the MODIS data's increase and subsequent decrease of phytoplankton, only more slowly. Statistically speaking, the cross-correlation value begins very positively, then declines throughout the month as the model results retain a bloom that has vanished within MODIS. The model variability overestimates MODIS variability throughout December 2003, but much more extremely in the latter half of the month with the persistent bloom. The often extreme differences in R values between the model with and without the river included are explained by the presence of the model artifact to the south of the cape; noise essentially random in nature, the artifact providing more or less concentration at a given time point can substantially alter the similarity of the model field to MODIS.

Table 3.6: Pattern cross-correlation (R) values and normalized standard deviation comparisons between December 2003 model results and MODIS data.

Model and week within December 2003	R	Normalized standard deviation
1 st week, w/river	0.529	1.2791666667
1 st week, w/o river	0.576	1.5416666667
2 nd week, w/river	0.02	1.184
2 nd week, w/o river	0.008	1.344
3 rd week, w/river	-0.398	2.5
3 rd week, w/o river	-0.348	2.4285714286
4 th week, w/river	-0.04	12.6666666667
4 th week, w/o river	0.3	12.6666666667

Vertically, even though the river has yet to have a major discharge event in the first week, there is the presence of a layer of slightly warmer, lower-salinity water in which there is slightly more phytoplankton than in the model sans river. At about -124.4 W, four kilometers offshore, the mixed layer in the no-river control is warmer, with a bloom that is not present in the with-river version. The meridional velocity flows more strongly to the north beneath this more distinct no-river thermocline.

In the second week, the effect of the river is visible, with lower-salinity water appearing to concentrate onshore and penetrate outwards in a layer up to 200m deep with a minimum salinity closer to 100m depth. The positive temperature anomaly caused by this layer relative to the no-river control is roughly twice as strong as the previous week, and phytoplankton grow to double the magnitude of the no-river control. This effect is near the surface within three kilometers of shore, with a second positive anomaly at eight kilometers and 150m depth, neatly following the low-salinity plume. The difference in meridional velocity is similar to the previous week, and though it is slightly intensified and elevated in depth, it is difficult to tell if this was induced by the river or simply a longer-term physical (or numerical) difference (see section 3.9). In the third week, this warmer low-salinity layer persists (if lessened in magnitude), and the bloom has intensified, particularly at the surface of the water column. Meridional velocity in the no-river control is now markedly stronger than in the fully coupled framework, in a layer of up to 200m depth.

The effect of the river declines in the final week, along with the expected reversal of the bloom anomaly; keeping in mind that this bloom has already declined much further in the MODIS data, it exists more strongly in the model without the river than in the one with it. The lower-salinity water onshore has nearly returned to pre-significant river discharge differences, with negligible differences in temperature. The momentum anomaly has also declined, though it retains its negative bias.

2005

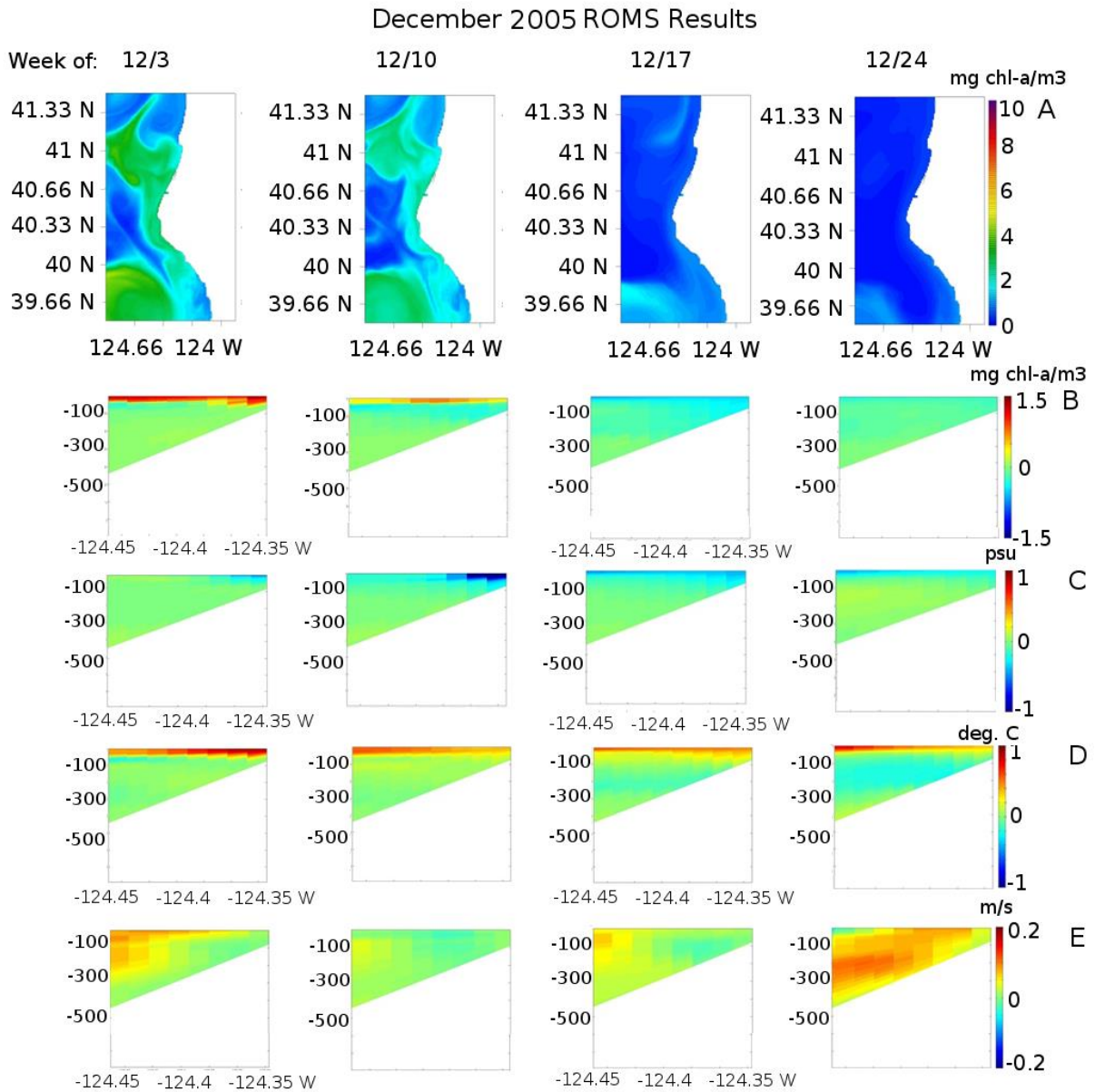


Figure 3.12: 8-day averaged model results for December 2005. A: Chlorophyll at 4m depth produced by the fully coupled modeling framework. B-E: Vertical transect of the model at 40.64 N, out to 10 km offshore, with the no-river control subtracted from the full model, for chlorophyll (B), salinity (C), temperature (D) and meridional velocity (E).

In 2005, the model reproduces the northern bloom present at the start of the month, which declines both spatially and temporally as indicated by the MODIS results. There is an offshore southern bloom consistent with the climatological anomaly, and it declines as well. R values improve throughout the month as the presence of the bloom (and its model artifact-driven concentration to the south of the cape) declines. However, even at its best in the fourth week, the model exhibits three times as much variability as the MODIS data. This can be taken with

caution, however, since in both cases it is comparing values very near zero (as little is going on in either the model or the results).

Table 3.7: Pattern cross-correlation (R) values and normalized standard deviation comparisons between December 2005 model results and MODIS data.

Model and week within December 2003	R	Normalized standard deviation
1 st week, w/river	-0.06	1.8214285714
1 st week, w/o river	-0.56	2.1071428571
2 nd week, w/river	-0.2	2
2 nd week, w/o river	-0.42	2.2162162162
3 rd week, w/river	-0.05	1.7142857143
3 rd week, w/o river	0.21	1.2857142857
4 th week, w/river	0.18	2.875
4 th week, w/o river	0.22	2.75

With the river present (and there is a significant river discharge at the beginning of the month), the mixed layer at the surface has a stronger phytoplankton bloom than is present in the control (though it must be remembered that all of these magnitudes are very small). This layer has slightly lower salinity and is up to 1 degree warmer, with a now positive momentum anomaly. Its strength is partially, but not entirely, due to longer-term model differences than the discrete river event.

Throughout the next three weeks, the surface of the mixed layer remains warmer and lighter due to the presence of the river, with the low-salinity layer expanding further offshore and down to 100m depth. Although the mixed layer retains a heat anomaly and salinity anomaly near the surface, it is also deepening (presumably due to the extreme storm events throughout the second half of the month), and this river-driven anomaly cannot counterbalance that past the second week (when it does, indeed, appear to cause a phytoplankton bloom that is otherwise both lower concentration and more diffuse throughout a deeper mixed layer in the no-river control). By the third week there is if anything more phytoplankton occurring without the river present, particularly near the surface; the magnitude is a fifth of the positive effect earlier in the month. And in the final week, despite the extreme river discharge, the phytoplankton is functionally identical throughout the water column, and near zero. The positive momentum anomaly coincides with the initial river event, and again at the end of the month, but does not seem spatially correlated with the surface low-salinity layer from the river.

2008

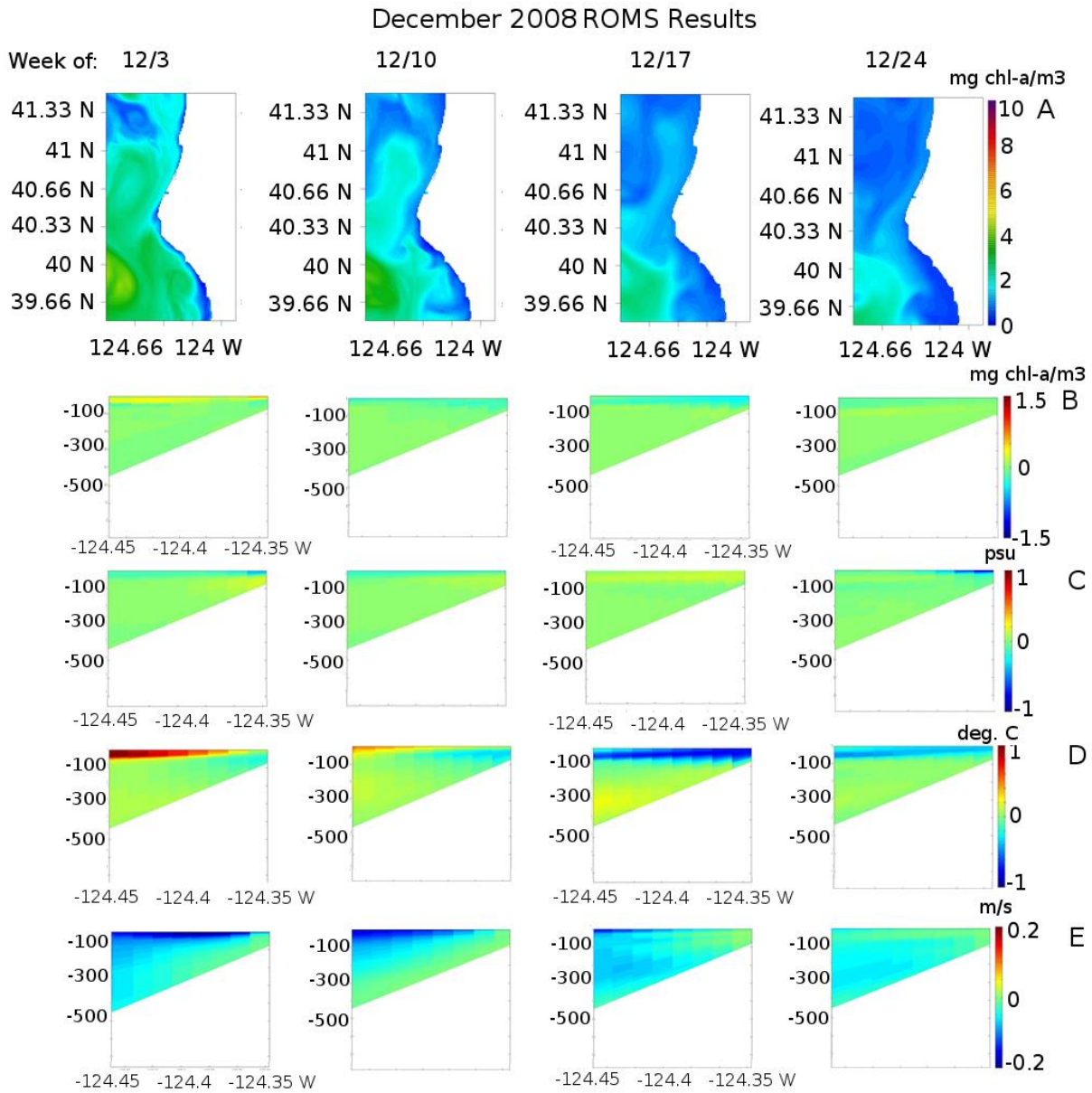


Figure 3.13: 8-day averaged model results for December 2008. A: Chlorophyll at 4m depth produced by the fully coupled modeling framework. B-E: Vertical transect of the model at 40.64 N, out to 10 km offshore, with the no-river control subtracted from the full model, for chlorophyll (B), salinity (C), temperature (D) and meridional velocity (E).

In 2008, the model reproduces a bloom that exists in the first week of December and declines through the third, with the usual concentration south of the cape (as reflected in the negative R values provided in Table 3.8). However, MODIS displays a bloom in the final week that is simply not present in the model, which coincides with the first elevated river discharge in the 2008-2009 water year. The normalized standard deviations, unusually, tend to underestimate MODIS variability early in the month, before overestimating them in the third week and matching them well in the fourth.

Table 3.8: Pattern cross-correlation (R) values and normalized standard deviation comparisons between December 2005 model results and MODIS data.

Model and week within December 2003	R	Normalized standard deviation
1 st week, w/river	-0.15	0.2842465753
1 st week, w/o river	-0.19	0.2431506849
2 nd week, w/river	-0.31	0.9146341463
2 nd week, w/o river	-0.28	0.6707317073
3 rd week, w/river	-0.31	4.9090909091
3 rd week, w/o river	-0.39	4.0909090909
4 th week, w/river	-0.09	0.9285714286
4 th week, w/o river	-0.04	0.9821428571

As the first three weeks in 2008 exhibit minimal river discharge, this provides us with an opportunity to estimate the approximate magnitude of minimal river discharge-driven nonlinear model drift from the no-river control up until, and throughout, the month of December. The phytoplankton are similar throughout the first week, with a small positive bias in the surface in the first week becoming an equally small negative bias by the third. There does appear to be a (-0.2 psu) low-salinity layer present at up to 75m depth, which declines, then inverts to a (+0.1 psu) positive-salinity in the third week. The heat also goes through transition; the mixed layer is up to 1 degree warmer, particularly offshore, in the fully coupled model, and 1 degree warmer in the no-river control by the third week. The extremity of this effect makes it very difficult to justify significant conclusions about heat-driven dynamics in other model years, as they are of the same order of magnitude of the anomalies in 2003 and 2005.

In momentum, the no-river control has a stronger northern current along the surface, which declines throughout the month, including when the river appears in the fourth week, and is unlikely to be a true river impact. However, when the river does appear (easily visible within three kilometers of the coast in the salinity anomaly), there is no apparent effect to the phytoplankton in the model. It is delivering the usual elevated concentrations of detritus and nitrate; the "missing bloom" in the fourth week of December is, perhaps, being driven by some other phenomena. The model mixed layer is deepening throughout the month; it is also possible that it is failing to capture a physically-driven bloom in the fourth week, but as the fourth week coincides with mixed layer-deepening storm events, that seems less likely.

3.4.4 Summary of interannual variability comparisons

In both December 2003 (average river discharge) and 2005 (extreme river discharge), for each 8-day average taken across the vertical transect, there is the presence of a low-salinity, warmer layer of water (which in turn is present at the same time as the first riverine deliveries in each December). Within these layers (e.g., within the plume), the model with the river has up to 40% more phytoplankton concentration than the no-river control. In 2005, at the end of the month (which is when the most extreme riverine delivery of the decade occurred), there is no significant difference in phytoplankton dependent on the presence or absence of the river in the model – the dominant control appears to be something else, surmised to be extreme mixed layer depth

generated by storm wind turbulence. December 2008 (lacking significant river discharge) has little difference between the fully coupled model and the no-river control, except for an up to 1 degree Celsius drift in temperature, which oscillates in either direction over the course of the month. This calls the meaningfulness of the temperature differences in 2003 and 2005 into question, while simultaneously indicating that temperature is not the driver of differences in phytoplankton growth between the fully coupled model and the no-river control. Finally, a small bloom present in the MODIS data at the end of 2008, coincident with the first meaningful discharge event of the water year, is wholly absent in the model. Whether this absence is due to a failure to capture river dynamics in sufficient detail, or for another reason, is unclear.

3.5 Event-driven comparison

To more closely consider the presence and absence of the river in this system, we consider the largest discharge events of each water year. Table 3.9 summarizes conditions during these events from 2002-2010. Note the systematic underestimation of these storm discharge events by HydroTrend, typically by a factor of two. HydroTrend is likely overestimating sediment by the same amount, leading to a roughly accurate estimate then used in the model's estimate of particulate organic nitrogen (see Chapter 2.6.4). However, this insufficient discharge undoubtedly had large physical effects on the modeled plumes, which likely were able to travel over wider areas before losing their form in reality.

Table 3.9: Summary of conditions near the Eel River mouth during the largest discharge event of each water year. **Maxima** and **minima** have been highlighted. Discharge from USGS gauging station @ Scotia (USGS 2012). Precipitation and surface stress from the ERA-Interim Reanalysis (Dee et al. 2011). Sea surface temperature is a model result.

Date	Mean daily discharge (m ³ s): USGS (left) and HydroTrend (right)		Mean sea surface temperature (Celsius)	Daily precip. (inches)	Consecutive days of extreme precipitation	Mean surface zonal stress (N/m ²)	Mean surface meridional stress (N/m ²)
12/16/2002	4899	3816	10.3	1.63	8	0.02	0.4
2/18/2004	4899	2609	10	0.45	6	0.04	0.04
5/19/2005	2172	1165	11.5	0.04	6	0.06	0.05
12/31/2005	7447	3369	10.2	0.53	8	-0.02	0.3
12/27/2006	1696	2637	9.2	0.13	7	0.04	-0.04
1/5/2008	2679	2072	10	0.41	3	0.005	0.3
3/3/2009	1583	1158	9.6	0.5	3	-0.03	0.25
1/26/2010	2282	1880	9.5	0.06	11	-0.04	0.1

A wide variety of conditions are present across these nine water years. In the 2002, 2005 and 2008 water years, onshore stratification in the model has broken down leading to a relatively deep mixed layer, over 100m in all cases. In the 2003, 2004, 2006 and 2009 water years, the water column is much more stratified, and the mixed layer shallow. 2007 lies somewhere in between these two extremes. This is a good first order separation with which to examine events; the second separation is then between the size of river events, since 2008's largest event is five times smaller than 2005's. That gives us four categories, summarized in Table 3.10:

Table 3.10: Categorization of oceanic conditions and relative strength of the largest Eel River discharge event (as Table 3.9) of each water year. Mixed Layer Depth is a model result.

Water Year	Large River Event	Small River Event
Deep Mixed Layer	2002, 2005	2006, 2008
Shallow Mixed Layer	2003	2004, 2007, 2009

Across all events, despite varying seasons, weather conditions, mixed layer depths, and discharge magnitudes, there is one consistent behavior that defines the Eel River's apparent effect on coastal ocean productivity in this modeling framework: during the largest discharge event of each year, in plume-dominated portions of the water column, there is always *simultaneously* less phytoplankton *and* less nitrate than in the no-river control (for a typical example, see Figure 3.14). This is an important result: given that phytoplankton take up nitrate as they grow, the expected result would be to have less available nitrate in the system that has more phytoplankton. For the no-river control to have more phytoplankton and more nitrate at the same time, compared to the same regions under the influence of the plume, implies that the low-nitrate Eel River plume creates nitrate limitation which *inhibits* phytoplankton growth compared to what could have grown in ambient, comparably nitrate-rich ocean conditions untouched by the river. Detritus, the slowly bioavailable biogeochemical tracer, is dominated by phytoplankton growth and mortality rather than riverine delivery, which despite its extremely high estimated quantity (described in Chapter 2), has no visible impact; if riverine detritus is enhancing phytoplankton growth, its effect is heavily outweighed by other considerations (such as nitrate depletion).

This biogeochemical effect occurs under all conditions, but there are different physical plume behaviors observed from year to year. Their overall importance on phytoplankton productivity is outweighed by plume nitrate depletion, but they are still of interest. Model skill also varies, providing insight into ways that the model is failing. These are summarized below, by category. To avoid an overwhelming number of figures, only one event in each category is shown.

3.5.1 Large River, Deep Mixed Layer:

The modeled events in 2002 (not shown) and 2005 (Figure 3.14) both have reasonable model skill at reproducing MODIS results (though as usual the presence of the model artifact makes overall regression values low at best; see Table 3.11). These events were generated by long and extreme storms, creating a deep mixed layer and a great deal of riverine discharge (shown in Table 3.9). Their water columns (at the typical station described in section 3.4.3) have nearly identical thermoclines (at 300m) and pycnoclines (starting at 200m onshore, rising to 100m by ten kilometers offshore). Phytoplankton grow at a roughly constant and low rate, creating a low concentration throughout the water column onshore. This follows the pycnocline, rather than the thermocline, offshore, with a similar depth of about 100m. As is expected, detritus is enhanced by mortality, while nitrate is depleted by growth, within the phytoplankton blooms.

However, there is a notable physical distinction between the two years; in 2002, the region of plume-lowered salinity descends to 150m and is very diffuse, accompanied by a relative warming of that region of the ocean. In 2005, the low-salinity, warmer region is four times more concentrated, and sinks only to an absolute maximum of 100m onshore, shallowing to 50m offshore. Examination of the conditions of each of these two years provides a reasonable explanation: 2002 is the interannual maxima in both precipitation (with 300% of the precipitation on the day of 2005's event) and meridional surface stress (30% more in 2002 than in 2005). In other words, 2002's discharge event occurs during storm conditions of greater intensity, and is mixed into the water column more thoroughly, accordingly. Additionally, 2005 delivers 150% of the freshwater discharge of 2002, increasing the potential for a buoyancy-driven plume to resist turbulent mixing for more of the 8-day average: it is thus much more visible.

Table 3.11: Pattern cross-correlation (R) values and normalized standard deviations for the 8-day averages around 2002 and 2005 events, comparing the model results with to MODIS data.

Date and Model	R	Normalized standard deviation
2002, day 345, w/river	0.158	0.6960784314
2002, day 345, w/o river	-0.211	0.7107843137
2005, day 361, w/river	0.18	2.875
2005, day 361, w/o river	0.22	2.75

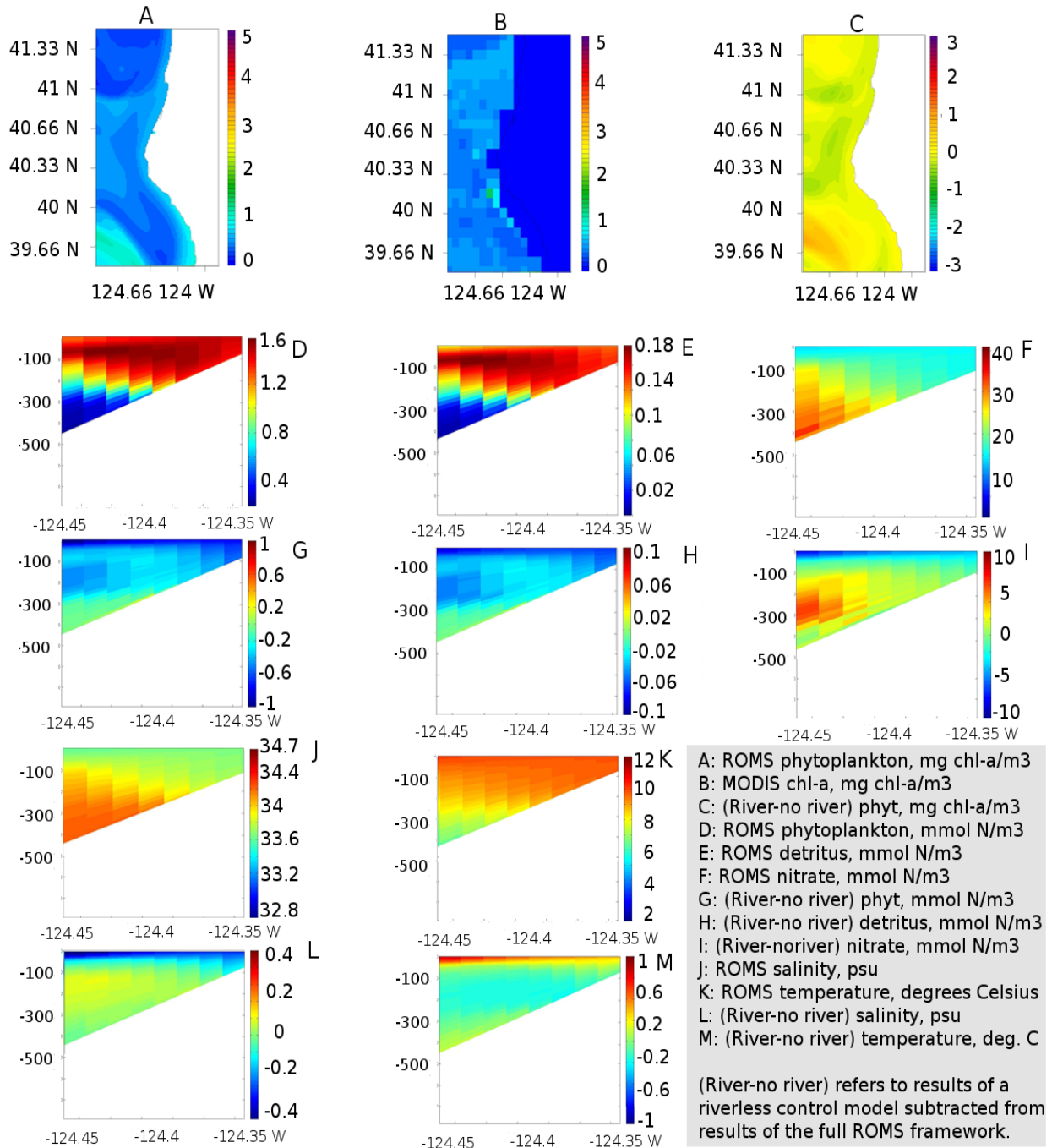


Figure 3.14: 8-day average starting at 12/31/2005, the highest Eel River discharge day in the 2005-2006 water year. A: ROMS phytoplankton. B: MODIS phytoplankton. C: ROMS results minus the no-river control model results for phytoplankton. D, E, F: ROMS phytoplankton, detritus, and nitrate respectively, at a 40.64 vertical transect (5 km north of the Eel River mouth) out to 124.45 W. G, H, I: As D, E, F, with the no-river control subtracted from the results. J, K: ROMS salinity and temperature along the same vertical transect. L, M: As J and K, with the no-river control subtracted from the results.

3.5.2 Small River, Deep Mixed Layer:

2006 (Figure 3.15) and 2008 (not shown) comprise the entries in this category. Both are extremely small river discharge events; 2008 is the smallest of all in the 2002-2009 water year period, occurring after one of the shortest storms. 2006 has the coldest sea surface temperature (with 2008 not far behind), and enjoys the outlier and minima of mean surface meridional stress; the winds are blowing very weakly southward on average, unusual for a December storm event. 2008 has the typical strong northblowing winds of a winter storm event, yet occurs in March, very late in the season.

The low calculated model chlorophyll-a (in 2006) compares well to MODIS data (particularly near the river); 2008 does not compare well, as it includes the presence of a 4 mg chla/m³ bloom all along the modeled coast that is largely not present in the satellite data. This behavior is essentially dominated by the climatological differences discussed in section 3.3, and appears in the differences in normalized standard deviation in Table 3.12; the 2008 modeled bloom not present in MODIS creates great variability, while the 2006 results are roughly accurate in variance, but spatially offset because of the southern model artifact (creating a negative R). In both cases, however, we see the same interesting physical effect: the plume, though far less massive than in 2002 or 2005, is highly concentrated and highly stratified within the water column, essentially floating across the top. The phytoplankton is similarly concentrated at the surface, markedly different from conditions in 2002/2005. Essentially what has happened is that a freshwater plume has entered the ocean during well-mixed but now-calm conditions, and it simply floats on the top, trapping the phytoplankton within a roughly 20m surface layer, where they proceed to grow. Without the presence of the river, the phytoplankton mix more deeply into the water column, but still enjoy more net productivity due to the greater available nitrate. The thermal profile is the opposite of 2002/2005, with the upper region cooler rather than warmer compared to the no-river control; given problems with thermal drift between the fully coupled model and the no-river control (first discussed in 3.3.3 and explored more thoroughly in 3.8), it is difficult to discuss the significance of this, as the magnitude of difference is near the noise threshold defined later in Section 3.9.

Table 3.12: Pattern cross-correlation (R) values and normalized standard deviations for the 8-day averages around 2006 and 2008 (water year; 2008's event falls in early 2009) events, comparing the model results with and without the river with MODIS data.

Date and Model	R	Normalized standard deviation
2009, day 57, w/river	-0.16	3.44
2009, day 57, w/o river	-0.1	4.08
2006, day 361, w/river	-0.38	0.8307692308
2006, day 361, w/o river	-0.12	1.0769230769

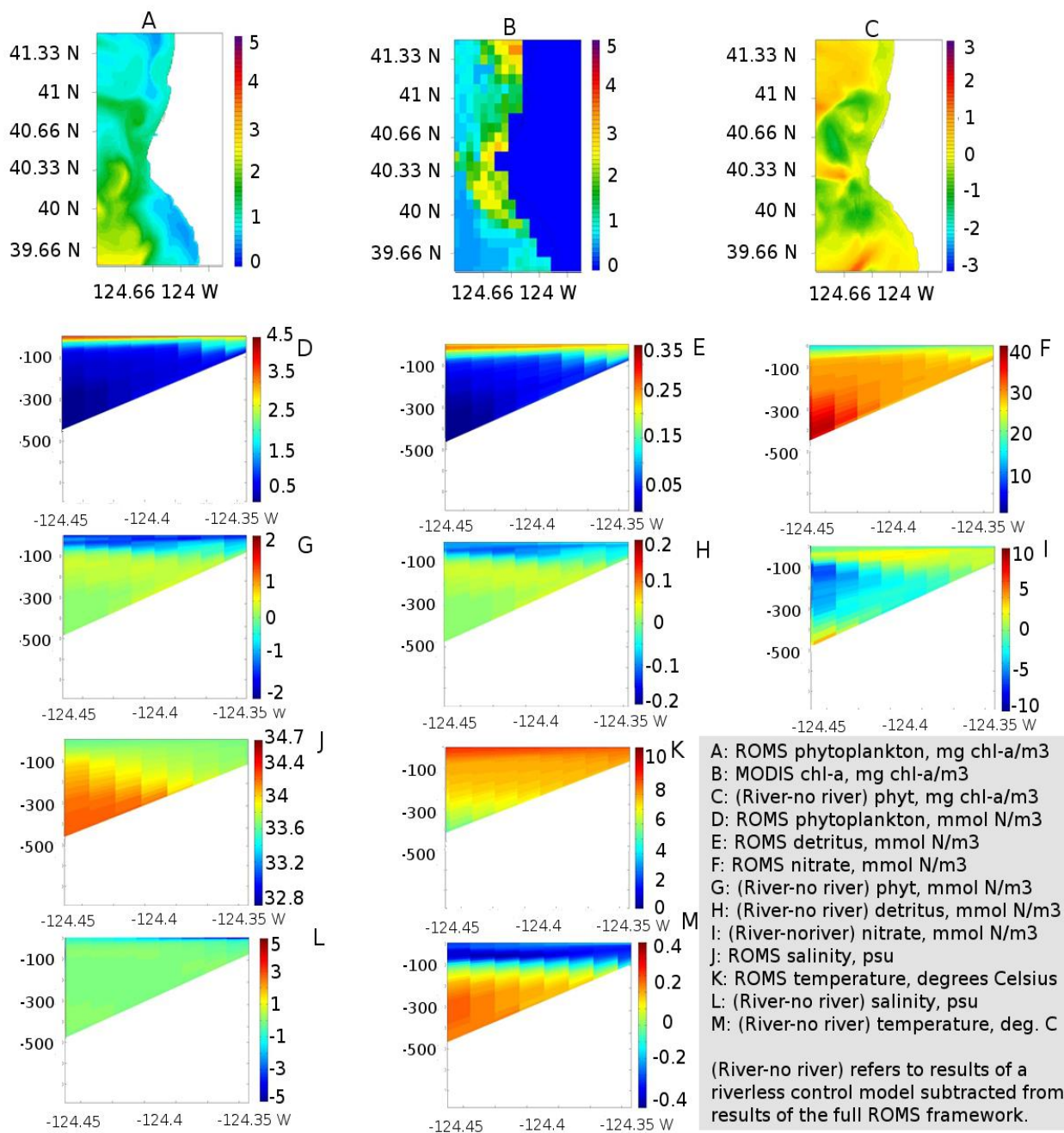


Figure 3.15: As Figure 3.14, for the 8-day average starting at 12/27/2006, the highest Eel River discharge day in the 2006-2007 water year.

3.5.3 Large River, Shallow Mixed Layer

Turning to the years of stratified water column, 2003 (Figure 3.16) has a river event of identical strength as the well-mixed 2002 (whereas the rest of the Shallow Mixed Layer events are, unsurprisingly, years with relatively minor storm events). What has changed between 2002/2005 and 2003 is the timing: it is now February instead of December. As it is February, the surface fields are fairly different (we know from the section 3.3 climatologies that the model overestimates blooms in February), with low R values. The general location of the bloom (as seen in Figure 3.16) is very roughly correct, however, north of the cape – only with the bloom considerably further offshore than in MODIS. February's storm event also has an order of magnitude less meridional stress than December 2002/2005 (see Table 3.13) providing turbulent mixing. The pycnocline, in particular, is quite shallow, with an absolute maximum depth of 100m (whereas in 2002 and 2005 it tended to be twice as deep onshore). Phytoplankton grow strictly above the pycnocline, trapped in that surface layer, with an according increase in detritus and depletion of nitrate. The effect of the river is, in turn, trapped within the same layer, with the same decrease in salinity that we see in 2005. The thermal effect is less consistent, and once again at that level of low significance compared to thermal drift from the no-river control.

The effect of the river on the phytoplankton depth profile is fascinating. The no-river control has up to 30% more growth in the top 20m; then, with the river present, this is reversed down to 100m depth. In other words: without the river, the phytoplankton concentrate much more closely to the surface. With the river present, they seem to mix down throughout the pycnocline more thoroughly. The differences in detritus follow this pattern, but nitrate, notably, does not: as usual, there is relatively more nitrate throughout the no-river pycnocline, implicating the nitrate-depleted freshwater as a relative suppressant of activity. Unlike in December, however, in February there is enough nitrate present in the water column for the with-river phytoplankton to grow anyway -- but not as effectively onshore at the surface, where the cooler river water appears to inhibit growth.

Table 3.13: Pattern cross-correlation (R) values and normalized standard deviations for the 8-day averages around the 2003 (water year; the event occurs in early 2004) event, comparing the model results with and without the river with MODIS data.

Date and Model	R	Normalized standard deviation
2004, day 49, w/river	0.06	2.12
2004, day 49, w/o river	-0.1	2.55

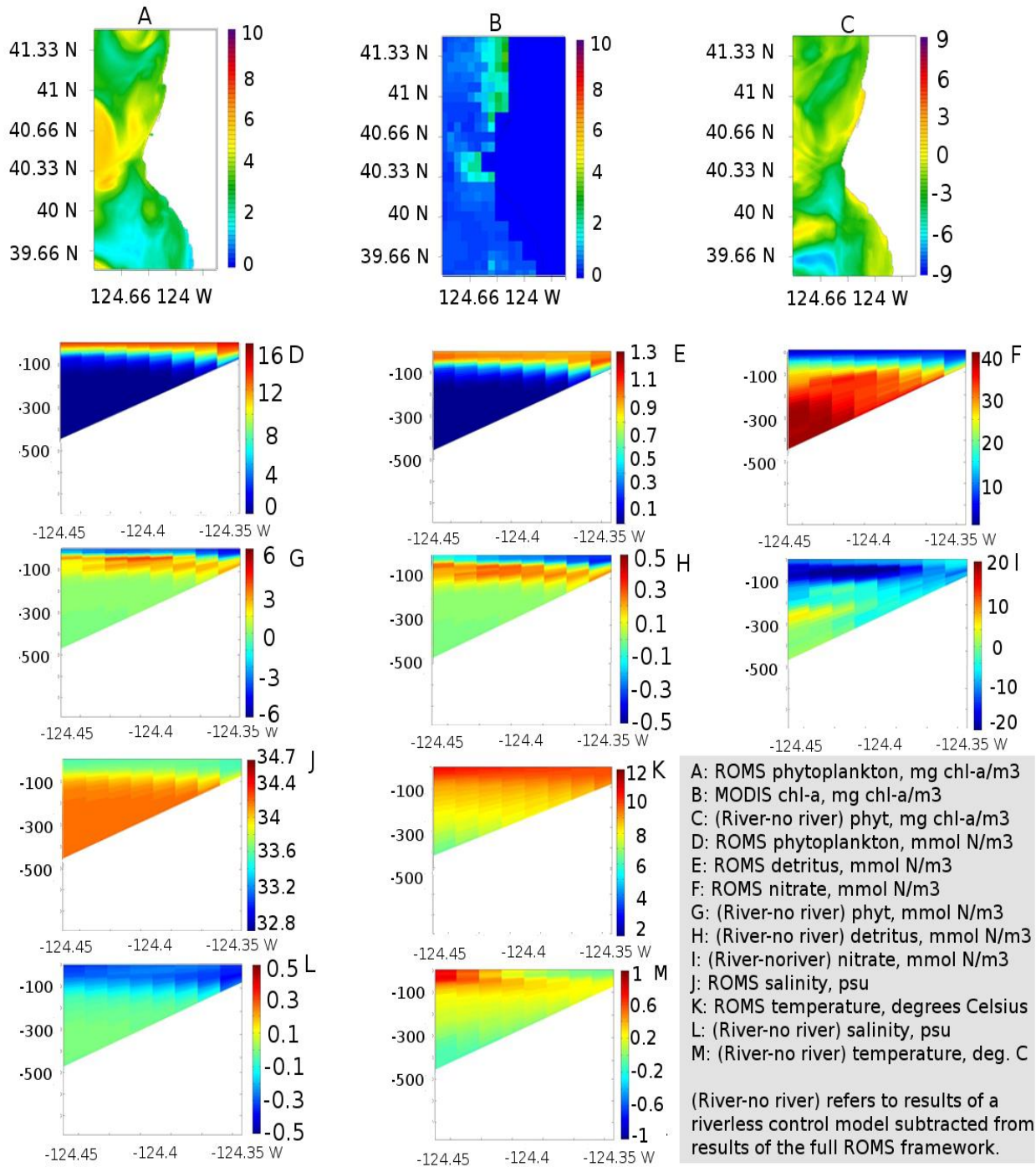


Figure 3.16: As Figure 3.14, for the 8-day average starting at 02/18/2004, the highest Eel River discharge day in the 2003-2004 water year.

3.5.4 Small River, Shallow Mixed Layer

This category is comprised of the drought years where storm (and river) events were small, and the ocean tended to be warm and well-stratified, and so we see a wide degree of variability within it: maximum river events ranging in timing from December to May, entering an ocean with an equally variable state as defined by the season. The event in 2007 (Figure 3.17) occurs at the beginning of January, and is thus directly comparable in season to most of the other events.

2007 has the typical southerly meridional stress of winter storm events, but the river event occurred after a very short storm. 2007 has a notably shallow pycnocline of only 80m, which phytoplankton follows. The river clearly contributes an apparently deepening layer of relatively fresh water as it proceeds offshore, but it is small enough in magnitude that the thermal effects of this especially cold plume (7.9 degrees Celsius, January plumes modeled as two degrees cooler than the December plumes) are not significant.

When discussing the biogeochemistry of this system it's important to start by noting that, correctly reproduced by the model, very little phytoplankton is growing; all magnitudes are small. Still, phytoplankton is clearly suppressed within the low-salinity surface plume. The nitrate profile, unusually, has more nitrate in the with-river model than the no-river control (though only outside of the plume); the small quantity of phytoplankton likely accounts for this difference in behavior, as even at their most distinct, the with-river model and no-river control have less than 1 mg chl_a/m³. The reason for this net positive nitrate is otherwise unclear; it is unique among the events in all four categories, including the other small river, shallow mixed layer events.

As usual, the southern model artifact creates small-to-negative negative R values. In the case of 2007, the very small values within the model create enormous normalized standard deviations, since the artifact's bloom (unreproduced by MODIS), while modest in concentration, is still orders of magnitude more than what's present in the satellite data. 2005's variances are of the same span as MODIS, though this tiny river event occurred during upwelling season and is essentially drowned out by it, while the January 2010 event has similarly small values (and a large, artifact-driven normalized standard deviation).

Table 3.14: Pattern cross-correlation (R) values and normalized standard deviations for the 8-day averages around the 2004, 2007 and 2009 (water year; all events occur in winter-spring of the following year) event, comparing the model results with and without the river with MODIS data.

Date and Model	R	Normalized standard deviation
2005, day 137, w/river	0.18	0.96
2005, day 137, w/o river	0.11	1.08
2008, day 1, w/river	-0.1	6.4
2008, day 1, w/o river	-0.02	5.4
2010, day 25, w/river	0.08	3.11
2010, day 25, w/o river	0.13	2.91

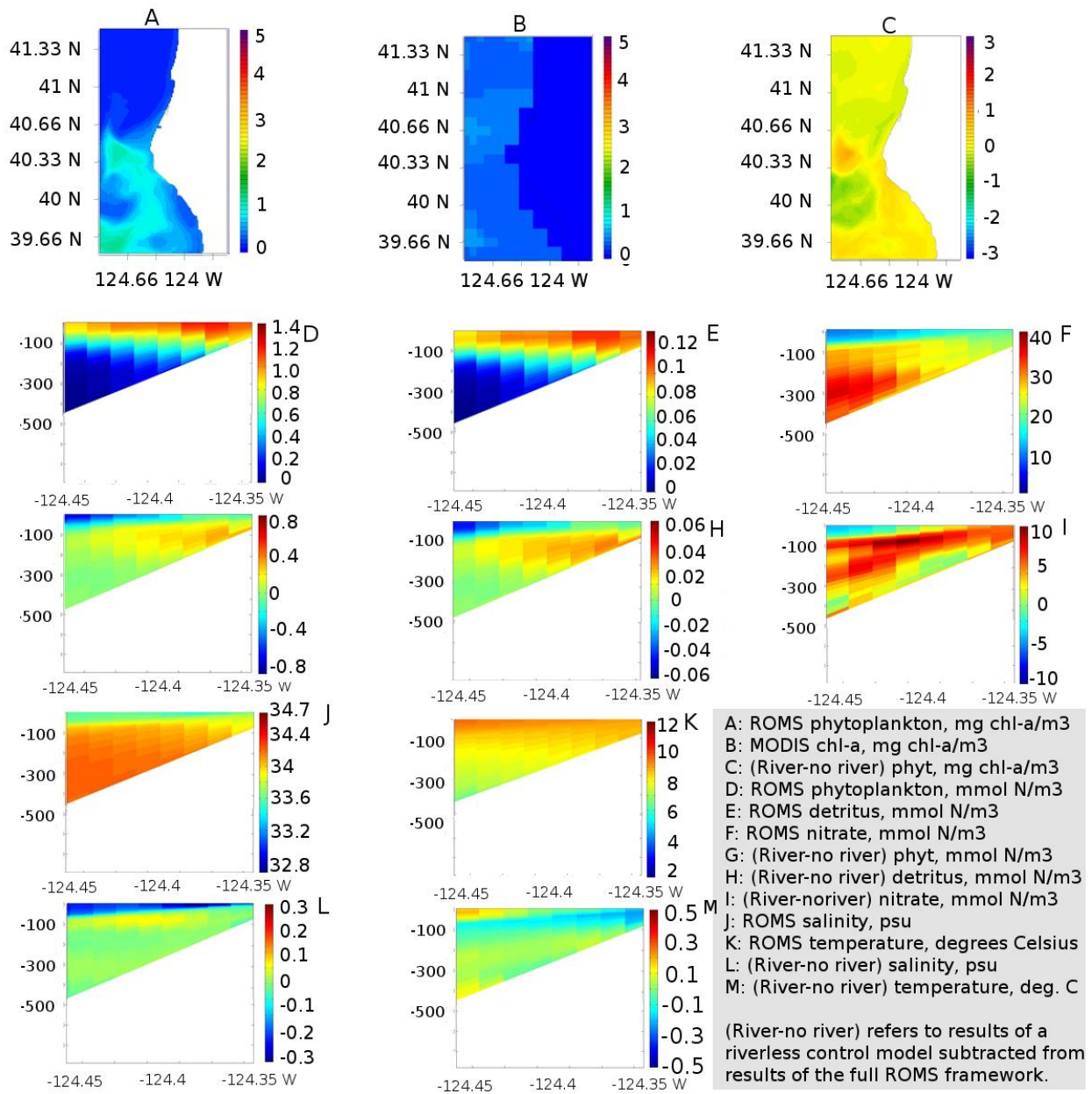


Figure 3.17: As Figure 3.14, for the 8-day average starting at 01/05/2008, the highest Eel River discharge day in the 2007-2008 water year.

3.5.5 Summary of event-driven comparisons

Across all of the largest discharge events in water years 2002-2009, regions of the water column heavily influenced by the freshwater plume (as visualized by the difference in pycnoclines between the fully coupled model and the no-river control) are universally nitrate limited as compared to the no-river control. This effect dominates biogeochemistry in the system, above any physical differences. Still, plume physical behavior varies widely; when entering an especially deep mixed layer in the midst of an ongoing, surface stressful storm, it is often rapidly mixed and heavily diluted by the time it reaches 5 km north over the course of eight days, though larger deliveries of freshwater can resist this to some degree with buoyancy. If weather conditions are calm, plumes can remain on top of the water column for several kilometers no matter how deep or shallow the water column may be, nor how relatively massive or tiny the plume. Plume-dominated regions are often warmer, but not consistently, and not significantly.

3.6 No-nutrient river testing

2005-2006, with the largest discharge event of the decade, was also selected to study the effects of the river's nutrient load in greater depth, by running a separate experiment: rather than the no-river control which lacks the river entirely, the no-nutrient control includes a physically identical river with nitrate and detritus concentrations set to zero. By subtracting the no-nutrient control from the with-nutrient river results, we can gauge how much of the river's effect within the model is physical rather than due to biogeochemical loading. Given the model's failure to precisely reproduce the spatial distribution of the coastal bloom, the application of this analysis to reality must be considered with some care.

In section 3.5 it became clear that in terms of nitrate contribution, the river functionally creates a region of nitrate deficiency due to its relatively low concentration (based on USGS data, USGS 2012) compared to the surrounding ocean (based on the World Ocean Atlas, NOAA 2013c). Detritus, however, is delivered by the river to the ocean in considerably higher quantities (described in Chapter 2.6.4), which can be remineralized by phytoplankton and used to grow. Despite this, at no point throughout the December-May season of river discharge was productivity enhanced by more than 4% in the with-nutrient river runs as compared to the control. The best example of this behavior occurs immediately after the river discharge event at the beginning of February 2006. Figures 3.18 to 3.20 show the region of elevated, nutrient-driven productivity. This productivity is small, of the same order of magnitude as inherent indeterminacy between the two models, but its timing (after a large river event) and location (near the mouth of the river) allow us to reasonably interpret it as dominated by the biogeochemical difference between the experiments rather than the numerics. Furthermore, throughout sections 3.4 and 3.5, the sign of the difference of detritus between models with and without the river was always determined by the sign of the difference in phytoplankton concentration; riverine-delivered detritus was overwhelmed by ongoing biological cycling. In summary, these results indicate that river-delivered nitrate (whether initially dissolved or later bioavailable through remineralization of detritus) is unimportant to the phytoplankton that grow around Cape Mendocino. It is of course, possible that a different nutrient, such as iron, would show much more interesting results. It is also possible that a mechanistic failure of the model is obscuring nitrate's true importance, such as an inability on the part of the phytoplankton to

uptake it to full depletion, or too much nitrate delivered in the first place during the model spin-up period.

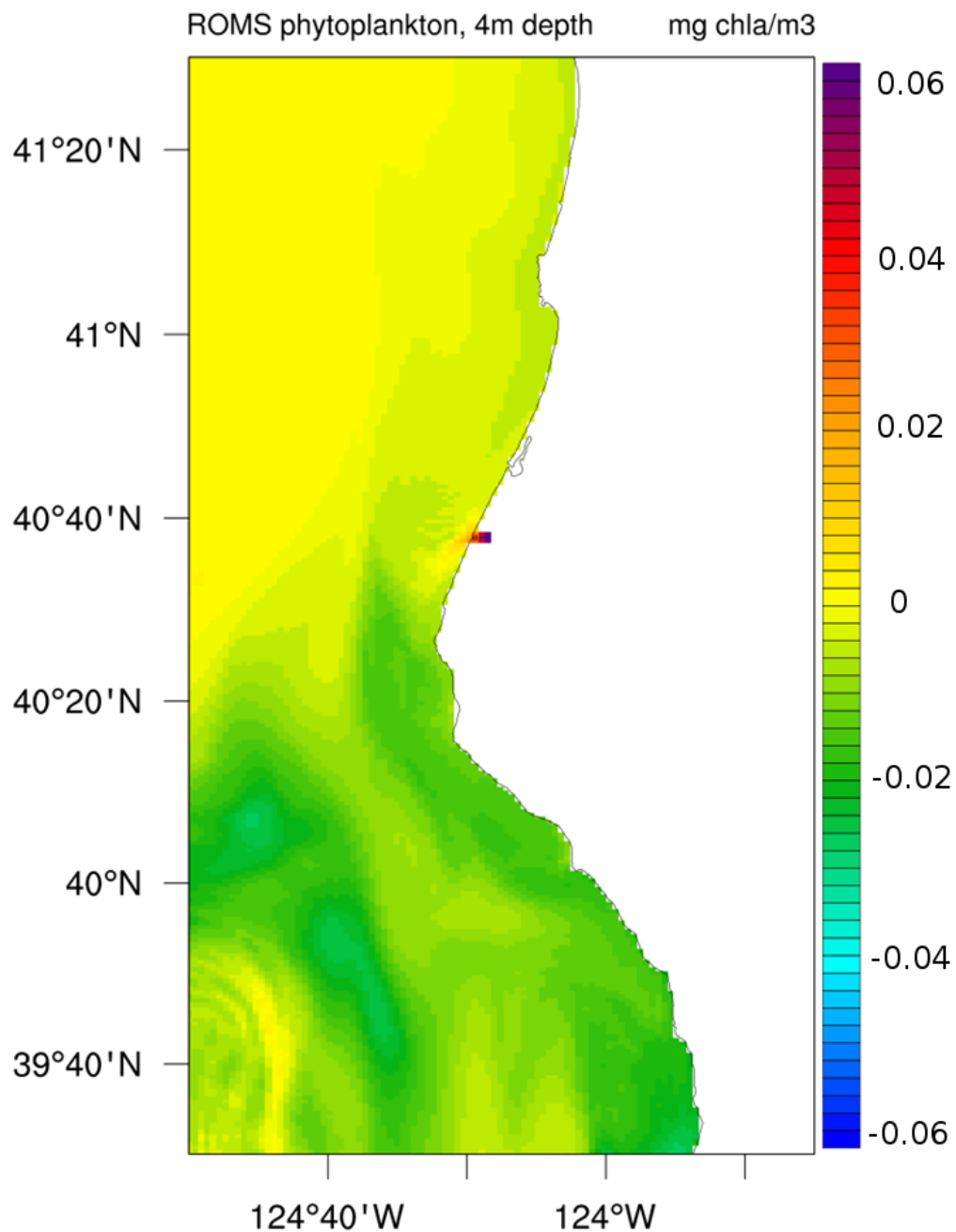


Figure 3.18: 8-day averaged phytoplankton results from the no-nutrient river control subtracted from the with-nutrient river, beginning 02/02/2006, which is also the time of delivery of the second-largest river discharge event of the water year. Note that ambient phytoplankton concentration at the mouth of the Eel River is 1.5 mg chl-a/m³, such that this difference accounts for no more than 4% of the total.

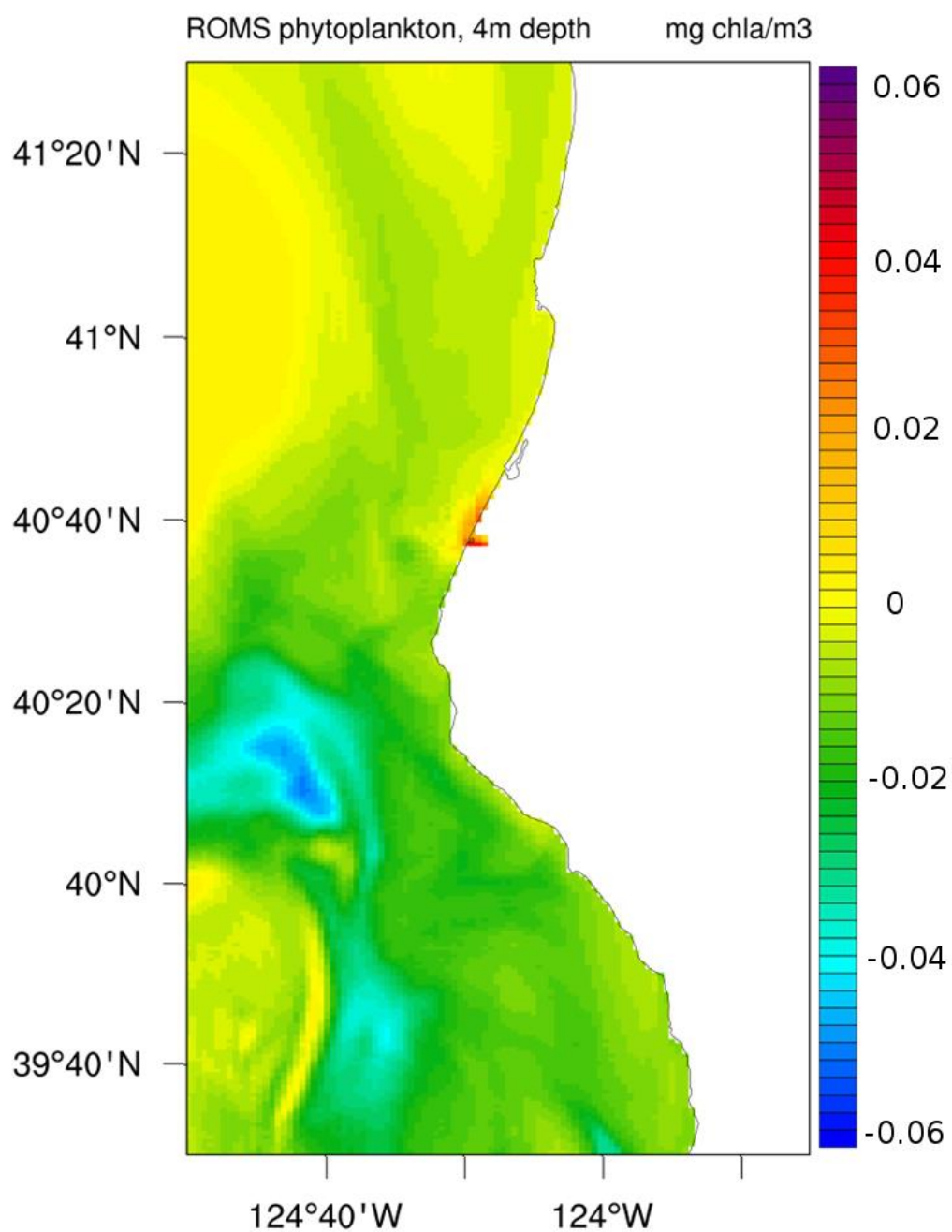


Figure 3.19: 8-day averaged phytoplankton results from the no-nutrient river control subtracted from the with-nutrient river, beginning 02/09/2006. Note that ambient phytoplankton concentration at the mouth of the Eel River is 0.5 mg chl-a/m³, such that this difference accounts, as in Figure 3.18, for no more than 4% of the total.

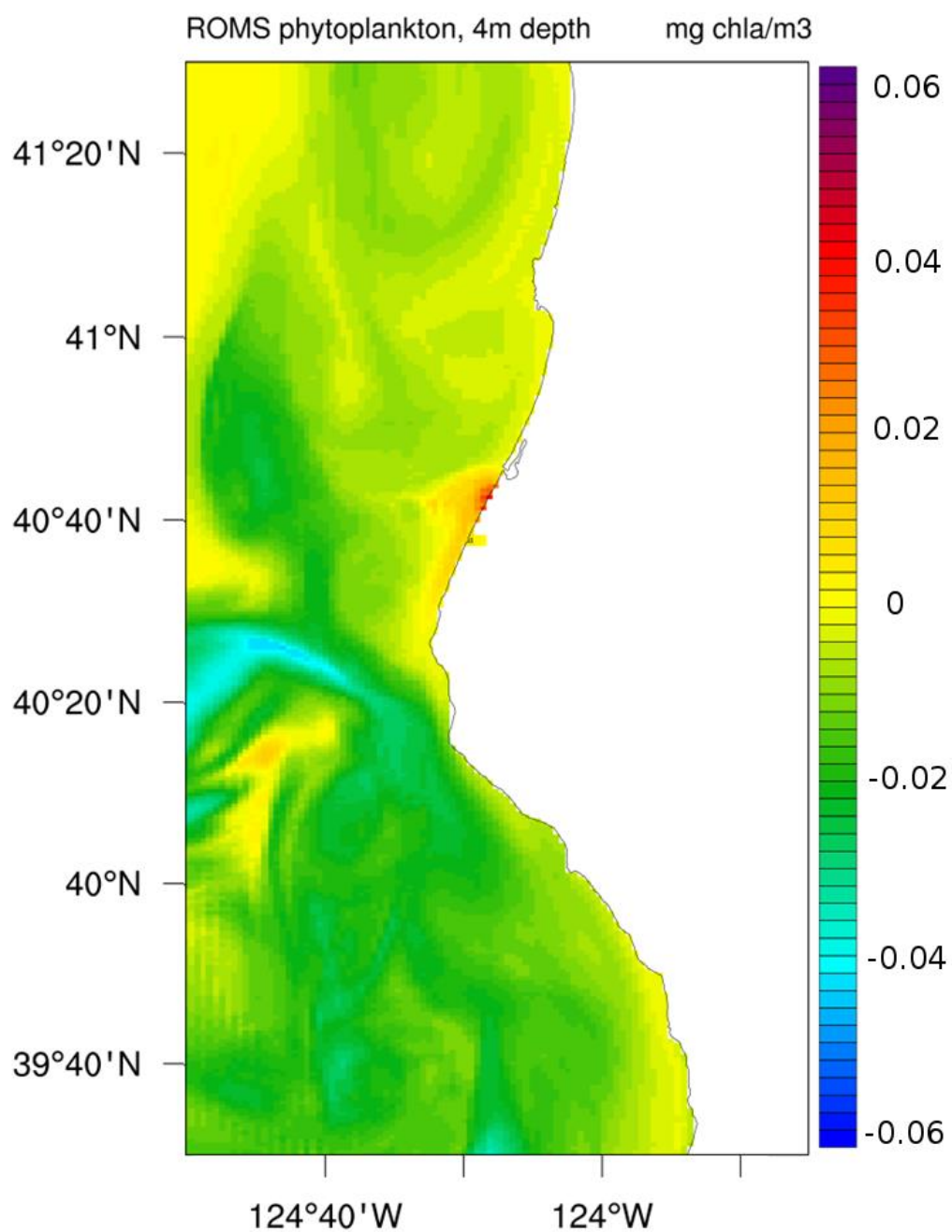


Figure 3.20: 8-day averaged phytoplankton results from the no-nutrient river control subtracted from the with-nutrient river, beginning 02/17/2006. Note that ambient phytoplankton concentration at the mouth of the Eel River is 0.5 mg chl-a/m³, such that this difference accounts, as in Figures 3.18-.3.19, for no more than 4% of the total.

3.7 Extra-nutrient river testing

While the lack of significance of riverine nutrient delivery is not improbable, it spurred the question of whether or not the modeling framework was capable of successfully modeling riverine nutrient-driven phytoplankton blooms at all. To test the model's capability in doing so, the Eel River was loaded with four hundred times its usual concentration of nitrate (roughly equaling the annual nitrate load of the Seine River, estimated at 80,000t by (Guillaud et al. 2000)). For comparison, the Columbia River's annual nitrate load is estimated at 50,000t (Aulenbach 2006), and the Mississippi River's can approach 1,000,000t (Aulenbach 2006), while the Amazon River is estimated to annually export over 1,300,000t (DeMaster and Aller 2001). As Figure 3.21 shows, with that level of nitrate delivery, even in the lowest-flow months of the year, like July, a phytoplankton bloom can easily be sustained. It is therefore not the inability of the model to resolve river nutrient delivery to the coastal biogeochemical system at work here, but rather the relatively low quantity of nutrients being delivered, that accounts for the model's lack of response in earlier sections.

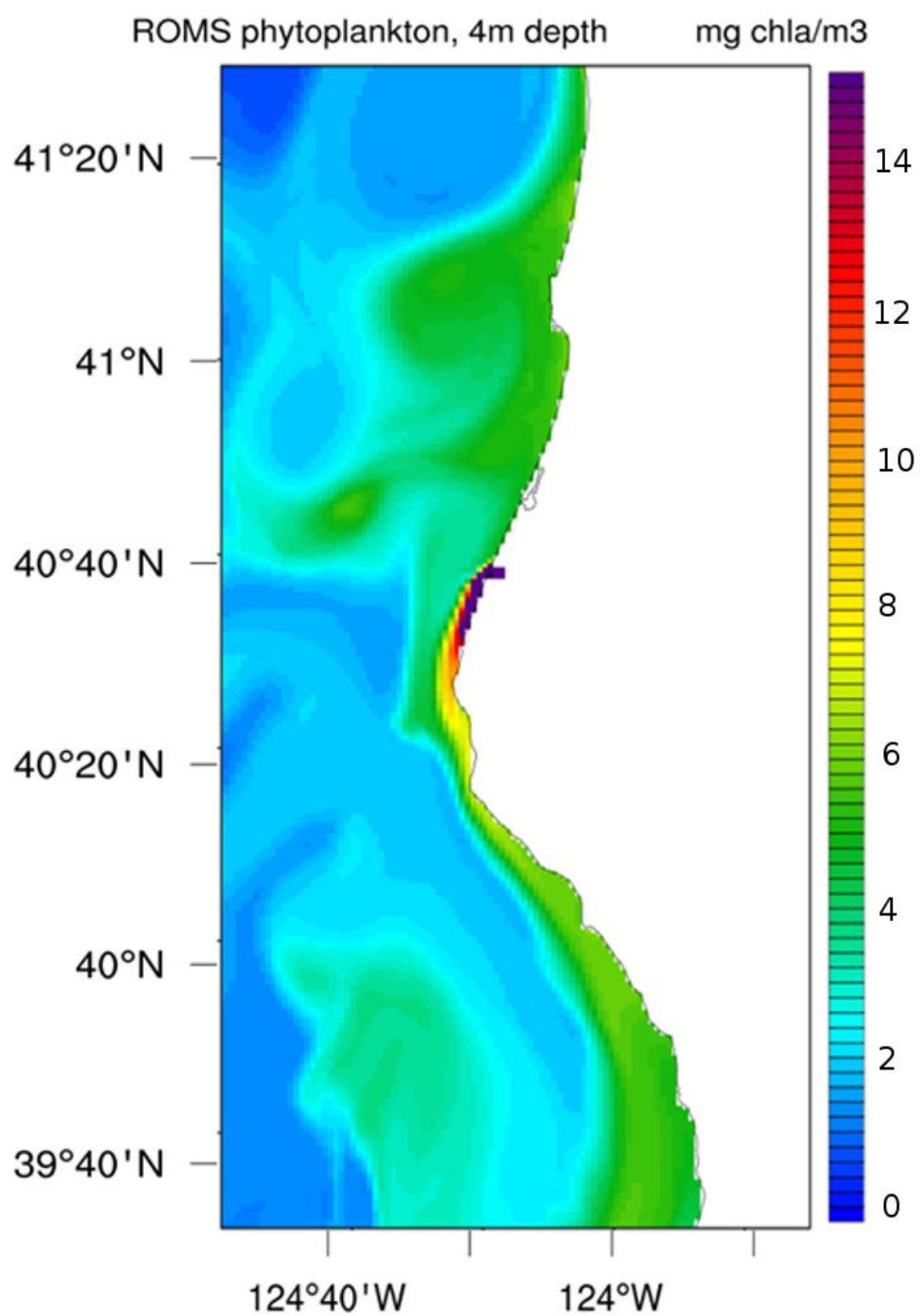


Figure 3.21: A large phytoplankton bloom generated by the coupled modeling framework during low-flow conditions in July, with the Eel River given 400x its normal load of dissolved inorganic nitrogen.

3.8 Chl:C sensitivity testing

As discussed in section 2.6.3, the Carbon:Chlorophyll ratio is a potential additional source of model uncertainty. It varies greatly by species and is affected nonlinearly by ambient nutrient, light, and temperatures (Wang et al. 2009). Its primary potential to alter model results is in defining the values for initialization of the model. In order to test the potential impact of an inaccurate constant ratio (50 C:Chl, per Li et al. [2010]), the 2005-2006 model year was spun up with ten times more initial phytoplankton. The effect was magnified on the southern boundary in the problematic region discussed in 3.8, but in terms of onshore results in the region of interest, the additional initial phytoplankton influenced results by no more than 0.1 mg chl-a/m³ by the end of the spin-up period in November.

3.9 Southwestern model artifact and nonlinear drift

The major failure of the modeling framework's ability to reproduce realistic coastal phytoplankton conditions clearly occurs to the southwest (for example, in Figure 3.3, the November-January climatologies); it routinely overestimates primary production by approximately a factor of two. This artifact is so dominant south of Cape Mendocino that it makes it difficult to interpret model results there. It is fortunate that the river is literally shielded from the worst of the artifact's impact by virtue of being further north.

The source of this model artifact is easy to find: open boundary conditions in ROMS are notoriously unstable, and the southern boundary in this model application exemplifies that behavior. Due to concerns about computational expense, 39 N was chosen as the southern extent of the 1 km domain, but this is clearly not far enough away from the region of interest – results would be improved by moving the southern boundary down another – probably several – hundred kilometers. Instability from the southern boundary is the likely driver of most of the otherwise inexplicable difference between models with and without the river – when there are significant differences between the model and the control two hundred kilometers offshore, it's unlikely that the lack of a river is the primary actor when comparing the two.

This boundary-driven artifact then interacts with the other major failure of model skill: the Mendocino Triple Junction, where the Gorda plate, the North American plate, and the Pacific Plate meet, is at 40.36 N, -124.6 W – in other words, just south of Cape Mendocino. Even smoothed to some degree in the model, this creates a change in bathymetry of 1000-1500m over 10 km (and thus ten grid cells). Resolving momentum over this region is a challenge. In the case of these results, what reliably occurs is the creation of an unrealistic vortex in the southeastern corner of the model (for a typical example, see Figure 3.22), which is clearly partially driven by the proximity of the southern boundary as well, and could be reduced in the same fashion. This rotating water draws anything nearby into itself – particularly, it transports the boundary-instability generated phytoplankton into itself, concentrating this nonphysical bloom right where it's visible in so many figures in this chapter, west and south of Cape Mendocino. In a way this artifact vortex is fortuitous; it cooperates with the presence of Cape Mendocino to draw the effects of the southern boundary away from the small and usually northern region potentially dominated by the river at certain times of year.

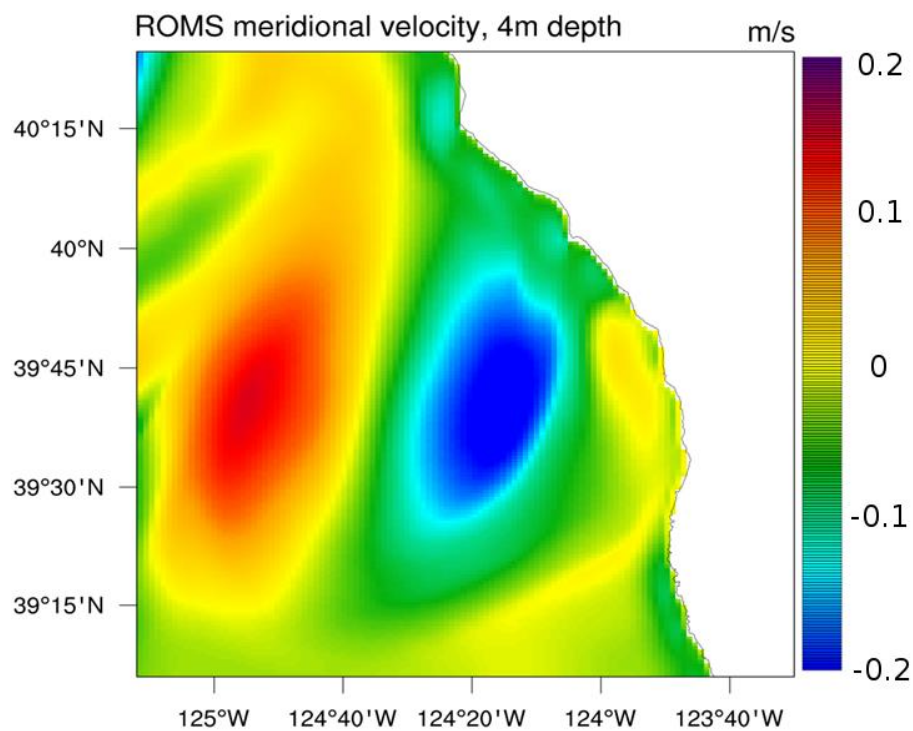
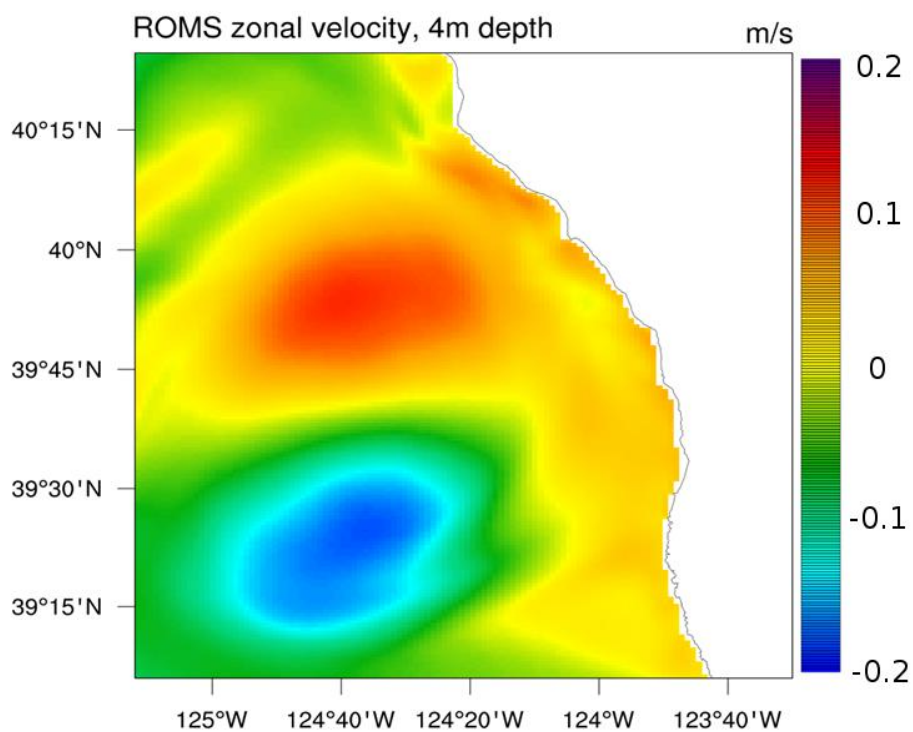


Figure 3.22: 11/25/05 example of the model artifact vortex created by momentum over the Mendocino Triple Junction, and further interactions with the unstable southern boundary.

That isn't to say that this problem would evaporate with the further distancing of the southern noise, however. In a nonlinear modeling framework, nonlinearities can amplify fluctuations in unpredictable fashion – and while the steady addition of fresh water during the low-flow months of spinup is not large in mass, it is certainly a continuous perturbation. Differences accumulate, both from the addition of the freshwater, and from the closed boundary in the no-river control replacing the river's mouth, where the ocean is forced to stop at the shore instead of mixing slightly inland. Some of these differences are potentially quite physically meaningful; the purpose of “turning off” the river, after all, is to explore all of the potential impacts of the river, and the altered boundary captures that! But others may well simply be nonlinear drift, as tiny differences accumulate during spinup, and the solutions diverge in potentially significant ways.

Trying to quantify this drift is both more difficult and more necessary than the southwestern boundary artifact because its effect is by definition concentrated near the river. A first order consideration, made regularly in previous analysis in this chapter, is that an order of magnitude estimate of inherent model differences can be estimated from the differences between the with-river model and no-river control that accumulate before the first major river discharge event. Differences significantly larger than that initial difference, during storm-driven river discharge events, are more likely to be event-driven than caused by longer-term effects, whether numerical or physical). The differences between the November climatologies with and without the river – November being the sole post-spinup, pre-storm event month modeled each year – provide a more systematic definition of this uncertainty.

Table 3.15: The absolute magnitudes of November minus No River November climatological results within 10 km of the mouth of the Eel River.

Nitrate (mmol/m³)	Detritus (mmol/m³)	Phytoplankton (mmol/m³)	Zooplankton (mmol/m³)	Temperature (deg. C)	Salinity (psu)	U velocity (m/s)	V velocity (m/s)
1	0.08	0.05	0.02	0.3	0.5	0.02	0.02

Compared to most of the model-control differences we see during large storm events, the biological tracer differences are especially minute, and the differences in momentum are also small, but salinity and temperature differences often fall within the same order of magnitude as the post-spinup drift in Table 3.15. That is not to say that the warm, low-salinity regions reproduced over and over in the right place at the right times are meaningless; their true magnitude, however, may up to a factor of two larger, or considerably smaller, depending on the (unknown) sign of the background noise.

3.10 Discussion

Although high levels of noise make it challenging to interpret the effect of the modeled Eel River, a few broad conclusions can be drawn. In the months of highest river activity, December and January, large discharge events usually have an inhibitory effect on phytoplankton growth, on time scales ranging from interannually, to monthly, to weekly. The delivery of an extreme amount of river water is generated by storm events: these storm events deepen the mixed layer, reducing light availability (and phytoplankton growth). While structured river plumes are

observed within the model at a distance of 5 km north of the mouth, the potential buoyancy-driven shallowing effect of freshwater delivery is often overcome by mixing, instead creating a region of lower salinity that is spread more evenly above the pycnocline. Onshore, the pycnocline is consistently shallower than the thermocline by at least 100m, and the phytoplankton grow above it.

Within this region, there are clear indications of nutrient limitation: the natural outcome of phytoplankton growth is to deplete dissolved inorganic nitrogen, but the no-river control consistently has simultaneously more phytoplankton and more nitrate than the with-river model. In other words, the lack of nitrate within the plume-dominated system is so dominating that even when phytoplankton grow to greater magnitudes in the riverless ocean, they still leave more nitrate behind than is available during periods of high river discharge!

There does seem to be the possibility of second-order thermal effects, but they are difficult to separate from the noise. The low-salinity water often appears to be slightly warmer, probably due to the elevated heat capacity compared to the surrounding ocean. This can come with a corresponding increase in phytoplankton concentration, but only when (as for example in December 2003) the mixed layer is shallow. At the moment that it enters the system, the December and especially January river is colder than the ocean, but the effect of that initial temperature is drowned out by the current ocean/atmosphere conditions: it can float, sink, or be mixed in evenly, irrespective of initial temperature.

It is when the river enters an ocean with a shallow mixed layer that light limitation appears to play a role; the difference in nitrate between the with-river model and the no-river control gets smaller, and the depth profile of the phytoplankton strongly favors the surface rather than being mixed more evenly throughout the mixed layer. Supported by a shallower mixed layer (and less turbulence), the low-salinity region of river influence is itself shallower, and sometimes distinctly above the pycnocline, forming its own layer on the surface. In other words, if the storm event that generates a river event clears up quickly enough that the ocean can calm down a bit, river plumes appear to have a chance to propagate without being as rapidly mixed into the water column.

A great degree of mixing by the time the plume reaches the vertical transect station at 5 km north of the mouth is not unexpected. The physical anatomy of a river plume is still a subject of active research, but a typical model involves rapid shear mixing and entrainment of ocean water, thus increasing the salinity, in the near-field, advective region; as the plume moves away from the mouth of the river, this far-field region becomes dominated by wind stress (Hetland 2005). It is the far-field, rather than the near-field, that is under examination (as the near-field at the mouth is acted on by freshwater year round, and while it is dynamically event-driven, it is that much more difficult to separate those events from the background). The basic mechanism was described by Fong and Geyer (2001): a buoyant layer is mixed by shear created by the wind-driven Ekman transport. The predicted result is a critical salinity value, derived from initial conditions, wind stress, and the Richardson number, that causes wind mixing to stabilize the water mass structure of the plume (whatever state it's in, after its initial near-field inertial mixing) towards that salinity value. This is consistent with our model's behavior; in the far-field, most of the mixing has already occurred, and what we see is often relatively diffuse.

Given the model's tendency to overestimate phytoplankton production, the occasional underestimated bloom event is of particular interest. For example, the failure of the 2008 model to generate a bloom at the end of December, coinciding with the year's first river delivery event, implies a mechanistic failure. It could be due to differences between the atmospheric representation and reality, but it could also be due to effects not accounted for in the model. If the river does play a role in the generation of that bloom, it is a particularly good time for nutrients to be meaningful -- with the first storm event/river delivery of the year most likely to carry a load of nutrients leached from the ground. Perhaps an alternative micronutrient, like iron, is important..

Using gradually remineralizable-to-nitrate detritus as a stand-in for a more detailed treatment of non-DIN nutrients is not an effective way to gauge this possibility. Especially problematic, the effect of river-added detritus, even at high levels, was totally overwhelmed by the detritus produced by plankton grazing and mortality. When comparing detritus with and without the river, it followed the difference in phytoplankton very consistently, which usually meant more detritus without the river than with it. There was no evidence that the river-delivered detritus was sinking out of the water column before it could be remineralized, so its overall effect on the system seems to be extremely minor. Zooplankton, the last piece of the NPZD puzzle, have gone largely unmentioned throughout the chapter because they behaved extremely predictably, maintaining populations roughly proportional to the phytoplankton throughout.

Something else not considered by the model is variable turbidity; the exponential decay of light through the water column is potentially much hastened by suspended sediment absorbing the light. This must account for some degree of model overestimation in near-mouth regions where the sediment has not yet left the euphotic zone, since its net effect would always be to inhibit growth whenever light limitation is a factor.

3.11 Future Directions

In the immediate term, reconfiguring the model with the boundaries further away from the region of interest would probably have the single largest impact on model skill. Beyond that, though, there are many interesting directions in which to take the model.

The use of an iron-limited NPZD model such as Fiechter et al. (2009) is a straightforward way to add iron to the system. Its major limitation in application to this effort is that this model continuously recharges shelf iron at a constant rate, on the assumption of riverine delivery; a model configured to study the specifics of riverine delivery would need to replace this framework with a more detailed structure. Chase et al. (2007) proposes a framework in which riverine iron must sink to anoxic depths, transform from ferric to the more soluble ferrous state, and be upwelled before biological uptake. Iron reduction and oxidation kinetics within the ocean are not so well understood that directly modeling their reactive transport would be reasonable, but there are first-order approximations to be made. Treating iron as a tracer with a delayed release, such that it only dissolves at a certain depth after a certain time (or at a certain oxygen content, if oxygen is modeled directly) is one possible strategy. Bioavailability as a function of the iron-scavenging ligand production by phytoplankton (Buck et al. 2007) is another mechanism for iron uptake that could be modeled directly.

Additionally, river sediment could be modeled directly (at great computational expense, if it were done with significant detail); some kind of tracer to represent turbidity, at the least, would add a potentially important piece to the model, while the sediment itself could provide more accurate representations of gradually bioavailable iron and nitrogen than 'detritus', which is constant in assumed size and sinking rate. Another constant that should be variable is the Carbon:Chlorophyll ratio. Although the model's sensitivity to this value was not shown to be large, an improved representation would help most at the validation stage; converting carbon to chlorophyll at any given moment to compare to MODIS (or other chlorophyll) results necessitates something of a leap of faith when using a constant. The true C:Chl ratio could easily be a factor of two different, depending on current environmental conditions. Gruber et al. (2006) is one example of an attempt to nest C:Chl dynamics into ROMS, and could be emulated. Although they found that while large horizontal and vertical variations in the ratio were present, they tended to cancel out within the integrated mean across the euphotic zone, they also showed that using a constant would have created a very substantial negative bias in their model, in contrast to model results in this work.

On a larger scale, there is interest in incorporating watershed models into global climate models such as the Community Earth System Model (CESM). Such problems as tracking sediment and nutrient transport from rivers to the ocean are currently largely unimplemented in comprehensive global climate models. Successful coupling on the mesoscale is an important first step in model development. The hindcast modeling framework could be forced forward with CESM results to explore decadal-scale variability under a variety of climate change emissions scenarios. Eventually the framework could even be implemented as an option within CESM, using its land parameterizations to automatically parameterize a nested HydroTrend or (more likely, given HydroTrend's limitations) another sufficiently simple watershed model.

3.12 Conclusion

The coupled modeling framework is a powerful tool to examine potential effects by the Eel River on coastal ocean productivity. In the current formulation, nitrogen limitation in freshwater plumes appears to be a major factor in the biogeochemical response to their offshore delivery. Typically, the same storm events that generate large plumes also create turbulence that deepens the mixed layer, inhibiting phytoplankton production. On 8-day timescales, storm wind-driven mixing appears to create relatively diffuse plume conditions by the time the plume is 5 km north. Occasionally, however, conditions clear up rapidly enough to allow an especially low-salinity plume to travel across the surface for tens of kilometers, trapping phytoplankton closer to the surface. Even under these conditions, nutrient limitation appears to inhibit production, however. The effect of gradually remineralizable detritus delivered by the river appears to be negligible, even given the very high upper bound chosen.

Potential improvements to the modeling framework range from the expansion of the model domain to diminish unstable boundary noise, to the inclusion of iron limitation or the direct simulation of turbidity caused by sediment load. Although it was run as a nine-year hindcast, there is also potential to force the framework forward with climate projections, in order to learn how the altered timing and magnitude of storm events might change the subsequent behavior of the river entering the coastal ocean. Although the impact of the river on ocean productivity appears to be small on short time scales, it is possible that the incremental shift of phytoplankton bloom locations might alter longer-term dynamics, such as nutrient availability during upwelling, later in the year.

Bibliography

- Alexander, C.R. and A.M. Simoneau, 1999. Spatial variability in sedimentary processes on the Eel continental slope. *Marine Geology* 154, 243-254.
- Allen, J.S., Newberger, P.A. and J. Federiuk, 1995. Upwelling circulation on the Oregon continental shelf. Part I: Response to Idealized Forcing, *J. Phys. Oceanogr.*, 25, 1843-1866.
- Allison, M.A., Bianchi, T.S., McKeen, B.A. and T.P. Sampere, 2007. Carbon burial on river-dominated continental shelves: Impact of historical changes in sediment loading adjacent to the Mississippi River. *Geophysical Research Letters* 34, L01606.
- Andrews, E.D. and R.C. Antweiler, 2012. Sediment Fluxes from California Coastal Rivers: The Influences of Climate, Geology, and Topography. *The Journal of Geology*, Vol. 120, No. 4, 349-366.
- Arai, T., Limbong, D., Otake, T, et al., 1999. Metamorphosis and inshore migration of tropical eels *Anguilla* spp. in the Indo-Pacific. *Marine Ecology Progress Series* 182, 283-293.
- Arakawa, A. and V. R. Lamb, 1977. *Methods of computational physics*, Academic Press, 174-265.
- Arango, H.G., 2014. ROMS documentation available on the World Wide Web, accessed 2014 at URL: <https://www.myroms.org/>
- Asselman, N.E.M., 2000. Fitting and interpretation of sediment rating curves. *Journal of Hydrology* 234, pp. 228-248.
- Aulenbach, B.T., 2006. Annual dissolved nitrite plus nitrate and total phosphorous loads for Susquehanna, St. Lawrence, Mississippi-Atchafalaya, and Columbia River Basins, 1968-2004. USGS Open File Report 06-1087.
- Bagnold, R.A., 1966. An approach to the sediment trans-port problem from general physics. U.S. Geological Survey Professional Paper 422-I, 37.
- Banas, N.S., MacCready, P. and B.M. Hickey, 2009a. The Columbia River plume as cross-shelf exporter and along-coast barrier. *Continental Shelf Research* 29, 292-301.
- Banas, N.S. et al, 2009b. Planktonic growth and grazing in the Columbia River plume region: A biophysical model study. *J. Geophys. Res.* 114, C00B06, doi:10.1029/2008JC004993.
- Bane, J.M., Levine, M.D., Samelson, R.M., Haines, S.M., Meaux, M.F., Perlin, N., Kosro, P.M. and T. Boyd, 2005. Atmospheric forcing of the Oregon coastal ocean during the 2001 upwelling season. *J. Geophys. Res.* 110, C10S02, doi:10.1029/2004JC002653.

- Barnett, T.P. and R. Preisendorfer, 1987. Origins and levels of monthly and seasonal forecast skill for United States surface air temperatures determined by canonical correlation analysis. *Monthly Weather Review* 115, 1825–1849.
- Bastow, J.L., J.L. Sabo, J.C. Finlay, and M.E. Power, 2002. A basal aquatic-terrestrial trophic link in rivers: algal subsidies via shore-dwelling grasshoppers. *Oecologia* 131:261-268.
- Beal, E.J., House, C.H. and V.J. Orphan, 2009. Manganese- and Iron-Dependent Marine Methane Oxidation. *Science* 325, 184-187.
- Becker, J. J., Sandwell, D.T., Smith, W.H.F, Braud, J., et al., 2009. Global Bathymetry and Elevation Data at 30 Arc Seconds Resolution: SRTM30_PLUS, *Marine Geodesy*, 32:4, 355-371.
- Bentley, S.J. and C.A. Nittrouer, 2003. Emplacement, modification, and preservation of event strata on a flood-dominated continental shelf: Eel Shelf, Northern California: *Continental Shelf Research* 23 (16), 1465-1493.
- Behrenfeld, M.J. and P.G. Falkowski, 1997a. Photosynthetic rates derived from satellite-based chlorophyll concentration. *Limnology and Oceanography* 42, 1-20.
- Behrenfeld, M.J. and P.G. Falkowski, 1997b. A consumer's guide to phytoplankton primary productivity models. *Limnology and Oceanography* 42, 1479-1491.
- Behrenfeld, M.J., Boss, E., Siegel, D.A. and D.M. Shea, 2005. Carbon-based ocean productivity and phytoplankton physiology from space. *Global Biogeochemical Cycles* 19.
- Bjornsson, H. and S.A. Venegas, 1997. A manual for EOF and SVD analyses of climate data. McGill University, CCGCR Report 97-1, Montreal, Quebec, 52p.
- Blair, N.E., Leithold, E.L., Ford, S.T., Peeler, K.A., Holmes, J.C. and D.W. Perkey, 2003. The persistence of memory: the fate of ancient sedimentary organic carbon in a modern sedimentary system: *Geochimica et Cosmochimica Acta*, v.67, p.63-73.
- Blair, N.E., Leithold, E.L. and R.A. Aller, 2004, From bedrock to burial: the evolution of particulate organic carbon across coupled watershed-continental margin systems: *Marine Chemistry*, v.92. 141-156.
- Borgeld, J.C., 1986. Flood history of the Eel River, California, preserved in offshore sediment. *Eos, Trans. Am. geophys. Un.*, 67,958.
- Borgeld, J.C., Clarke, J.E.H., Goff, J.A., et al., 1999. Acoustic backscatter of the 1995 flood deposit on the Eel shelf. *Marine Geology* 154, 197-210.
- Branstetter, M.L., and Famiglietti, J.S. 1999. Testing the sensitivity of GCM-simulated runoff to climate model resolution using a parallel river transport algorithm. Preprints, 14th Conference on Hydrology, Dallas, TX, Amer. Meteor. Soc., 391-392.

Branstetter, M.L. 2001. Development of a parallel river transport algorithm and applications to climate studies. Ph.D. dissertation, University of Texas at Austin.

Bretherton, C.S., Smith, C., and J.M. Wallace, 1992. An intercomparison of methods for finding coupled patterns in climate data. *Journal of Climate* 5, 541–560.

Brown, W.M. and J.R. Ritter, 1971. Sediment transport and turbidity in the Eel river basin, California. USGS Water supply Pap., 1986, 70 pp.

Buck, K. N., Lohan, M.C., Berger, C.J.M., and K.W. Bruland, 2007. Dissolved iron speciation in two distinct river plumes and an estuary: implications for riverine iron supply. *Limnol. Oceanogr.*, 52(2), 843-855.

Cacchione, D.A., Wiberg, P.L., Lynch, J., et al., 1999. Estimates of suspended-sediment flux and bedform activity on the inner portion of the Eel continental shelf. *Marine Geology* 154, 83-97.

Capet, X.J., Marchesiello, P. and J.C. McWilliams, 2004. Upwelling response to coastal wind profiles. *Geophysical Research Letters* 31, L13311, doi:10.1029/2004GL020123.

Carlson P.R. and D.R. Harden, 1975. E.R.T.S. observations of surface currents along the Pacific Coast of the United States. In: *Principal Sources and Dispersal Patterns of Suspended Particulate Matter in Nearshore Surface Waters of the Northeast Pacific Ocean* (Ed. by P. R. Carlson, T. J. Conomos, R. J. Janda and D. H. Peterson). Final Report, N.T.I.S., E75-10266, 100-126.

Carton, J. A. and B. S. Giese, 2008: A Reanalysis of Ocean Climate Using Simple Ocean Data Assimilation (SODA). *American Meteorological Society*, 136, 2999-3017.

Castellano, P.J. and J.T. Kirby, 2011. Validation of a Hydrodynamic Model of Delaware Bay and the Adjacent Coastal Region. Center for Applied Coastal Research, Research Report No. CACR-11-03.

Chapman, D.C., 1985. Numerical treatment of cross-shelf open boundaries in a barotropic coastal ocean model, *J. Phys. Oceanogr.*, 15, 1060--1075.

Chase, Z., Strutton, P.G., and B. Hales, 2007. Iron links river runoff and shelf width to phytoplankton biomass along the U.S. West Coast. *Geophysical Research Letters* 34.

Computational and Information Systems Laboratory, 2012. Yellowstone: IBM iDataPlex System (Climate Simulation Laboratory). Boulder, CO: National Center for Atmospheric Research. <http://n2t.net/ark:/85065/d7wd3xhc>.

Corson, W.D., Abel, C.E., Brooks, R.M., Farrar, P.D., Groves, B.J., Jensen, R.E., Payne, J.B., Ragsdald, E.S., and B.A. Tracey, 1986. Pacific Coast Hindcast Deepwater Wave Information. WIS Rept. US. Army Engineers Waterways Experiment Station, Vicksburg, MS, 14, BILB6.

- Crocket, J.S., and Nittrouer, C.A., 2004, The anatomy of a sandy inner shelf: an example from northern California: *Continental Shelf Research*, v. 24, p. 55–73.
- Curran, K.J., Hill, P.S. and T.G. Milligan, 2002. Fine-grained suspended sediment dynamics in the Eel River flood plume. *Continental Shelf Research* 22 (17), 2537-2550.
- Cutter, G.R. and R.J. Diaz, 2000. Biological alteration of physically structured flood deposits on the Eel margin, northern California. *Continental Shelf Research* 20 (3), 235-253.
- Dee, D.P., et al., 2011. The ERA-Interim reanalysis: configuration and performance of the data assimilation system. *Q.J.R. Meteorol. Soc.* 137, 553-597.
- Delworth, T.L., et al., 2006. GFDL's CM2 Global Coupled Climate Models. Part I: Formulation and Simulation Characteristics. *Journal of Climate – Special Section* 19, 643-674.
- DeMaster, D.J. and R.C. Aller, 2001. Biogeochemistry of Major World Rivers, eds Degens, E.T., Kempe, S. and J.E. Richey. Wiley, New York, pp 323-347.
- Dodd, J.R., Stanton, R.J and M. Johnson, 1984. Oxygen Isotopic Composition of Neogene Mullscan Fossils From The Eel River Basin of California. *Geological Society of America Bulletin* 95 (10), 1253-1258.
- Drake, D.E., 1999. Temporal and spatial variability of the sediment grain-size distribution on the Eel shelf: the flood layer of 1995. *Marine Geology* 154, 169-182.
- Drenzek, N.J., Huguen, K.A., Montlucon, D.B., et al., 2009. A new look at old carbon in active margin sediments. *Geology* 37 (3), 239-242.
- Environmental Protection Agency, U.S., 1999. South Fork Eel River Total Maximum Daily Loads for Sediment and Temperature. EPA Region IX, approved by Alexis Strauss, 12/16/99. Available on the World Wide Web, accessed 2014 at URL <http://www.epa.gov/region9/water/tmdl/eel/eel.pdf>
- Environmental Protection Agency, U.S., 2002. North Fork Eel River Total Maximum Daily Loads for Sediment and Temperature. EPA Region IX, approved by Cathrine Kuhlman, 12/30/2002. Available on the World Wide Web, accessed 2014 at URL <http://www.epa.gov/region9/water/tmdl/northfork/final.pdf>
- Environmental Protection Agency, U.S., 2003. Middle Fork Eel River Total Maximum Daily Loads for Temperature and Sediment. EPA Region IX, approved December, 2003. Available on the World Wide Web, accessed 2014 at URL <http://www.epa.gov/region9/water/tmdl/middleeel/tmdl.pdf>
- Evans, R.L., Law, L.K., St. Louis, B., et al., 1999. The shallow porosity structure of the Eel shelf, northern California. results of a towed electromagnetic survey. *Marine Geology* 154, 211-226.

- Fairall, C.W., E.F. Bradley, D.P. Rogers, J.B. Edson and G.S. Young, 1996. Bulk parameterization of air-sea fluxes for tropical ocean global atmosphere Coupled-Ocean Atmosphere Response Experiment, *J. Geophys. Res.*, 101, 3747-3764.
- Feminella, J.W., Power, M.E. and V.H. Resh, 1989. Periphyton responses to invertebrate grazing and riparian canopy in 3 northern California coastal streams. *Freshwater Biology* 22 (3), 445-457.
- Ferguson, R.I., 1986. River Loads Underestimated by Rating Curves. *Water Resources Research*, Vol. 22, No. 1, pp. 74-76.
- Fiechter, J., Moore, A.M., Edwards, C.A., Bruland, K.W., Di Lorenzo, E., Lewis, C.V.W., Powell, T.M., Curchitser, E.N. and K. Hedstrom, 2009. Modeling iron limitation of primary production in the coastal Gulf of Alaska. *Deep-Sea Research II* 56, 2503-2519.
- Fiechter, J., Herbei, R., Leeds, W., Brown, J., Milliff, R., Wikle, C., Moore, A. and T. Powell, 2013. A Bayesian parameter estimation method applied to marine ecosystem model for the coastal Gulf of Alaska. *Ecological Modelling* 258, 122-133.
- Finlay, J.C., Power, M.E. and G. Cabana, 1999. Effects of water velocity on algal carbon isotope ratios: Implications for river food web studies. *Limnology and Oceanography* 44 (5), 1198-1203.
- Fishman, M.J., and Friedman, L.C., 1989. Methods for the determination of inorganic substances in water and fluvial sediments: U.S. Geological Survey Techniques of Water-Resources Investigations, book 5, chap. A1, 545 p.
- Fishman, M.J., 1993. Methods of analysis by the U.S. Geological Survey National Water Quality Laboratory--Methods for the determination of inorganic and organic constituents in water and fluvial sediments: U.S. Geological Survey Open-File Report 93-125, 217 p.
- Fishman, M.J., Raese, J.W., Gerlitz, C.N. and R.A. Husband, 1994. U.S. Geological Survey Approved Inorganic and Organic Methods for the Analysis of Water and Fluvial Sediment, 1954-94. USGS Open-File Report 94-351.
- Flather, R. A., 1976. A tidal model of the northwest European continental shelf. "Memoires de la Societe Royale de Sciences de Liege, 6, 141-164.
- Fong, D.A. and W.R. Geyer, 2001. Response of a river plume during an upwelling favorable wind event. *J. Geophys. Res.* 106, 1067-1084.
- Franks, P.J.S., 2002. NPZ Models of Plankton Dynamics: Their Construction, Coupling to Physics, and Application. *Journal of Oceanography*, Vol. 58: 379-387.
- Freeze, R.A., 1974. Streamflow generation. *Reviews in Geophysics and Space Physics* 12, 627-647.

- Freeze, R.a. and J.A. Cherry, 1979. Groundwater. Prentice Hall Inc., Eaglewood Cliffs, NJ, 604pp.
- Friedrichs, C.T., Wright, L.D., Hepworth, D.A. and S.C. Kim, 2000. Bottom-boundary-layer processes associated with fine sediment accumulation in coastal seas and bays. *Continental Shelf Research* 20, 807-841.
- Friedrichs, C.T., and L.D. Wright, 2004. Gravity-driven sediment transport on the continental shelf: implications for equilibrium profiles near river mouths. *Coastal Engineering*, 51: 795-811
- Galperin, B., Kantha, K.H., Hassid, S. and A. Rosati, 1988. A quasi-equilibrium turbulent energy model for geophysical flows, *J. Atmos. Sci.*, 45, 55-62.
- Gent, P. R., et al, 2011: The Community Climate System Model Version 4. *J. Climate*, 24, 4973–4991.
- Geyer, W.R., Hill, P., Milligan, T. and P. Traykovski, 2000. The structure of the Eel River plume during floods. *Continental Shelf Research* 20 (16), 2067-2093.
- Goff, J.A., Orange, D.L., Mayer, L.A., et al., 1999. Detailed investigation of continental shelf morphology using a high-resolution swath sonar survey: the Eel margin, northern California. *Marine Geology* 154, 255-269.
- Goñi, M.A., Hatten, J.A., Wheatcroft, R.A. and J.C. Borgeld, 2013. Particulate organic matter export by two contrasting small mountainous rivers from the Pacific Northwest, U.S.A. *JGR Biogeosciences* 118 (1), 112-134.
- Granger, C.W.J., 1969. Investigating Causal Relations by Econometric Models and Cross-spectral Methods. *Econometrica* 37 (3), 424-438.
- Grant, G.E. and A.L. Wolff, 1991. Long-term patterns of sediment transport after timber harvest, western Cascade Mountains, Oregon, USA. In: Peters, N.E., Walling, D.E. (Eds.), *Sediment and Stream Water Quality in a Changing Environment: Trends and Explanation*. International Association of Hydrological Sciences Publication, Vol. 203, 31–40.
- Griggs, G.B. and J.R. Hein, 1980. Sources, Dispersal, and Clay Mineral Composition of Fine-Grained Sediment off Central and Northern California. *Geology* 88 (5), 541-566.
- Gruber, N., et al, 2006. Eddy-resolving simulation of plankton ecosystem dynamics in the California Current System. *Deep-Sea Research I* 53, 1483-1516.
- Guerra, J.V., Ogston, A.S., Sternberg, R.W., 2006. Winter variability of physical processes and sediment-transport events on the Eel River Shelf, northern California. *Continental Shelf Research* 26: 2050-2072.

- Guillaud, J-F., Andrieux, F. and A. Menesguen, 2000. Biogeochemical modeling in the Bay of Seine (France): an improvement by introducing phosphorous in nutrient cycles. *Journal of Marine Systems* 25 (3-4): 369-386.
- Haidvogel, D.B., Arango, H., Budgell, W.P., Cornuelle, B.D., Curchitser, E., Di Lorenzo, E., Fennel, K., Geyer, W.R., Hermann, A.J., Lanerolle, L., Levin, J., McWilliams, J.C., Miller, A.J., Moore, A.M., Powell, T.M., Shchepetkin, A.F., Sherwood, C.R., Signell, R.P., Warner, J.C. and J. Wilkin, 2008. Ocean forecasting in terrain-following coordinates: Formulation and skill assessment of the Regional Ocean Modeling System. *Journal of Computational Physics* 227, 3595-3624.
- Harris, C.K., Traykovski, P.A. and W.R. Geyer, 2005. Flood dispersal and deposition by near-bed gravitational sediment flows and oceanographic transport: A numerical modeling study of the Eel River shelf, northern California. *Journal of Geophysical Research* 110 (C9).
- Hedstrom, K.S., 2012. Technical Manual for a Coupled Sea-Ice/Ocean Circulation Model (Version 4). OCS Study BOEM 2012-0xx, accessed on the World Wide Web, 2014, at URL http://www.people.arsc.edu/~kate/ROMS/manual_2012.pdf
- Heinle, A. and T. Slawig, 2013. Impact of parameter choice on the dynamics of NPZD type ecosystem models. *Ecological Modeling* 267, 93-101.
- Hermann, A.J., Curchitser, E.N., Haidvogel, D.B. and E.L. Dobbins, 2009. A comparison of remote vs. local influence of El Niño on the coastal circulation of the northeast Pacific. *Deep-Sea Research II* 56, 2427-2443.
- Hetland, R.D., 2005. Relating River Plume Structure to Vertical Mixing. *Journal of Physical Oceanography* 35, 1667-1688.
- Hickey, B.M., Kudela, R.M., Nash, J.D., Bruland, K.W., Peterson, W.T., MacCready, P., Lessard, E.J., Jay, D.A., Banas, N.S., Baptista, A.M., Dever, E.P. and P.M. Kosro, 2010. River Influences on Shelf Ecosystems: Introduction and synthesis. *Journal of Geophysical Research* 115.
- Hickin, E.J., 1995. *River geomorphology*. Wiley, University of California, 255pp.
- Hill, P.S., Milligan, T.G. and W.R. Geyer, 2000. Controls on effective settling velocity of suspended sediment in the Eel River flood plume. *Continental Shelf Research* 20 (16), 2095-2111.
- Hinrichs, K., Summons, R.E., Orphan, V., Sylva, S.P., and J.M. Hayes, 2000. Molecular and isotopic analysis of anaerobic methane-oxidizing communities in marine sediments. *Organic Geochemistry* 31, 1685-1701

- Homoky, W.B., Severmann, S., Mills, R.A., Statham, P.J. and G.R. Fones, 2009. Pore-fluid Fe isotopes reflect the extent of benthic Fe redox recycling: Evidence from continental shelf and deep-sea sediments. *Geology* 37 (8), 751-754.
- Hordoir, R., Nguyen, K.D. and J. Polcher, 2006. Simulating tropical river plumes, a set of parameterizations based on macroscale data: A test case in the Mekong Delta region. *Journal of Geophysical Research*, Vol. 111, C09036.
- Horowitz, A.J., 2003. An evaluation of sediment rating curves for estimating suspended sediment concentrations for subsequent flux calculations. *Hydrological Processes* 17, 3387-3409.
- Hothorn, T., 2014. Package 'lmtest' documentation available on the World Wide Web, accessed 2014 at URL: <http://cran.r-project.org/web/packages/lmtest/lmtest.pdf>
- Hutton E.W.H. and J.P.M. Syvitski, 2008. Sedflux 2.0: An advanced process-response model that generates three-dimensional stratigraphy. *Computers&Geosciences*, 34: 1319~1337, 10.1016/j.cageo.2008.02.013
- Jochum, M., Danabasoglu, G., Holland, M., Kwon, Y.O. and W.G. Larger, 2008. Ocean viscosity and climate. *Journal of Geophysical Research: Oceans* 113 (C6).
- Keister, J.E. and P.T. Strub, 2008. Spatial and interannual variability in mesoscale circulation in the northern California Current system. *Journal of Geophysical Research*, Vol. 113, C04015.
- Kettner, A.J., and J.P.M. Syvitski, 2008. HydroTrend v.3.0: A climate-driven hydrological transport model that simulates discharge and sediment load leaving a river system. *Computers & Geosciences*, 34, 1170-1183.
- Kisi, O., Dailr, A.H., Cimen, M. and J. Shiri, 2012. Suspended sediment modeling using genetic programming and soft computing techniques. *Journal of Hydrology* 450-451, 48-58.
- Kmusser, K., 2009. Map of the Eel River watershed available on the World Wide Web, accessed 2010, at URL: <http://en.wikipedia.org/wiki/File:Eelrivermap.png>
- Kniskern T., J.A. Warrick, K.L. Farnsworth, R.A. Wheatcroft, and M.A. Goñi, 2011, Coherence of river and ocean conditions along the U.S. west coast during storms: *Continental Shelf Research*, vol. 31, no. 7-8, pp. 789-805
- Krishnamurthy, A., Moore, J.K., Mahowald, N., Luo, C., Doney, S.C., Lindsay, K. and C.S. Zender, 2009. Impacts of increasing anthropogenic soluble iron and nitrogen deposition on ocean biogeochemistry. *Global Biogeochemical Cycles*, Vol. 23, GB3016.
- Kvenvolden, K.A. and M.E. Field, 1981. Thermogenic hydrocarbons in unconsolidated sediment of Eel River Basin, Offshore Northern California. *AAPG Bulletin* 65 (9), 1642-1646.

- Large, W. G., McWilliams, J.C. and S.C. Doney, 1994. Oceanic vertical mixing: a review and a model with a nonlocal boundary layer parameterization, *Rev. Geophys.*, 32, 363-403.
- Lee, H., Locat, J., Dartnell, P., et al., 1999. Regional variability of slope stability: application to the Eel margin, California. *Marine Geology* 154, 305-321.
- Legaard, K.R. and A.C. Thomas, 2006. Spatial patterns in seasonal and interannual variability of chlorophyll and sea surface temperature in the California Current. *J. Geophys. Res.* 111, C06032.
- Leithold, E.L., 1974. Plume of the Eel River (1974) graphic available on the World Wide Web, accessed 2014 at URL <http://www4.ncsu.edu/~elleitho/>
- Leithold, E.L., 1989. Depositional processes on an ancient and modern muddy shelf, northern California. *Sedimentology* 36, 179-202.
- Leithold, E.L. and R.S. Hope, 1999. Deposition and modification of a flood layer on the northern California shelf: lessons from and about the fate of terrestrial particulate organic carbon. *Marine Geology* 154, 183-195.
- Leithold, E.L. and N.E. Blair, 2001. Watershed control on the carbon loading of marine sedimentary particles: *Geochimica et Cosmochimica Acta*, v. 65, p.2231-2240.
- Leithold, E.L., Perkey, D.W., Blair, N.E., and T.N. Creamer, 2005, Sedimentation and carbon burial on the northern California continental shelf: the signatures of land-use change: *Continental Shelf Research*, v.25, p.349-371.
- Lisle, T. E. 1990. The Eel River, northwestern California; high sediment yields from a dynamic landscape. In: M.G. Wolman and H.C. Riggs (ed.), *Surface Water Hydrology*, v. O- 1, *The Geology of North America*, Geological Society of America. p. 311-314.
- Lemarié, F., Debreu, L., Shchepetkin, A.F. and J.C. McWilliams, 2012. On the stability and accuracy of the harmonic and biharmonic isoneutral mixing operators in ocean models. *Ocean Modelling* 52-53, 9-35.
- Levin, L.A. and R.H. Michener, 2002. Isotopic evidence for chemosynthesis-based nutrition of macrobenthos: The lightness of being at Pacific methane seeps. *Limnol. Oceanogr.* 47 (5), 1336-1345.
- Levin, L.A., Ziebis, W., Mendoza, G.F., et al., 2003. Spatial heterogeneity of macrofauna at northern California methane seeps: influence of sulfide concentration and fluid flow. *Marine Ecology Progress Series* 265, 123-139.
- Levin, L.A., Mendoza, G.F., Gonzalez, J. and A. Thurber, 2010. Diversity of bathyal macrobenthos on the northeastern Pacific margin: the influence of methane seeps and oxygen minimum zones. *Marine Ecology* 31: 94-110.

Li, M., Zhong, L. and W.C. Boicourt, 2005. Simulations of Chesapeake Bay estuary: Sensitivity to turbulence mixing parameterizations and comparison with observations. *J. Geophys. Res.* 110, C12004, doi:10.1029/2004JC002585.

Li, Q.P., Franks, P.J.S., Landry, M.R., Goericke, R. and A.G. Taylor, 2010. Modeling phytoplankton growth rates and chlorophyll to carbon ratios in California coastal and pelagic ecosystems. *Journal of Geophysical Research* 115, G04003, doi:10.1029/2009JG001111.

Liu, W.T., K.B. Katsaros, and J.A. Businger, 1979. Bulk parameterization of the air-sea exchange of heat and water vapor including the molecular constraints at the interface, *J. Atmos. Sci.*, 36, 1722-1735.

Locat, J., Lee, H., Kayen, R., Israel, K., Savoie, M. and E. Boulanger, 2002. Shear Strength Development with Burial in Eel River Margin Slope Sediments. *Marine Georesources & Geotechnology* 20 (2), 111-135.

Lutkepohl, H., 2006. *New Introduction to Multiple Time Series Analysis*. Springer, Berlin.

MacCready, P., Banas, N.S., Hickey, B.M., Dever, P.E. and Y. Liu, 2009. A model study of tide- and wind-induced mixing in the Columbia River Estuary and plume. *Continental Shelf Research* 29, 278-291.

Madej, M.A., Bendros, G. and R. Klein, 2012. Assessing effects of changing land use practices on sediment loads in Panther Creek, north coastal California. In: Standiford, Richard B. et al., tech cords., *Proceedings of coast redwood forests in a changing California: A symposium for scientists and managers*. Gen. Tech. Rep. PSW-GTR-238. Albany, CA: Pacific Southwest Research Station, Forest Service, U.S. Department of Agriculture, pp. 101-110.

Mann, K.H. and J.R.N. Lazier, 2006. *Dynamics of Marine Ecosystems: Biological-Physical Interactions in the Oceans*, Third Edition. Blackwell Publishing Ltd., Carlton, Victoria, Australia, 496pp.

Mantua, N., 2014. Pacific Decadal Oscillation Index available on the World Wide Web, accessed 2014 at URL <http://jisao.washington.edu/pdo/PDO.latest>

Marchesiello, P., McWilliams, J.C. and A.F. Shchepetkin, 2001. Open boundary conditions for long-term integration of regional ocean models, *Ocean Modelling*, 3, 1-20.

Marchesiello, P., Debreu, L., and X. Couvelard, 2009. Spurious diapycnal mixing in terrain-following coordinate models: The problem and a solution. *Ocean Modelling* 26, 156-169.

Marks, J.C. ME Power, MS Parker, 2000. Flood disturbance, algal productivity, and interannual variation in food chain length. *Oikos* 90: 20-27.

Maxson, J.H., 1952. Deformed stream terraces of the Eel and Van Duzen Rivers, Humboldt County, California. *Geological Society of America Bulletin* 63 (12), 1338-1339.

McManus J., Berelson, W.M., Severmann, S., Johnson, K.S., Hammond, D.E., Roy, M. and K.H. Coale, 2012. Benthic manganese fluxes along the Oregon-California continental shelf and slope, *Continental Shelf Research*, 43: 71-85.

Mello, U.T. and L.F. Pratson, 1999. Regional slope stability and slope-failure mechanics from the two-dimensional state of stress in an infinite slope. *Marine Geology* 154, 339-356.

Mellor, G. L. and T. Yamada, 1982. Development of a turbulence closure model for geophysical fluid problems, *Rev. Geophys. Space Phys.*, 20, 851-875.

Menemenlis, D. et al, 2008. ECCO2: High resolution global ocean and sea ice data synthesis. *Mercator Ocean Quarterly Newsletter*, 31, 13-21.

Mesinger, F. et al, 2006: North American Regional Reanalysis. *Bull. Amer. Meteor. Soc.*, 87, 343–360.

Meybeck M., Laroche L., Dürr H. and J.P. Syvitski, 2003. Global variability of daily Total Suspended Solids and their fluxes., *Global Planetary Changes*, 39 :65-93.

Milliff, R.F., Fiechter, J., Leeds, W.B., Herbei, R., Wikle, C.W., Hooten, M.B., Moore, A.M., Powell, T.M. and J. Brown, 2013. Uncertainty management in coupled physical-biological lower trophic level ocean ecosystem models. *Oceanography* 26 (4), 98-115.

Milliman, J.D. and J.P.M. Syvitski, 1992. Geomorphic/Tectonic Control of Sediment Discharge to the Ocean: The Importance of Small Mountainous Rivers. *Geology* 100, 525-544.

Monaghan, E.J. and K.C. Ruttenberg, 1999. Dissolved organic phosphorus in the coastal ocean: Reassessment of available methods and seasonal phosphorus profiles from the Eel River Shelf, *Limnol. Oceanogr.*, 44(7), 1702–1714.

Morehead, M.D. and Syvitski, J.P., 1999. River-plume sedimentation modeling for sequence stratigraphy: Application to the Eel margin, northern California. *Marine Geology* 154, 29-41.

Morehead, M., Syvitski, J.P.M, and E.W.H. Hutton, 2001. The link between abrupt climate change and basin stratigraphy: A numerical approach. *Global and Planetary Change*, 28, 115-135., 10.1016/S0921-8181(00)00068-0

Morel, A and J.F. Berthon, 1989. Surface pigments, algal biomass profiles, and potential production of the euphotic layer: Relationships reinvestigated in view of remote-sensing applications. *Limnol. Oceanogr.* 34, 1545-1562.

Mullenbach, B.L. and C.A. Nittrouer. 2000. Rapid deposition of fluvial sediment in the Eel Canyon, northern California, *Continental Shelf Research.*, 20, 2191-2212.

Mullenbach, B.L., Nittrouer, C.A., Puig, P. and D.L. Orange, 2004. Sediment deposition in a modern submarine canyon: Eel Canyon, northern California. *Marine Geology* 211, 101-119.

Mullenbach, B.L. and C.A. Nittrouer, 2006. Decadal record of sediment export to the deep sea via Eel Canyon. *Continental Shelf Research*, 26, 2157-2177.

National Aeronautics and Space Administration 2012, MODIS Aqua graphics available on the World Wide Web, accessed 2014 at URL <http://earthobservatory.nasa.gov/IOTD/view.php?id=79965>

National Aeronautics and Space Administration 2013, MODIS Aqua and Terra R2013.1 reprocessing results available on the World Wide Web, regridded by Oregon State University, accessed 2014 at URL <http://orca.science.oregonstate.edu/2160.by.4320.8day.hdf.chl.modis.php>

National Oceanic and Atmospheric Administration, 2009. F00579: NOS Hydrographic Survey, Humboldt Bay, California. DOC/NOAA/NOS/OCS, Hydrographic Services Division.

National Oceanic and Atmospheric Administration, 2012a. NOAA Comprehensive Large Array-Data Stewardship System (CLASS) data available on the World Wide Web, accessed 2012, at URL http://www.nsof.class.noaa.gov/saa/products/search?datatype_family=SST14NA.

National Oceanic and Atmospheric Administration, 2012b. NOAA Medium Resolution Shoreline available on the World Wide Web, accessed 2012, at URL <http://shoreline.noaa.gov/data/datasheets/medres.html>

National Oceanic and Atmospheric Administration, 2013a. Pacific Fisheries Environmental Laboratory Coastal Upwelling Indices available on the World Wide Web, accessed 2013, at URL http://www.pfeg.noaa.gov/products/pfel/modeled/indices/upwelling/NA/upwell_menu_NA.html.

National Oceanic and Atmospheric Administration, 2013b. The World Ocean Database available on the World Wide Web, accessed 2013, at URL <http://www.nodc.noaa.gov/OC5/SELECT/dbsearch/dbsearch.html>

National Oceanic and Atmospheric Administration, 2013c. The World Ocean Atlas available on the World Wide Web, accessed 2013, at URL <http://www.nodc.noaa.gov/OC5/woa13/>

National Oceanic and Atmospheric Administration, 2014a. National Data Buoy Center data and sensor specifications available on the World Wide Web, accessed 2014, at URL http://www.ndbc.noaa.gov/station_page.php?station=46022.

National Oceanic and Atmospheric Administration, 2014b. Oceanic Nino Index available on the World Wide Web, accessed 2014, at URL http://www.cpc.ncep.noaa.gov/products/analysis_monitoring/ensostuff/ensoyears.shtml.

National Weather Service, 2014. National Weather Service ID (NWS) data for Eureka, CA (EKA) weather station available on the World Wide Web, accessed 2014, at URL http://www.nws.noaa.gov/climate/local_data.php?wfo=eka

- Nelson, C.S., 1977. Wind stress and wind stress curl over the California current. NOAA Tech. Rep., NMFS SSRF-714, 89 pp.
- Nitttrouer, C.A. 1999. STRATAFORM: overview of its design and synthesis of its results. *Marine Geology*, 54, 3-12.
- Nitttrouer, C.A., Austin, J.A., Field, M.E., et al., 2009. *Continental Margin Sedimentation: From Sediment Transport to Sequence Stratigraphy*. Published by John Wiley & Sons, 560pp.
- North Coast Integrated Water Management Plan, 2014. Map available on the World Wide Web, accessed 2014, at URL:
<http://www.northcoastirwmp.net/imgManager/1000006165/EelRiverWMA.jpg>
- Nourani, V. and O. Kalantari, 2010. Integrated Artificial Neural Network for Spatiotemporal Modeling of Rainfall-Runoff-Sediment Processes. *Environmental Engineering Science* 27 (5), 411-422.
- Nourani, V., Parhizkar, M., Vousoughi, F., and B. Amini, 2014. "Capability of Artificial Neural Network for Detecting Hysteresis Phenomenon Involved in Hydrological Processes." *J. Hydrol. Eng.*, 19(5), 896–906.
- Ogston, A.S., Cacchione, D.A., Sternberg, R.W. and G.C. Kineke, 2000. Observations of storm and river flood-driven sediment transport on the northern California continental shelf. *Continental Shelf Research* 20 (16), 2141-2162.
- Ogston, A.S., Guerra, J.V., Sternberg, R.W., 2004. Interannual variability of sediment transport on the northern California shelf, *Continental Shelf Research* 24 (1), 117-136.
- Okin, G.S., et al., 2011. Impacts of atmospheric nutrient deposition on marine productivity: Roles of nitrogen, phosphorous, and iron. *Global Biogeochemical Cycles*, Vol. 25, GB2022.
- Oregon State University, 2014. Ocean productivity products accessed 2014, at:
<http://www.science.oregonstate.edu/ocean.productivity/index.php>
- Orlanski, I., 1976. A simple boundary condition for unbounded hyperbolic flows. *J. Comp. Sci.*, 21(3), 251-269.
- Orphan, V.J., Ussler III, W., Naehr, T.H., House, C.H., Hinrichs, K.U. and C.K. Paull, 2004. Geological, geochemical, and microbiological heterogeneity of the seafloor around methane vents in the Eel River Basin, offshore California. *Chemical Geology* 205, 265-289.
- Pickett, M.H. and J.D. Paduan, 2003. Ekman transport and pumping in the California current based on the US Navy's high resolution atmospheric model (COAMPS). *J. Geophys. Res.* 108 (C10), doi:10.1029/2003.JC001902.

Pimenta, F.M., Campos, E.J.D., Miller, J.L. and A.R. Piola, 2005. A numerical study of the Plata River plume along the southeastern South American continental shelf. *Brazilian Journal of Oceanography*, Vol. 53 No. 3-4, July/Dec. 2005.

Piper, D.J.W., Normark, W.R. and J.C. Ingle, 1976. Rio Dell Formation - Plio-Pleistocene Basin Slope Deposit in Northern California. *Sedimentology* 23 (3), 309-328.

Pirie, D.M. and D.D. Steller, 1977. California coastal processes study. LANDSAT I, final report, NTIS E77-10158, 164 pp.

Platt, T. and S. Sathyendranath, 1993. The estimation of phytoplankton production in the ocean from chlorophyll and light data. *J. Geophys. Res.* 8, 14561-14576.

Powell, T.M., Lewis, C.V.W., Curchitser, E.N., Haidvogel, D.B., Hermann, A.J. and E.L. Dobbins, 2006. Results from a three-dimensional, nested biological-physical model of the California Current System and comparisons with statistics from satellite imagery. *J. Geophys. Res.* 111, C07018, doi:10.1029/2004JC002506.

Power, M.E., 1990a. Benthic turfs vs. floating mats of algae in river food webs. *OIKOS* 58 (1), 67-79.

Power, M.E., 1990b. Effects of fish in river food webs. *Science* 250 (4982), 811-814.

Power, M. E., J. C. Marks and M. S. Parker. 1992a. Variation in the vulnerability of prey to different predators: Community-level consequences. *Ecology* 73: 2218-2223.

Power, M. E. 1992b. Top down and bottom up forces in food webs: do plants have primacy? *Ecology* 73: 733-746.

Power, M. E. 1992c. Habitat heterogeneity and the functional significance of fish in river food webs. *Ecology* 73: 1675-1688.

Power, M.E., 2014. List of publications accessible on the World Wide Web, at URL: <https://ib.berkeley.edu/labs/power/publications.php>

Preisendorfer, R.W., 1988. *Principal Component Analyses in Meteorology and Oceanography*. Elsevier.

Prieß, M., Piwonski, J., Koziel, S., Oschlies, A., and T. Slawig, 2013. Accelerated Parameter Identification in a 3D Marine Biogeochemical Model Using Surrogate-Based Optimization. *Ocean Modeling* 68, 22-36.

Puig, P., Ogston, A.S., Mullenbach, B.L, Nittrouer, C.A., and R.W. Sternberg, 2003. Shelf-to-canyon sediment-transport processes on the Eel continental margin (northern California). *Marine Geology* 193, 129-149.

- Puig, P., Ogston, A.S., Mullenbach, B.L., et al, 2004. Storm-induced sediment gravity flows at the head of the Eel submarine canyon, northern California margin. *Journal of Geophysical Research-Oceans* 109 (C3).
- Pullen, J.D. and J.S. Allen, 2000. Modeling studies of the coastal circulation off Northern California: shelf response to a major Eel river flood event. *Continental Shelf Research* 20 (16), 2213-2238.
- Pullen, J.D., and Allen, J.S., 2001. Modeling studies of the coastal circulation off northern California: Statistics and patterns of wintertime flow. *Journal of Geophysical Research* 106: doi: 10.1029/2000JC000548. issn: 0148-0227.
- Rasch, P.J., 1994. Conservative shape-preserving two-dimensional transport on a spherical reduced grid, *Mon. Wea. Rev.*, 122, 1337-1350.
- Rathburn, A.E., Levin, L.A., Held, Z. and K.C. Lohmann, 2000. Benthic foraminifera associated with cold methane seeps on the northern California margin: Ecology and stable isotopic composition. *Marine Micropaleontology* 38, 247-266.
- Raymond, W.H. and H.L. Kuo, 1984. A radiation boundary condition for multi-dimensional flows, *Quart. J. R. Met. Soc.*, 110, 535-551.
- Redfield, A.C., 1934. On the proportions of organic derivations in sea water and their relation to the composition of plankton. In *James Johnstone Memorial Volume*. (ed. R.J. Daniel). University Press of Liverpool, pp. 177–192.
- Reed, C.W., Niedoroda, A.W. and D.J.P. Swift, 1999. Modeling sediment entrainment and transport processes limited by bed armoring. *Marine Geology* 154, 143-154.
- Reynolds, R.W., Rayner, N. A., Smith, T. M., Stokes, D. C., and W. Wang, 2002. An improved in situ and satellite SST analysis for climate. *J. Climate* 15, 1609–1625.
- Richardson, M.D., Briggs, K.B., Bentley, S.J., Walter, D.J. and T.H. Orsi, 2002. The effects of biological and hydrodynamic processes on physical and acoustic properties of sediments off the Eel River, California. *Marine Geology* 182, 121-139.
- Ritter, J.R., 1972. Sand transport by the Eel river and its effect on nearby beaches. *USGS Open-File Report*: 73-236.
- Roy, M., McManus, J., Goñi, M.A., Chase, Z., J.C. Borgeld, et al., 2013. Reactive iron and manganese distributions in seabed sediments near small mountainous rivers off Oregon and California (USA). *Continental Shelf Research* 54, 67-79.
- Ryther, J.H. and C.S. Yentsch, 1957. The estimation of phytoplankton production in the ocean from chlorophyll and light data. *Limol. Oceanogr.* 2, 281-286.

Saba, V.S., Friedrichs, M.A.M., Antoine, D., Armstrong, R.A., Asanuma, I., Behrenfeld, M.J., Ciotti, A.M., Dowell, M., Hoepffner, N., Hyde, K.J.W., Ishizaka, J., Kameda, T., Marra, J., Melin, F., Morel, A., O'Reilly, J., Scardi, M., Smith, W.O.Jr., Smyth, T.J., Tang, S., Waters, K., and T.K. Westberry, 2011. An evaluation of ocean color model estimates of marine primary productivity in coastal and pelagic regions across the globe. *Biogeosciences*, 8, 489-503.

Sabo, J.L. and M.E. Power. 2002. River-watershed exchange: Effects of riverine subsidies on riparian lizards and their terrestrial prey. *Ecology* 83: 1860-1869. Sabo, J.L. and M.E. Power. 2002. River-watershed exchange: Effects of riverine subsidies on riparian lizards and their terrestrial prey. *Ecology* 83: 1860-1869.

Sasaki, H., Sasai, Y., Nonaka, M., Masumoto, Y. and S. Kawahara, 2006. An eddy-resolving simulation of the quasi-global ocean driven by satellite-observed wind field. *Journal of the Earth Simulator* 6, 35-49.

Schade, J.D., K. MacNeill, S. A. Thomas, F. C. McNeely, J. R. Welter, J. Hood, M. Goodrich, M. E. Power, and J. C. Finlay. 2010. The stoichiometry of nitrogen and phosphorus spiraling in heterotrophic and autotrophic streams. *Freshwater Biology*. doi:10.1111/j.1365-2427.2010.02509.x

Schlosser, S. and A. Eicher, 2012. The Humboldt Bay and Eel River Estuary Benthic Habitat Project. California Sea Grant Publication T-075. 246 p.

Scully, M.E., C.T. Friedrichs, and L.D. Wright, 2002. Application of an analytical model of critically stratified gravity-driven sediment transport and deposition to observations from the Eel River continental shelf, northern California. *Continental Shelf Research*, 22: 1951-1974.

Scully, M.E., C.T. Friedrichs, and L.D. Wright, 2003. Numerical modeling results of gravity-driven sediment transport and deposition on an energetic continental shelf: Eel River, Northern California. *Journal of Geophysical Research*, 108 (C4): 17-1 - 17-14.

Severmann, S., McManus, J., Berelson, W.M. and D.E. Hammond, 2010. The continental shelf benthic iron flux and its isotopic composition. *Geochimica et Cosmochimica Acta* 74 (14), 3984-4004.

Shapiro, R., 1970. Smoothing, filtering, and boundary effects. *Rev. Geophys. Space Phys* 8, 359-87.

Shchepetkin, A.F., and J.C. McWilliams, 1998. Quasi-monotone advection schemes based on explicit locally adaptive dissipation, *Monthly Weather Rev.*, 126, 1541-1580.

Shchepetkin, A.F., and J.C. McWilliams, 2005. The Regional Ocean Modeling System: A split-explicit, free-surface, topography following coordinates ocean model, *Ocean Modelling*, 9, 347-404.

Signell, R., 2013. SeaGrid Orthogonal Grid Maker for Matlab available on the World Wide Web, accessed 2013 at <http://woodshole.er.usgs.gov/operations/modeling/seagrid/index.html>

Sivapalan, M., Ruprecht, J. K. and N.R. Viney, 1996. Water and salt balance modelling to predict the effects of land-use changes in forested catchments. I. Small catchment water balance model. *Hydrological Processes* 10, 393-411.

Smith R. L. 1992. Coastal upwelling in the modern ocean. Geological Society, London, Special Publications 64: 9-28.

Smolarkiewicz, P. K., 1984. A fully multidimensional positive definite advection transport algorithm with small implicit diffusion. *J. Comp. Phys.*, 54, 325-362.

Smolarkiewicz, P. K. and T. L. Clark, 1986. The multidimensional positive definite advection transport algorithm: further development and applications. *J. Comp. Phys.*, 67, 396-438.

Smolarkiewicz, P. K. and W. W. Grabowski, 1990. The multidimensional positive definite advection transport algorithm: non-oscillatory option. *J. Comp. Phys.*, 86, 355-375.

Sommerfield, C.K. and C.A. Nittrouer. 1999. Modern accumulation rates and a sediment budget for the Eel shelf: a flood-dominated depositional environment. *Marine Geology*, 154, 227-241.

Sommerfield, C.K., Nittrouer, C.A. and C.R. Alexander, 1999. Be-7 as a tracer of flood sedimentation on the northern California continental margin. *Continental Shelf Research* 19 (3), 335-361.

Sommerfield, C.K., Aller, R.C. and C.A. Nittrouer, 2001. Sedimentary Carbon, Sulfur, and Iron Relationships in Modern and Ancient Diagenetic Environments of the Eel River Basin (U.S.A). *Journal of Sedimentary Research, Section A: Sedimentary Petrology and Processes* 71 (3), 335-345.

Sommerfield, C.K., Drake, D.E. and R.A. Wheatcroft, 2002. Shelf record of climatic changes in flood magnitude and frequency, north-coastal California. *Geology* 30 (5), 395-398.

Sommerfield, C.K. and R.A. Wheatcroft, 2007. Late Holocene sediment accumulation on the northern California shelf: Oceanic, fluvial and anthropogenic influences. *Geological Society of America Bulletin* 119: 1120-1134.

Song, Y. and D. B. Haidvogel, 1994. A semi-implicit ocean circulation model using a generalized topography-following coordinate system, *J. Comp. Phys.*, 115 (1), 228-244.

Spaulding, M.L., 2010. Estuarine and Coastal Modeling. *Proceedings of the Eleventh International Conference*. ASCE ISBN 978-0-7844-1121-6.

Sternberg, R.W., Berhane, I. and A.S. Ogston, 1999. Measurement of size and settling velocity of suspended aggregates on the northern California continental shelf. *Marine Geology* 154, 43-53.

Stopa, J.E. and K.F. Cheung, 2014. Intercomparison of wind and wave data from the ECMWF Reanalysis Interim and the NCEP Climate Forecast System Reanalysis. *Ocean Modeling*, 75, 65-83.

Strub, P.T. and C. James, 2000. Altimeter-derived variability of surface velocities in the California Current System: 2. Seasonal circulation and eddy statistics. *Deep Sea Res., Part II*, 47, 831-870.

Syvitski, J.P.M. and Alcott, J.M., 1993. GRAIN2: Predictions of particle size seaward of river mouths. *Computers & Geosciences* 19 (3), 399-446.

Syvitski, J.P. and J.M. Alcott, 1995. RIVER3: Simulation of water and sediment river discharge from climate and drainage basin variables. *Computers and Geoscience* 21: 89-151 DOI: 10.1016/0098-3004(94)00062-Y

Syvitski, J.P., Morehead, M.D. and M. Nicholson, 1998a. HYDROTREND: A climate-driven hydrologic transport model for predicting discharge and sediment load to lakes or oceans. *Computers & Geoscience* 24 (1), 51-68.

Syvitski, J. P. M., Nicholson, M., Skene, K., and Morehead, M. D., 1998b, Plume 1.1: Deposition of sediment from a fluvial plume: *Computers & Geosciences*, 24 (2), 159-171.

Syvitski, J.P. and M.D. Morehead, 1999. Estimating river-sediment discharge to the ocean: application to the Eel margin, northern California. *Marine Geology* 154, 13-28.

Syvitski, J.P., Morehead, M.D., Bahr, J.B. and T. Mulder, 2000. Estimating fluvial sediment transport: The rating parameters. *Water Resources Research* 36 (9), 2747-2760.

Syvitski, J.P.M. and E.W.H. Hutton, 2001. 2D SEDFLUX 1.0C: an advanced process-response numerical model for the fill of marine sedimentary basins. *Computer & Geosciences*, 27: 731-753., 10.1016/S0098-3004(00)00139-4

Syvitski, J.P., Peckham, S.D., Hilberman, R. and T. Mulder, 2003. Predicting the terrestrial flux of sediment to the global ocean: a planetary perspective. *Sedimentary Geology* 162, 5-24.

Syvitski, J.P.M. and J.D. Milliman, 2007. Geology, Geography and Humans Battle for Dominance over the Delivery of Fluvial Sediment to the Coastal Ocean. *Journal of Geology* 115, 1-19.

Talling, J.F., 1957. The phytoplankton population as a compound photosynthetic system. *New. Phytol.* 56, 133-149.

Taylor, K.E., 2001. Summarizing multiple aspects of model performance in a single diagram. *J. Geophys. Res.* 106, 7183-7192.

Thomas, R.B., 1988. Monitoring baseline suspended sediment in forested basins: the effects of sampling on suspended sediment rating curves. *Hydrological sciences Journal* 33, 499-514.

Thornton, P.E., M.M. Thornton, B.W. Mayer, N. Wilhelm, Y. Wei, R. Devarakonda, and R.B. Cook. 2014. Daymet: Daily Surface Weather Data on a 1-km Grid for North America, Version 2. Data set. Available on-line [<http://daac.ornl.gov>] from Oak Ridge National Laboratory Distributed Active Archive Center, Oak Ridge, Tennessee, USA. Date accessed: 2014/09/01. Temporal range: 1985/01/01-2010/12/31. Spatial range: N=42, S=40, E=-122, W=-124. <http://dx.doi.org/10.3334/ORNLDAAAC/1219>

Toda, H.Y. and T. Yamamoto, 1995. Statistical inferences in vector autoregressions with possibly integrated processes. *Journal of Econometrics* 66, 225-250.

Traykovski, P., Geyer, W.R., Irish, J.D. and J.F. Lynch, 2000. The role of wave-induced density-driven fluid mud flows for cross-shelf transport on the Eel River continental shelf. *Continental Shelf Research* 20 (16), 2113-2140.

Tsujino, H., et al, 2010. Reference manual for the meteorological research institute community ocean model (MRI.COM) version 3. Technical Reports of the Meteorological Research Institute, No. 59.

Underwood, M.B., 1985. Sedimentology and hydrocarbon potential of Yager structural complex - possible Paleogene source rocks in Eel River Basin, Northern California. *AAPG* 67 (7), 1088-1100.

U.S. Geological Survey, 2011, National Elevation Dataset available on the World Wide Web, accessed 2011, at URL <http://ned.usgs.gov/>.

U.S. Geological Survey, 2012, National Water Information System data available on the World Wide Web (Water Data for the Nation), accessed 2012, at URL http://http://nwis.waterdata.usgs.gov/usa/nwis/qwdata/?site_no=11477000.

Wajsowicz, R.C., 1993. A consistent formulation of the anisotropic stress tensor for use in models of the large-scale ocean circulation, *J. Comput. Phys.*, 105, 333-338.

Walling, D.E., 1977a. Assessing the Accuracy of Suspended Sediment Rating Curves for a Small Basin. *Water Resources Research* Vol. 13, No. 3, pp. 531-538.

Walling, D.E., 1977b. Limitations of the rating curve technique for estimating suspended sediment loads, with particular reference to British rivers. *Erosion and solid matter transport in inland waters*. IAHS publication, Wallingford, 122, 34-48 (proceedings of the Paris symposium, July 1977)

- Walsh, J.P. and C.A. Nittrouer. 1999. Observations of sediment flux on the Eel continental slope, northern California, *Marine Geology*, 154, 55-68.
- Wang, X. J., Behrenfeld, M., LeBorgne, R. Murtugudde, R., and E. Boss. 2009. Regulation of phytoplankton carbon to chlorophyll ratio by light, nutrients and temperature in the equatorial Pacific Ocean: A basin-scale model, *Biogeosciences*, 6, 391–404.
- Warner, J.C., Geyer, W.R. and J.A. Lerczak, 2005. Numerical modeling of an estuary: A comprehensive skill assessment. *J. Geophys. Res.* 110, C05001, doi:10.1029/2004JC002691.
- Warrick, J.A., Madej, M.A., Goñi, M.A. and R.A. Wheatcroft, 2013. Trends in the suspended-sediment yields of coastal rivers of northern California, 1955-2010. *Journal of Hydrology* 489, 103-123.
- Warrick, J.A., 2014. Eel River margin source-to-sink sediment budgets: Revisited. *Marine Geology* 351, 25-37.
- Wheatcroft, R.A., Borgeld, J.C., et al, 1996. The Anatomy of an Oceanic Flood Deposit. *Oceanography* 9(3):158–162, <http://dx.doi.org/10.5670/oceanog.1996.03>
- Wheatcroft, R.A., Sommerfield, C.K., Drake, D.E., et al., 1997. Rapid and widespread dispersal of flood sediment on the northern California margin. *Geology* 25 (2), 163-166.
- Wheatcroft, R.A. and J.C. Borgeld, 2000. Oceanic flood deposits on the northern California shelf: large-scale distribution and small-scale physical properties. *Continental Shelf Research* 20 (16), 2163-2190.
- Wheatcroft, R.A. and D.E. Drake, 2003. Post-depositional alteration and preservation of sedimentary event layers on continental margins, I. The role of episodic sedimentation. *Marine Geology* 199: 123-137.
- Wheatcroft, R.A. and C.K. Sommerfield, 2005. River sediment flux and shelf accumulation rates on the Pacific Northwest margin. *Continental Shelf Research* 25: 311-332.
- Wheatcroft, R.A., Goñi, M.A., Hatten, J.A., Pasternack, G.B. and J.A. Warrick, 2010. The role of effective discharge in the ocean delivery of particulate organic carbon by small, mountainous river sisters. *Limnol. Oceanogr.* 55 (1), 161-171.
- Wright, L.D., Kim, S.C., and C.T. Friedrichs, 1999. Across-shelf variations in bed roughness, bed stress and sediment suspension on the northern California shelf. *Marine Geology* 154, 99-115.
- Wright, L.D., C.T. Friedrichs, S.C. Kim, and M.E. Scully, 2001. The effects of ambient currents and waves on gravity-driven sediment transport on continental shelves. *Marine Geology*, 175: 25-45.

Wright, L.D., Friedrichs, C.T. and M.E. Scully, 2002. Pulsational gravity-driven sediment transport on two energetic shelves. *Continental Shelf Research* 22, 2443-2460.

Wright, L.D. and C.T. Friedrichs, 2007. Gravity-driven sediment transport on continental shelves: A status report. *Continental Shelf Research* 26, 2092-2107.

Yu, Y., Zhang, H. and C.J. Lemckert, 2011. The response of the river plume to the flooding in Moreton Bay, Australia. *Journal of Coastal Research*, Vol. 2, SI 64, 1214-1218.

Yun, J.W., Orange, D.L. and M.E. Field, 1999. Subsurface gas offshore of northern California and its link to submarine geomorphology. *Marine Geology* 154, 357-368.

Zhang, Y., Swift, D.J.P., Fan, S.J., et al., 1999. Two-dimensional numerical modeling of storm deposition on the northern California shelf. *Marine Geology* 154, 155-167.

Zhang, Y. and A.M. Baptista, 2008. SELFE: A semi-implicit Eulerian-Lagrangian finite-element model for cross-scale ocean circulation. *Ocean Modelling* 21, 71-96.